Cosmology With Planck: An All-Sky Temperature And Polarisation Analysis

Christopher M Crowe
Institute of Astronomy & Sidney Sussex College
University of Cambridge

Under the supervision of
Professor George Efstathiou

A thesis submitted for the degree of
Doctor of Philosophy
28th September 2013

This dissertation is the result of work I have undertaken between 2009 and 2013 as a research student at the Institute of Astronomy and the Kavli Institute for Cosmology, Cambridge. I hereby declare that my thesis is not substantially the same as any that I have submitted for a degree or diploma or other qualification at any other University. I further state that no part of my thesis has already been, or is concurrently being, submitted for any such degree, diploma or other qualification.

Except where stated in the text, all of the work in this thesis has been carried out by the author. Various figures throughout the text are reproduced or adapted from the work of other authors, for illustration or discussion. Such figures are always credited in the associated caption.

This thesis contains fewer than sixty thousand words.

Christopher M Crowe September 2013

I dedicate this thesis to my parents.

Acknowledgements

Over the last 5 years in Cambridge I have thoroughly enjoyed living in one of the most enchanting cities in the world. It was during my one-year Part III course in mathematics that I first met my second supervisor, Anthony Challinor, when he suggested that I should apply for a PhD. Later in 2009 I also met my primary supervisor-to-be George Efstathiou who informed me that it would be a good time to get involved with the Planck project. That has proved to be a sound suggestion, as I have found my work to be engaging, varied, and most of all interesting. Following our many conversations about sports cars or racing motorbikes, George would often mention another 'interesting avenue for exploration' which would then keep me busy for several weeks. His coding is always helpful and efficient, although I would not describe wading through thousands of lines of uncommented Fortran as my perfect night in! He is an inspiring teacher and a distinguished cosmologist. His engaging lectures and vast knowledge of every area of astrophysics has been an inspiration to me and had such a positive impact on my way of life, and I hope to continue learning from him in the future. Anthony Challinor has also been a huge help (often when I came out of a meeting with George rather frazzled) and has the amazing ability to recite from memory without a moment's thought any and all derivations that I enquired about, and I am forever indebted to both of them for the time they have spent and the patience they have shown with me throughout my time in Cambridge.

Steven Gratton has been a great help to me whenever I ran into problems, particularly with Fortran and C++, and he helped me to correct some of my code used in Chapter 2. Without him I would have almost certainly spent twice as long debugging my code. Mark Ashdown, Michael Bridges, Paul Hewett, Carolin Crawford, and all the administrative team have also been very supportive to me at the Institute of Astronomy, whether helping with supercomputer access, preparing lectures for public observing nights, or running school visits.

Sidney Sussex College has also been a large part of my PhD life. I threw myself headfirst into University boards, students unions, and extracurricular societies, and I'd like to thank all the people who made life that little bit easier, who number far too many to list individually. The Master(s) and Fellows of the college and the entire MCR community have been so supportive of my activities, and the college has financially supported a number of overseas conferences I have travelled to during my PhD. I'd particularly like to thank: Julius Ross, Iain Black, Andrew Wallace-Hadrill, Max Beber, Kirsten Dickers, Marianne Oyler, Stephen Mather, Colin Maxted and all the porters who have made life that bit more enjoyable in college. I am also very grateful to the STFC who have funded my PhD studentship and travel expenses. My friends have made the social aspect of life in Cambridge and elsewhere hugely fulfilling and enjoyable, and I'd like to thank Tom Rix, Steve Casey, Jon Budzynski, Stacie Powell, Anjali Tripathi, and my officemate Alex Hall (who makes the cut due to a reciprocal acknowledgement in his thesis). A special mention goes to Jonathon for hours of proofreading. You will all almost certainly never read this but I am truly blessed to have such amazing friends. I am also hugely thankful to have such an amazing girlfriend and partner

in crime, Kelly, who has always been supportive and brought me cups of tea during my all-night coding marathons at 4am.

Last but certainly not least, completing a PhD is not possible without the unwavering support from my family. In addition to the support from Sylv, Carl, and Katie, I would like to thank my Mother Rita Crowe, who has always been there for me every step of the way, and my Father Tom Crowe who I hope is looking down on me from somewhere among the stars, smiling.

Thesis Summary

Cosmology With Planck: An All-Sky Temperature And Polarisation Analysis

Christopher M Crowe September 2013

Cosmology is now a precision science. The temperature anisotropies in the cosmic microwave background (CMB) have been exquisitely mapped by many experiments over the last decade. The Planck satellite was launched in 2009, observed the sky in temperature and polarisation, and released the nominal mission temperature data to the public in 2013. Planck has shed new light on CMB polarisation anisotropies and the polarisation signal from our own galaxy, and knowledge of the galactic emission forms a central part of this analysis presented in this thesis.

I first introduce the background cosmology and review what we know about CMB temperature and polarisation anisotropies, including their mathematical formulation and representation on the sphere. I review our knowledge of the origin of galactic polarised foregrounds, particularly electron synchrotron and thermal dust emission. I then describe the generation of polarised CMB maps from an input cosmological model, and the generation of CMB polarised foregrounds using a variety of methods to create full-sky maps of the microwave sky at the Planck observing frequencies between 30 and 353 GHz. I develop a parametric fitting maximum-likelihood polarised component separation routine with correlated foreground parameters to extract the CMB and associated foregrounds to a high precision, and show that my method can reliably recover a primordial B-mode polarisation signal at $r = 0.1$ at multiple map resolutions.

I then test the sky model against the full mission Planck data to examine how accurately the foregrounds are simulated, and find that along the galactic plane the simulations are accurate, but at high latitudes the agreement worsens. I also compare the polarisation morphology to that seen in the WMAP data and find a tension between Planck and WMAP. I present an analysis of the dx8 polarisation data in terms of polarised amplitudes and orientations, and investigate a variety of foreground separation routines to get a feel for the reliability of the data. Significant systematic issues are found and I conclude that in their current state, the polarisation data are not reliable enough for precise cosmology.

Finally I develop a Fisher matrix analysis of the temperature power spectrum using the full mission covariance matrix to explore the parameter space around a CosmoMC simulation, and extract the principal components for different models. I use this to explore a strange oscillation in the power spectrum and conclude that it is a statistical fluke, a conclusion confirmed in a recent data release. I close by offering extensions to the work and a look into the future of the field.

Contents

Contents vii

List of Figures xi

1 Introduction 1

1.1 Cosmology . . . 3
1.1.1 The History of Cosmological Ideas . . . 3
1.1.2 The Big Bang . . . 4
1.1.3 The Friedmann Equations . . . 5
1.1.4 Inflation . . . 6
1.1.5 Dark Matter and Dark Energy . . . 17
1.1.6 Precision Cosmology . . . 18
1.2 The Cosmic Microwave Background . . . 19
1.2.1 The Black Body Spectrum . . . 20
1.2.2 Temperature Anisotropies . . . 20
1.2.3 Polarization Anisotropies . . . 24
1.2.4 Gravitational Waves and B-modes . . . 26
1.2.5 Observational Parameters . . . 28
1.3 The Planck Satellite . . . 34
1.4 Foregrounds . . . 37
1.5 CMB Notation . . . 39
1.5.1 Stokes Parameterisation . . . 39
1.5.2 Spin-weighted Fields on the Sphere . . . 41
1.5.3 E and B-Modes . . . 42
1.5.4 Power Spectra . . . 43
1.5.5 Units . . . 43
1.5.6 HEALPix . . . 43
1.6 Goals of the Thesis . . . 45

2 Sky Simulation and Parametric Fitting 47

2.1 Introduction . . . 47

2.1.1 Knowledge of Polarised Emission . . . 48
2.1.2 CMB . . . 48
2.1.3 Synchrotron . . . 49
2.1.4 Thermal Dust . . . 53
2.1.5 Free-Free . . . 55
2.1.6 Other Sources . . . 55
2.2 Foreground Separation Techniques . . . 56
2.2.1 Internal Linear Combination . . . 57
2.2.2 Spectral Matching Independent Component Analysis . . . 58
2.2.3 Maximum Entropy Method . . . 59
2.2.4 Template Cleaning . . . 60
2.2.5 Parametric Fitting . . . 61
2.3 Sky Simulation . . . 62
2.3.1 CMB . . . 62
2.3.2 Synchrotron . . . 64
2.3.3 Thermal Dust . . . 69
2.3.4 Noise . . . 70
2.4 Parametric Fitting . . . 75
2.4.1 Motivation for Correlated Spectral Indices . . . 75
2.4.2 Method . . . 76
2.4.3 Likelihood . . . 77
2.5 Results . . . 83
2.5.1 Testing for Bias: Foreground-Free Simulations . . . 84
2.5.2 Foreground Separation . . . 84
2.5.3 Likelihoods . . . 91
2.6 Conclusion . . . 96

3 Comparing Planck Data to the Sky Model 98
3.1 Introduction/PSM Overview . . . 99
3.2 Level of Polarisation . . . 100
3.2.1 Synchrotron . . . 100
3.2.2 Dust . . . 103
3.3 Amplitude and Polarisation angle . . . 109
3.3.1 Synchrotron . . . 109
3.3.2 Dust . . . 111
3.4 Spectral Index Models . . . 115
3.4.1 Synchrotron . . . 115
3.4.2 Dust . . . 116
3.5 Behaviour with Frequency . . . 125
3.6 CAM-SPEC Spectra . . . 126

3.6.1 CAM-SPEC . . . 126
3.7 Conclusion . . . 134

4 Probing Planck dx8 Polarisation maps 136
4.1 Preparing DX8 Maps . . . 137
4.1.1 Bandpass Correction . . . 137
4.1.2 Degrading Resolution . . . 139
4.1.3 Creating Galactic Polarisation Masks . . . 139
4.2 Comparison with WMAP . . . 147
4.3 Template Fitting . . . 149
4.3.1 WMAP23-WMAP61-HFI353 Results . . . 150
4.3.2 WMAP23-LFI70-HFI353 . . . 151
4.3.3 WMAP23-HFI100-HFI353 Results . . . 151
4.3.4 WMAP23-HFI143-HFI353 . . . 156
4.4 Comparison with ILC . . . 161
4.4.1 ILC Results . . . 162
4.5 Parametric Fitting . . . 164
4.6 Systematics . . . 167
4.7 QML Power Spectrum Estimates . . . 168
4.7.1 The QML Estimator . . . 169
4.7.2 QML Results . . . 170
4.8 Conclusion . . . 172

5 Fisher Analysis and Parameter Degeneracies for Planck 174
5.1 Parameter Degeneracies for Planck . . . 174
5.1.1 Breaking Degeneracies . . . 176
5.1.2 Calculating C_ℓ Derivatives . . . 177
5.2 Parameter Estimation for Planck . . . 178
5.3 Fisher Approximation . . . 178
5.3.1 Fisher Framework . . . 178
5.3.2 Results . . . 180
5.4 Parameter Degeneracies . . . 182
5.4.1 Eigenvectors of the Fisher Matrix . . . 182
5.5 Oscillations in the Power Spectrum . . . 188
5.5.1 Quantising the Planck Data . . . 188
5.5.2 Testing Models . . . 189
5.6 Conclusion . . . 191

6 Conclusion 193

A CAM-SPEC Cosmological Model Parameters 197

Appendices **197**

References **198**

List of Figures

1.1 Small, large, and hybrid models of inflation . . . 15
1.2 FIRAS black-body CMB spectrum . . . 21
1.3 Temperature power spectrum from WMAP, ACBAR and others . . . 22
1.4 WMAP 9-year CMB temperature anisotropies . . . 24
1.5 Thomson scattering . . . 25
1.6 Summary of B-mode spectrum upper limits . . . 27
1.7 Concordance CMB power spectra . . . 29
1.8 MCMC parameter forecasts for Planck . . . 32
1.9 n_s and r constraints from WMAP+BAO+H_0 . . . 33
1.10 Planck all-sky public release . . . 36
1.11 Synchrotron and thermal dust radiation illustration . . . 38
1.12 HEALPix spherical partition . . . 45

2.1 WMAP 3-year E and B-mode spectra . . . 51
2.2 Synchrotron polarisation fraction from WMAP . . . 52
2.3 Archeops Q and U data at 353 GHz . . . 54
2.4 CAMB-generated CMB power spectra . . . 65
2.5 Haslam 408 MHz radio intensity map . . . 66
2.6 Synchrotron spectral index map simulations and histograms . . . 67
2.7 Synchrotron polarisation angle simulation . . . 69
2.8 Thermal dust intensity at 100 μm . . . 70
2.9 Temperature and polarisation rms fluctuations 30-353 GHz . . . 72
2.10 Full-sky coadded Planck Q/U simulations 30-100 GHz . . . 73
2.11 Full-sky coadded Planck Q/U simulations 143-353 GHz . . . 74
2.12 Normalised low-resolution noise covariance matrices . . . 82
2.13 Foreground-free parametric fitting inputs and outputs . . . 85
2.14 Foreground-free posterior distributions . . . 86
2.15 Pixel residual distribution for one simulation . . . 86
2.16 Parametric fitting full solutions with correlation . . . 88
2.17 Recovered synchrotron emission from parametric fitting . . . 89

2.18 Recovered dust emission from parametric fitting . . . 90
2.19 Pixel residuals plot with galactic latitude . . . 91
2.20 Pixel rms residuals and averaged CMB Fisher errors . . . 92
2.21 Recovered B-mode Q/U maps . . . 93
2.22 Posterior likelihood distributions for 10 simulations . . . 95

3.1 LFI 30 and 44 GHz fractional polarisation . . . 101
3.2 LFI 30 GHz fractional polarisation at higher resolutions . . . 101
3.3 Fractional polarisation change with galactic latitude . . . 102
3.4 PSM fractional polarisation at 30 GHz . . . 103
3.5 PSM fractional polarisation at 217 and 353 GHz . . . 104
3.6 Fractional polarisation with galactic latitude at 217 and 353 GHz . . . 105
3.7 Fractional polarisation at 353 GHz with geometric depolarisation . . . 106
3.8 PSM-Planck fractional polarisation residuals . . . 108
3.9 Bandpass corrected 30 GHz LFI maps . . . 110
3.10 HFI 353 GHz data with PSM model and residuals . . . 112
3.11 30 and 353 GHz polarisation angle . . . 114
3.12 Synchrotron spectral index variation for LFI . . . 117
3.13 Smoothed synchrotron spectral index variation for LFI . . . 118
3.14 Synchrotron spectral index variation with latitude . . . 119
3.15 Dust spectral index variation for HFI . . . 121
3.16 Smoothed dust spectral index variation for HFI . . . 122
3.17 Dust spectral index variation with galactic latitude . . . 124
3.18 Average spectral index variation with frequency . . . 126
3.19 Polarisation masks for CAM-SPEC analysis . . . 128
3.20 Beam transfer functions . . . 129
3.21 CAM-SPEC TE cross spectra averaged over detectors . . . 131
3.22 CAM-SPEC EE cross spectra averaged over detectors . . . 132
3.23 Mask 1 - Mask 2 residuals averaged over detectors . . . 133

4.1 LFI bandpass correction maps . . . 141
4.2 Low resolution bandpass correction maps . . . 142
4.3 Low resolution bandpass corrected LFI Q maps . . . 143
4.4 Low resolution bandpass corrected LFI U maps . . . 144
4.5 Fraction of sky masked with cutoff amplitude . . . 145
4.6 Polarisation masks with decreasing cutoff amplitude . . . 146
4.7 WMAP-LFI 70 GHz correspondence . . . 148
4.8 Template cleaning with 23 GHz, 61 GHz, and 353 GHz contours . . . 151
4.9 Template cleaning with 23 GHz, 61 GHz, and 353 GHz . . . 152
4.10 Contributions from 23 GHz and 353 GHz to 61 GHz . . . 153

4.11 Template cleaning with 23 GHz, 70 GHz, and 353 GHz . . . 154
4.12 Contribution from 23 GHz and 353 GHz to 70 GHz . . . 155
4.13 Template cleaning with 23 GHz, 100 GHz, and 353 GHz . . . 157
4.14 Contribution from 23 GHz and 353 GHz to 100 GHz . . . 158
4.15 Template cleaning with 23 GHz, 143 GHz, and 353 GHz . . . 159
4.16 Contribution from 23 GHz and 353 GHz to 143 GHz . . . 160
4.17 ILC Solutions for different map combinations . . . 163
4.18 Parametric fitting solutions for CMB Q/U . . . 165
4.19 Parametric fitting solutions for synchrotron and dust Q/U . . . 166
4.20 Estimated systematic contribution maps . . . 168
4.21 100 GHz nominal mission noise covariance matrices . . . 171
4.22 QML estimation for low resolution E and B-mode spectra . . . 172

5.1 Nearly degenerate cosmological models in CAMB . . . 175
5.2 Temperature power spectrum derivatives . . . 178
5.3 Diagonal components of the covariance matrix . . . 181
5.4 Initial and final temperature power spectra . . . 181
5.5 TT, TE, and EE power spectra for Planck and WMAP . . . 186
5.6 Raw unbinned temperature power spectrum with fiducial model . . . 187
5.7 Improved temperature power spectrum with residuals . . . 188
5.8 Derivative of the temperature power spectrum with respect to H_0 . . . 189
5.9 Derivative of the temperature power spectrum with respect to w . . . 191

Astronomy? Impossible to understand and madness to investigate
-Sophocles

Chapter 1

Introduction

Over the last one hundred years there has been an exponential increase in our understanding of the Universe in which we live. Astrophysics has evolved into a highly numerical discipline, and observational astronomers spend most of their time at a computer terminal, analysing the increasingly large amount of data created from ever more complex experiments, rather than at an observatory. Over the last twenty years, the field of cosmology has evolved from a theoretically-driven discipline into a precise data-driven science. This evolution has largely been due to the impressive computational and technological breakthroughs that have facilitated many of the modern cosmological experiments. The modern standard cosmological model is underpinned by a variety of astrophysical observations, and increases in precision with each experimental iteration. Observations of the cosmic microwave background (hereafter CMB) [1] [2] [3] [4] , spectral measurements of Type Ia supernovae [5] [6] [7], and detailed galaxy clustering catalogues such as the 2dF Galaxy Redshift Survey and the Sloan Digital Sky Survey (SDSS) [8] [9] have culminated in the concordance ΛCDM cosmological model, defined by its constituent baryonic, dark matter, and dark energy content. Observational evidence strongly supports a Universe that is spatially flat and dominated by a component responsible for driving the accelerating expansion. Approximately 5% of the universe is composed of observable baryonic matter, with a further 27% contribution from *cold dark matter* (hereafter CDM) [10]. The existence of dark matter was originally inferred by Zwicky in 1933 from observations of the mass-to-light ratio of clusters of galaxies [11], and then in 1969 from discrepencies between observations of galactic rotation curves and the expected rotation curves inferred from the luminosity distributions [12]. Subsequent observations including X-ray measurements of massive galaxy clusters and their gravitational interaction [13] [14], Lyman-α fluxes [15], and constriants from CMB data [4] have helped further to characterise the elusive dark matter. Many competing theories for dark matter candidates have been proposed, and many high-profile experiments are underway to try directly to detect candidate particles, particularly weakly-interacting relic particles. [16] [17]. The remaining 68% of the energy density is modelled as the mysterious *dark energy* component, a theoretical construct developed to try and explain supernovae measurements that

imply the expansion of the Universe is accelerating. Dark energy may represent an as yet unknown constituent of our Universe such as a scalar field, or alternatively it may reflect an error in the basic physical laws we use to model the evolution of the Universe. The cosmological constant Λ in Einstein's equations is the current observationally and theoretically favoured framework for dark energy, and leads to the concordance ΛCDM model that has been extensively tested by modern cosmological experiments.

To understand our present universe, we must look back to the origin of the structure we see around us today, to a time when the Universe was very dense and hot, to an era when the microwave background was generated and to when a period of rapid exponential expansion took place. As we discuss in Section 1.1.4, the Universe must have gone through an inflationary phase. In inflationary models, quantum fluctuations generated immediately after the big bang seeded the curvature fluctuations which grew throughout inflation eventually to form the large-scale structure we measure today. The fluctuations imprint characteristic features on the CMB which can be measured to high accuracy and grow by gravitational instability to produce the observed non-linear cosmic web we see today in large scale surveys.

The theory and observation of the angular power spectrum of the CMB temperature fluctuations is now a very well developed textbook subject. Many experiments have characterised the shape of the spectrum over a large range of angular scales, and the ESA Planck satellite (hereafter Planck) will stand as the final word in the temperature analysis [18]. CMB polarisation observations however, are still in their infancy, and were observed for the first time in 2002 by DASI [19]. There are currently many experiments attempting to characterise the polarisation spectra, both to break degeneracies with the temperature spectrum and to learn more about physics of the early Universe. The detection of a divergence-free magnetic-type pattern in the polarisation fluctuations would be an important piece of evidence in favour of the inflationary scenario, and as will become clear in what follows, the correct interpretation of the polarisation data can teach us a great deal about the underlying physics of the early Universe and about inflation itself.

In this chapter, we shall first introduce the standard background cosmology, then introduce inflation and its predictions for the CMB polarisation. We then look at measurements of the CMB angular power spectrum and their consequence for cosmological parameter estimation, followed by an introduction to the Planck satellite and its capabilities for polarisation. Finally we summarise the objectives of the thesis.

1.1 Cosmology

1.1.1 The History of Cosmological Ideas

The cornerstone of modern cosmology is the powerful and simple idea that we occupy no special place in the Universe. This is known as the *cosmological principle*. This is now widely accepted among astrophysicists, however it sits in stark contrast to previously long-held ideas about our special place in the Universe.

The majority of ancient Greeks firmly believed that the Earth sat at the centre of the cosmos, encircled by the Sun and Moon. This idea was further developed by Ptolemy of Alexandria to include a fixed background of stars more distant than our Solar System. A complex system of circular orbits called Ptolemy's epicycles was devised to explain the observed motion of the planets, and this included the observed retrograde motion where some temporarily reverse direction. It was not until the 1500s that Copernicus forcefully stated the view that that the anthropocentric cosmos placing the Earth at the centre, should be replaced with one that views the Earth as orbiting the Sun. He too though held that the Sun should still occupy the centre of the Universe.

In the 1600s Newton formulated his mathematical model of the Solar System, and set the theoretical framework for Kepler's then empirical observations of the elliptical orbits of the planets. Newton also believed that every distant star was a sun just like our own. He thought these to be distributed randomly throughout space, constant and unevolving.

Further observations over the next few hundred years started to convince astronomers that the distribution of stars was not in fact uniform, but direction dependent, with a significant excess in the direction we now know to be our Galactic centre. In the 1700s, Herschel identified the disc-like structure of our Galaxy, but incorrectly concluded that our Solar System was the centre of the Galaxy. It was not until the 1900s that Shapley deduced the Solar System to be some two-thirds of the radius of the Galaxy away from its centre, which we now know to be correct.

The famous Shapley-Curtis debate in 1920 was a turning point for cosmology. Shapley argued that observed nebulae were but small structures within our own Galaxy. Curtis argued that each such nebula was in fact a separate distinct entity, much like our own Galaxy. The work of Hubble later on in the decade showed that our Galaxy is but one of millions of others in our patch of the Universe, each largely similar but unique [20]. Baade's work in the 1960s further demonstrated that the Milky Way is a fairly typical galaxy, which led to the modern view known as the *cosmological principle*: the Universe we inhabit is the same wherever you observe it from, and in whichever direction you look [21].

This seemingly simple statement has far-reaching and important consequences. It also holds more accurately as larger scales are considered. At the level of individual galaxies the Universe is extremely inhomogeneous and anisotropic, but as one considers groups of galaxies and superclusters

of such groups, the large-scale structure tends towards statistical isotropy and homogeneity. This cosmological principle underpins the idea of big bang cosmology, the modern view of how the Universe is evolving and how it looked in its infancy. Big bang cosmology had to compete with the steady-state view, pioneered by Bondi, Gold and Hoyle. The steady-state universe stands in direct opposition to the evolving view presented by the big bang, but the observations explained in the following section support the big bang so comprehensively that the steady-state view is now almost never considered.

1.1.2 The Big Bang

One piece of evidence in favour of the (hot) big bang is the observation that everything appears to be moving away from us (with the exception of a very small number of galaxies). This is observed via the stretching of light from distant galaxies, known as the *redshift* z defined as

$$z = \frac{\lambda_{\text{obs}} - \lambda_{\text{em}}}{\lambda_{\text{em}}}, \tag{1.1}$$

where λ_{obs} is the observed wavelength of light and λ_{em} is the wavelength at emission. If a nearby (i.e. low redshift) galaxy is receding from us with velocity v then its redshift is given by

$$z = \frac{v}{c}. \tag{1.2}$$

Hubble observed a linear relationship between the distance r to a galaxy and its recession velocity, dependent on a factor called the Hubble constant, given for a particular object by

$$H_0 = \frac{v}{r}. \tag{1.3}$$

This is known as *Hubble's law* with the constant of proportionality H_0 known as *Hubble's constant*. Hubble's law is not accurate for very nearby objects, as the cosmological principle does not hold precisely in the local neighbourhood, but it does provide an excellent description of the average motion of galaxies. Many experiments over the last decade have tried to place tighter constraints on H_0 with some success, one of the most recent values calculated using Planck data given as $H_0 = 67.80 \pm 0.77$ km/s/Mpc [22]. As we shall see in Section 1.2.5, the exact prescription for the cosmological model affects the degeneracies between H_0 and other model parameters. Hubble's law is important because it shows that our Universe is expanding. Only for a linear relationship is the expansion consistent with homogeneity and isotropy. If we trace this expansion back in time, we must conclude that at a previous time the Universe's scale factor (relating comoving to physical distances, and described in the following section) must have been much smaller than it is now and consequently, much denser and hotter. If we extrapolate back far enough, we arrive at a singularity

known as the big bang. Cosmologies built upon such a foundation are therefore known as big bang cosmologies, and form the basis for the models considered in this thesis.

1.1.3 The Friedmann Equations

In the mathematical framework of general relativity, a key concept is that of the *metric*. The metric describes geometry by expressing the distance between elements of a set in terms of their coordinates, and for a metric with maximally symmetric spatial sections, a factor k termed the *spatial curvature*. If we impose the cosmological principle, then the Universe should not have any preferred location. This implies that the spatial part of the metric should have a constant curvature. Evaluated in spherical polar coordinates the most general metric is given by

$$ds^2 = c^2dt^2 - a^2(t)\left[\frac{dr^2}{1-kr^2} + r^2(d\theta^2 + \sin^2 d\theta d\phi)\right], \tag{1.4}$$

where r, θ and ϕ are the spherical polar coordinates, and $a(t)$ is the *scale factor of the Universe* and its time derivative controls the rate of expansion (or contraction). This metric is known as the *Friedmann-Robertson-Walker* (FRW) metric. The curvature k can be positive, negative, or zero. Positive curvature corresponds to a spherical geometry in a closed finite universe, negative curvature corresponds to a hyperbolic geometry in an open infinite universe, and zero curvature corresponds to a flat geometry in an asymptotic universe (without a cosmological constant a flat universe expands forever but at a continually decelerating rate, with expansion asymptotically approaching zero). The expansion history of the Universe is described by the scale factor, and the equations of general relativity dictate how a universe of given constituents evolves. If we approximate the universe as filled with a homogeneous and isotropic perfect fluid with pressure $p(t)$ and energy density $\rho(t)$, then the Einstein equations of general relativity reduce to the Friedmann equations:

$$H^2 = \frac{8\pi}{3{M_P}^2}\rho - \frac{k}{a^2} + \frac{\Lambda}{3} \tag{1.5}$$

$$\left(\frac{\ddot{a}}{a}\right) = -\frac{4\pi}{3{M_P}^2}(\rho + 3p) + \frac{\Lambda}{3}. \tag{1.6}$$

Here dots represent time derivatives. The Hubble parameter here is $H = \dot{a}/a$, and Λ is Einstein's cosmological constant. The Planck mass has been used instead of the gravitational constant $G = 1/{M_P}^2$, and we have chosen to work in units such that $c = \hbar = 1$. Encoded into these equations is the history, current state, and future evolution of a Universe, with each constituent component described by a term in the Friedman equations. These equations form the basis for the modern view of the cosmos.

The cosmological constant Λ is a parameter inserted by Einstein into his equations to allow the

Universe to be static (his favoured scenario). Hubble's observations in the 1930s that the Universe was expanding seemed to contradict this description and the non-zero Λ model fell out of favour. In the 1990s, observations of distant supernovae suggested that the expansion was accelerating. One mechanism which could drive such an acceleration is a non-zero cosmological constant.

1.1.4 Inflation

The hot big bang model does an excellent job of explaining many phenomena in our Universe, not just the observed expansion. The relative abundance of light elements via nucleosynthesis can be predicted precisely using the temperature and density of the young Universe to calculate the ratio of photons to baryons. Another prediction of the big bang model is the CMB radiation, which itself can be used as a verification of primordial nucleosynthesis, and the calculations agree well. Measurements of galaxies too provide a strong piece of evidence in favour of expansion; both observations and theory suggest that the first quasars/galaxies formed roughly one billion years after the big bang, and larger structures subsequently formed, such as clusters of galaxies and superclusters. Stellar populations have also been ageing and evolving, so that distant galaxies appear very different from nearby galaxies. These observations are strong arguments against the steady-state model. Despite the numerous successes, there are several significant problems associated with the big bang model. We shall examine the problems first before discussing how inflation can solve these problems.

1.1.4.1 The Horizon Problem

The horizon problem arises from the existence of particle horizons in FRW cosmologies. Given the assumption of a finite amount of time since the big bang singularity, photons can only travel a finite distance within the age of the universe. Consider a photon moving on a radial trajectory in a spatially-flat universe ($k = 0$; the generalisation to non-flat cases is straightforward), with the scale factor normalised to $a_0 = 1$. A radial geodesic in such a universe obeys

$$ds^2 = 0 = -dt^2 + a^2 dr^2, \tag{1.7}$$

so the distance travelled by a photon between times t_1 and t_2 in comoving coordinates is

$$\Delta r = \int_{t_1}^{t_2} \frac{dt}{a(t)}. \tag{1.8}$$

Multiplication by the scale factor gives the physical distance measured by an observer at time t. If the Universe has entered a matter-dominated phase, for which

$$a = \left(\frac{t}{t_0}\right)^{2/3}, \tag{1.9}$$

then the Hubble parameter is given by

$$H = \frac{2}{3}t^{-1} = a^{-3/2}H_0, \tag{1.10}$$

where H_0 is the Hubble parameter today. The photon thus travels a comoving distance

$$\delta r = 2H_0^{-1}(\sqrt{a_2} - \sqrt{a_1}). \tag{1.11}$$

The comoving horizon when $a = a_*$ is the distance that the photon travels since the big bang,

$$r_h(a_*) = 2H_0^{-1}\sqrt{a_*}, \tag{1.12}$$

and the physical horizon as measured on a spatial hypersurface at a_* is therefore given by

$$d_h(a_*) = a_* r_h(a_*) = 2H_*^{-1}, \tag{1.13}$$

where H_*^{-1} is the Hubble distance at that particular epoch. In fact, $d_h(a_*) \approx H_*^{-1}$ approximately holds for any nearly-flat universe composed of a mixture of matter and radiation (the exact mixture just modifying the prefactor). The horizon problem is then the observation that the CMB is isotropic to a very high degree (one part in 10^5), even though lines of sight separated by more than a few degrees correspond to points on the last scattering surface that are not causally connected (outside each other's horizons). When observing the CMB, we are observing the Universe at the time of recombination when the scale factor $a_0 \approx 1/1200$. The comoving distance between a region on the CMB and an observer on Earth is given by

$$\Delta r = 2H_0^{-1}(1 - \sqrt{a_{\rm CMB}}) \approx 2H_0^{-1}, \tag{1.14}$$

which is equivalent to the angular diameter distance for a flat model. The comoving horizon distance for such a region is given by

$$r_h(a_{\rm CMB}) = 2H_0^{-1}\sqrt{a_{\rm CMB}} \approx 6 \times 10^{-2} H_0^{-1}. \tag{1.15}$$

Therefore if we measure two points of the CMB that are widely separated, they will have non-overlapping horizons due to not being in causal connection at recombination. However, the CMB

sky is observed to have a very uniform temperature distribution of about 3 K. What gave rise to the large-scale homogeneity and isotropy? FRW models require very special initial conditions.

1.1.4.2 The Flatness Problem

The current generation of cosmological probes strongly favour a spatially-flat Universe, and this has important implications for the fine-tuning of the initial conditions. Consider a modified form of Eq. (1.5):

$$\Omega(a) - 1 = \frac{k}{(aH)^2}, \tag{1.16}$$

where $\Omega(a)$ is the density parameter. Given that the universe we are considering only contains matter and radiation (in the standard FRW model), the comoving Hubble radius $(aH)^{-1}$ will grow with time and hence so will $|\Omega(a) - 1|$. It follows that $\Omega = 1$ can be thought of as an unstable point. If current observations are correct, and our Universe is indeed an approximately spatially-flat spacetime, the density parameter Ω needs to be incredibly close to unity. At early times even a small departure from flatness in the early Universe would have been hugely magnified by the expansion and would lead to a significant departure from the spatial flatness measured today. Whilst not itself inconsistent with the standard big bang theory, the fine tuning problem does hint that there may be some other underlying mechanism responsible for driving the flatness.

1.1.4.3 Unwanted Relics

Modern particle physics presents us with another problem with the hot big bang model. At very high temperatures relic objects are produced that survive to the present, and should be detectable with current experiments. The gravitino (the supersymmetric partner of the graviton) with mass $m \sim 100$ GeV interacts very weakly, and decays late after big bang nucleosynthesis. Also, if the symmetry of a Grand Unified Theory (GUT) is broken in a spontaneous symmetry breaking phase transition, magnetic monopoles are produced. They are point-like topological defects that are stable and massive, with a high mass $m \sim 10^{14}$ GeV. Their expected number density is such that their contribution to the energy density today is much greater than the critical density, however none have ever been detected.

1.1.4.4 Solving Problems with Inflation

The need for inflation was originally developed in the 1970s by Starobinsky, Mukhanov and Linde [23] [24] [25] and further refined in the 1980s by Alan Guth [26] as a solution to the problems

outlined above. Inflation is a period during which the scale factor is accelerating i.e. $\ddot{a}(t) > 0$, which implies an extremely rapid period of expansion. Recalling the acceleration equation

$$\frac{\ddot{a}}{a} = -\frac{4\pi G}{3}(\rho + 3p), \tag{1.17}$$

for the scale factor to undergo acceleration, we require a negative pressure,

$$p < -\frac{\rho}{3}. \tag{1.18}$$

As mentioned earlier, one mechanism which could drive such an evolution is a Universe with a cosmological constant Λ. We can show that this equates to a fluid with $p = -\rho$, which satisfies the condition in Eq. 1.18. The terms in the Friedmann equation relating to matter and curvature are reduced by the expansion, whereas the cosmological constant term $\Lambda/3$ remains constant. At large times, only the cosmological constant term will remain and we will have expansion described by:

$$H^2 = \frac{\Lambda}{3} \Rightarrow \dot{a} = \sqrt{\frac{\Lambda}{3}}a, \tag{1.19}$$

which has the solution

$$a(t) = \exp\left(\sqrt{\frac{\Lambda}{3}}t\right). \tag{1.20}$$

A homogeneous scalar field can lead to an equation of state that is like a cosmological constant. One can parameterise the dynamics by considering the inflation to be driven by a homogeneous scalar field ϕ defined by a potential $V(\phi)$. This field is known as the *inflaton*. The inflaton is characterised by energy density and pressure $\rho_\phi = \dot{\phi}^2/2 + V(\phi)$ and $p_\phi = \dot{\phi}^2/2 - V(\phi)$, which then give

$$\rho + 3p = 2(\dot{\phi}^2 - V(\phi)). \tag{1.21}$$

Inflation must end at some point, and the energy constrained in the field, the *inflaton*, must decay into ordinary matter. At this point, the big bang proceeds as before, and given that the Universe was very young during inflation, none of the advantages of the big bang model are lost. Many models of inflation propose that the Universe was 10^{-34} s old when inflation ended. This is approximately the timescale appropriate to the GUT scale of 10^{16} GeV.

Inflation hugely increases the size of a particular region of the Universe while keeping the Hubble scale fixed. A small region that is causally connected *before* inflation occurs can expand to be much larger than the size of the observable Universe today. Thus, CMB radiation originating from opposite sides of the sky can be at the same temperature because the corresponding points on the

last-scattering surface were once in causal contact, and inflation eliminates spatial gradients. When the inflaton decays, the decay products then rapidly thermalise. This solves the horizon problem. E-folding measures how the scale factor increases, defined as the amount of time for a to grow by a factor of e. A minimum of roughly 60 e-foldings occurred between the time that our present Hubble volume crossed the horizon and the end of inflation (though the exact number depends on the reheating mechanism and temperature). All scales relevant to large-scale structure sample a small window of this 60 e-foldings (roughly 8) [26]. Recall the flatness problem arises because $|\Omega(t)-1|$ always increases with time, which forces Ω away from unity. Inflation solves this problem since

$$\ddot{a} > 0 \Rightarrow \frac{d}{dt}(\dot{a}) > 0 \Rightarrow \frac{d}{dt}(aH) > 0 \Rightarrow \frac{|k|}{a^2H^2} \to 0. \tag{1.22}$$

Hence the condition that drives Ω towards unity rather than away from unity is precisely that prescribed by inflation. An outcome of inflation is to force Ω so close to unity that even all the subsequent expansion occurring after inflation is not enough to pull it away, and this has important implications for the amount of inflation that had to occur. Inflation will also dilute the density of any relic particles produced before inflation, because their density is reduced by expansion much more quickly than the cosmological constant. If we allow for enough inflation, we can dilute the relic particles to such an extent that the probability of detecting them today is essentially zero, explaining why we have never observed any. A necessary condition is that we do not reheat to such a high temperature that a monopole problem is recreated.

Despite these successes, inflation is not without its problems. No known physical field exists to drive such a period of rapid expansion, and indeed there is a large collection of differing inflation models put forward that satisfy the above conditions. No experiment thus far has been able to fully characterise the dynamics of inflation.

1.1.4.5 Inflation Theory

Combining this requirement for inflation with the Friedmann equation we see that accelerated expansion occurs for $\dot{\phi}^2 < V(\phi)$. If $\ddot{\phi}$ is also appropriately small, inflation will last long enough to solve the above-mentioned problems. This is standard *slow-roll* inflation, and is usually parameterised in terms of the slow-roll parameters

$$\epsilon = \frac{{M_\mathrm{P}}^2}{16\pi}\left(\frac{V'}{V}\right)^2 \tag{1.23}$$

$$\eta = \frac{{M_\mathrm{P}}^2}{8\pi}\left[\frac{V''}{V} - \frac{1}{2}\left(\frac{V'}{V}\right)^2\right], \tag{1.24}$$

where these parameters measure the gradient and the curvature of the inflaton potential respectively. Primes represent derivatives with respect to ϕ. If the field 'rolls' slowly enough down the potential $V(\phi)$, then one can easily achieve the required amount of inflation to solve the initial-value problems. Measurements of the CMB should be able to constrain the inflaton parameters to a particular region of parameter space. The potential can take many forms, some driven by particle theory such as the Higgs potential [27], or a simple massive scalar field $V(\phi) = m^2\phi^2/2$. In all slow-roll models, inflation occurs as the inflaton rolls into the true vacuum state, and the Universe is reheated through the coupling to other matter fields as the inflaton oscillates around the minimum of the potential. Reheating must occur to generate the high temperatures of the hot big bang model. The large potential energy of the inflaton will decay into Standard Model particles (including radiation), which will then initiate the radiation-dominated phase of the hot big bang.

Inflation also provides a mechanism to generate structure in the early Universe. Quantum fluctuations in the inflaton field will be stretched beyond the horizon, and converted into classical curvature fluctuations. Gravitational interaction of these under/over-dense regions then drive the formation of the structure we measure today.

We can parameterise the duration of accelerated expansion in terms of the number of *e-foldings*:

$$N_e = \ln\left(\frac{a_f}{a_i}\right) = \int_{t_i}^{t_f} H dt \approx -8\pi G \int_{\phi_i}^{\phi_f} \frac{V}{V'} d\phi, \tag{1.25}$$

where the final step is made using the slow-roll approximation to the equation of motion for ϕ. In a single field description of inflation, we can split the inflaton ϕ into two parts $\phi_0(t)$ and $\delta\phi(x,t)$, which represent the classical scalar field and the quantum fluctuation respectively. The quantum fluctuation (which generates structure) acts as a small perturbation around the classical field (which determines the background evolution of the unperturbed Universe). The metric perturbation around the homogeneous and isotropic FRW background is

$$ds^2 = g_{\mu\nu}dx^\mu dx^\nu = (1+2\psi)dt^2 - 2aB_i dt dx^i - a^2[(1-2\phi)\delta_{ij} + E_{ij}]dx^i dx^j, \tag{1.26}$$

where the scalar perturbations are given by ψ and ϕ, the vector perturbation is given by B_i, and the tensor perturbation is given by the symmetric and trace-free E_{ij}. Given the symmetry of the FRW metric, we can always decompose the perturbations into scalar, vector, and tensor components [28].

For the scalar perturbations, the comoving curvature perturbation ζ can be defined in terms of the spatial curvature scalar of a comoving hypersurface $\mathcal{R}$ by

$$\mathcal{R} = \frac{4}{a^2}\nabla^2\zeta. \tag{1.27}$$

The power spectrum of the scalar fluctuations is then

$$\langle \zeta_{\mathbf{k}} \zeta^*_{\mathbf{k}'} \rangle = (2\pi)^3 \delta^3(\mathbf{k} - \mathbf{k}') \frac{2\pi^2}{k^3} \mathcal{P}_s(k), \tag{1.28}$$

and we can characterise the scale dependence of the power spectrum with the spectral index n_s given by

$$n_s - 1 = \frac{d \ln \mathcal{P}_s(k)}{d \ln k}, \tag{1.29}$$

with the spectral index 'running', given by

$$\alpha_s = \frac{dn_s}{d \ln k}. \tag{1.30}$$

Utilising the slow-roll parameters in Eq. 1.24, the spectral index can be approximated as

$$n_s = 1 - 4\epsilon + 2(\eta - \epsilon). \tag{1.31}$$

The power spectrum is then approximately

$$\mathcal{P}_s(k) = A_s(k_*) \left(\frac{k}{k_*} \right)^{n_s(k_*)-1}, \tag{1.32}$$

where A_s is the normalisation and k_* is some pivot scale at which to normalise [29].

Vector perturbations are not excited by general inflationary models. We can analyse the non-relativistic matter by using classical perturbation theory. The Euler equation can be expressed as

$$\delta_t \mathbf{v} + H\mathbf{v} = -\frac{1}{a\bar{\rho}} \nabla \delta P - \frac{1}{a} \nabla \phi, \tag{1.33}$$

where ϕ is the gravitational potential. The velocity perturbation has both a scalar and a vector component $\nabla v + \mathbf{v}_\perp$, and the vector component does not contribute to the matter collapse because $\mathbf{v}_\perp$ does not source δ. Taking the curl of the Euler equation above, we see that

$$\nabla \times \partial_t \mathbf{v} = \partial_t (\nabla \times \mathbf{v}) = -H \nabla \times \mathbf{v}_\perp. \tag{1.34}$$

As the universe expands, the physical vorticity will decay as $1/a^2$ since $\nabla \times \mathbf{v}_\perp$ scales as $1/a$.

Models of inflation will also produce tensor perturbations, which are transverse traceless perturbations in the metric, also referred to as *gravitational waves*. The spectrum of tensor perturbations, $P_t(k)$ is also expected to be almost scale invariant, and the amplitude is dependent only on the

energy scale of inflation. Following a similar formalism as for the scalar perturbations, the tensor power spectrum can be approximated as

$$\mathcal{P}_t(k) = A_t(k_*) \left(\frac{k}{k_*}\right)^{n_t(k_*)}, \tag{1.35}$$

with the normalisation factor A_t, and a tensor spectral index defined as

$$n_t = \frac{d \ln \mathcal{P}_t(k)}{d \ln k}. \tag{1.36}$$

A goal of modern cosmological measurements is to characterise this primordial tensor power spectrum and in particular, measure the ratio of the tensor to scalar fluctuation amplitude

$$r = \frac{\mathcal{P}_t}{\mathcal{P}_s} \approx \frac{{M_P}^2}{\pi} \left(\frac{V'}{V}\right)^2 \approx 16\epsilon, \tag{1.37}$$

.

where we have used the slow-roll approximation to calculate the power spectra of density fluctuations. The value of the tensor to scalar ratio r is dependent on the exact cosmological prescription, and can be used to distinguish between competing models of inflation. For slow-roll inflation the spectral indices are directly related to the slow-roll parameters $n_s - 1 = 2\eta - 6\epsilon$ and $n_t = -2\epsilon$. Given that the normalisation of the scalar power spectrum at the Hubble radius from the WMAP data is $\mathcal{P}_s \approx 2 \times 10^{-9}$ (at their pivot scale $k_* = 0.002$ Mpc^{-1}), we can calculate the dependence of r on the energy scale as

$$V^{1/4} = 1.06 \times 10^{16} \text{ GeV} \left(\frac{r}{0.01}\right)^{1/4} \tag{1.38}$$

Therefore if we measure a large value of r we can deduce that inflation must have occurred at a high energy level comparable to the GUT energy scale at $\sim 10^{16}$ GeV.

1.1.4.6 Vacuum Fluctuations

Recall that quantum fluctuations in the inflaton field during the inflationary epoch are stretched during inflation and become classical fluctuations. Consider the physical origin of the scalar and tensor fluctuations. Since inflation dilutes all matter fields, the Universe enters a pure vacuum state shortly after the onset of inflation. In the simple case of exponential inflation, the vacuum state is associated with a particular Gibbons-Hawking temperature [30], and the inflaton undergoes flutuations that are the same for each wavelength $\delta\phi_k = T_{GH}$ (where T_{GH} is the Gibbons-Hawking temperature). We can relate these fluctuations to density fluctuations via

$$\delta\rho = \frac{dV}{d\phi}\delta\phi. \tag{1.39}$$

Inflation therefore produces density perturbations with almost equal amplitude at each wavenumber. Differences in amplitudes arise from the gradual change in V as the inflaton slowly rolls down the field. The spectrum of scalar fluctuations is related to the potential by

$$A_s^2(k) \sim \left.\frac{V^3}{M_P^6 (V')^2}\right|_{k=aH}, \tag{1.40}$$

evaluated at the moment when the physical scale of the perturbation $\lambda = a/k$ equals the Hubble radius H^{-1}. Scalar fluctuations are tied to the energy-momentum distribution, and density fluctuations produced by inflation are adiabatic and Gaussian. These aspects of inflationary perturbations are consistent with current observations.

Any other nearly-massless particle will be excited during inflation. The graviton (a propagating excitation of the gravitational field) corresponds to tensor perturbations in the metric which have a spectrum

$$A_T^2(k) \sim \left.\frac{V}{M_P^4}\right|_{k=aH}. \tag{1.41}$$

Crucially, inflation predicts the the existence of tensor perturbations which may be observable via measurements of the CMB polarisation. Current knowledge of the amplitude of the perturbations already allows estimation of the energy scale of inflation. Tensor perturbations depend on V alone, so observations of these modes yield direct estimations of the energy scale (at least for simple models of inflation featuring a single canonical, slowly-rolling scalar field).

1.1.4.7 Models of Inflation

Within the restriction of single-field slow-roll inflation, there are a large number of different models, separated by their inflationary potential. Let us define three general types of model; small-field, large-field and hybrid (with a fourth linear type at the boundary between small-field and large-field) by the n_s-r relationship. The different models are shown in Figure 1.1.

Small-field models are defined when the variation in the inflation field is less than the reduced Planck mass i.e. $|\Delta\phi| \equiv |\phi_* - \phi_{end}| < M_{pl}$ where ϕ_* is the field at the the time t_* when observable scales first crossed the Hubble radius during inflation. In typical models, the amplitude of gravitational waves generated is undetectably small, and the discriminating observational factor is the spectral index. The general form for the small-field inflaton potential is

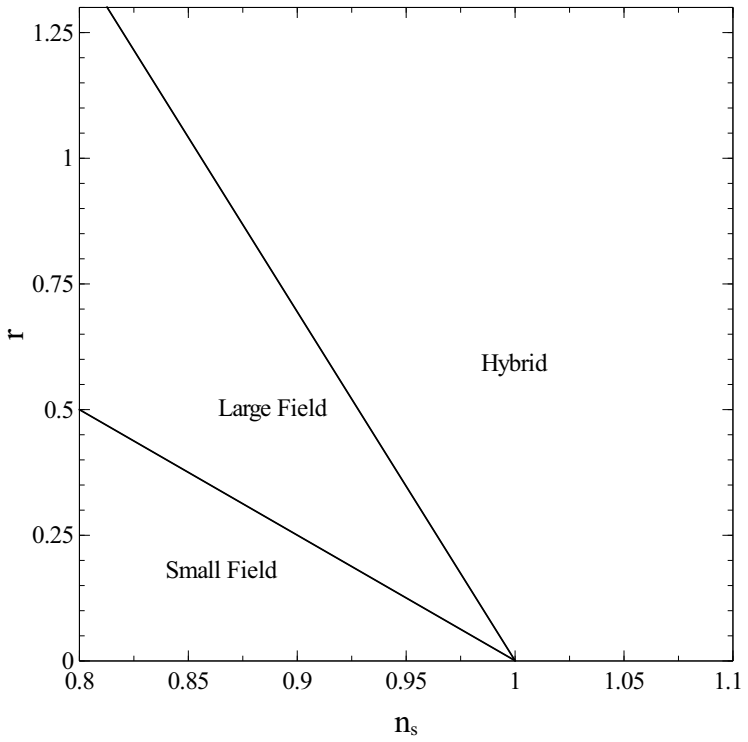

Figure 1.1: The n_s-r parameter space divided into regions for small-field, large-field,and hybrid models. The linear case is the dividing line between large and small-field.

$$V = V_0 \left[1 - \left(\frac{\phi}{\mu}\right)^p\right], \tag{1.42}$$

where V_0, μ, and p are constants. This form of potential arises in various models including modular and braneworld inflation [31], as well as some supersymmetric models [32]. All small-field inflationary scenarios are related via their predictions for the value of the spectral index. The slow-roll parameter η dominates over ϵ, which implies that the spectral index can be given approximately by $n_s - 1 = 2\eta$. Because ϵ is a continuously increasing function of the field ϕ during inflation, we can relate the spectral index to the number of e-foldings as

$$n_s = 1 - 2\left(\frac{p-1}{p-2}\right)\frac{1}{N}. \tag{1.43}$$

Large-field models are defined by the condition $|\Delta\phi| \gtrsim M_{Pl}$, and such models can generate an observable tensor to scalar ratio. We can define a simple class of large-field inflation models by $V \propto \phi^x$ where x is a positive or negative constant. Chaotic inflation corresponds to $x > 0$, while 'intermediate' inflation corresponds to a negative constant [33]. Many models of inflation require a braneworld explanation within the framework of type IIa string theory, where the leading-order term in the inflaton potential is a monomial with $x = 2/3$ or $x = 2/5$ [34]. Assuming that the

allowed range of n_s values is similar to the seven-year WMAP data, a tensor background will not be detectable for $x < 2/3$ if the number of e-foldings before the end of inflation is taken to be 54 ± 7, but could be theoretically seen if $N \approx 30$. If however $x = 2/5$, then $r \lesssim 0.05$ for all $N \gtrsim 30$ [35].

Hybrid inflation occurs frequently in models which incorporate inflationary behaviour into supersymmetry. The inflaton field evolves toward a minimum with a non-zero vacuum energy. In the hybrid scenario, it is the action of a second field which is responsible for the end of inflation. Typically, hybrid models are characterised by $V''(\phi) > 0$, and $0 < \epsilon < \eta$. If we consider a generic inflaton potential of the form

$$V(\phi) = \Lambda \left[1 + \left(\frac{\phi}{\mu} \right)^p \right], \tag{1.44}$$

where we treat (ϕ_N/μ) as an adjustable parameter (ϕ_N being the value of the field at the end of inflation), then we can show that the slow-roll parameters are related as

$$\frac{\eta}{\epsilon} = \begin{cases} \frac{p-1}{p} & \text{for } \phi_N/\mu \gg 1 \\ \frac{2(p-1)}{p} \left(\frac{\mu}{\phi_N} \right)^p & \text{for } \phi_N/\mu \ll 1 \end{cases}. \tag{1.45}$$

When $\phi_N/\mu \gg 1$ the large-field result is recovered, and when $\phi_N/\mu \ll 1$ the result is analogous to the small-field case. Of note in many hybrid models is the prediction of a blue spectral index ($n_s > 1$), which corresponds to $\eta > 2\epsilon$. The nine-year WMAP results have almost completely ruled out models predicting a blue spectral index, eliminating some hybrid models from the zoo of possible inflationary scenarios [36].

There are many flavours of inflation, and we do not list these exhaustively. Several assumptions have been made in considering the above models. Firstly, the curvature perturbation is entirely due to quantum field fluctuations in single-field slowly-rolling scalar inflation, and as such is purely adiabatic. The slow-roll approximation is applied to leading order in power. It is also assumed that the running in the spectral index vanishes, that is $dn_s/d\ln k = 0$. This is a reasonable assumption and is supported by the WMAP data. One also assumes that the specified potential remains valid until the end of inflation. A varying potential could have different implications for the evolution, and force the universe into a different state during inflation. Finally, one assumes that the universe reheats instantaneously after the end of inflation. This is perhaps the weakest assumption of these models. The duration of the reheating phase of the universe is unknown. The number of e-foldings depends on the effective equation of state after inflation, which varies with the duration of reheating. Knowing the precise equation of state would allow a more accurate determination of N. With regard to the slow-roll approximation, although it works well in many cases, it must eventually fail if inflation is to end. Furthermore, even weak violations of the approximation can result in significant deviations from the usual predications for observables such as the density perturbation spectra, or the density of the gravitational wave background. As errors

in observational data decrease, it will be important to derive not just a single prediction, but a class of predictions for the observables that are as accurate as possible, and which cover all possible inflationary models.

With particular regard to small-field models, one point to note is that it is the lower-order terms which are constrained by the data. This is important from a theoretical point of view, because it is difficult to motivate the suppression of lower-order terms in a small-field theory. Such suppression demands either a major fine-tuning of the coupling terms, or the inclusion of a suitable symmetry [37]. This only applies for one case however, and in the majority of models, fine-tuning is employed to suppress the quadratic term. The use of fine-tuning highlights the difficulty of building a small-field model of inflation where a higher-order term is responsible for inflation coming to an end. This is an interesting problem and is an open question in inflationary cosmology.

1.1.5 Dark Matter and Dark Energy

One striking success of concordance cosmology is the ease of predicting the observed structure in the Universe, provided that we stipulate that dark matter is composed of slowly-moving particles. This defines *cold* dark matter. We also require that the initial power spectrum of density perturbations is almost scale-invariant i.e. $P(k) \sim k^{n_s}$ with $n_s \approx 1$. Dark energy then affects the development of structure via its effect on the expansion rate when density perturbations are growing. Given the quality and quantity of large-scale structure data, probing dark energy is thus a powerful and sensitive probe of structure formation.

On scales much smaller than the Hubble radius small-amplitude density perturbations are described by

$$\ddot{\delta}_k + 2H\dot{\delta}_k - 4\pi G\rho_M\delta_k = 0, \tag{1.46}$$

where perturbations are treated for each wavenumber k, and the matter is assumed to be pressureless (always true for CDM and valid for baryons on large mass scales after photon-baryon decoupling). The 'Hubble damping' term $2H\dot{\delta}_k$ describes how the dark energy affects the growth of structure. We can use the solution to this perturbation equation to describe the three main epochs of expansion; $\delta_k(t)$ grows as $a(t)$ during the matter-dominated epoch, and is approximately constant during both the radiation and dark energy-dominated epochs. Once dark energy dominates and accelerated expansion occurs, the Hubble damping time becomes shorter than the timescale for perturbation growth, therefore the growth of linear perturbations ends.

The equation-of-state parameter w for dark energy has a large effect on the evolution of structure. If we assume a fixed dark energy density Ω_Λ but increase w, dark energy will dominate at earlier times, causing an end to linear perturbation growth. The expansion factor since decoupling must therefore be smaller, and to achieve the same amplitude today the initial perturbation must begin with a larger amplitude and will be larger at all redshifts until the present epoch. This is also true

if we impose a fixed w but a larger Ω_Λ. Dark matter interacts gravitationally, whereas dark energy does not. In principle, *dynamical* dark energy can be inhomogeneous i.e. an imperfect fluid, and therefore cannot be fully characterised by w. However, in FRW cosmology, spatial homogeneity and isotropy requires the stress-tensor to assume the perfect fluid form thus w determines the evolution of the energy density.

1.1.6 Precision Cosmology

As little as 40 years ago, cosmology was regarded as a discipline somewhere between philosophy and metaphysics, and yet today our cosmological probes scan the Universe with astounding precision and detail. We now know that everything we can observe makes up less than a percent of the cosmic density, and that repulsive dark energy dominates (at least) our patch of the Universe. The ΛCDM theory developed over the last 30 years explains the large-scale structure of galaxies, as well as the preceding CMB radiation, and for the first time humanity has a theory explaining the origin and nature of the Universe that may turn out to be consistent even in one thousand years.

Starting with Einstein's general relativity in the early 20th century, Friedmann among others predicted cosmic expansion, which was subsequently observed by Slipher and Hubble. The CMB radiation was later predicted by Gamow in 1948, which was then measured in 1965 by Penzias and Wilson. Twenty-five years later, spectacular confirmation of its black body spectrum was revealed with the FIRAS instrument on the COBE satellite, which can be regarded as the starting point for CMB cosmology as a precision science. Numerical calculations built on nuclear reaction networks allowed a rudimentary calculation of the products of big bang nucleosynthesis (BBN), such as primordial abundances of deuterium, helium-3, helium-4, and lithium-7. The consistency of the helium-4 prediction with the as then unexplained large primordial abundance was an early success for big bang cosmology, and the end of the steady-state view. Another important realisation was that Deuterium production fell with the baryon density. An upper limit to the baryon density can be calculated from the present-day Deuterium level. Measurements of the Deuterium abundance in the local interstellar medium in the 1980s led to an upper limit of about 10% of ρ_{crit} on the baryon density. Ten years later the the primordial Deuterium abundance was measured in high-z Hydrogen clouds, and the baryon density was pinned down to 4.5%. At the same time, the total matter density indicated a value only 20% of ρ_{crit}, and pointed towards a significant dark matter composition. This discrepancy formed the main argument that dark matter is not made of baryons.

Also on the COBE satellite, the DMR instrument detected the fluctuations in the CMB temperature at the level of 30 μK, which were predicted from cold dark matter theory. By the mid 1990s, the CDM theory had become either ΛCDM, with $\Omega_m \approx 0.3$ and $\Omega_\Lambda \approx 0.7$, or CHDM (cold and hot dark matter) with $\Omega_m \approx 1$ and $\Omega_\nu \approx 0.2$-0.3. With the development of higher-power telescopes including the Hubble Space Telescope, very-high redshift galaxies were discovered in abundance. This coupled with the high-redshift supernovae evidence pointing towards Λ cosmologies eliminated

the CHDM models completely. ΛCDM models predicted precise structure in the angular peaks of the CMB power spectrum, which were measured by the BOOMERANG and MAXIMA balloon experiments [38] [39], and also by a number of ground-based experiments around the same time [40] [41]. WMAP was launched in 2001 and extended the detailed anisotropy measurements to the whole sky, cementing ΛCDM as the model of choice. WMAP has determined the angular structure from about 0.1-90°, and the cosmological parameter set to about percent-level precision. The wealth of post-WMAP data has driven up the accuracy on these parameters even further, with complementary datasets providing useful cross-checking and degeneracy breaking. The agreement between quite different methods of observation, for example the baryon density as measured by the primordial deuterium abundance and that inferred from the CMB anisotropies is quite striking and one of the great successes of the cosmological model as it stands today.

The Hubble constant inferred from the Planck 2013 data release is estimated to be 67.4 ± 1.4 $\mathrm{kms}^{-1}\mathrm{Mpc}^{-1}$, the age of the universe is estimated at 13.81 ± 0.06 Gyr, and the spatial curvature is within a percent of the flat critical density model [10]. However, these parameters are CMB-derived for the base ΛCDM model, and are therefore model-dependent.

1.2 The Cosmic Microwave Background

Within the framework of the hot big bang, the early Universe was composed of a proton-electron plasma coupled to photons via the Thomson scattering reaction $\gamma + e^- \leftrightarrow \gamma + e^-$. Neutrinos have a (relativistic) thermal distribution and also make a significant contribution to the total energy density. If the energy level is sufficiently high, the plasma phase will be energetically favoured, and bound atoms form only a tiny fraction of the mixture. In such a state the photon mean-free path is very short, and light is unable to propagate through the plasma, forming an information barrier before which no information can be transmitted via photons. The photons and electrons/protons move together as a single fluid (electrons and protons are tightly-coupled via coulomb interactions). In this tightly-coupled regime, the photons/baryons cannot therefore propagate on cosmic scales. As the Universe expanded, the typical photon energy level dropped such that the bound Hydrogen state became energetically favourable, and the fraction of photons with enough energy to ionise Hydrogen at 13.6 eV became minimal. This process is known as recombination (despite the fact this is the *first* time neutral Hydrogen could form). Once recombination proceeded to such a point that the mean-free path of photons became larger than the Hubble length, the photons effectively decoupled from the matter, and propagated freely through the Universe. The last surface at which photons could Thomson scatter from the plasma is thus known as the *last-scattering surface*, and a simple calculation shows that this occurs at approximately $z \approx 1100$. These last-scattered photons have travelled mostly unhindered through the Universe to the present day where we can observe them. Due to the expansion of space, the photons have been redshifted to a temperature of about 3 K today (in the microwave regime of the electromagnetic spectrum). Given that the plasma was

in thermal equilibrium prior to recombination, the spectrum of the last-scattered photons should have a black-body spectrum.

1.2.1 The Black Body Spectrum

In 1964 Penzias and Wilson inadvertently discovered the microwave background radiation while experimenting with the 6 m radio horn antenna at Bell laboratories, only realising exactly what the mysterious radiation was some time later when Dicke, Peebles et al. [42] learned of their work. For their work, Penzias and Wilson were awarded the Nobel Prize in Physics in 1978. In the 1990s, NASA's FIRAS instrument on board the COBE satellite stunningly mapped the spectrum of the CMB radiation finding it to be at a temperature of 2.725 ± 0.002 K, and measuring it to be the most precise black-body in nature. Figure 1.2 shows the FIRAS data plotted over a theoretical blackbody spectrum. The error bars are too small to be seen on a plot of this scale, demonstrating the accuracy achieved. A blackbody is characterised by the Planck function

$$I_\nu = \frac{\hbar\nu^3}{2\pi^2 c^2} \frac{1}{\exp(\frac{\hbar\nu}{kT}) - 1}, \tag{1.47}$$

where ν is the frequency and k is the Boltzmann constant, and the FIRAS data match the theoretical spectrum to high precision over the frequency range 1-600 GHz. One of the great successes of the hot big bang is its prediction of the almost perfect black-body spectrum, a result of the thermal equilibrium. Previous experiments had already shown some anisotropy of the background radiation due to the motion of the Solar System through the Milky Way, but the COBE data showed fluctuations in the background itself. Some fluctuations in the background are necessary to give enough non-uniformity for galaxies to form. The more recent WMAP mission gave a much higher resolution picture of the anisotropies in the background radiation, and is discussed in the next section.

1.2.2 Temperature Anisotropies

Whilst the CMB sky is isotropic to a high degree, it is the deviations from isotropy that hold the most power for constraining cosmology. Irregularities imprinted in the early Universe will affect the properties of the CMB that we observe today. Curvature perturbations will alter the gravitational potential well that the photon has to propagate through, and will consequently alter the photons via the Sachs-Wolfe effect [43]. Thus the CMB anisotropies map the perturbations at the last-scattering surface. For the largest scales, where there is not enough time between the creation of perturbations and recombination for significant evolution, inflation predicts a scale-invariant spectrum of Gaussian anisotropies.

The COBE satellite's Differential Microwave Radiometer (DMR) scanned the entire sky to produce

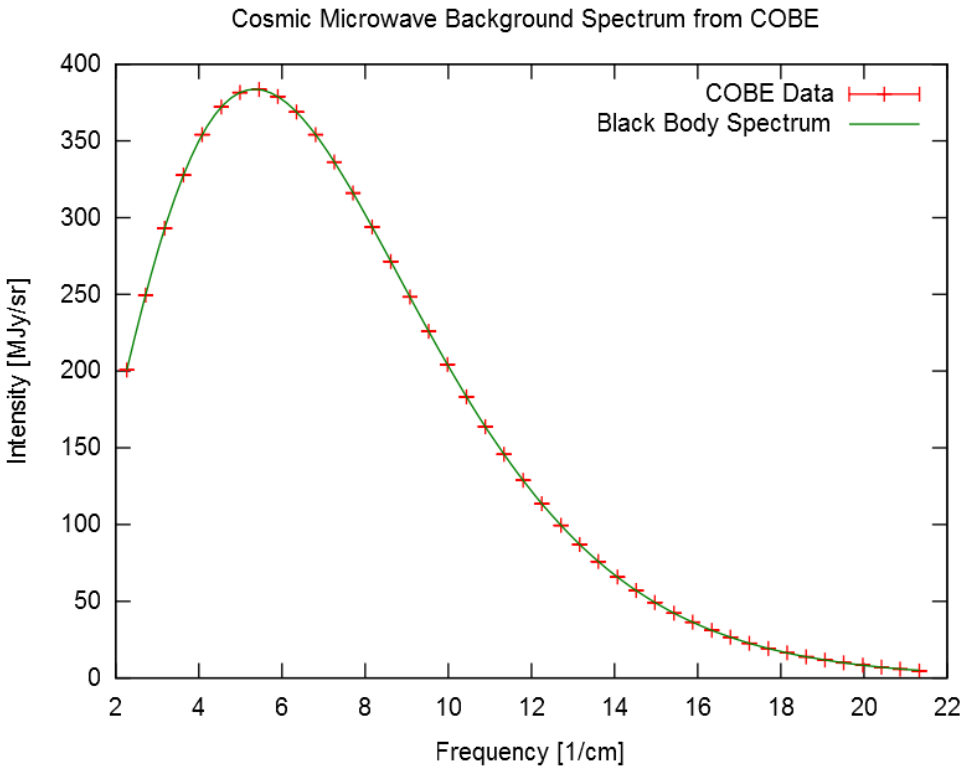

Figure 1.2: The CMB black-body spectrum as observed by the FIRAS instrument on board the COBE satellite. The data agree exceptionally well with the theoretical black-body spectrum. Figure plotted with data obtained from the FIRAS Lambda online data archive.

a map of the anisotropies in the CMB. The DMR data confirmed that, following subtraction of both the dipole due to the Earth's movement through the Galaxy, and the emission excess from the galactic plane, large-scale anisotropies were present at a level of about one part in 10^5. The DMR data also illustrate the highly isotropic nature of the Universe on large scales, in line with the cosmological principle.

Since COBE, many experiments have further characterised the anisotropy of the CMB on various angular scales. The most significant of these is the Wilkinson Microwave Anisotropy Probe (WMAP), launched in 2001. The WMAP satellite probed the angular power spectrum to sub-degree scales, and Figure 1.3 shows the best measurements up to the angular limit of the ACBAR data at $\ell \sim 1500$ (where ℓ is the harmonic multipole). To describe the structure, is is helpful to use the following statistical formalism. Given the CMB originated from a spherical shell around us, we can expand the temperature fluctuations on the sky in terms of the spherical harmonic functions as

$$\Delta T(\hat{\mathbf{n}}) = \sum_{\ell m} a_{lm} Y_{lm}(\hat{\mathbf{n}}), \tag{1.48}$$

where a_{lm} is the coefficient of the spherical harmonic Y_{lm}, and $\hat{\mathbf{n}}$ is the direction on the sky. If the coefficients a_{lm} are Gaussian random variables, then all the statistical information about the fluctuations is encoded in the power spectrum C_ℓ where

$$\langle a_{\ell m} a^*_{\ell m} \rangle = C_\ell \delta_{\ell \ell'} \delta_{m m'} \tag{1.49}$$

$$C_\ell = \frac{1}{2\ell + 1} \sum_m \langle |a_{\ell m}|^2 \rangle. \tag{1.50}$$

Here angle brackets denote ensemble averages. Nine years of WMAP data point to a sky that is very close to Gaussian. Non-Gaussian fluctuations arise in certain cosmological models and can be measured with more precise CMB datasets, but these are not considered in any further detail in this work.

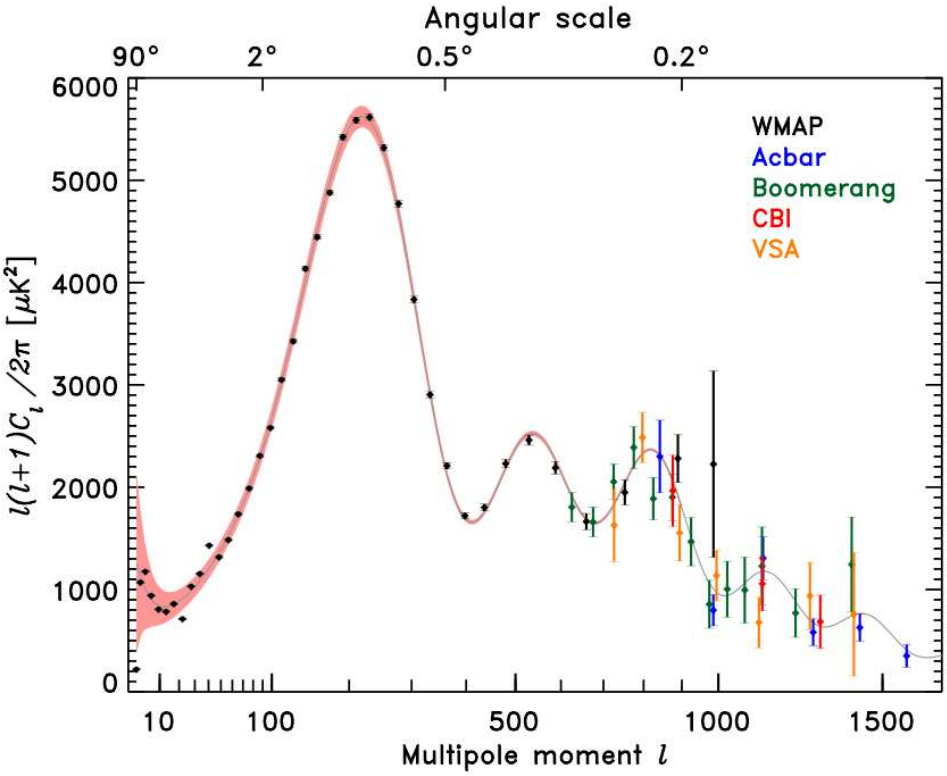

Figure 1.3: The CMB temperature anisotropies angular power spectrum as observed by WMAP (2006), ACBAR (2004) Boomerang (2005), CBI (2004), and VSA (2004) instruments. Also shown is a theoretical model (solid line). The limit imposed by cosmic variance is shown shaded in red. The rich structure in the acoustic peaks is modified by the particular choice of cosmological model. Image adapted from Bennett et. al [44]

The structure of the peaks in the angular power spectrum is a result of the physics governing the fluctuations during expansion. Anisotropy on a given angular scale is related to density perturba-

tions with wavelengths corresponding to the length projected by that angle on the last-scattering surface. The Sachs-Wolfe plateau at large angular scales ($\ell < 50$) arises from perturbations with wavelengths longer than the Hubble radius at the time of last scattering, which have not had time to evolve and hence represent the 'initial conditions'. Photons lose energy leaving the potential associated with these long-wavelength density perturbations, and if the density fluctuations are approximately scale-invariant, as inflation predicts, then the Sachs-Wolfe plateau is flat. The integrated Sachs-Wolfe effect results from the line of sight integral of the Sachs-Wolfe equation

$$\frac{\Delta T}{T} = -2 \int d\tau \dot{\phi}, \tag{1.51}$$

where CMB photons pass through peaks and troughs of the gravitational potential ϕ. If the gravitational potential decays while the photons are propagating inside the well/trough, then there will be a net shift in the photon temperature, and this is a non-zero effect on large scales in ΛCDM models.

At sub-degree scales, roughly between $100 < \ell < 1000$, the detailed structure of the peaks is sourced by gravity-driven acoustic oscillations in the plasma before it became neutral. Perturbations with characteristic size smaller than the horizon at last-scattering have had enough time to evolve causally and produce anisotropy at last-scattering, which we observe as the series of peaks in the angular spectrum. The frozen-in phases of these density waves give rise to a dependence on important cosmological parameters, which as we shall see in Section 1.2.5 gives the angular power spectrum great constraining power.

When the proton-electron plasma was coupled tightly to photons, it behaved as a single fluid, with photons providing most of the pressure and the baryons providing the inertia. Perturbations in the gravitational potential are steadily evolving (with dark matter dominating), and drive oscillations in the photon-baryon fluid, with photon pressure providing the restoring force. The perturbations are small and so evolve linearly. Each mode thus evolves independently and is described by a driven harmonic oscillator, with a frequency determined by the sound speed in the fluid and its wavenumber. Thus there is an oscillation of the fluid density, with a velocity $\pi/2$ out of phase, and an amplitude reduced by the sound speed. After recombination the phases of the oscillations were frozen-in, and imprinted on the sky as a series of peaks in the power spectrum. The main peak is the mode that went through 1/2 of a period, reaching maximum compression. Even peaks represent maximum under-densities, which have smaller amplitudes because the baryon inertia slows the rebounding fluid. The troughs are at the velocity maximum, and so are partially filled. Another effect arises from the reionisation of the universe at redshift z_r. A fraction of photons will be isotropically scattered at $z < z_r$, which will damp anisotropies at angular scales smaller than those subtended by the Hubble radius at z_r, which corresponds typically to multipoles above about a few tens. The acoustic peaks are therefore reduced relative to the plateau by reionisation.

At the highest multipoles $\ell > 1000$, the shape of the spectrum is known as the damping tail.

Recombination is not instantaneous, which gives the last-scattering surface a characteristic thickness. Anisotropies on scales smaller than this thickness will be averaged out through the width of last-scattering. Diffusion between the two components of the fluid also occurs since the coupling between photons and baryons is imperfect, and the oscillations decrease with time. These effects lead to a damping of the C_ℓs, referred to as Silk damping [45], which rapidly cuts off the anisotropies at multipoles above about 1000. The 9-year WMAP temperature anisotropies are shown in Figure 1.4 plotted using the HEALPix software, details of which are discussed in Section 1.5.6.

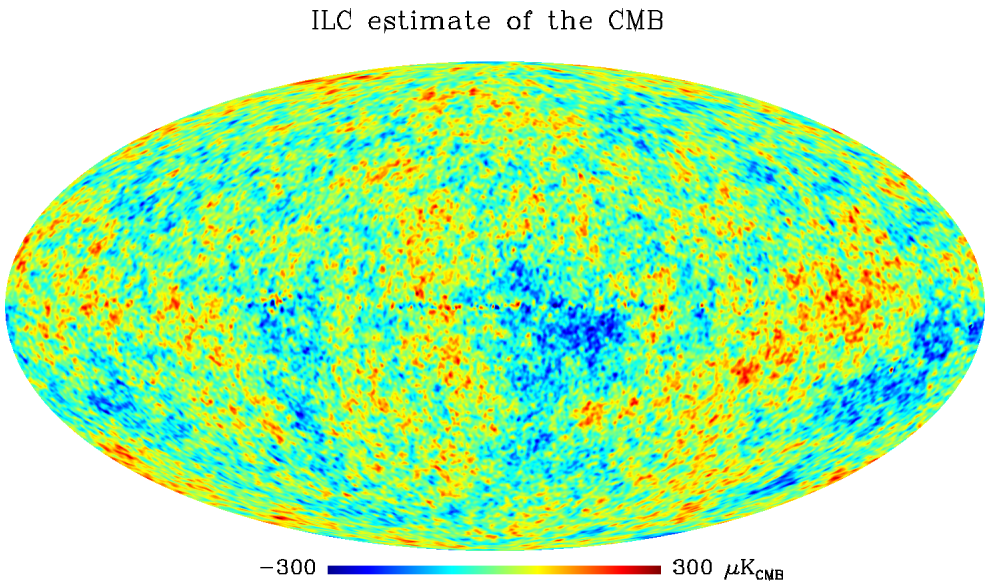

Figure 1.4: The CMB temperature anisotropies as observed by the WMAP satellite over 9 years. The image is a galactic Mollweide projection of the sphere, and represents a best-fit CMB model with foregrounds subtracted. The units are CMB thermodynamic equivalent temperature in μK.

1.2.3 Polarization Anisotropies

The CMB sky also exhibits polarisation anisotropies. This can be readily explained by considering the photon-baryon fluid towards the end of recombination when the photons began to decouple from the baryons. The baryon and photon field fluctuations were sourced by primordial fluctuations, and a quadrupolar photon anisotropy developed. In the frame of reference of a free electron, if the incoming photons were isotropic, orthogonal polarisation states from incident directions separated by $\pi/2$ would balance such that the outgoing radiation would remain unpolarised. Conversely, if the incident photons possessed a quadrupolar variation in intensity or temperature, the result is a linear polarisation of the scattered radiation because Thomson scattering is anisotropic. This is illustrated in Figure 1.5. Non-zero linear polarisation in the CMB is generated around the decoupling era because the Thomson scattering which couples the electrons to the radiation is not isotropic but instead varies with scattering angle.

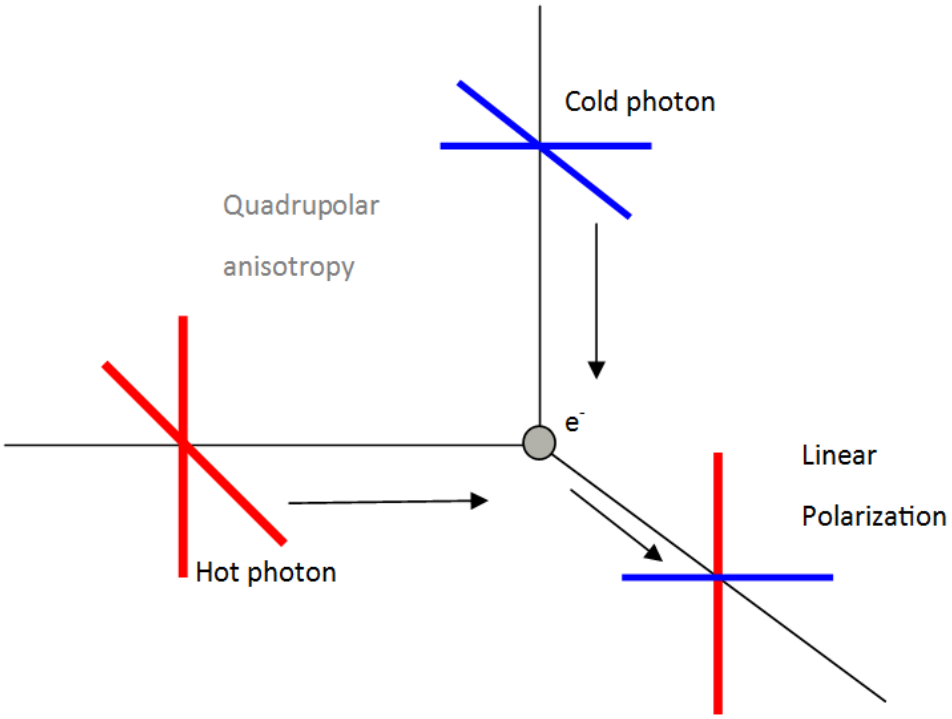

Figure 1.5: Thomson scattering of a quadrupolar photon anisotropy from a free electron generates linear polarisation. Hot photons are shown in red and cold photons in blue.

A reversal in sign of the temperature quadrupole corresponds to a $\pi/2$ rotation of the polarisation, which reflects the spin-2 nature of the polarisation field. The relationship between the polarisation and temperature anisotropies depends on the Thomson scattering and the fluid state. Given that such a quadrupolar anisotropy could form only towards the end of recombination, we should expect the polarisation signal to be a small fraction of the temperature signal. Also, because polarisation is probing a different part of the physical process (primarily the velocity rather than the density field), it contains information complementary to the temperature data. As we will see in Section 1.2.5, polarisation data can also break degeneracies between fundamental parameters and act as an independent probe of cosmological models.

We can define the total scattering cross-section as the radiated power per unit solid angle as a fraction of the incoming intensity

$$\frac{d\sigma}{d\Omega} = \frac{3\sigma_T}{8\pi}|\hat{\epsilon}' \cdot \hat{\epsilon}|^2, \tag{1.52}$$

where $\hat{\epsilon}$ and $\hat{\epsilon}'$ are unit vectors in planes perpendicular to the propagation directions and aligned with the incoming and outgoing polarisation respectively. The parameter σ_T is the isotropic Thomson cross section. This scattering cross section can give rise to no net circular polarisation, and so

circularly-polarised CMB photons will not be discussed further. A measurement of a circular polarisation could provide useful information on instrumental systematics or foreground contamination but is not indicative of any underlying cosmology within the standard model.

Just as for the temperature fluctuations, the polarisation pattern we observe on the sky is expected to vary as a result of not only density perturbations but also gravitational waves present at recombination. The polarisation pattern is often decomposed into E-mode and B-mode contributions. As is discussed later in Section 1.5, this decomposition transforms the traditional spin-2 Stokes Q and U parameters into two scalar fields; a curl-free electric-type E-mode and a divergence-free magnetic-type B-mode. These fields have corresponding spherical harmonic coefficients a^E_{lm} and a^B_{lm} respectively, and their power spectra are defined in a similar manner to C^T_ℓ. The E and B-modes completely describe the polarisation field, and given that the temperature and polarisation signals are sourced by the same underlying physics, we can also correlate the signals to give auto and cross spectra TT, TE, TB, EE, EB, and BB defined as

$$\langle a^X_{\ell m} a^{Y*}_{\ell' m'} \rangle = C^{XY}_\ell \delta_{\ell\ell'} \delta_{mm'} \tag{1.53}$$

$$C^{XY}_\ell = \frac{1}{2\ell+1} \sum_{lm} \langle a^X_{lm} a^Y_{lm} \rangle, \tag{1.54}$$

where $X, Y = T, E, B$. Given their curl-free nature, the multipoles of T and E transform with a factor $(-1)^\ell$ under parity, while the divergence-free B-mode transforms with a factor $(-1)^{\ell+1}$. Consequently if the physics generating the fluctuations respects parity, the TB and EB cross spectra vanish and we are left with a measurable TE cross-correlation spectrum and EE, BB auto-correlation spectra. Figure 1.6 shows the current best measurement of these spectra using WMAP, DASI, CBI, Boomerang, QUaD, BICEP, MAXIPOL, and CAPMAP data. Polarization was first detected by the DASI experiment (Kovac et al. 2002) and recent years have seen increasingly precise measurements. Because the velocity of the photons is out of phase with the density perturbations, the E-mode polarisation spectrum peaks will be out of phase with the temperature peaks. Indeed this is the case for measured and theoretical spectra. Also, the phase relation tells us that the polarisation is correlated with the temperature perturbations, and because the correlation power C^{TE}_ℓ is the product of the two, it exhibits oscillations with the same acoustic frequency. The EE signal has also been measured (also shown in Figure 1.6), and Planck will be able to characterise the EE spectrum to a high precision up to high ℓ.

1.2.4 Gravitational Waves and B-modes

An area on the cutting edge of cosmological research is the hunt for a primordial B-mode polarisation signal, one of the most interesting prospects for CMB polarisation analysis. Many modern experiments such as BICEPII [47], Quijote [48], Spider [49] have been built with this goal in mind,

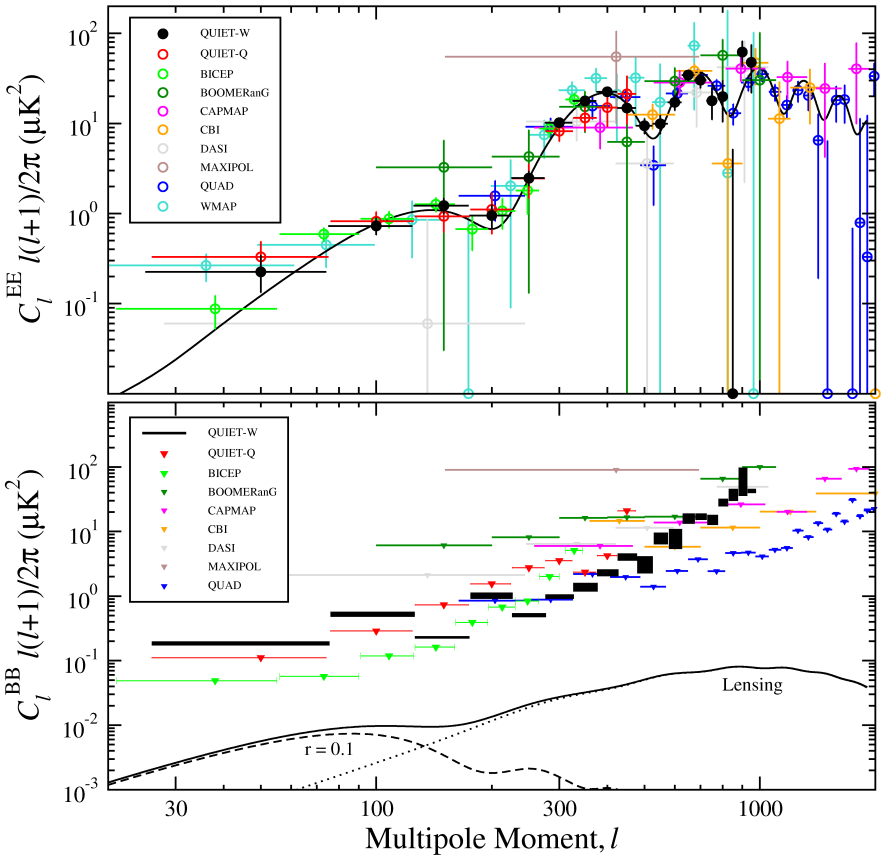

Figure 1.6: Summary of published CMB polarisation EE power spectrum (top) and 95% C.L. upper limits on BB power (bottom) measured by different experiments. The solid line in the upper panel shows the ΛCDM EE spectrum; the dashed and dotted lines in the bottom panel show the BB spectrum from gravitational waves (for $r = 0.1$) and lensing, respectively. Image adapted from Araujo et al. 2012 [46]

and whilst the TE and EE spectra have been measured (with relatively large errors on EE), only upper limits have so far been placed on the BB spectrum, shown in Figure 1.6.

Inflation predicts a stochastic background of gravitational waves, which generate a primordial B-mode polarisation in the CMB sky. A time-variable tensor metric perturbation will leave a signal in the temperature anisotropy. Such a perturbation produces a quadrupolar distortion in the spatial metric. As we have seen, inflation predicts a nearly scale-invariant spectrum of gravitational waves. Their amplitude depends strongly on the energy scale of inflation, and its relationship to the curvature fluctuations discriminates between the different models of inflation. The quadrupole generated by a gravitational wave has its main angular variation transverse to the wavevector. The resulting polarisation has orientation either along or orthogonal to the wavevector and at 45° to it. Gravitational waves therefore generate a nearly equal amount of E and B-mode polarisation when viewed at a distance much greater than the wavelength of the fluctuation [50] [51]. Because density

perturbations do not produce a B-mode signal, it is a relatively clean way to study inflation, and a detection of gravitational waves in the CMB will therefore provide the best opportunity to study the inflationary epoch.

1.2.4.1 Gravitational Lensing

As well as gravitational waves, other sources of a B-mode polarisation exist that will contaminate the primordial signal. The gravitational potential of bound structures (galaxies, clusters and superclusters of galaxies) in the Universe will distort the CMB photons as they travel to us from the last-scattering surface. Gravitational lensing is the mapping of source photons onto the image plane conserving surface brightness, therefore only the anisotropies are affected. The photons are deflected by an angle dependent on the angular gradient of the potential projected along the line-of-sight, with a more massive object producing more deflection. Lensing acts to smooth the acoustic peaks in the power spectrum. It is straightforward to see why this effect will generate secondary B-modes. For the polarisation, photon remapping by the gravitational lenses will preserve the orientation of the polarisation vector, but will warp the spatial distribution in a Gaussian random manner, and will hence not preserve the symmetry of the original E-mode. The B-modes from lensing therefore set a confusion threshold for experiments that only probe a part of the sky. Full-sky experiments like Planck can access the reionisation bump at low ℓ, which is less confused by the lensing signal. Given that the lensed CMB is slightly non-Gaussian, there is some hope that utilising this property may help distinguish between primordial and secondary B-modes [52].

For values of $r \approx 0.1$, lensing dominates the primordial signal on all but the largest scales $\ell < 100$, and for $r \approx 0.01$ lensing dominates on all scales for which $\ell < 10$. The current generation of CMB polarisation experiments are expected to reach approximately the latter level, and for levels much below this, excellent control of lensing separation will be required to probe small scales. Figure 1.7 shows all the spectra discussed in this section, with a lensing signal simulated within the concordance model, and two primordial B-mode signals for $r = 0.1$ and $r = 0.01$.

1.2.5 Observational Parameters

Rapid advances in observational cosmology have led to the establishment of the standard cosmological model, described earlier in this chapter. Many of the key cosmological parameters are now determined to one or two significant figures, with the current generation of experiments aiming to build on this precision. Of particular use in parameter estimation is the CMB power spectrum, which, following the WMAP 9-year data release [4], has strongly constrained the parameters of the base six-parameter ΛCDM model. More general models however, require the combination of a wide range of different types of observation, lifting parameter degeneracies by combining complementary datasets, and providing consistency checks between methods to strengthen constraints.

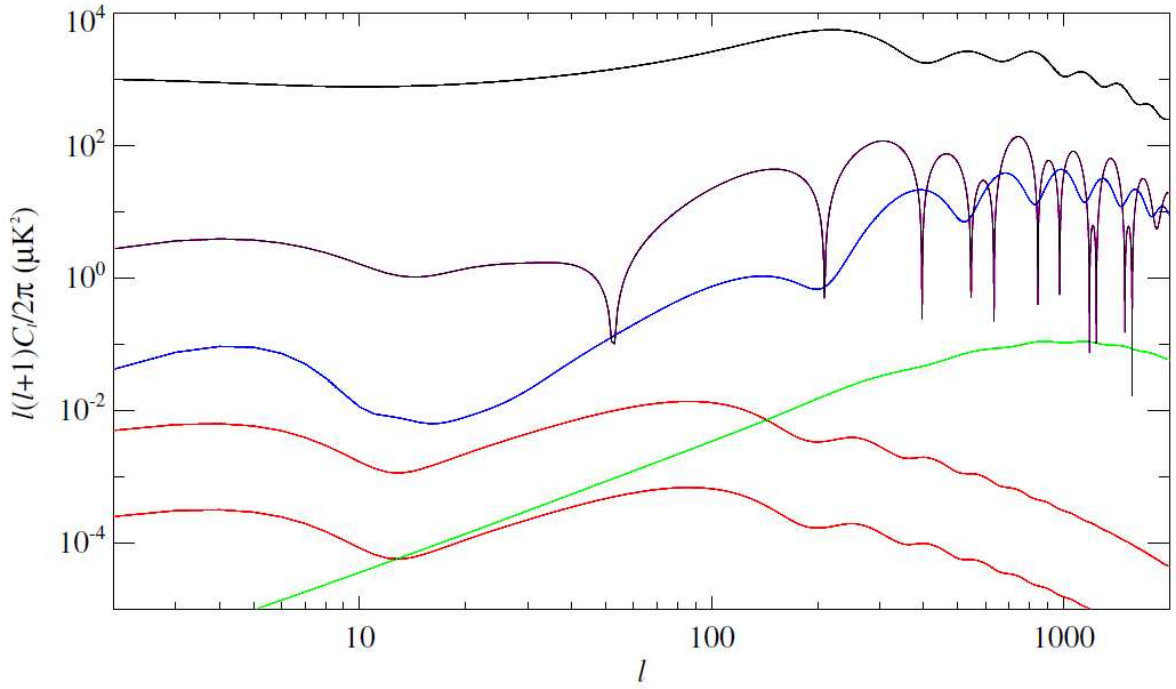

Figure 1.7: CMB power spectra generated with the cosmological concordance model. The TT spectrum is shown in black, the E-mode spectrum in blue and the TE spectrum in purple. The gravitational lensing B-mode spectrum is shown in green, and the gravitational wave B-mode is shown in red for a tensor-to-scalar ratio of 0.2 (upper) and 0.01 (lower). The value $r = 0.2$ is roughly the current upper limit, and $r = 0.01$ around the expected sensitivity of the upcoming generation of experiments.

The modern cosmological model not only contains information on the global dynamics of the Universe, such as the curvature and expansion rate, but also the composition in terms of the baryonic, dark matter, dark energy content, neutrino, and photon densities. Basic models typically feature 6-10 parameters, but more exotic models can be composed of many more.

Within the framework of the perturbed Robertson-Walker spacetime described by the Einstein equations, the Friedmann equation can be written as:

$$\sum_i \Omega_i + \Omega_\Lambda - 1 = \frac{k}{a^2 H^2}, \tag{1.55}$$

where the density parameter Ω_i contains the densities of the matter species relative to the critical density, Ω_Λ represents the cosmological constant, and $h = H_0/100$ is the Hubble parameter. If neutrinos are non-relativistic today (with $m_\nu \gg T_{\nu,0}$), they can be described by their density parameter

$$\Omega_\nu h^2 = \frac{\sum m_\nu}{93 \text{ eV}}, \tag{1.56}$$

where we sum over the species with mass in that range. As we have seen previously, a description of the perturbations from homogeneity is required to complete the model, and one such parameterisation is the curvature perturbation ζ, which measures the spatial curvature of a comoving slice of space-time. The spectrum can be approximated by a power law

$$\Delta^2_\zeta(k) = \Delta^2_\zeta(k_*) \left[\frac{k}{k_*}\right]^{n_s - 1}, \tag{1.57}$$

where n_s is the spectral index, and k_* is some arbitrarily chosen pivot scale. We can thus define our simple model of the primordial perturbations with r, A_s, n_s, and n_t.

To complete the model we also require a measure of the ionization of the Universe, and the most relevant ionization parameter for the CMB is the optical depth to reionisation τ, where $1-\exp(-\tau)$ corresponds to the probability that a given photon scatters at least once (which approximately equals τ for $\tau \ll 1$). If reionization occurred abruptly, then τ could also be described as a measure of the redshift of reionization z_r. The basic set of cosmological parameters as estimated by WMAP [4] are shown in Table 1.1.

Parameter	Symbol	Value
Hubble parameter	h	0.704 ± 0.025
Cold dark matter density	Ω_{cdm}	$\Omega_{cdm}h^2 = 0.112 \pm 0.006$
Baryon density	Ω_b	$\Omega_b h^2 = 0.0225 \pm 0.0006$
Cosmological constant	Ω_Λ	$\Omega_\Lambda = 0.73 \pm 0.03$
Radiation density	Ω_r	$\Omega_r h^2 = 2.47 \times 10^{-5}$
Density perturb. amplitude	$\Delta^2_\mathcal{R}(k = 0.002\text{Mpc}^{-1})$	$(2.41 \pm 0.11) \times 10^{-9}$
Density perturb. spectral index	n	$n = 0.967 \pm 0.014$
Tensor to scalar ratio	r	$r < 0.36$ (95% conf.)
Ionization optical depth	τ	$\tau = 0.088 \pm 0.015$

Table 1.1: The basic set of cosmological parameters. We give values as obtained using a fit of a ΛCDM cosmology with a power-law initial spectrum to WMAP7 data alone. Tensors are assumed zero except in quoting a limit on them. The exact values and uncertainties depend on both the precise data-sets used and the choice of parameters allowed to vary. Limits on Ω_Λ and h weaken if the Universe is not assumed flat. Uncertainties are 1σ/68% confidence unless otherwise stated.

Almost exact degeneracies exist between various cosmological parameters (e.g., Efstathiou & Bond 1998 [53]; Eisenstein, Hu & Tegmark 1998 [54]) such that (for example) models with the same

matter densities can have the same CMB anisotropies on all but the largest scales, but at the same time have very different geometries. Consequently, measurement of CMB anisotropies will be able to yield strong constraints on the products $\Omega_m h^2$ and $\Omega_b h^2$, but not on the individual values of h and Ω_m directly for any models beyond ΛCDM. Hence, earlier suggestions that such cosmological parameters could be measured from CMB anisotropies to precisions of 1% or better (e.g., Bond, Efstathiou & Tegmark 1997 [55]) will unfortunately not be realised. However, degeneracy breaking can be achieved by using the CMB data in combination with other observables such as the shape of the galaxy power spectrum, Baryon Acoustic Oscillations (BAO) in the galaxy power spectrum, and type Ia supernovae (SN1a). Figure 1.8 shows the parameter fits found using the WMAP 5-year data and the Planck nominal survey predictions for comparison. Figure 1.9 shows the $n_s - r$ plane, a particularly important degeneracy for CMB polarisation studies, and also how the introduction of extra data breaks degeneracies (in this case between the dark energy equation of state parameter w and the curvature density Ω_k).

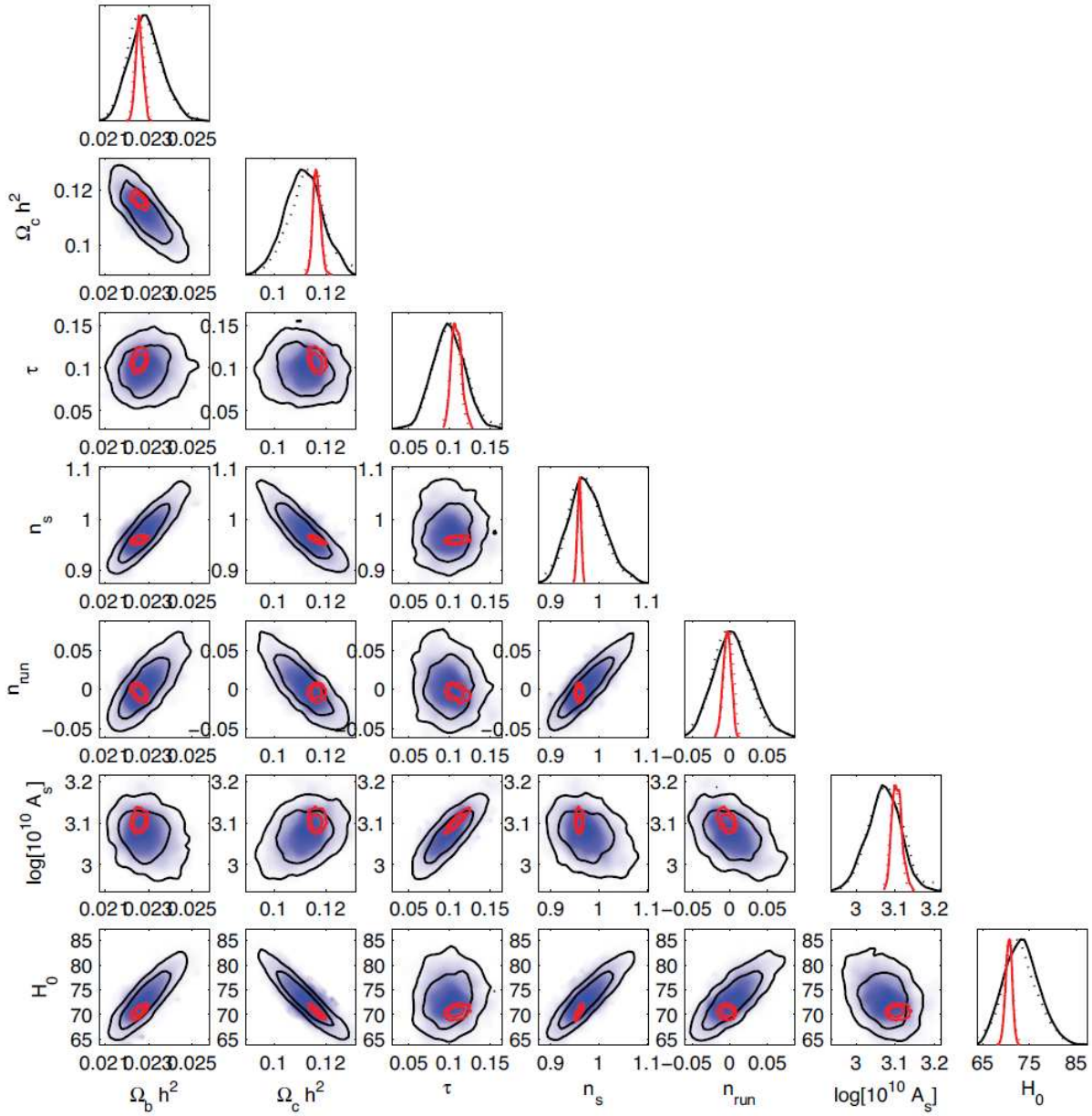

Figure 1.8: Forecasts for Planck of 1 and 2σ contour regions for the main cosmological parameters when the spectral index n_s is allowed to run. Black contours show WMAP after 5 years of observation and red contours show projected results for Planck after 1 year of observation. The curves show marginalized posterior distributions for each parameter. Image adapted from the Planck Blue Book [18]

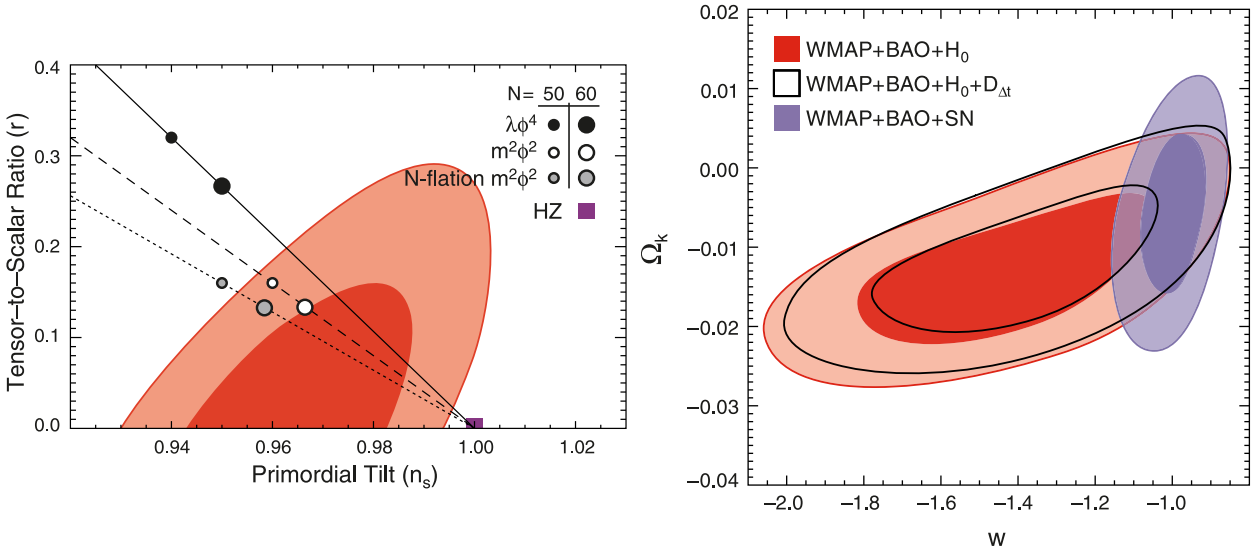

Figure 1.9: *Left:* Two-dimensional joint constraint (68% and 95% limits) on the scalar spectral index n_s and the tensor-to-scalar ratio r, from a combination of WMAP+BAO+H_0. Also shown are predictions from three different models of inflation with the potentials given in the key, modelled with 50 or 60 e-foldings. *Right:* Marginalized constraints on the dark energy equation of state w, and the curvature parameter Ω_k. The different combinations of datasets are indicated by different coloured shadings. Image adapted from Komatsu et al, 2009 [56].

1.3 The Planck Satellite

Planck is a space-based multi-frequency microwave observatory launched in April 2009, designed to measure the temperature and polarisation anisotropies of the CMB over a wide frequency range 30 - 857 GHz, with polarisation sensitivity over the range 30 - 353 GHz. The satellite arrived at its destination in January 2010 and has since occupied a Lissajous orbit around the L2 Lagrange point of the Earth-Sun system. It completely scans the sky about every eight months. Since its launch in 2009, it has completed five full sky surveys with both instruments; the Low Frequency Instrument (LFI) with detectors at 30, 44, and 70 GHz, and the High Frequency Instrument (HFI) with detectors at 100, 143, 217, 353, 545, and 857 GHz (see Table 1.2 for more details on the technical performance of the detectors). The HFI focal plane is cooled to 0.1 K, making Planck the coldest known body in outer space. Planck is the third-generation space-based CMB experiment following COBE (launched in 1989) and WMAP (launched in 2001). Whilst the primary goal is cosmology, Planck was built with many secondary objectives in mind. It has surveyed the whole sky with an unprecedented combination of angular resolution, frequency coverage and sensitivity, and provides a wealth of data applicable to a broad range of astrophysical phenomena.

Secondary anisotropies, or distortions of the CMB caused by large-scale matter structures which formed long after the CMB decoupled, can be mapped in detail across a large range of frequencies across the whole sky. Many other experiments can map these effects, but only Planck can produce all-sky maps. Hot gas in galaxy clusters also distorts the CMB photons as they travel to us, called the Sunyaev-Zel'dovich effect, which depends on frequency. Again, Planck's large frequency coverage allows for detailed reconstructions of this effect. Planck can also map the gravitational lensing signal, another interesting effect that has only recently been explored in detail. These effects trace the large-scale distribution of matter in the Universe and hence provide an additional and independent source of information on the early Universe. Following the initial public data release in 2013, Planck has studied galactic and extragalactic sources of emission such as bright radio galaxies, compact sources and galactic supernovae, and hot thermal dust clouds. Follow-up observations are now underway with higher-resolution dedicated telescopes/satellites. The gas and dust in the Milky Way has also been studied, as it radiates strongly at the Planck frequencies (and indeed is the main topic of this thesis). Detailed maps of the galactic magnetic field can be drawn, as well as a new view of cool objects in our own Solar System. The scientific return from Planck is spectacular. It would not be unreasonable to suggest, that with such an improvement over previous experiments, one could even anticipate new physics.

Table 1.2 outlines the main instrumental characteristics of the Planck Satellite, as taken from the pre-flight mission statement, or the 'blue book' [18]. The in-flight characteristics will differ slightly from those detailed here, but the values given here are at the desired level, with subsystems designed to meet or exceed these specifications.

The low Frequency Instrument (LFI) is based on a 22-channel multifrequency receiver array with

	LFI			HFI					
Instrument Characteristic									
Central frequency (GHz):	30	44	70	100	143	217	353	545	857
Fractional bandwidth ($\Delta\nu/\nu$):	0.2	0.2	0.2	0.37	0.37	0.37	0.37	0.37	0.37
Transmission:	1.0	1.0	1.0	0.3	0.3	0.3	0.3	0.3	0.3
Angular resolution (arcmin):	33	23	14	10.6	7.4	4.9	4.5	4.5	4.5
$\Delta T/T$ Intensity (μK):	2.0	2.7	4.7	2.5	2.2	4.8	14.7	147	6700
$\Delta T/T$ Polarisation (μK):	2.8	3.9	6.7	4.0	4.2	9.8	29.8	...	...

Table 1.2: The assumed observational parameters for the Planck satellite. Angular resolution is quoted as FWHM ($= 2\sqrt{2\ln 2}\sigma$) for a Gaussian beam. Sensitivities are quoted per beam FWHM for two full-sky surveys (14 months of observation). The 535 and 857 GHz channels are not polarisation sensitive. Note that all subsystems are designed to meet or exceed this performance.

ultra-low noise cryogenically-cooled amplifiers built with high-electron-mobility transistors (HEMTs). The LFI (and HFI) focal plane is cooled to 20K, and is separated into two subassemblies which are connected by a series of waveguides. The front-end of the LFI instrument is cooled to 20 K via a close-cycle Hydrogen sorption cryocooler, which also provides precooling to the HFI at 18 K. The configuration of multiple compressors acts to minimise any vibration caused by the compression and expansion of gas and transport to the radiators. This property of this kind of cooler is very beneficial to Planck's observation. For maximum possible accuracy, great control of systematic errors is needed, and detailed analytic and numerical studies of the main sources of systematic error have been carried out pre-flight. These include, but are not limited, to sidelobe pickup of the Galaxy, distorted beam shapes, non-idealities in the radiometer, pointing errors and nutation, and calibration errors [57]. Particularly for polarisation studies, these systematic errors will likely be the dominant source of spurious signal, and detailed analyses are essential in-flight as well as those carried out pre-launch. The LFI goal as stated in the blue book is that the combination of all systematic errors in the final sky maps will be less than 3 μK per resolution element.

The High Frequency Instrument (HFI) observes at six frequencies from 100 - 857 GHz, with all but the two highest frequency channels polarisation-sensitive. The sensitivity in the lower frequencies is close to the fundamental limit set by the photon background statistics itself [58]. The HFI uses bolometer detectors which are designed to be extremely sensitive to the CMB photons yet insensitive to ionizing radiation and other microphonic effects [59] (high-energy cosmic rays have however been a significant in-flight issue [60]). The 52 bolometers are spread over the six channels, with the frequencies chosen to maximise foreground-removal and SZ cluster detection. Thirty-two bolometers sensitive to linear polarisation absorb the polarised component with electric field parallel to the bolometer wires. Measurements from different bolometers are then combined to produce maps of the sky and its polarisation. The coupling between the detectors and the telescope is designed for high optical efficiency, and the readout electronics are based on ultra-low noise amplifiers. The data are finally compressed to 50 kbps for transmission to the ground receiving stations.

The first-light survey, performed in August 2009, demonstrated the stability of the instrumentation,

and the calibration accuracy achievable over long periods, with analyses indicating that the data quality is very high [61]. After completion of the nominal survey in February 2010, the mission was extended by a further 12 months, with data collection anticipated until at least December 2011. By this point Planck had achieved a 95% sky coverage, with the remaining regions to be scanned by mid-2010. The first public imagery released following the first-light snapshot was an all-sky image released in June 2010, shown in Figure 1.10. It highlights the CMB and diffuse galactic emission, as well as localised sources such as the Large Magellanic Cloud, the Andromeda galaxy, and the Orion nebula.

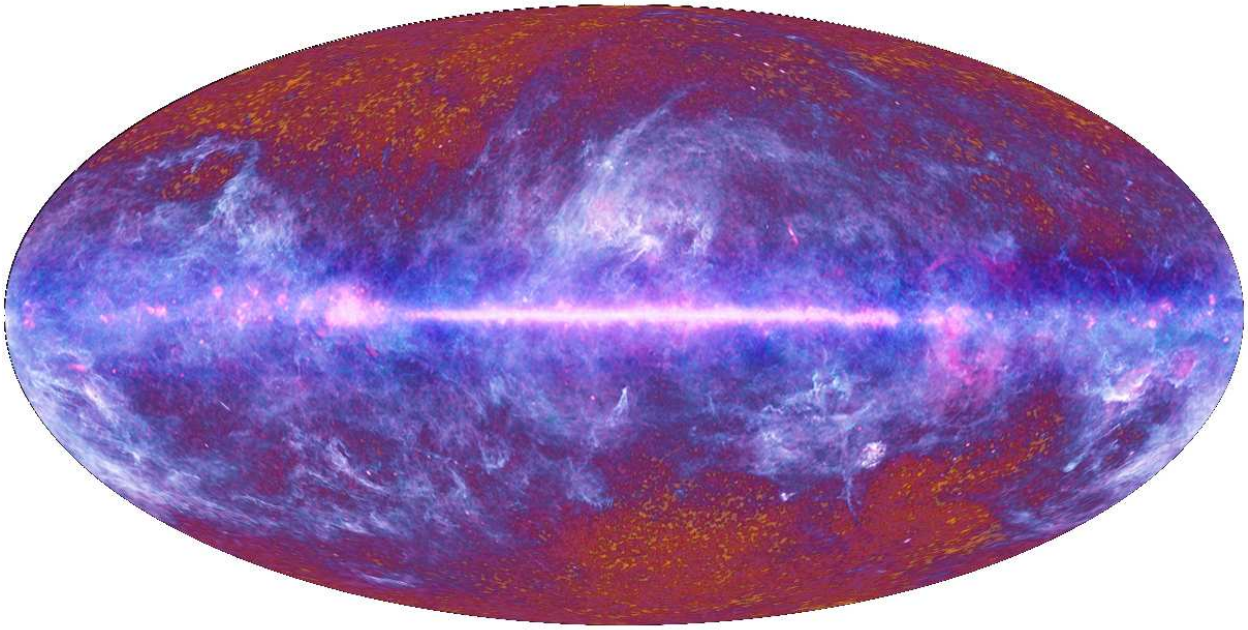

Figure 1.10: A false-colour image of the whole sky as seen by Planck. Thermal dust radiation is shown in blue, hot gas is shown in red, and the CMB is shown in yellow. This image is a low-resolution version of the full sky image. Image adapted from ESA. Image Credits: ESA, LFI and HFI Consortia (2010)

A catalog of compact sources was released in January 2011 including the Early Cold Cores (ECC) and the Early Sunyaev-Zel'dovich (ESZ) cluster catalogues, containing over 15,000 distinct objects [62]. The liquid Helium cooling the HFI detectors was depleted in January 2012, and the instrumentation began to warm. The LFI can operate at warmer temperatures and continued to collect data for another six months. The nominal mission data and results were published in March 2013, the mission having far exceeded the minimum specification of two full sky scans. A more detailed description of Planck's instrumentation and sensitivity can be found in the Scientific Programme for Planck [18].

Most Planck measurements will be limited by how well foregrounds can be subtracted, rather than by detector performance. This is particularly important for the polarisation measurements. The dominant foreground depends on observation frequency and includes electron synchrotron radiation

from the Milky Way Galaxy at low frequencies, and thermal dust emission at high frequencies. These important foregrounds are detailed in the following section.

1.4 Foregrounds

The Milky Way is an energetically active galaxy composed of interacting clouds of gas and dust, which radiate strongly across the entire electromagnetic spectrum. Of particular relevance to Planck are the physical mechanisms responsible for producing microwave emission at the observing frequencies between 30 and 857 GHz. Several processes generate polarised radiation, a major problem for CMB analyses. Planck is at an advantage over many other experiments because of its wide frequency coverage and ability to scan the whole sky, making signal separation methods more robust. In this section we briefly review the main physical processes that give rise to polarised microwave emission in the Planck frequency range, and the expected strength of the foregrounds compared to the CMB. Details of analytic formulae, simulation mechanisms, and detailed explanations of foreground templates are left for Chapter 2.

Many experiments are actively hunting B-modes in the CMB, and the greatest challenge for all these experiments is accurate foreground separation. Many sources of emission confuse the polarised CMB signal, and whilst this has not been a major issue for temperature and E-mode studies, the B-mode is expected to be much weaker by at least an order of magnitude and thus the foregrounds pose a much greater problem. At typical B-mode levels with $r = 0.1$ the polarised foregrounds dominate across the entire frequency range and across much of the sky, and by several orders of magnitude across the Galactic plane. There is a wealth of previous work on this issue for temperature, but for polarisation the foregrounds are much less understood, and poorly constrained by current data. Indeed several experiments currently in operation have been built primarily to observe foregrounds.

The two main sources of polarised microwave emission are electron synchrotron and thermal dust emission. Electron synchrotron emission arises from helical gyration of electrons around the Galactic magnetic field, an intrinsically polarising process. The emission is highly dependent on the local Galactic magnetic field, and can be polarised up to 70% perpendicular to the field. Regions of strongest emission are found along the Galactic plane. Polarized thermal dust emission arises from elongated grains of dust aligned with their long axis perpendicular to the magnetic field, which emit radiation preferentially along their inertial axis. This generates emission polarised perpendicularly to the magnetic field, correlating with the synchrotron emission. Again, regions of stronger Galactic magnetic field will produce a stronger alignment to the field, increasing the level of polarisation, and the strongest magnetic field is found along the Galactic plane. These sources of emission are illustrated in Figure 1.11.

A third important mechanism that could potentially confuse the polarised CMB signal is anomalous microwave emission (sometimes referred to as spinning dust emission). It has been proposed that

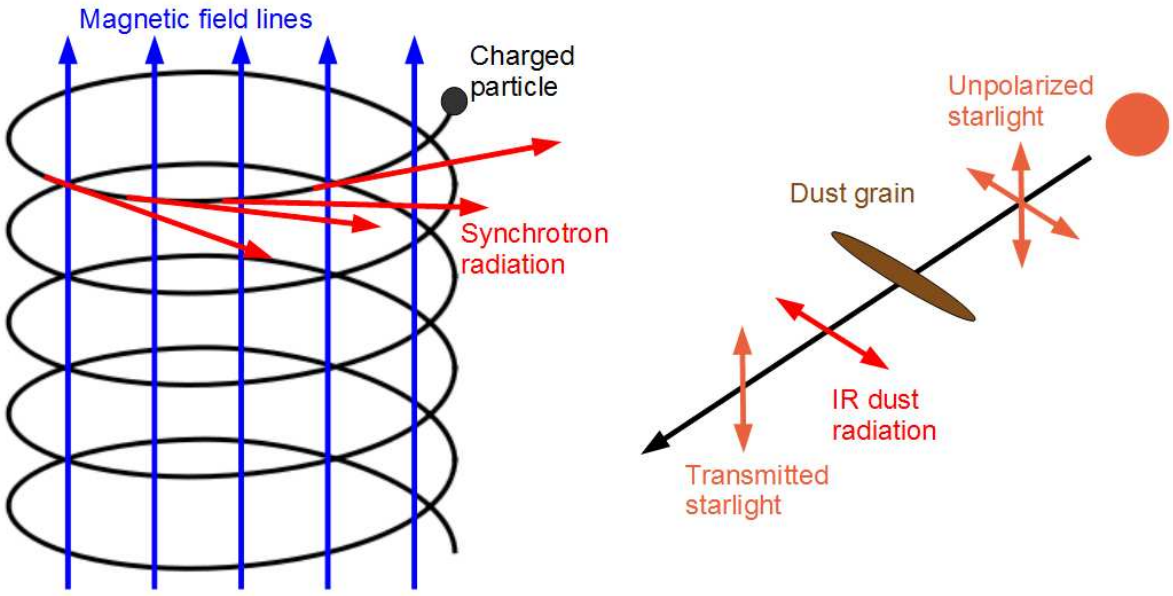

Figure 1.11: Left: Synchrotron radiation is generated by a charged particle spiralling around a magnetic field, with the radiation emitted perpendicularly to the field. Synchrotron radiation is highly polarised. Right: Polarised thermal dust emission generated by elongated dust grains aligned to the magnetic field emitting thermal radiation. More elongated grains and a stronger magnetic field give rise to a higher level of polarisation.

very small elongated dipolar dust grains very rapidly spinning along the magnetic field can produce a strong polarisation signal [63]. The anomalous microwave emission was first reported in 1996[64], and has been studied in limited detail since. The emission correlates with the far-infrared dust profile, but with a much higher intensity than estimates from extrapolating higher frequency data down to the microwave regime suggest. If this hypothesis is correct, the spinning dust intensity emission will be important up to about 100 GHz, but the polarised fraction is predicted to be low [63], and negligible above the 30 GHz channel. Alternate mechanisms to explain the anomalous microwave emission have also been proposed, such as magnetic dipole radiation via thermal fluctuations of the grain magnetisation [65], which could have a significant polarisation fraction. The initial Planck results however do not suggest a strong polarised signal from the anomalous component [66].

The two main contributions from synchrotron and dust behave very differently across the Planck frequency range, with synchrotron emission dominating the low-end channels (30, 44, 70 GHz) and in fact peaking at a frequency much lower than 30 GHz. Thermal dust emission conversely becomes increasingly bright at higher frequencies above 100 GHz, and totally dominates from 217 GHz and above.

The main body of work in this thesis focusses on the synchrotron and dust foregrounds. In Chapter 2 we look at different models of synchrotron and dust emission using templates and theoretical

models for the Galactic magnetic field, and Planck noise characteristics. These simulations are then used in a maximum-likelihood foreground parameterisation method to separate the foregrounds from the simulated CMB polarisation. The separated CMB polarisation can then be analysed for discrepancies between input and output, particularly for the B-mode signal, which we can artificially inject into the simulated maps. Testing such methods on simulated data is important to get a handle on the foreground leakage into cleaned maps and the effect on the resultant B-mode likelihood.

In Chapter 3 we look at the real data from the complete Planck survey, and compare the simulations described previously to the actual sky. We investigate the polarisation behaviour across the galaxy in terms of the polarisation fraction and morphology away from the plane. Even with Planck-level sensitivity, noise is still an important component of the high-resolution polarisation maps and so we degrade these to lower resolution for such analyses.

1.5 CMB Notation

It is helpful to outline the conventions and notation used in this thesis, and also to briefly describe the HEALPix visualisation software used extensively in this work. As we have seen, the E and B decomposition of the sky is useful for characterising polarisation, however these expressions are non-local transformations of the CMB distribution across the sky, and are not observed directly. The standard method of expressing polarisation is in terms of the Stokes parameterisation, which we will outline first before moving on to consequent notation.

1.5.1 Stokes Parameterisation

The Stokes parameters are a set of values that fully describe the polarisation state of electromagnetic radiation. They are expressed in terms of a co-ordinate basis, and the most natural co-ordinate basis to choose given we are observing photons originating from a spherical shell is the spherical polar coordinate system. A point in spherical polar space is defined by a radial parameter $\hat{r}$, a polar angle $\hat{\theta}$, and an azimuthal angle $\hat{\phi}$. If we choose to work in a right-handed basis, in accordance with IAU specification, our radially inward basis is defined as $(\hat{r}, \hat{\theta}, -\hat{\phi})$, and we can then define the Stokes parameters for an electromagnetic wave $\mathbf{E}$ as

$$I = \langle E_\theta E_\theta^* + E_\phi E_\phi^* \rangle \tag{1.58}$$

$$Q = \langle E_\theta E_\theta^* - E_\phi E_\phi^* \rangle \tag{1.59}$$

$$U = -\langle E_\theta E_\phi^* + E_\phi E_\theta^* \rangle \tag{1.60}$$

$$V = i\langle E_\theta E_\phi^* - E_\phi E_\theta^* \rangle. \tag{1.61}$$

The angle brackets are included to show averaging over a timescale long compared to the period of **E**. For a completely polarised wave, there are three independent parameters which are related by

$$I^2 = Q^2 + U^2 + V^2, \tag{1.62}$$

whereas for a partially polarised wave Eq.(1.62) becomes the inequality

$$I^2 \geq Q^2 + U^2 + V^2. \tag{1.63}$$

The Stokes parameters characterise the magnitude and relative phase, and hence the polarisation of the wave. The parameter I is equal to the total power (density) of the wave; Q is equal to the difference in power in the linear horizontal/vertical polarised components; U gives the difference in power in the linearly polarised component inclined at $\theta = 45^\circ$ or 135° to the basis; and V is the power in the circularly-polarised component of the wave. If any of the parameters Q, U, V has a non-zero value, then the plane wave is polarised. The parameter V is positive for right-handed polarisation (i.e. when an observer observes the electric vector rotate clockwise in time), but the CMB is not expected to be circularly polarised, and hence we are most interested in Q and U. The parameters I and V are physical observables which are independent of the coordinate system, but since Q and U are defined relative to the coordinate axes, they will change upon transformation of coordinate system. If we rotate the $\theta - \phi$ plane through an angle of ψ, the same wave is now described by the modified parameters

$$\begin{aligned} Q' &= Q\cos(2\psi) + U\sin(2\psi), \\ U' &= -Q\sin(2\psi) + U\cos(2\psi). \end{aligned}$$

The quantity $I^2 = Q^2 + U^2$ is conserved under rotation, and the angle

$$\alpha = \frac{1}{2}\tan^{-1}\frac{U}{Q} \tag{1.64}$$

defines a constant angle of polarisation which is parallel to the electric field of the wave. A useful property of the Stokes parameters is that they are additive for superposition of coherent radiation, a quality not true for the magnitude or orientation of polarisation. The transformation above is representative of a rank-2 tensor, and in the θ, ϕ basis we can express the polarisation tensor as

$$P = \frac{1}{2}\begin{pmatrix} I+Q & U+iV \\ U-iV & I-Q \end{pmatrix}. \tag{1.65}$$

As we will see, it is usually convenient to work with complex linear combinations of Q and U, which

transform irreducibly under rotation as

$$(Q \pm iU)'(\hat{\mathbf{n}}) = (Q \pm iU)e^{\mp 2i\psi}(\hat{\mathbf{n}}), \tag{1.66}$$

where, again, ψ is the rotation angle.

1.5.2 Spin-weighted Fields on the Sphere

Let us consider a function ${}_sF(\theta,\phi)$ on the sphere. This function is said to have spin-s if, under a right-handed rotation of the basis vectors $(\hat{\mathbf{e}}_\theta, \hat{\mathbf{e}}_\phi)$ by an angle ψ, it transforms as:

$${}_sF(\theta,\phi)' = e^{-is\psi}F(\theta,\phi). \tag{1.67}$$

We can expand a scalar field on the sphere in terms of spherical harmonics which form a complete and orthonormal basis. We cannot use this expansion to express spin-weighted functions with $s \neq 0$ in the same way, however similar sets of functions can be used for such an expansion, the spin-s spherical harmonics ${}_sY_{\ell m}(\theta,\phi)$. These functions satisfy the completeness and orthogonality relations,

$$\int_0^{2\pi} d\phi \int_{-1}^{1} d\cos\theta \; {}_sY^*_{\ell' m'}(\theta,\phi) \; {}_sY_{\ell m}(\theta,\phi) = \delta_{l\ell'\ell}\delta_{m'm} \tag{1.68}$$

$$\sum_{\ell m} {}_sY^*_{\ell m}(\theta,\phi) \; {}_sY_{\ell m}(\theta',\phi') = \delta(\phi-\phi')\delta(\cos\theta - \cos\theta'), \tag{1.69}$$

and there is one set of functions for each spin level. A useful set of spin-raising and spin-lowering operators can be defined as:

$$\eth \; {}_sF(\theta,\phi) = -\sin^s(\theta)\left[\frac{\partial}{\partial\theta} + i\csc(\theta)\frac{\partial}{\partial\phi}\right]\sin^{-s}(\theta) \; {}_sF(\theta,\phi) \tag{1.70}$$

$$\bar{\eth} \; {}_sF(\theta,\phi) = -\sin^{-s}(\theta)\left[\frac{\partial}{\partial\theta} - i\csc(\theta)\frac{\partial}{\partial\phi}\right]\sin^{s}(\theta) \; {}_sF(\theta,\phi), \tag{1.71}$$

which operate to raise and lower the spin-weight of the function ${}_sF(\theta.\phi)$. The ${}_sY_{\ell m}$ can be expressed in terms of the zero-spin spherical harmonics as

$${}_sY_{\ell m} = \left[\frac{(\ell-s)!}{(\ell+s)!}\right]^{\frac{1}{2}} \eth^s \; Y_{\ell m} \quad (0 \leq s \leq l) \tag{1.72}$$

$${}_sY_{\ell m} = \left[\frac{(\ell+s)!}{(\ell-s)!}\right]^{\frac{1}{2}} (-1)^s \bar{\eth}^{-s} \; Y_{\ell m} \quad (-l \leq s \leq 0). \tag{1.73}$$

We can expand the T, Q, and U in the spin-basis as

$$T(\hat{\mathbf{n}}) = \sum_{\ell m} a_{T,\ell m} Y_{\ell m}(\hat{\mathbf{n}}) \tag{1.74}$$

$$(Q + iU)(\hat{\mathbf{n}}) = \sum_{\ell m} a_{2,\ell m}\ {}_2Y_{\ell m}(\hat{\mathbf{n}}) \tag{1.75}$$

$$(Q - iU)(\hat{\mathbf{n}}) = \sum_{\ell m} a_{-2,\ell m}\ {}_{-2}Y_{\ell m}(\hat{\mathbf{n}}), \tag{1.76}$$

where Q and U are defined for a direction $\hat{\mathbf{n}}$ on the sky.

1.5.3 E and B-Modes

Given the spin-raising and lowering operators, we can construct spin-zero quantities for polarisation as well as for temperature. Spin-zero quantities have the advantage of being rotationally-invariant, and thus no ambiguities with rotation of the coordinate system will arise. Operating twice with $\eth$ and $\bar{\eth}$ on $Q \pm iU$ gives

$$\bar{\eth}^2(Q + iU)(\hat{\mathbf{n}}) = \sum_{\ell m} \left[\frac{(\ell+2)!}{(\ell-2)!}\right]^{1/2} a_{2,\ell m} Y_{\ell m}(\hat{\mathbf{n}}) \tag{1.77}$$

$$\eth^2(Q - iU)(\hat{\mathbf{n}}) = \sum_{\ell m} \left[\frac{(\ell+2)!}{(\ell-2)!}\right]^{1/2} a_{-2,\ell m} Y_{\ell m}(\hat{\mathbf{n}}). \tag{1.78}$$

The expansion coefficients can be calculated as

$$a_{T,\ell m} = \int d\Omega\ Y^*_{\ell m}(\hat{\mathbf{n}}) T(\hat{\mathbf{n}}) \tag{1.79}$$

$$a_{2,\ell m} = \int d\Omega\ {}_2Y^*_{\ell m}(\hat{\mathbf{n}})(Q + iU)(\hat{\mathbf{n}}) \qquad = \left[\frac{(\ell+2)!}{(\ell-2)!}\right]^{-1/2} \int d\Omega\ Y^*_{\ell m}(\hat{\mathbf{n}}) \bar{\eth}^2 (Q + iU)(\hat{\mathbf{n}}) \tag{1.80}$$

$$a_{-2,\ell m} = \int d\Omega\ {}_{-2}Y^*_{\ell m}(\hat{\mathbf{n}})(Q - iU)(\hat{\mathbf{n}}) \qquad = \left[\frac{(\ell+2)!}{(\ell-2)!}\right]^{-1/2} \int d\Omega\ Y^*_{\ell m}(\hat{\mathbf{n}}) \eth^2 (Q - iU)(\hat{\mathbf{n}}). \tag{1.81}$$

We can use these definitions to motivate E and B modes encountered in Section 1.2.4 as parity states. Let us introduce a linear combination of $a_{2,\ell m}$, $a_{-1,\ell m}$ as

$$a_{E,\ell m} = -(a_{2,\ell m} + a_{-2,\ell m})/2 \tag{1.82}$$

$$a_{B,\ell m} = i(a_{2,\ell m} - a_{-2,\ell m})/2, \tag{1.83}$$

where $a_{E,\ell m}$ and $a_{B,\ell m}$ are the coefficients for the electric-type and magnetic-type modes.

1.5.4 Power Spectra

A complete parameterisation of the CMB perturbations requires four power spectra, those for T, E, B and TE. As discussed earlier, the TB and EB spectra vanish because of the opposite parity of B to T and E. Building on the formalism in Section 1.5.3, the power spectra are defined as

$$\begin{aligned} C_\ell^T &= \frac{1}{2\ell+1}\sum_m \langle a_{T,\ell m}^* a_{T,\ell m}\rangle \\ C_\ell^E &= \frac{1}{2\ell+1}\sum_m \langle a_{E,\ell m}^* a_{E,\ell m}\rangle \\ C_\ell^B &= \frac{1}{2\ell+1}\sum_m \langle a_{B,\ell m}^* a_{B,\ell m}\rangle \\ C_\ell^X &= \frac{1}{2\ell+1}\sum_m \langle a_{T,\ell m}^* a_{E,\ell m}\rangle. \end{aligned} \tag{1.84}$$

1.5.5 Units

Intensity is traditionally measured in the Jansky unit, defined as $1\ \mathrm{Jy} = 1\times10^{-26}\ \mathrm{Wm^{-2}Hz^{-1}}$, and a specific intensity can be given in terms of MJy/steradian. It is common to express TQU images and E and B-mode plots in terms of a temperature, using the black body specific intensity given in Eq.(1.47). If $\Delta I(x)$ is the fluctuation in the specific intensity at some frequency ν in the direction $\hat{\mathbf{n}}$, then the corresponding fluctuation in the equivalent CMB thermodynamic temperature is given by

$$\Delta T(\hat{\mathbf{n}},\nu) = \frac{\Delta I(\hat{\mathbf{n}},\nu)}{(\partial B/\partial T)|_{T=T_0}} \tag{1.85}$$

where $B(\nu,T)$ is the Planck function and $T_0 = 2.726$ K is the temperature of the CMB (Mather et al. 1994). The equivalent CMB thermodynamic temperature is defined as the temperature such that the true intensity is equal to the Planck black-body intensity expanded to linear order about the CMB temperature. In these units, the result is equivalent to a frequency-dependent scaling of the total intensity and, for black-bodies with a temperature close to the CMB monopole temperature of $2.726K$, this is equal to the true temperature. The Q, U, E and B fields can be similarly scaled to units of temperature. Throughout this work, we will make use of the CMB thermodynamic temperature units for the Stokes parameters, and E and B-fields.

1.5.6 HEALPix

Throughout this work we make extensive use of the Hierarchical Equal Area iso-Latitude Pixellisation (HEALPix) software suite [67]. HEALPix is a curvilinear partition of the 2-sphere into

equal-area quadrilaterals of varying shape. The base-resolution comprises twelve pixels in three rings around the poles and equator (shown in Figure 1.12). The resolution of the grid is expressed by the parameter $N_{\rm side}$, which defines the number of divisions along the side of a base-resolution pixel that is needed to reach a desired high-resolution partition, giving a total number of pixels $N_{\rm pix} = 12N_{\rm side}^2$ for a given $N_{\rm side}$. All pixel centres are placed on $4N_{\rm side}-1$ rings of constant latitude, and are equidistant in azimuth (on each ring). All iso-latitude rings located between the upper and lower corners of the equatorial base-resolution pixels, the equatorial zone, are divided into the same number of pixels $N_{\rm eq} = 4N_{\rm side}$. The remaining rings are located within the polar cap regions and contain a varying number of pixels, increasing from ring to ring with increasing distance from the poles by one pixel within each quadrant. Pixel boundaries are non-geodesic and take the very simple forms $\cos(\theta) = a \pm b \cdot \phi$ in the equatorial zone, and $\cos(\theta) = a + b/\phi^2$, or $\cos(\theta) = a + b/(\pi/2 - \phi)^2$ in the polar caps, where a and b are the latitude and longitude coordinates.

The HEALPix software package comprises a set of Fortran and IDL utilities for performing operations on CMB maps on the sphere. *Synfast* simulates full-sky CMB temperature and polarisation maps as realisations of random Gaussian fields, with an option to constrain the realisation with prior information. *Anafast* analyses full-sky CMB temperature and polarisation maps resulting in power spectra and/or spherical harmonic coefficients. *Ismoothing* performs a global smoothing of sky maps with a Gaussian kernel. *Ud_grade* downgrades and upgrades the resolution of discrete maps. *Mollview* allows for visualisation of the HEALPix formatted sky maps in the Mollweide, orthographic, Cartesian, cylindrical, and gnomonic projections of the whole sky or small areas of it. Extra utilities also allow for global searches on the maps for nearest-neighbours, maxima/minima of the discretised functions, algebraic conversion of the maps between the RING and NESTED numbering schemes, mapping back and forth between positions on the sphere and discrete pixel index space, and pixel queries for various geometrical shapes. We make extensive use of the Mollview package for visualisation of full-sky maps and templates in a Galactic coordinate system.

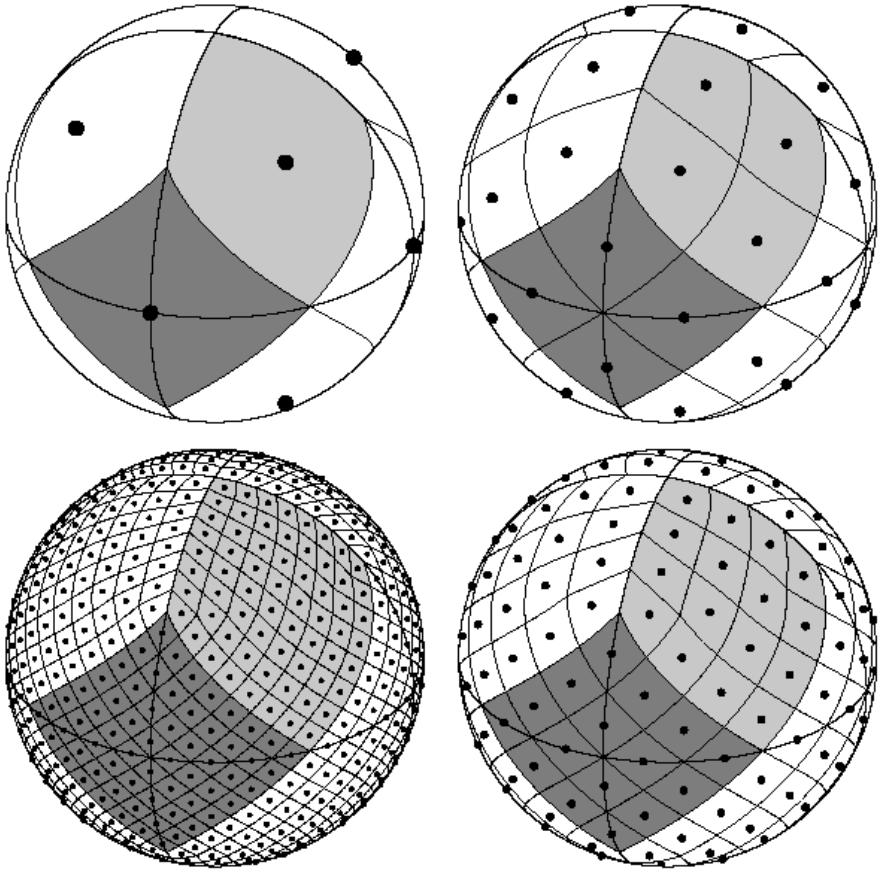

Figure 1.12: Orthographic view of the HEALPix partition of the sphere. The equator and meridians illustrate the octahedral symmetry of the pixellisation. Light-gray shading shows one of the eight (four north, and four south) identical polar base-resolution pixels. Dark-gray shading shows one of the four identical equatorial base-resolution pixels. Moving clockwise from the upper left panel the grid is hierarchically subdivided with the grid resolution parameter equal to $N_{\rm side} = 1$, 2, 4, 8, and the total number of pixels equal to $N_{\rm pix} = 12 \times N_{\rm side}^2 = 12$, 48, 192, 768. All pixel centres are located on $N_{ring} = 4 \times N_{\rm side} - 1$ rings of constant latitude. Within each panel the areas of all pixels are identical. Image adapted from Gorski et al. [67]

1.6 Goals of the Thesis

This thesis is structured into four main parts. In Chapter 2 we describe the problem of foregrounds in terms of CMB polarisation, and explore the literature on current separation methods. We look at generating simulations of the polarised Galactic emission and the data that these models are built on. We then develop a pixel-based polarised foreground separation method to separate full-sky polarised Planck maps over the entire Planck polarisation range. We develop this model further by incorporation of information about the correlation of the foreground spectral indices, and examine the effect this has on the ability of the method to recover a primordial B-mode at expected values of r. In Chapter 3 we look at the full Planck data set for temperature and polarisation and compare with the models available in the Planck Sky Model. In Chapter 4 we use

different foreground separation methods for polarisation to check for residual systematic structure with corrected maps, and examine the contribution of foregrounds at different frequencies and compare with maps from the WMAP satellite. In Chapter 5 we look at parameter estimation from the angular power spectrum based on 15 months of Planck data, and examine the pattern of residuals between the Planck data and theoretical spectra generated with the CAMB software. We then use a Fisher matrix approach to implement a fast step-based algorithm to explore parameter space, and characterise the real parameter sensitivity achievable with Planck

Hystrices numquam moriuntur
- The Porcupines

Chapter 2

Sky Simulation and Parametric Fitting

A multitude of component separation algorithms exist for temperature analyses, and many of these can also be applied to polarisation data. A central consideration for cosmological analyses is the recovery of the CMB fluctuations, while secondary data on the diffuse foreground components is often rejected. Information on the Galactic foregrounds may well be recovered in some methods, and indeed this has been the focus of many previous studies [68] [69] [70]. A common theme for temperature component separation is to utilise information on the spectral characteristics of the components across frequency space, and subtract foreground information either in pixel space or in harmonic space (operating on the angular power spectrum C_ℓ). Some techniques however have not been tested with polarisation data, so it is uncertain how these will perform in a low signal-to-noise regime with foreground components dominant over the polarised CMB at all Planck observing frequencies. It is important with all component separation studies to check results against simulations. Possible biasing or artifact effects inherent to the method can be analysed given full knowledge of the input cosmological model, and the estimated full-sky CMB contribution. Thus simulations form a useful testing suite for any separation routines and they can be used to directly compare such methods and their effectiveness in recovering either the CMB or Galactic foregrounds.

2.1 Introduction

In this chapter we first explore our current knowledge of polarised emission from the CMB, diffuse synchrotron, thermal dust, free-free, and other low-level polarised components. We then examine how this motivates simulations of these components for testing component separation routines. We then examine existing temperature and polarisation component separation techniques and compare their potential effectiveness in the low signal-to-noise regime (as is the case in polarisation for

Planck). Next we describe a suite of full-sky simulations for polarised CMB, synchrotron, and dust emission based on simple models, and observations at low and high frequencies. We inject a B-mode component into the maps at low resolution and compare with the overall level of polarisation. We describe the noise properties of the Planck satellite and use these to form a complete set of high-resolution full-sky simulations from 30 GHz up to 353 GHz designed to emulate what Planck will see. Different spectral index models are described and constraints placed on the applicability of these models. We then use these models in a pixel-based maximum-likelihood parametric fitting method which estimates the CMB, synchrotron, and dust emission and their associated errors. The output B-mode is analysed and compared to the input B-mode in terms of the global amplitude and pixel residuals. We form a likelihood for the output B-mode and sample over the tensor-to-scalar ratio r to build a posterior distribution and compare to the input level. We then incorporate a spatial correlation of the foreground spectral indices to improve the B-mode recovery at different resolutions and show that this gives an improvement in the estimated B-mode. We finally outline how the method could be modified to improve performance and accuracy, and comment on the outlook for polarised foreground removal in the near future, with reference to the accuracy achievable with Planck, and upcoming ground-based and space-based experiments.

2.1.1 Knowledge of Polarised Emission

CMB temperature anisotropies have been mapped exquisitely, however polarisation anisotropies have yet to be fully characterised. The DASI experiment [71] was the first to measure the small amount of polarisation (~ 5 μK rms) in 2002, and subsequently several groups have also measured the signal. Whilst noise is still a dominant factor in the measurements, important constraints have already emerged on cosmological parameters, and a large amount of work is in progress to fully characterise the polarisation power spectrum. One of the driving forces behind current experiments and planned missions is the potential to detect a weak primordial B-mode polarisation, which would have important implications for gravitational wave observations, inflationary model-building [72] and constraints on various models of string theory [73].

2.1.2 CMB

An isotropic photon distribution incident on a free electron will generate unpolarised radiation, whereas a quadrupolar temperature distribution gives rise to linearly polarised photons aligned in parallel to the cold lobe of the incident quadrupole. A quadrupolar temperature distribution at the last scattering surface can be produced by a density inhomogeneity seeded by scalar perturbations. When recombination proceeded to a point where both hot and cold photons could meet to scatter off the same electron, polarised emission was produced. This diffusion of photons into different temperature regions was thus only possible for a period towards the end of recombination when the primordial plasma was optically thin enough. Moreover, diffused photons could only scatter

off electrons while they were still free, again towards the end of recombination. Thus only a small percentage of CMB photons are polarised.

The CMB temperature anisotropies are usually expanded in spherical harmonics,

$$T(\theta,\phi) = \sum_{\ell=0}^{\infty} \sum_{m=-\ell}^{+\ell} a_{\ell,m} Y_{\ell,m}(\theta,\phi). \tag{2.1}$$

If we assume the CMB obeys Gaussian statistics, all the information extractable is contained in the angular power spectrum, defined as $C_l = \langle |a_{\ell m}|^2 \rangle$, where angular brackets denote an average over all possible realisations of the sky. We can express the best estimator for the angular power spectrum as

$$C_\ell = \frac{1}{2\ell+1} \sum_{m=-\ell}^{m=\ell} a^*_{\ell,m} a_{\ell,m}. \tag{2.2}$$

The definition of the angular power spectrum for polarisation is slightly more complex. Linearly polarised waves are described by the two Stokes parameters Q and U, which we can use to express the total polarised intensity as $I = \sqrt{Q^2+U^2}$, and the angle of polarisation as $\phi = 0.5 \arctan(Q/U)$. The definition of ϕ depends on our choice of coordinates, and the values of Q and U change if we rotate the coordinate system. Typically one defines a rotationally invariant angular power spectrum, following the formalism of Zaldarriaga and Seljak [74] by expressing the polarisation field in terms of two quantities; $E(\hat{\mathbf{n}})$, a curl-free 'electric-type' mode, and $B(\hat{\mathbf{n}})$, a divergence-free 'magnetic-type' mode. The relationship between Q,U, and E,B is nonlocal. From the harmonic expansion of the electric and magnetic modes we define the polarisation spectra C_ℓ^E and C_ℓ^B. This is covered in greater detail in Chapter 1. Details of the numerical simulation of the CMB are covered in Section 2.3.1.

2.1.3 Synchrotron

The Galactic magnetic field strength is typically a few μG in both the coherent and turbulent parts, and has been extensively probed by Faraday rotation of background sources and pulsars [75]. Relativistic electrons spiralling around the magnetic field emit strongly polarised synchrotron emission, potentially up to 75% of the total emisison level [76]. For cosmic-ray electrons with a distribution of electron energies $N(E) \sim E^{-p}$ propagating within a uniform magnetic field, the resultant emission will exhibit partial polarisation with a fractional linear polarisation

$$f_s = \frac{3(p+1)}{3p+7}, \tag{2.3}$$

aligned with the polarisation axis perpendicular to the magnetic field [77]. The frequency dependence of the emission is related to the electron energy distribution $T(v) \sim \nu^{\beta_s}$ with a spectral index

given by

$$\beta_s = -\frac{p+3}{2}, \tag{2.4}$$

where T is defined in units of antenna temperature. It has been observed that the spectral index for emission is $\beta_s \approx -3$ with spatial variations about the Galactic plane [68], and that the fractional polarisation can be as high as 75%, although such a level is rarely found except in small regions [78]. The Galactic magnetic field is composed of a uniform and turbulent component, and one could expect the turbulent component to cause the spectral index and fractional polarisation to vary locally over small spatial scales. Due to beam and line-of-sight smearing, the observed polarisation will not reflect the true nature of the emission, as neighbouring regions with a different electron energy distribution or magnetic field orientation will be smoothed upon observation (integration along the line-of-sight).

We can represent the polarised synchrotron emission as:

$$\begin{aligned} Q(\hat{n}) &= I_s^P(\hat{n})\cos(2\gamma(\hat{n}))\left(\frac{\nu}{\nu_0}\right)^{\beta_s(\hat{n})+C(\hat{n})\log\left(\frac{\nu}{\nu_0}\right)} \\ U(\hat{n}) &= I_s^P(\hat{n})\sin(2\gamma(\hat{n}))\left(\frac{\nu}{\nu_0}\right)^{\beta_s(\hat{n})+C(\hat{n})\log\left(\frac{\nu}{\nu_0}\right)} \end{aligned} \tag{2.5}$$

where Q and U are the Stokes parameters, I_s^P is the polarised amplitude, γ is the polarisation angle, β_s is the spectral index, and the constant C parameterises any spectral curvature in addition to a single power law. Estimates of the synchrotron polarisation have been calculated using the lowest frequency WMAP channel where the synchrotron emission is strongest. Full-sky maps generated by Page et al. [79] at 4° pixelation show a coherent structure aligned with the magnetic field. The Northern Galactic spur is clearly visible (thought to be the remnant from a single supernova event), and the typical polarisation fraction and angle is coherent over large scales. Figure 2.1 shows the polarisation power spectra generated by Page et al. at the WMAP observation frequencies [79].

The synchrotron polarisation power spectrum dominates over the CMB polarisation at all WMAP frequencies for full sky analyses, even at the higher observing frequencies where the synchrotron emission is lower. However, emission is strongly dependent on sky coverage, and there are regions of the sky where the synchrotron polarisation power spectra are at least an order of magnitude lower than shown in Figure 2.1. There is roughly equal power in E and B-modes. A single power law fitted to the spectrum gives a spectral dependence of $\ell(\ell+1)C_\ell/2\pi \sim \ell^{-0.6}$, shown in Figure 2.1 in red. Comparison with radio maps has shown that this derived spectrum is consistent [69].

The polarisation fraction is non-uniform and can vary wildly with environment and gas density. One can estimate the fraction by comparing WMAP full-sky data at 23 GHz, to unpolarised radio maps giving the total emission level. However, extraction of the pure synchrotron signal depends

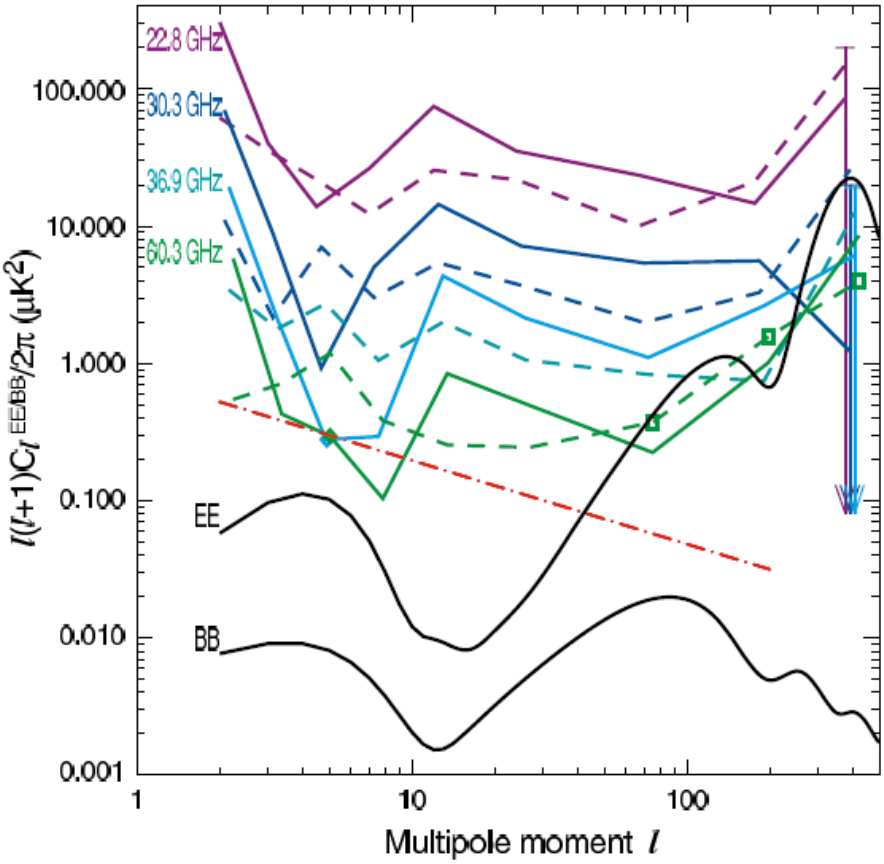

Figure 2.1: Power spectra for the WMAP 3-year polarisation maps are dominated by foreground emission. The solid lines show the E-mode spectra and dashed lines show the B-mode spectra outside the Galactic plane. The color indicates the frequency band. The rise in power for $\ell < 100$ is an artifact of the instrumental noise. The red dot-dashed line shows the estimated B-mode foreground power at 60 GHz, using a parameterised model fit to the multi-frequency data. Diamonds (EE) and boxes (BB) show points with negative values. The model shown has values $r = 0.3$ and $\tau = 0.09$. Image adapted from Page et al. [79].

heavily on model assumptions, since it can be confused with free-free, dust emission and indeed the CMB itself. Nevertheless, maps produced using this method by Kogut et al. [70] (shown in Figure 2.2) using the three-year maximum-entropy synchrotron map as the intensity tracer are consistent with radio maps.

The depolarisation mentioned earlier is clearly visible in the Galactic plane, where the average polarisation fraction $f_s \approx 0.05$. Other regions of the sky have much higher fractions; the northern spur exhibits $f_s \lesssim 0.4$, and other high-latitude regions show a wide variation with mean $f_s = 0.15$. Individual regions can peak up to $f_s \approx 0.5$, but the level is heavily dependent on whether one considers an additional anomalous dust component detailed in [80] and in Section 2.1.6. Figure 2.2 shows the polarisation fraction map with an anomalous unpolarised component contributing to the total emission level, which leads to an increase in the predicted synchrotron polarisation fraction.

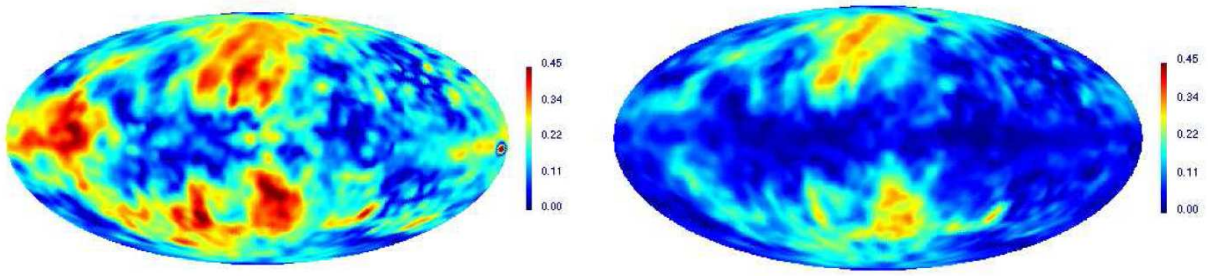

Figure 2.2: Polarisation fraction $f_s = P/I$ at 5° resolution estimated from the WMAP K-band data with the intensity I modelled including (left), and excluding (right), an unpolarised anomalous dust component. Image adapted from Kogut et. al [70]

If the anomalous dust component has a non-negligible polarisation fraction, then the estimated synchrotron polarisation would be further modified.

Whilst the WMAP data provide a reasonable estimate of the synchrotron polarisation fraction at angular scales of $\sim 1°$ or larger, the spectral index is much more uncertain. Due to environment and temperature differences in the gas, it is likely that a non-global index will be required to fully model the emission, as well as a possible spectral curvature, parameterised by the constant C in Equation 2.5. The curvature is dependent on the energy spectrum of the cosmic ray electrons. Very high energy electrons can lose energy faster, which can alter the frequency dependence of emission. When the characteristic cooling time and the escape time of the electrons are of comparable value, the spectrum is thought to break at a frequency dependent on environment [81]. Current estimates put the break between 10-100 GHz within the Planck observing range. The break will cause the largest confusion between 70-100 GHz, where thermal emission from dust is of comparable magnitude to the synchrotron emission. Observations from Planck will help to break this degeneracy, along with higher frequency observations of dust emission, and lower frequency observations of synchrotron emission, such as the C-band All Sky Survey (C-BASS) [82]. Despite the possible confusion from curvature, and the contamination with thermal dust emission, the spectral index has been estimated to be ≈ -3 across the whole sky, with variation dependent mainly on latitude. The WMAP team have used a global index of -3.3 to clean all-sky maps with promising results [83]. Electron diffusion limits the amount of spatial variation in the spectral index, both for polarised and unpolarised emission. Even with Faraday depolarisation effects, this facilitates the use of data at a lower resolution if we specify that the index should not vary significantly within some characteristic range.

The synchrotron polarisation has been mapped in a large proportion of the sky by the Dominion Radio Astronomical Observatory at 1.4 GHz [84]. Whilst the morphology is largely recognisable from the WMAP data, and the angular resolution of the maps is high, significant Faraday depolarisation is clearly present in the Galactic plane, which shows a low level of polarisation compared to the north Galactic spur. Such depolarisation limits the use of low frequency maps for foreground analysis, as at higher frequencies of relevance to Planck such depolarisation does not occur as

strongly [85].

2.1.4 Thermal Dust

The interstellar medium is largely composed of gas as molecular hydrogen, and dust grains formed in supernovae remnants and the winds of evolved red giant stars [86]. Dust grains absorb ultraviolet and optical light from nearby stars, and radiate back into the interstellar medium mainly in the infrared and submillimetre domain. Such dust emission is responsible for approximately 30% of the total energy radiated by the galaxy, and is the most intense astrophysical source at frequencies above $\sim$100 GHz.

There is a wealth of data characterising the intensity of dust emission, stemming from the pioneering work of Hiltner and Hall in the 1940s [87]. The polarisation of starlight was measured to show that absorption generates polarised emission. The intuitive explanation is that the emitting grains are aspherical in nature, and this morphology leads to inertial alignment with the magnetic field. A compilation of such data shows that this alignment is indeed highly correlated with the magnetic field [88]. Optical starlight polarisation is seen to align with the field, which implies that the dust grains are aligned orthogonally to the field. This behaviour has also been seen in other galaxies [89].

Qualitatively, the incident radiation generates electric dipoles in the aspherical grains, which in turn radiate electromagnetically. The total observed intensity is then a superposition of the scattered radiated wave, and the remaining starlight after partial absorption by the grains (which act as non-perfect dielectrics). The observed polarisation in the optical regime is then due to unabsorbed background starlight which will be aligned orthogonally to the longest axis of the grain, while the submillimetre radiation will be polarised in the direction of the main axis of the grain. The two sources of radiation are thus expected to be orthogonal.

Due to significant polarisation, dust is one of the main foregrounds for CMB polarisation measurements. The exact mechanism responsible for producing the alignment is still debated, and it is likely that several alignment mechanisms are occurring. Since the Davis-Greenstein mechanism [90], many competing methods have been proposed (see Lazarian's 2003 paper for a comprehensive review [91]).

Most observations of dust intensity have focussed on small areas of the sky typically at low Galactic latitudes. This adds to the confusion in simulating the full-sky emission as assumptions have to be made about the nature of the magnetic field, and the cirrus cloud behaviour extrapolated from the dense regions covered by low-latitude observations. Archeops was the first experiment to successfully map the dust polarisation fraction over a large area and at high angular resolution ($15'$). The results show that the dust alignment is indeed perpendicular to the magnetic field, at the level of a few percent, up to $\sim 10\%$ in regions [92]. The final Q and U Stokes images are shown

Survey	Frequency	Angular Resolution
Haslam et al 1982	408 MHz	0.85°
Reich et al 1982, 1986, 2001	1.4 GHz	0.5°
Jonas et al 1998	2.32 GHz	0.33°
Miville-Deschenes et al 2008	23 GHz	0.93°
Finkbeiner et al 1999	3000 GHz	0.7°

Table 2.1: Summary of radio and microwave sky templates described in the text.

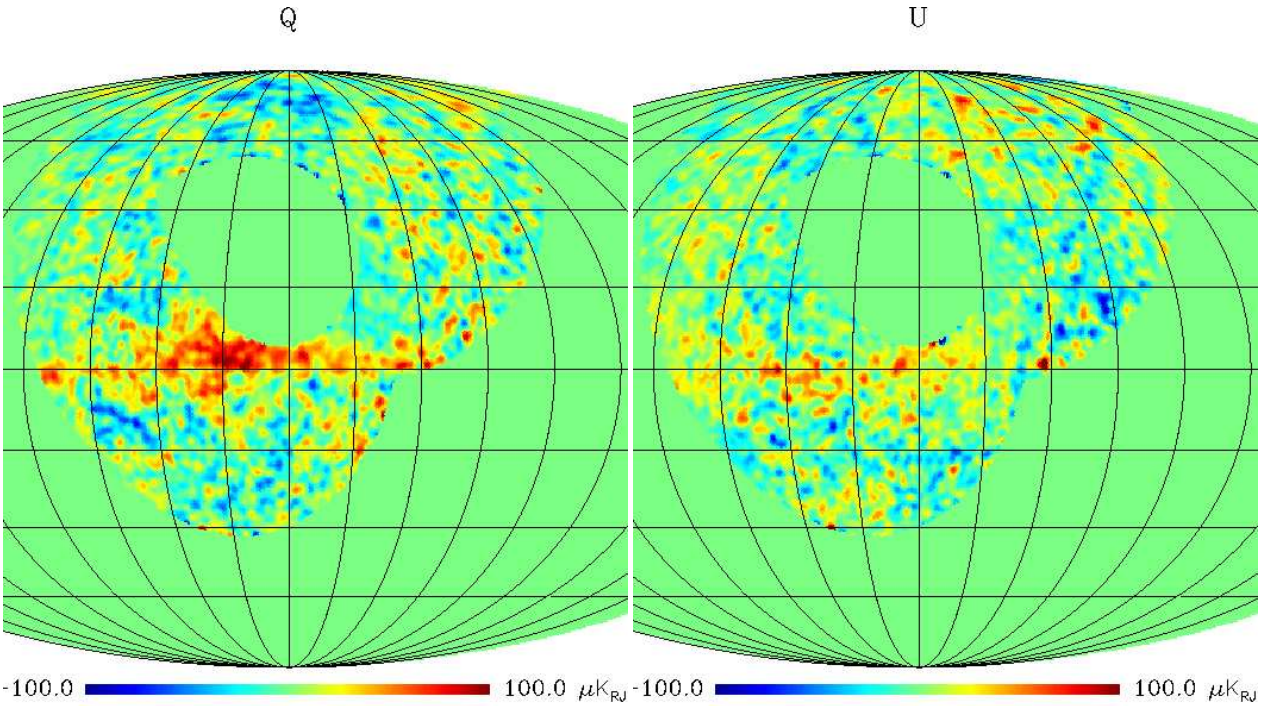

Figure 2.3: Stokes parameters measured by Archeops at 353 GHz. Map centered on Galactic longitude $l = 120°$ in Galactic coordinates. The pixel size is $27'$ smoothed with a $2°$ beam FHWM. Significant dust polarisation is evident along the Galactic plane.

in Figure 2.3. Regions of low polarisation seen to correlate with the spiral arms signify the imprint of a magnetic field aligned with the arms, as seen in other nearby galaxies. Some simulations have been based on the observation of high-latitude clouds at $\sim$ 100 GHz, however these are still chosen from a small part of the sky, and with multiple assumptions about the underlying magnetic field [93]. They show that dust should not dominate the CMB E-mode signal at $\sim$100 GHz, but should severely contaminate the estimation of the B-mode signal (again this is heavily dependent on sky area). The emission is strongly dependent on both frequency and sky area. There is therefore a need for further experimental observations. Table 2.1 details the templates used in this work both for synchrotron and dust emission along with central frequencies and angular resolution.

2.1.5 Free-Free

Free-free emission occurs via the interaction of free electrons with ions which generates thermal Bremsstrahlung radiation. When a thermally hot electron is accelerated in an encounter with an atom or ion, radio-frequency emission is produced. It is the least well known of the three main diffuse Galactic emission processes, and suffers from confusion with synchrotron emission at low frequencies, particularly away from the Galactic plane where total Galactic emission is much weaker. At frequencies less than about 10 GHz synchrotron emission dominates at intermediate and high latitudes. The free-free spectrum follows a well-defined power-law in frequency with a spectral index of $\beta_{ff} \approx -2.1$, exhibiting a very small variation with frequency. The exact value depends on the temperature assumed for the medium, but for WMAP observations an index of $\beta_{ff} \approx -2.14$ was found assuming an electron temperature of $T_e \sim 8000$ K [94]. Diffuse hydrogen α ($H\alpha$) is thought to be a good tracer of diffuse free-free emission since both are emitted from the same ionised medium, and both have intensities proportional to the emission measure (an integral of n_e along the line-of-sight). We can estimate the free-free contribution from a $H\alpha$ map, with a correction for the dust extinction [95], or by using a maximum-entropy-method (MEM) map obtained from WMAP data.

It is reasonable to assume that free-free emission should not be significantly polarised, since the scattering of electrons is intrinsically isotropic. However, if one considers the edge of an ionised cloud (a bright free-free feature), we could expect that Thomson scattering could induce a secondary polarisation signature, which could be of the order of 10% [77]. This feature will only be evident in high resolution maps, and largely within the Galactic plane, where such morphological features are more numerous. With maps at Planck's native resolution, and in clean areas of the sky, the residual level of polarisation is expected to be less than 1% [96].

2.1.6 Other Sources

Several studies have shown that there could be a third major component to the Galactic polarisation: anomalous dust emission. Kogut et al. showed in 1998, along with a number of similar high Galactic latitude studies, that the observed total emission at CMB frequencies is in excess of that expected if one only considers the synchrotron, dust and free-free emission [97]. The emission is highly correlated with large-scale far-infrared emission, which itself is due to thermally emitting dust grains. Draine and Lazarian have predicted that emission from a spinning dust grain population could theoretically be polarised as highly as 7% at frequencies around 2 GHz [98].

Non-thermal emission from dust via a population of small rapidly-spinning dust grains, or partially magnetised grains, has been suggested to account for the observed correlation between the far-infrared and microwave emission in the interstellar medium. Emission from spinning dust would contaminate the polarisation at primarily low frequencies, typically at a temperature of ≈100 K

[99] [100] (mid-IR emission $\lambda \sim 10 - 30$ μm). The alternate model considers vibrating grains experiencing fluctuations in magnetisation, and predicts that emission from this species will peak in the far-infrared band ($\lambda \sim 50 - 200$ μm). Studies have shown that the correlation between the anomalous excess emission and the predicted emission from spinning grains is stronger than that between the magnetic-type grains at longer wavelengths [101], and this observation is strengthened by correlations of Hα with the microwave excess at 40 GHz [102].

Whilst spinning dust grains are the currently-favoured mechanism for the microwave excess, larger grains are known to be produced in the ionized medium, and contribute to the observed far-IR emission. Ferromagnetic material produced in a supernova explosion would be of particular interest for polarisation as the grains (if elongated along a particular axis as proposed by some models) could be expected to align more efficiently than the spinning grains. The 23 GHz WMAP data, combined with Galactic cloud observations ([103], [104], [105]) suggest that the polarisation of the anomalous emission is low, $\lesssim 5\%$, with a measurement of $3.4^{+1.5}_{-1.9}\%$ by Battistelli et al. Whilst this does not eliminate a significant contribution from a magnetic grain, it is consistent with the polarised spinning dust models mentioned above. A study in the Planck Early Release paper XX [66] revisited the issue of anomalous microwave emission, particularly in the Perseus molecular cloud, the area where anomalous emission was first detected. The study finds that spinning dust in the dense molecular gas can account for most of the excess, with a small contribution from atomic gas. Lopez-Caraballo et al. [106] obtain upper limits on the fractional linear polarisation of 1.0%, 1.8%, and 2.7%, at 23, 33, and 41 GHz respectively. These measurements rule out a large number of models based on magnetic dipole emission of grains. One can reason that since low levels of polarisation are observed in the ultraviolet waveband, and spinning grains are the same grains responsible for starlight extinction at UV wavelengths, the population of spinning grains should exhibit little polarisation at all frequencies, and it can safely be neglected for simple studies.

2.2 Foreground Separation Techniques

We now review various methods used to separate diffuse foregrounds from the CMB. Methods that have been applied to polarisation are considered, and their performance presented in the context of accuracy achievable with Planck. Broadly speaking, separation methods can be split into those that operate in the pixel domain, and those that operate in the harmonic domain (via Fourier/spherical transforms). Real-space methods typically rely on some prior knowledge of the foregrounds either via spatial dependence, or some assumption about their frequency dependence, whereas blind or semi-blind methods aim to separate the CMB signal with few or no assumptions about the foreground behaviour.

2.2.1 Internal Linear Combination

The pixel-based internal linear combination (ILC) method has been extensively used throughout the WMAP experiment to produce CMB temperature maps, and is formed from a weighted linear combination of five smoothed intensity maps, where the weights are chosen carefully to maintain a unity response to the CMB anisotropy signal while minimising the foreground contribution. It was first described by Tegmark and Efstathiou in 1995 [107] for use with temperature data, but it can also be applied to polarisation data. The ILC method can be applied either in pixel or harmonic space. In harmonic space we can estimate the CMB signal as a combination of the observed $a^i_{\ell m}$ in each frequency band i,

$$a_{\ell m} = \sum_i w^i_\ell a^i_{\ell m}, \tag{2.6}$$

where we have chosen the weights w_i to minimise foreground contribution. Consider a simple model consisting of CMB, thermal dust, synchrotron and noise. We can parameterise the signal at each multipole as the decomposition

$$a^i_{\ell m} = c_{\ell m} + s^i_{\ell m} + d^i_{\ell m} + n^i_{\ell m}, \tag{2.7}$$

where c, s, d and n represent the CMB, synchrotron, thermal dust and noise signals respectively. The number of fitted components must be less than the number of frequency channels available to ensure non-degeneracy between components. Planck has seven polarisation sensitive channels, allowing for a maximum of six foreground components, however wide degeneracies can occur for a small number of degrees of freedom. The weights are found by minimising the power spectrum

$$\langle |a_{\ell m}|^2 \rangle = w^T_\ell C_\ell w_\ell, \tag{2.8}$$

to optimally remove the foregrounds. Here, $C_\ell = \langle (a^i_{\ell m})^\dagger a^j_{\ell m} \rangle$, which for Planck would be a 7×7 matrix-valued cross-power spectrum. The minimised weights can be calculated as

$$w_\ell = \frac{C^{-1}_\ell \mathbf{e}}{e^T C^{-1}_\ell e}, \tag{2.9}$$

where $\mathbf{e}$ is a unity-valued column vector. The ILC method has proved to be reliable for temperature recovery, and can also be applied to polarisation using exactly the same methodology. Indeed the polarisation is usually modelled with fewer components than the temperature, which will lead to a reduction in degeneracy for a multifrequency experiment such as Planck. One advantage of the ILC method is that no assumptions are made about the frequency dependence of the foregrounds, the

response to the CMB signal is always unity, since it is independent of the frequency (in thermodynamic units), and the weights may be chosen to minimise the impact of the residuals. The method is also computationally efficient when working in harmonic space, so that multiple Monte-Carlo simulations can be performed simultaneously to propagate systematics and calculate an estimate of the errors. One drawback of this method is that one has to assume that the foregrounds have a spatially uniform frequency dependence, which is clearly not the case for either synchrotron or thermal dust emission. This can be somewhat alleviated by a 'needlet ILC' modification, whereby the sky is split into separate regions and an analysis performed for each [95]. Another issue is that the total power spectrum is also minimised, not just the foreground power spectra. A biased power spectrum may lead to errors propagating into the cosmological parameters. The ILC method can also be applied similarly in pixel space, and we discuss this in detail for Planck DX8 maps in Chapter 4.

2.2.2 Spectral Matching Independent Component Analysis

Spectral Matching Independent Component Analysis (SMICA) is a blind component separation technique that overcomes the inseparability of Gaussian sources using standard ICA methods, by relying on their assumed spectral diversity. Typically, the CMB and foreground power spectra are calculated using a parametric model for the angular spectra. Cardoso et al. [108] simulate Planck data and parameterise the angular spectra and cross-spectra C_ℓ^{ij} (measured at N_ν frequencies) as

$$C_\ell^{ij} = C_\ell^{CMB,ij} + F_\ell^{ij} + N_\ell^{ij} \tag{2.10}$$

where $C_\ell^{ij} = 1/(2\ell+1)\sum_m (a_{\ell m}^i)^\dagger a_{\ell m}^j$ for frequencies i and j. For easier implementation the spectra are usually grouped in bins of N_b. The resulting spectra are then represented as C_ℓ^{ij}. The foreground is parameterised by G possibly correlated angular power spectrum templates, with $F_b = A^T P_b A$. Here A is a matrix of size $N_b \times D$, and P_b is a symmetric matrix of size D × D. The implementation SMICA [109] allows for correlated foregrounds which is useful for the synchrotron and dust (which are naturally correlated due to the nature of the Galactic magnetic field). To model the polarisation, at least two maps will be needed for synchrotron and dust Q and U. Since the ICA methods are similar to ILC with regard to the way that weights are chosen for the spectra, similar limitations and drawbacks apply. Noise spectra are considered to be additional components in each channel, and are either known (in which case the noise spectra are fixed) or estimated along with the CMB and foreground spectra. The proposed model is fit to the measured spectra of multi-frequency sky maps, which can be separated into regions using apodised masks, to remove the sharp features of the Galactic plane.

2.2.3 Maximum Entropy Method

The Maximum Entropy Method (MEM) can be used to separate not just diffuse Galactic emission but also point-sources and SZ effects. Practical implementations of MEM work in harmonic space, and operate using a mode-by-mode separation reducing a huge optimisation problem to a number of smaller problems. The solution can thus be obtained reasonably rapidly, indeed giving the FastMEM implementation its name. This is fully described by Hobson et al. [110] for flat patches of the sky utilising Fourier modes, and by Stolyarov et al. [111] for the full-sky case.

For a model M in which the measured data $\mathbf{d}$ is a function of an underlying signal $\mathbf{s}$, we can use Bayes' theorem to evaluate the posterior probability as

$$P(\mathbf{s}|\mathbf{d}, M) = \frac{P(\mathbf{d}|\mathbf{s}, M)P(\mathbf{s}|M)}{P(\mathbf{d}|M)}. \tag{2.11}$$

We want to maximise the posterior probability of the signal given the data. The denominator is the Bayesian evidence and acts here as a normalisation factor. We thus want to maximise the product of the likelihood and the prior. If the instrumental noise in each frequency channel is Gaussian-distributed, then the log-likelihood takes on the χ^2 statistic. If the beams are azimuthally symmetric then a mode (ℓ,m) has a log-likelihood

$$\chi^2(\mathbf{s}_{\ell m}) = (\mathbf{d}_{\ell m} - B_\ell \mathbf{A}\mathbf{s}_{\ell m})^T N_{\ell m}^{-1}(\mathbf{d}_{\ell m} - B_\ell \mathbf{A}\mathbf{s}_{\ell m}), \tag{2.12}$$

where $\mathbf{A}$ is the fixed frequency conversion matrix describing how the components mix to form the data, $N_{\ell m}^{-1}$ is the inverse noise covariance matrix for the mode, and B_ℓ is the beam transfer function in harmonic space (a signal mapping function dependent on the instrument geometry). Provided the instrument noise is uncorrelated between channels, the noise covariance matrix is diagonal. For a Gaussian prior, the Wiener filter is recovered with the analytic solution for $\mathbf{s}$. Diffuse foregrounds however, are strongly non-Gaussian, especially at low Galactic latitudes, and Hobson et al. suggest using an entropic prior instead. Maximising the posterior is now equivalent to minimising the following function for each harmonic mode

$$\phi_{MEM}(\mathbf{s}_{\ell m}) = \chi^2(\mathbf{s}_{\ell m}) - \alpha S(\mathbf{s}_{\ell m}) \tag{2.13}$$

where $S(\mathbf{s}_{\ell m})$ is the entropic term and α is the regularisation parameter. Since $\mathbf{A}$ is fixed, the spectral properties of the components must be identical everywhere on the sky. Small variations in e.g. the synchrotron spectral index, can be accounted for by introducing them as another component in the model. Priors on the components are flexible, and the process can be run iteratively to update the priors after each run. Since most implementations of MEM use priors, the solutions for the signals could be biased, particularly if the signal-to-noise ratio is low.

2.2.4 Template Cleaning

The three methods described above can all operate in harmonic space, and tend to be computationally fast due to the smaller amount of data to process. Pixel-space routines have the advantage of full freedom in terms of spatial variation in amplitude and spectral indices of the foregrounds, but tend to be more numerically demanding due to the large quantity of data (e.g. each full resolution Planck map contains $\sim 5 \times 10^7$ pixels). A template cleaning method assumes that sky maps can be described as a sum of fixed spatial templates, including CMB, foregrounds, and noise. We can parameterise the microwave sky as

$$T(p,\nu) = \sum_i \alpha_i(\nu) X_i(p) + n(p,\nu) \tag{2.14}$$

where X_i are the spatial templates to fit, $\alpha_i(\nu)$ is a coefficient describing the emission mapped by the i^{th} template at a frequency ν, and $n(p,\nu)$ is the noise. Equation 2.14 can then be solved for the template coefficients $\alpha_i(\nu)$. An important consideration is the correct propagation of noise to calculate errors on the final CMB polarisation maps and ultimately, cosmological parameters. We can represent the noise in the cleaned map as

$$T_c(p,\nu) = T(p,\nu) - \sum_i \alpha_i(\nu) X_i(p), \tag{2.15}$$

and its value is only slightly affected by the template cleaning. Importantly the noise retains properties of the original noise map.

This technique utilises all possible spatial information in the templates, which is important for non-Gaussian emission associated with foregrounds. The method is also insensitive to any spatial correlations between the foreground templates. Whilst spatial correlations will produce a non-zero covariance in the fitted parameters α_i, this does not place any bias on the total foreground estimate over all templates, it merely adds complication to the identification of the individual emission traced by that template. One problem with template fitting is that one has to assume that the spatial and frequency dependence of each foreground can be described by a separable function for the dependences i.e. $T(p,\nu) = X(p)Y(\nu)$. This is not the case for the two main polarised foregrounds; synchrotron and dust. The synchrotron spectral index is known to vary with Galactic latitude and environment for example, and dust emission is estimated to require multiple temperature components for accurate fitting, whose ratios can vary on the sky. For an experiment like Planck, which has a large coverage in frequency (30-353 GHz in polarisation), this spatial variation in spectral indices can significantly alter the emission distribution.

Several temperature templates exist for various foregrounds and the method has been tested extensively for temperature [94]. With Planck, we have for the first time high frequency polarisation

maps which can be used as polarised dust templates, in addition to the WMAP/LFI low frequency polarised maps. Unpolarised foregrounds at high latitudes are weaker than the CMB temperature signal, and template cleaning is straightforward. Due to a much weaker CMB signal polarised cleaning requires a much deeper analysis, especially for B-modes. Detecting a signal with $r = 0.01$ at $\ell < 10$ will require cleaning the foreground emission by a factor of roughly 20 [112]. As more templates become available from Planck and other foreground experiments in the next few years, the accuracy of such methods will increase.

2.2.5 Parametric Fitting

Instead of relying on templates to fit to the total sky maps, one can instead parameterise the foreground and sample around known values to construct a likelihood for various models of the Galactic emission. Such Bayesian estimation methods have been applied to the foreground problem, and typically estimate a single CMB map from maps at all observing frequencies. This is in contrast to template cleaning, which can produce a CMB map at each observing frequency. These methods are heavily reliant on assumed knowledge of foregrounds, and their efficiency is dependent on the priors placed on foreground parameters. One benefit of these methods is the ease of propagation of errors from foreground uncertainty into final CMB maps. Parametric methods can be computationally challenging (particularly at high resolution), and can produce biased results if the priors placed on the foreground emission are incorrect. Methods can be split into those that fit the Q and U Stokes parameters in each pixel [113], and those that simultaneously fit the CMB power spectrum [114] [115]. In the simultaneous approach, the angular power spectrum is estimated alongside map parameters. Another advantage of this method is the simple incorporation of newer foreground templates for use as priors, as they become available.

Following the formalism outlined in Eriksen et al. [116], we can use Bayes' theorem to calculate the posterior probability as

$$P(\theta|\mathbf{d}) \propto P(\mathbf{d}|\theta)P(\theta) = \mathcal{L}(\theta)P(\theta), \tag{2.16}$$

where θ represents the model parameters, $\mathbf{d}$ represents the data set, and $\mathcal{L} = P(\mathbf{d}|\theta)$ gives the probability (likelihood) of the observed data given the model parameters. The likelihood is then given by

$$-2\ln\mathcal{L} = \sum_{\nu}[\mathbf{d}_\nu - \mathbf{S}_\nu(\theta)]^T\mathbf{N}_\nu^{-1}[\mathbf{d}_\nu - \mathbf{S}_\nu(\theta)]. \tag{2.17}$$

Here superscript T represents a transpose, $\mathbf{N}_\nu$ is the covariance matrix at each frequency channel ν, and typically the maps used are pixel-space cubes constructed from the I, Q and U images. The total model of the sky is taken to be the sum of the CMB, synchrotron and dust for polarisation:

$$T_\nu = k_{cmb,\nu}I_{cmb} + k_{synch,\nu}I_{synch} + k_{dust,\nu}I_{dust}, \tag{2.18}$$

where $k_{i,\nu}$ is a coefficient to be fitted to the data. We should expect that the foreground components will largely follow power laws in frequency and can therefore be parameterised by $k_{i,\nu}(\hat{n}) = (\nu/\nu_0)^{\beta(\hat{n})}$ (in antenna temperature). Each amplitude map used as a prior is defined at a pivot frequency ν_0, and the aim is to recover an estimate of the CMB map I_{cmb}.

In studies of this kind, a Metropolis-Hastings algorithm [117] MCMC code is used to sample the posterior distribution for the parameters using intensity data (I). If we assume that the noise is diagonal, then we can fit the model to each pixel individually. For temperature, Eriksen et al. [116] have performed a low resolution analysis. They increase the map resolution and resample using the low resolution linear parameter results as the priors for the high resolution analysis. This two-step fitting works well for temperature because Galactic emission dominates on the largest of scales. Such a fitting process for polarisation is difficult due to large uncertainties on the prior models. This technique has been applied to the WMAP data by Dunkley et al. [118] by assuming that the spectral indices are the same for Q and U in any given pixel, and only allowing the index to vary on a very coarse-grained grid ($N_{pix} = 48$). In regions where the signal-to-noise is very low, tight priors can be imposed on the indices to improve the sampling efficiency. A suitable choice for priors on the indices was chosen to be $\beta_s = -3.0 \pm 0.3$ for synchrotron, and $\beta_d = 2 \pm 0.3$ for the dust. The recovered estimates can then be compared to what should be expected from the theoretical power spectrum, using the method described in Page et al. [83]. This method can be used to estimate the limit on a recoverable value of the tensor-to-scalar ratio r taking into account the statistical uncertainty generated by the foreground fitting.

2.3 Sky Simulation

Adequate testing is important for any foreground separation method. Sky simulations are an ideal way to analyse any potential biasing or gain effects that the method may imprint on the CMB signal. In this section we describe a suite of full-sky Galactic simulations built in the HEALPix environment, using various datasets at radio, microwave, and submillimetre frequencies as templates. Multiple models can be created for each sky component depending on the chosen spectral index and base template used to model the emission. We also describe the generation of polarised CMB power spectra using the CAMB software, and the subsequent generation of full-sky CMB maps from these spectra. Additionally, Planck-level noise is calculated at each observing frequency and added to the final simulations.

2.3.1 CMB

Following the formalism outlined in Chapter 1, the 'electric' and 'magnetic' components of polarisation are eigenstates of parity and may be defined as

$$a^E_{\ell m} = -\frac{a_{2,\ell m} + a_{-2,\ell m}}{2} \tag{2.19}$$

$$a^B_{\ell m} = i\frac{a_{2,\ell m} + a_{-2,\ell m}}{2}, \tag{2.20}$$

where the coefficients are defined in terms of the spin-2 spherical harmonics

$$a_{\pm 2,\ell m} = \int d\hat{n} \quad {}_{\pm 2}Y^*_{\ell m}(\hat{n})(Q \pm iU)(\hat{n}). \tag{2.21}$$

These variables are expanded in terms of the ordinary spherical harmonics as

$$E = \sum_{\ell m} a^E_{\ell m} Y_{\ell m}(\theta, \phi), \quad B = \sum_{\ell m} a^B_{\ell m} Y_{\ell m}(\theta, \phi). \tag{2.22}$$

The E and B fields then respectively describe a scalar and pseudo-scalar field on the sphere, with even and odd parity. The intensity and polarisation of the sky is fully described by the Stokes parameters I, Q, U, and V. The spatial power spectrum of the intensity and polarisation field of the CMB is then given by

$$C^{XY}_\ell = \langle a^X_{\ell m} a^{Y\dagger}_{\ell m} \rangle = \begin{pmatrix} C^{TT}_\ell & C^{TE}_\ell & 0 & 0 \\ C^{TE}_\ell & C^{EE}_\ell & 0 & 0 \\ 0 & 0 & C^{BB}_\ell & 0 \\ 0 & 0 & 0 & 0 \end{pmatrix}. \tag{2.23}$$

In the absence of parity-violating physics, the different parity of the fields involved in the C^{TB}_ℓ, and C^{EB}_ℓ mean these fields vanish. Similarly the CMB is not expected to be circularly polarised (explained in detail in Chapter 1), so power spectra involving V are all assumed to be zero. Hence the intensity and polarisation of the CMB is fully described for each ℓ by the four quantities $C^{TT}_\ell, C^{TE}_\ell, C^{EE}_\ell$, and C^{BB}_ℓ.

Scalar and tensor spectra are generated using the CAMB software [119], that computes CMB spectra given a set of input cosmological parameters. It is based on the CMBFAST [120] code which evolves the Boltzmann equation governing primordial density fluctuations. The WMAP 7-year cosmological parameters are used to generate full-sky CMB realisations using the HEALPix package [67]. The spherical harmonic coefficients are calculated as Gaussian realisations of the power spectra, that is:

$$\begin{pmatrix} a^T \\ a^E \end{pmatrix} = M \begin{pmatrix} r_1 \\ r_2 \end{pmatrix} \tag{2.24}$$

where r_1 and r_2 are Gaussian distributed random variables and M is a matrix such that a_T and a_E are some linear combination of r_1 and r_2. By using Cholesky factorisation to decompose M we can show that

$$\begin{pmatrix} a^T \\ a^E \end{pmatrix} = \begin{pmatrix} \sqrt{C_\ell^{TT}} & 0 \\ \frac{C_\ell^{TE}}{\sqrt{C_\ell^{TT}}} & \sqrt{C_\ell^{EE} - \frac{C_\ell^{TE^2}}{C_\ell^{TT}}} \end{pmatrix} \begin{pmatrix} r_1 \\ r_2 \end{pmatrix}, \tag{2.25}$$

from which we can draw spherical harmonic coefficients using the scalar and tensor power spectra estimates (similarly for a^B). For the purposes of this study only low resolution maps are required. The HEALPix routine ALM2MAP is used to transform the complex spherical harmonic coefficients into full-sky temperature and polarisation maps in the form of T, Q, and U images. High resolution maps at $N_{side} = 2048$ (the final Planck map resolution, which corresponds to ~ 50 million pixels of size $1.7'$) can be degraded to low resolution by transforming into harmonic space with MAP2ALM and applying a smoothing function $a_{\ell m} \longrightarrow a_{\ell m} \exp(-\frac{1}{2}(\theta_s \ell)^2)$ where θ_s is a smoothing parameter related to the smoothing beamwidth at full width half maximum as $\theta_s = \theta_{FWHM}(2\pi/360)*0.425$ (in degrees). Transforming back into real space yields smoothed maps at the desired lower resolution. The power spectra of the generated CMB maps are shown in Figure 2.4 with an input cosmological model taken from the WMAP 7-year results, generating tensor modes with $r = 0.1$ and $r = 0.01$.

2.3.2 Synchrotron

The destriped 408 MHz radio continuum all-sky map from the Haslam survey [121] provides a model of synchrotron emission. The template does not however contain any information on scales smaller than $\sim 1^\circ$, so for studies at small angular scales, one can artificially add structure by extrapolating the angular power spectrum (for example as $C_\ell \propto \ell^{-3}$). This is not strictly necessary when considering low resolution maps, as any power on small scales will be diluted by the smoothing kernel, however it is worth noting for completeness, and is an option in the Planck Sky Model. The base Haslam map has a resolution of $N_{side} = 512$ giving approximately $12N_{side}^2 = 3 \times 10^6$ pixels. The destriped map is shown in Figure 2.5.

For the simulations considered in this study, the synchrotron maps at the Planck observing frequencies are generated using a power-law model for each pixel, and a non-uniform polarisation fraction. The maps are formed for T,Q and U according to

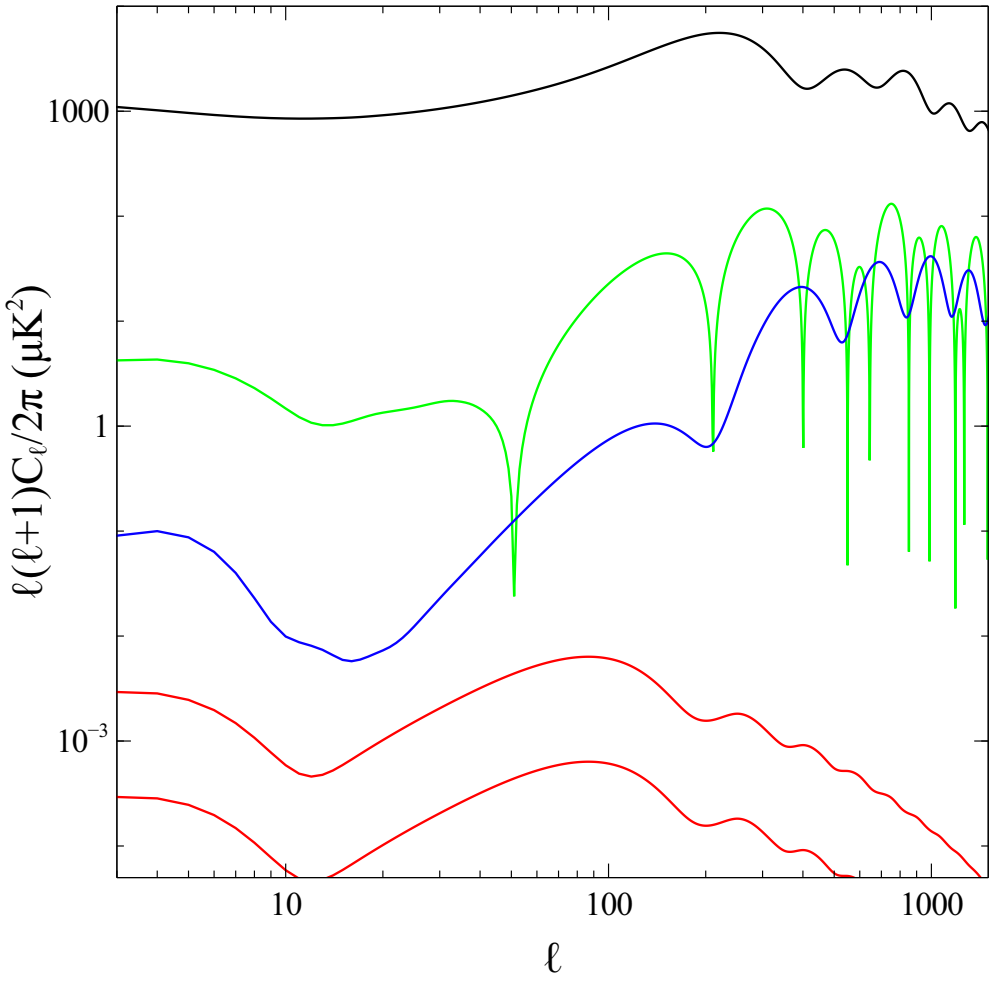

Figure 2.4: The power spectra of the generated CMB full-sky maps in temperature (black) and polarisation E-mode (blue). The modulus of the temperature-polarisation cross spectrum (TE) is shown in green. The B-mode spectrum is shown in red with values of $r = 0.1$ (upper) and $r = 0.01$ (lower)

$$T_s(\nu, \hat{n}) = I_{408}(\hat{n}) \left(\frac{\nu}{\nu_0}\right)^{\beta_s(\hat{n})}, \tag{2.26}$$

$$Q_s(\nu, \hat{n}) = f_s(\hat{n}) I_{408}(\hat{n}) \cos(2\gamma(\hat{n})) \left(\frac{\nu}{\nu_0}\right)^{\beta_s(\hat{n})}, \tag{2.27}$$

$$U_s(\nu, \hat{n}) = f_s(\hat{n}) I_{408}(\hat{n}) \sin(2\gamma(\hat{n})) \left(\frac{\nu}{\nu_0}\right)^{\beta_s(\hat{n})}, \tag{2.28}$$

where I_{408} is the Haslam intensity map, ν is the frequency of observation, β_s is the spectral index map, γ is the polarisation angle, and f_s is the polarisation fraction map.

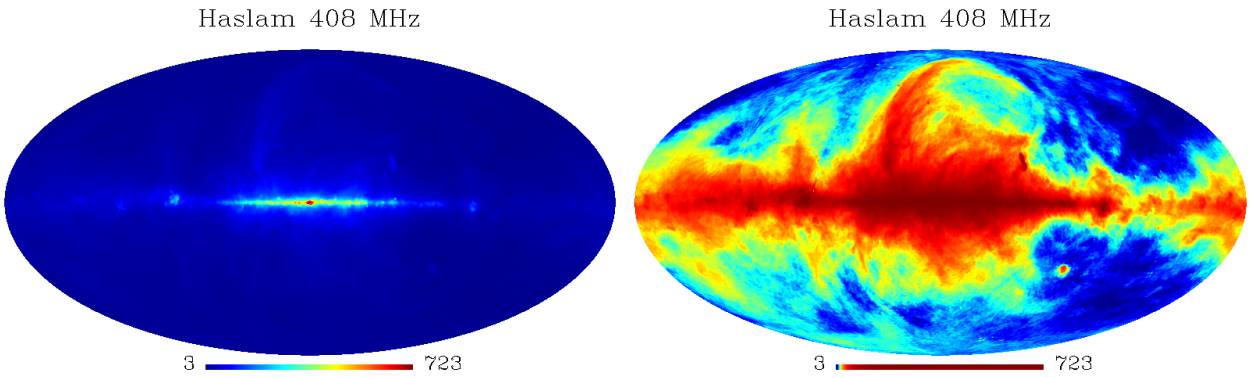

Figure 2.5: The full-sky destriped 408 MHz radio intensity map created at a HEALPix resolution $N_{side} = 512$ in units of Kelvin antenna temperature using data from the observations compiled by Haslam et al. The dominant emission mechanism is electron synchrotron. The global morphology reflects the underlying emission although lacks any structure below $\sim 1^\circ$ resolution. The right panel uses a histogram-equalised colour bar to increase the dynamic range.

Radio frequency observations from 408 MHz to 10 GHz have shown spatial variation of the spectral index from -2.8 to 3.2 [122] [123] [44], with a slight steepening of the spectrum at high Galactic latitudes. In a more recent analysis, Miville-Deschenes et al. [124] find a lower dispersion of the index by accounting for the presence of additional spinning dust grain emission in the radio domain, consistent with $\beta_s = -3.00 \pm 0.06$. Thus the inferred synchrotron index map depends on assumptions made about other diffuse components. There are multiple methods for simulating the spectral index map. A basic model sets the global index at $\beta_s = -3$, however this is almost certainly too simplistic to reflect the true distribution. A more detailed estimate is formed from multiple observations at 408 MHz, 1420 MHz [125] and 2326 MHz [126], and by padding the unobserved area around the south celestial pole with the mean spectral index, at a resolution (FWHM) of 10°, shown in the left panel of Figure 2.6. The index varies from -2.5 in the Galactic plane, to isolated regions with a steeper spectrum of -3.2 out of the plane in the Galactic spur (the band of stronger emission in the northern hemisphere), and at about $(\theta, \phi) = (90, 20)$ from the Galactic centre. The distribution of the synchrotron index is also shown in Figure 2.6, exhibiting an approximately Gaussian distribution with $\bar{\beta}_s = -2.82$ and $\sigma = 0.10$. The third model is created in a similar manner to the second, and is based on a combination of the 408 MHz map, and the WMAP 23 GHz data [124], without padding since both surveys cover the entire sky. This is the preferred option in the Planck Sky Model, and when simulated at a resolution higher than 1° (the native 408 MHz resolution), additional small-scale structure is added as described by Delabrouille et al. [127]. The two models are shown in Figure 2.6. The third model appears significantly different to the second, due to the inclusion of the WMAP data. The WMAP data probe smaller angular scales than the low frequency observations, and hence smaller-scale variations are seen. The synchrotron morphology differs significantly between 1420 MHz and 23 GHz, and this leads to the change in spectral index seen in Figure 2.6.

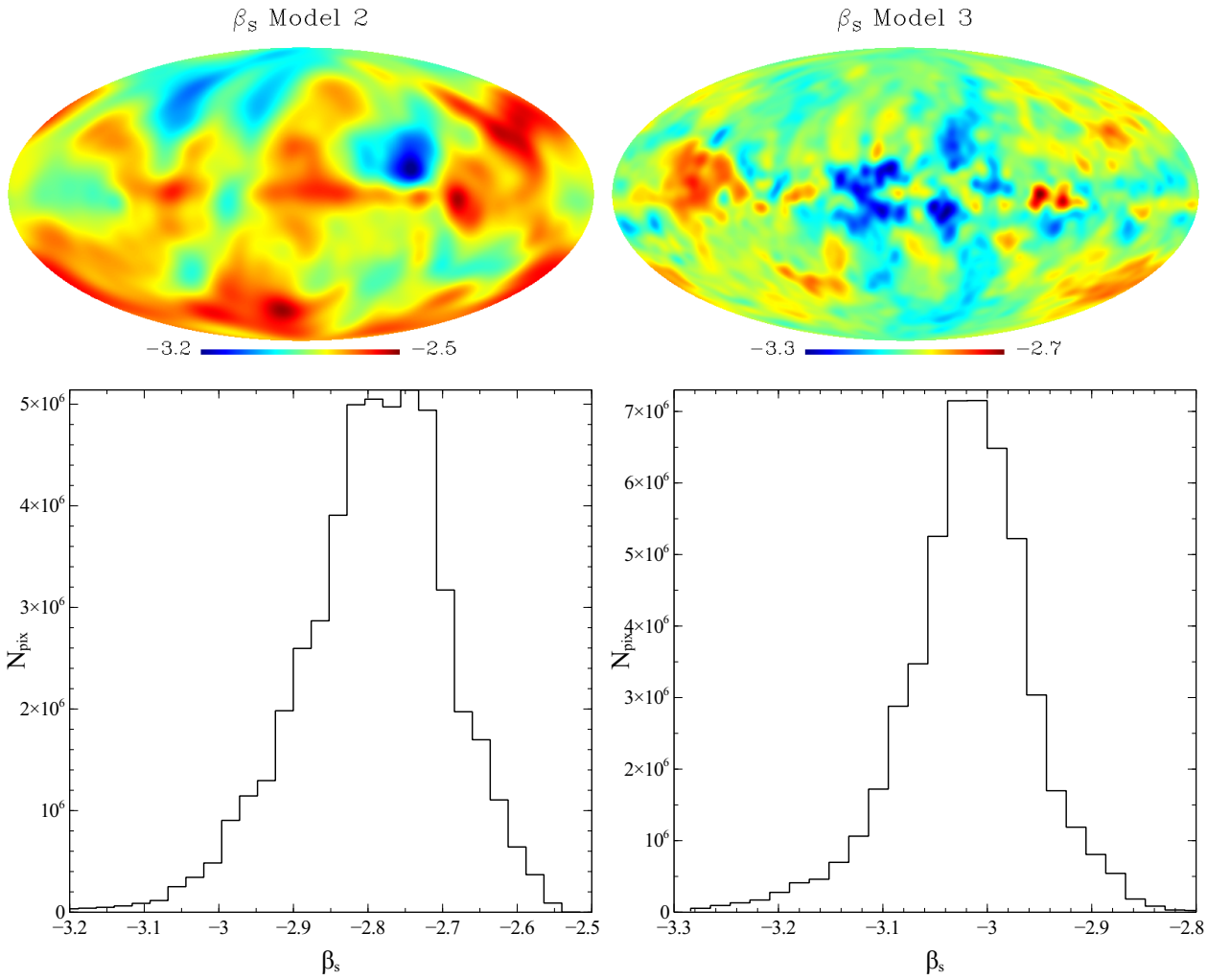

Figure 2.6: Left: Simulated synchrotron spectral index map formed using multiple frequency maps at 408, 1420 and 2326 MHz and histogram. A steeper index is found in the north Galactic spur, while a shallower index is found in the Galactic plane. Right: Simulated spectral index calculated using 408 MHz and WMAP 23 GHz with histogram. Map resolution for both is N_{side}=2048

Giardino et al.[128] assumed a theoretical polarisation degree of 75% correlated with the Haslam template at 408 MHz, and the polarisation angle assumed random. They assume that the temperature emission obeys the power spectrum derived from the high resolution radio observations mentioned above. This level of polarisation is adopted in the PSM for the second model. The advance in data since the 2002 study has shown this level of polarisation to be high, and indeed a lower level has been estimated by the WMAP team [80]. They assume the WMAP 23 GHz Q/U maps trace synchrotron polarisation, and for temperature scale the total intensity map from the 408 MHz radio emission. The level of polarisation is highly dependent on modelling considerations, particularly on whether an anomalous dust component is included (discussed in Section 2.1.6). For the favoured model including an anomalous unpolarised dust component, an average level of polarisation $f_{pol} \approx 0.3$ is found, with a maximum around the Galactic spur region of $f_{pol} \approx 0.45$. This

estimate would be modified if the anomalous component has a non-negligible polarisation fraction.

2.3.2.1 Polarisation Angle

Knowing the electron energy distribution, one can calculate the theoretical polarisation fraction as described in Section 2.1.3. This calculation however is only correct for a uniform magnetic field, and does not take into account geometric depolarisation, which is particularly important at low Galactic latitudes. Depolarisation occurs due to variations along the line-of-sight of the angle between the magnetic field and the observation direction. The direction of the field varies with any turbulent motion in addition to the smooth field oriented along the spiral arm. For synchrotron (and thermal dust) emission, variation in the Galactic magnetic field leads to a varying polarisation degree and orientation across the sky. Thus, to accurately model the polarisation one needs a coherent model of the Galactic magnetic field. The WMAP K-band data gives the highest signal-to-noise ratio over the five frequency channels, and indicates a large-scale coherence for the Galactic magnetic field. We also observe that other spiral galaxies typically exhibit magnetic fields that follow the spiral arm pattern, and assume that the Milky Way also follows this behaviour. There are two differing models for the polarisation angle in the PSM. For the first model, as an approximation to the real structure we can parameterise the field in cylindrical coordinates as:

$$\mathbf{B}(r,\phi,z) = B_0[\cos\psi(r)\cos\chi(z)\hat{r} + \sin\psi(r)\cos\chi(z)\hat{\phi} + \sin\chi(z)\hat{z}] \tag{2.29}$$

where $\psi(r) = \psi_0 + \psi_1 \ln(r/8 \text{ kpc})$, $\chi(z) = \chi_0 \tanh(z/1 \text{ kpc})$, r and z are measured in kpc with respect to the centre of the galaxy, r ranges from 3 kpc to 20 kpc, and the angles are in degrees. This formalism follows that of Taylor et al. [129], and describes the logarithmic spiral arm (LSA) model. The distance to the centre of the galaxy is taken to be 8 kpc. Other model parameters are determined by Page et al. [83] by fitting to the WMAP K-band data. The magnetic field is fit as a loosely-wound spiral with $\psi_0 \approx 35^\circ$.

The electrons are modelled with a power-law distribution in energy with slope given by Equation 2.4, and are distributed in an exponential disk as

$$n_e = n_0 \exp(-r/h_r)\text{sech}^2(z/h_d). \tag{2.30}$$

where $h_r = 5$ kpc is the radial scale length, and $h_d = 1$ kpc is the scale height. The polarisation direction may be computed in this model as:

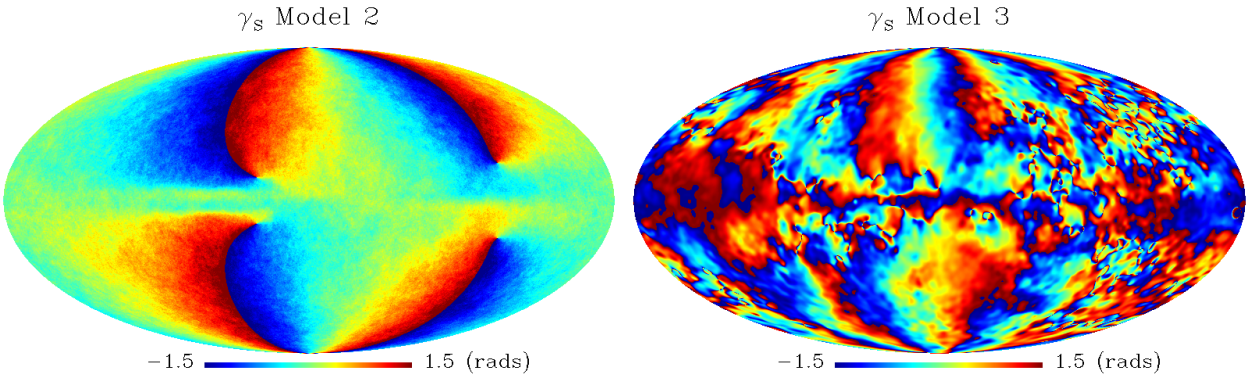

Figure 2.7: Left: The angle of the magnetic field given by a logarithmic spiral model (Equation 2.31) with parameters derived from the synchrotron radiation in the WMAP K-band data. Right: The polarisation angle derived directly from the WMAP 23 GHz Q/U images.

$$\begin{aligned} \tan 2\gamma(\hat{n}) &= \frac{U(\hat{n})}{Q(\hat{n})} \\ &= \frac{\int n_e(x,\hat{n}) 2B_s(x,\hat{n}) B_t(x,\hat{n})\, dx}{\int n_e(x,\hat{n}) \left[B_s^2(x,\hat{n}) - B_t^2(x,\hat{n})\right] dx}, \end{aligned} \tag{2.31}$$

where $\hat{n}$ is the line-of-sight direction, x is the distance along that direction, n_e is the electron distribution, and B_t and B_s are orthogonal components of the field perpendicular to the line of sight, with B_t the component perpendicular to the z axis of the Galactic plane. The parameters of this model are determined by again fitting the predicted directions to the measured K-band field directions. The resultant ϕ field is shown in Figure 2.7. The second model uses the raw Q and U K-band maps to calculate ϕ directly as $\phi = 0.5\arctan(Q/U)$, and is thus more realistic in terms of irregularity and knotting in the field, but also produces a much noisier distribution of orientations, as shown in Figure 2.7.

2.3.3 Thermal Dust

The Galactic thermal dust emission is modelled using the DIRBE-FIRAS 100 μm full-sky dust map [130]. The angular resolution of the map is $\approx 5'$, which is comparable to Planck's resolution in the highest frequency channels. Figure 2.8 shows the dust emission map in units of MJy/Sr. The dust emission exhibits a significantly larger variance than the synchrotron emission across the sky, with the Galactic plane dust emission several orders of magnitude brighter than the emission at high Galactic latitude.

The dust model from Finkbeiner et al. [130] which gave the best fit to the data available at the time of publication (the 2013 Planck data now provide us with much more information) is a two-

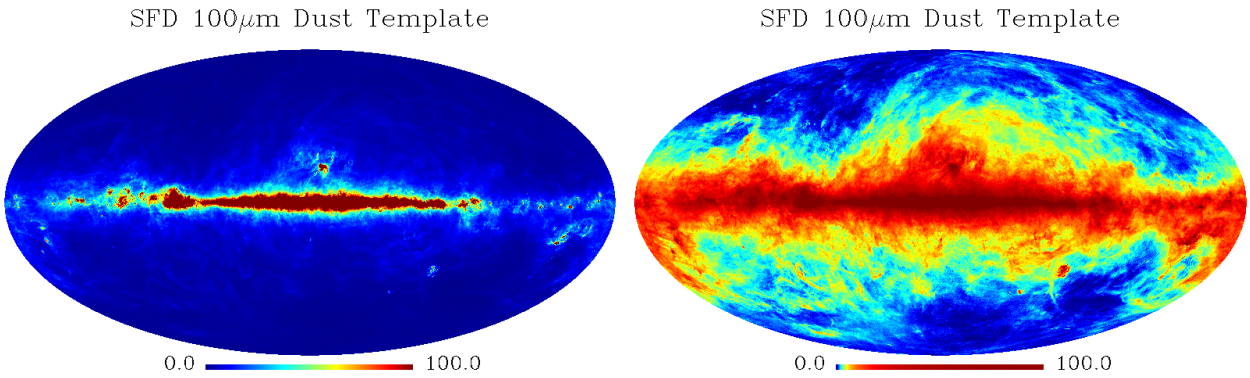

Figure 2.8: Left: Thermal dust intensity observed by FIRAS at 100 μm shown in units of MJy/Sr. This map is commonly used to identify regions of expected low dust emission, with the minimum at Galactic coordinates (l, b) = (240,-70). The map serves as a useful tool for estimating polarised dust templates. Right: 100 μm map with histogram-equalised colourbar to increase the dynamic range.

component black-body dust model with temperatures and spectral indices $T_1 = 9.4$ K, $\alpha_1 = 1.67$ and $T_2 = 16.2$ K, $\alpha_2 = 2.7$. This black-body model is used to construct dust templates at the Planck observing frequencies by assuming that each dust component has a power-law emissivity over the FIRAS frequency range. The model is then constructed as a sum of the dust components:

$$I_{p,\nu} = \frac{\sum_k f_k Q_k(\nu) B_\nu(T_{pk})}{\sum_k f_k Q_k(\nu_0) B_{\nu_0}(T_{pk}) K_{100}(\alpha_k, T_{pk})} I_{p,100} \tag{2.32}$$

where f_k is a normalisation constant for the k$^{\text{th}}$ component, T_{pk} is the temperature in the pixel p of component k, K_{100} is the DIRBE colour-correction factor, and $I_{p,100}$ is the 100 μm flux at pixel p. The emission efficiency Q is as defined as the ratio of the emission cross-section to the classical cross-section of the grains. The parameters are set at the best-fit values for Finkbeiner et. al model 8 with temperatures and indices as above, f_1=0.0363, and Q1/Q2 = 13.0, and full-sky maps of the dust emission are generated at each of the Planck observing frequencies by assuming that the dust emission is polarised at an average level of 5%. This level is consistent with the best-fit derived from WMAP [83]. The polarisation orientation is calculated similarly to the synchrotron orientation with an LSA field model, but with a scale height of 100 pc and a radial scale length of 3 kpc. This has the effect of tightening the spiral distribution, but the overall morphology remains consistent with that for synchrotron, and the map is very similar to that in Figure 2.7.

2.3.4 Noise

The foreground component maps in the Planck Sky Model are generated at HEALPix resolution $N_{side} = 2048$ and coadded to produce a total intensity map in temperature and polarisation as T, Q, and U images at each of the Planck observing frequencies. Synchrotron is generated as in

model 3 described above. Gaussian noise is generated at the level specified in the Planck Blue Book (Table 2 in Chapter 1) calculated at $N_{side} = 2048$. The noise is assumed to be white (which is not quite true). To generate Gaussian noise with a given variance, consider a symmetric bivariate Gaussian distribution in x_1 and x_2

$$dP = \frac{1}{2\pi\sigma^2} \exp\left(-\frac{x_1^2}{2\sigma^2}\right) \exp\left(-\frac{x_2^2}{2\sigma^2}\right) dx_1 dx_2, \tag{2.33}$$

where σ^2 is the variance. If we now change to polar coordinates $r^2 = x^2 + y^2$ and integrate from 0 to r and $0 < \theta < 2\pi$ we have:

$$P(< r) = 1 - \exp\left(\frac{-r^2}{2\sigma^2}\right). \tag{2.34}$$

We can substitute $y = 1 - P(< r)$ so that $r = \sqrt{-2\sigma^2 \ln(y)}$, and since $x_1 = r\cos\theta$ and $x_2 = r\sin\theta$, $x_1 = \sqrt{-2\sigma^2 \ln(y)}\cos\theta$. Given θ varies between $0 \rightarrow 2\pi$, we thus generate noise for each Planck channel with noise level σ_i (which is different for temperature and polarisation) as $n_i = \sigma_i\sqrt{-2\ln(R_i)}\cos(2\pi R_i)$ with uniformly distributed random numbers R_i.

The rms fluctuations for the CMB, dust, synchrotron, and noise, in equivalent thermodynamic temperature are shown in Figure 2.9.

The maps are then spherically transformed and convolved with a 7° beam (B-modes above about $\ell \sim 20$ are inaccessible to Planck given the signal-to-noise ratio, and this convolution also helps to minimise pixel aliasing effects) before repixellisation at a lower resolution at $N_{side} = 8, 16, 32$ corresponding to 768, 3072, and 12,288 pixels respectively. The full resolution coadded foreground sky maps in polarisation are shown in Figures 2.10 and 2.11.

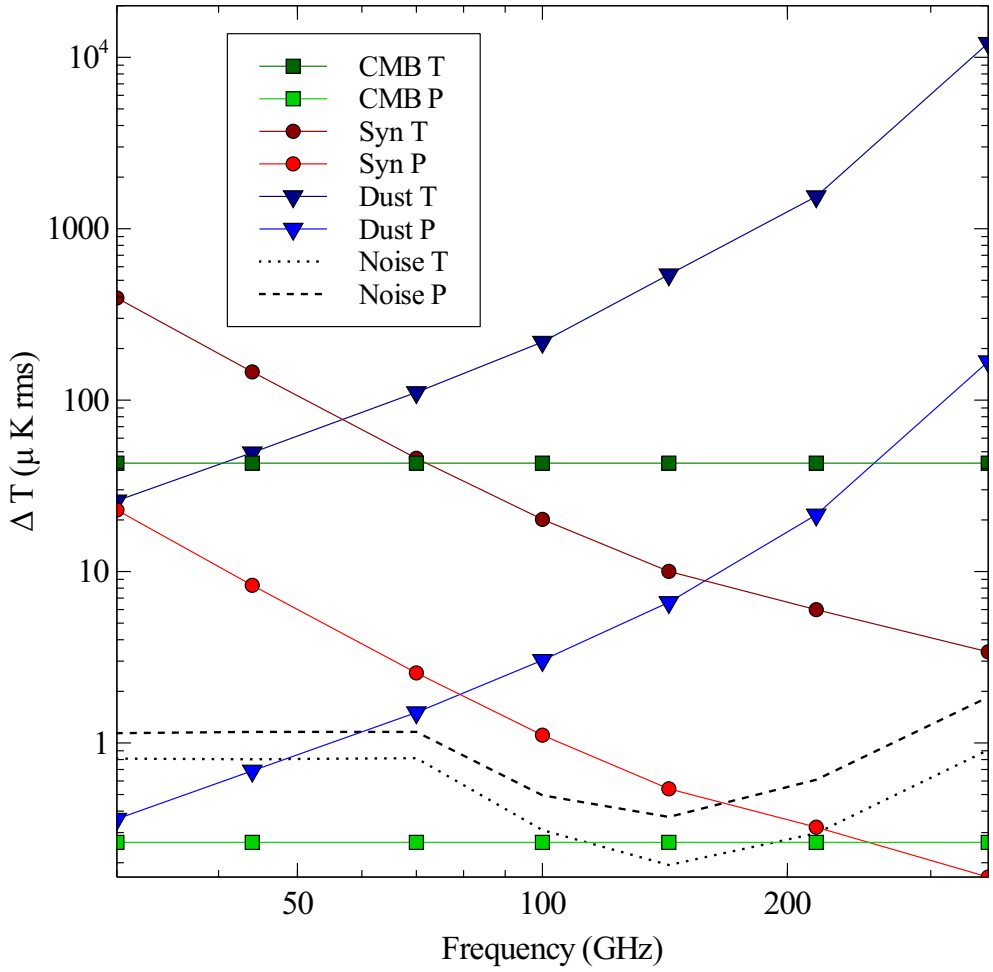

Figure 2.9: The rms equivalent thermodynamic fluctuations for temperature and polarisation per pixel at each of the polarisation-sensitive Planck observing frequencies, in the region of sky with Galactic latitude $60° < b < 90°$. The rms instrumental noise per pixel in each frequency channel is also plotted, for pixel size $1.7'$.

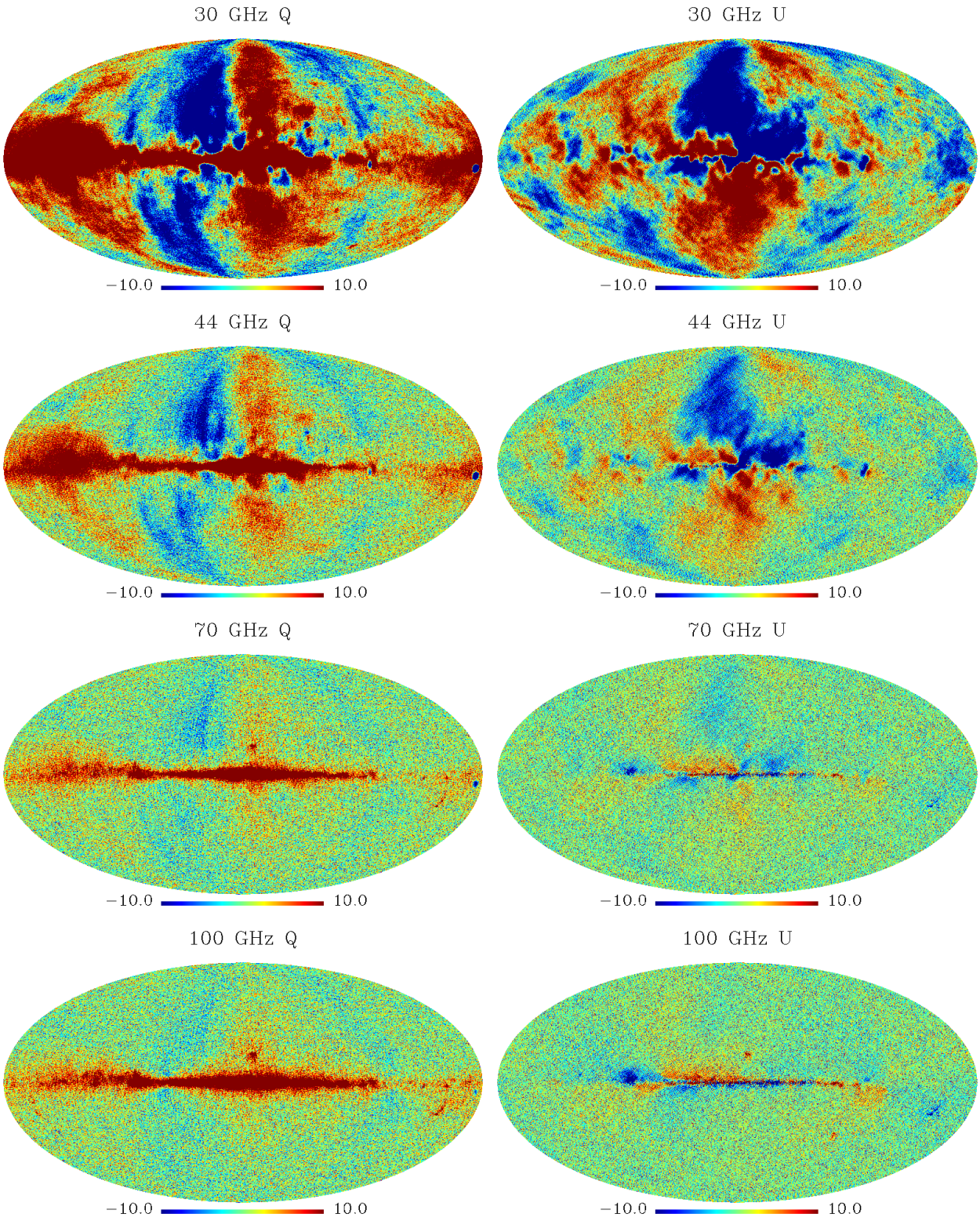

Figure 2.10: Full-sky coadded foreground and noise Q and U maps generated at $N_{side} = 2048$ resolution ($\sim$ 50 million pixels) for 30, 44, 70, and 100 GHz. The units are μK CMB equivalent thermodynamic temperature. The 70 GHz channel exhibits minimum foreground emission in both temperature and polarisation.

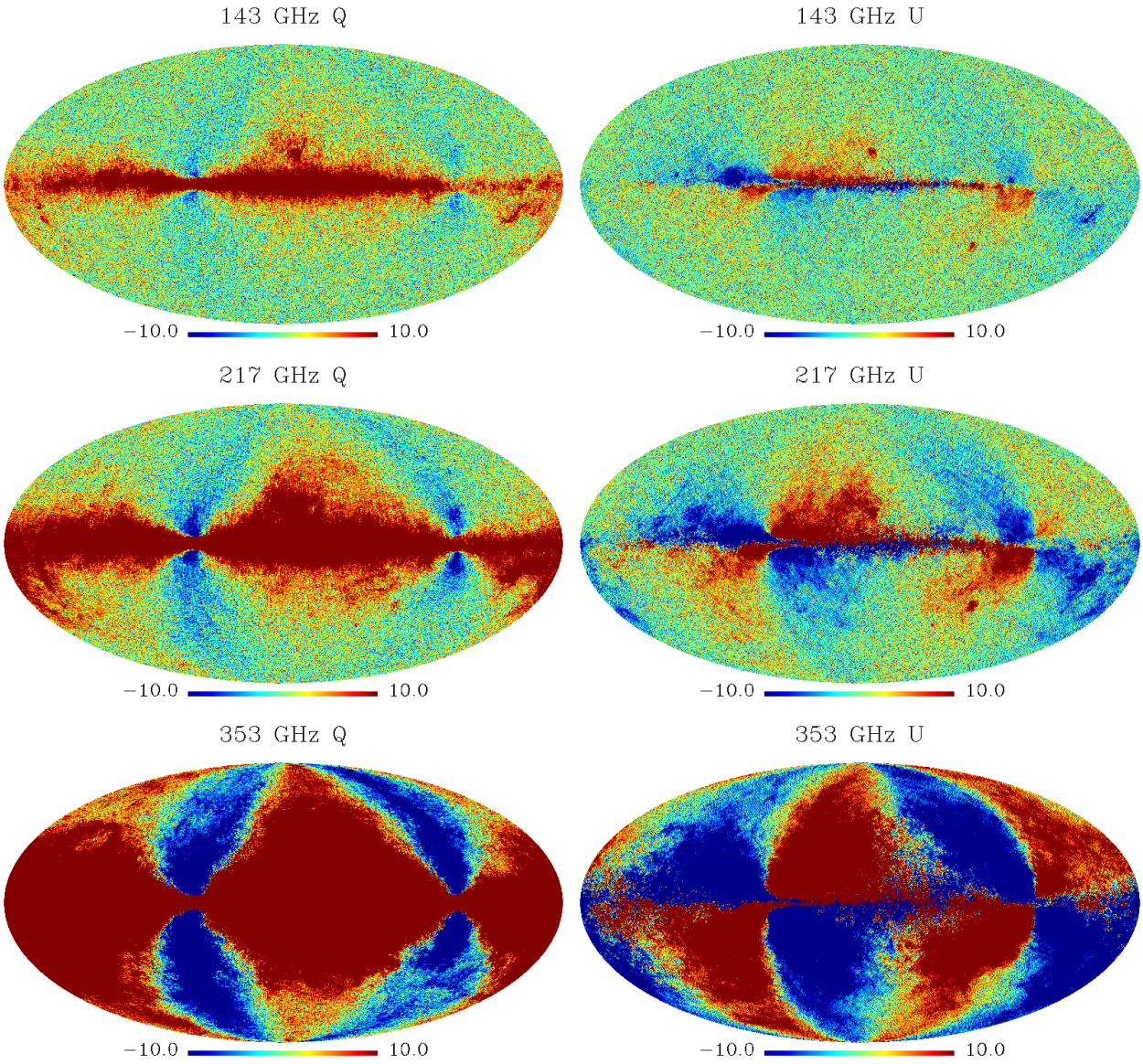

Figure 2.11: Full-sky coadded foreground and noise Q and U maps generated at $N_{side} = 2048$ resolution ($\sim$ 50 million pixels) for 143, 217, and 353 GHz. The units are μK CMB equivalent thermodynamic temperature.

2.4 Parametric Fitting

The problem of B-mode detection in the presence of Galactic foregrounds has been investigated by a number of authors. Tucci et al. (2005) [131] performed a Fisher matrix analysis for idealised experiments including foregrounds. Amblard, Cooray and Kaplinghat (2007) [132] investigated harmonic ILC subtraction for B-mode detection at high multipoles ($\ell > 20$) for various experimental configurations. Betoulle et al. (2009) [133] considered the application of Spectral Matching Independent Component Analysis (SMICA) to perform a Fisher matrix analysis for various experiments, including Planck. The works most closely related to ours are the studies by Dunkley et al. (2008b) [134], Efstathiou et al. (2009) [135] and Armitage-Caplan et al. (2011) [113] in which the former focusses on B-mode detection with a future satellite with high signal-to-noise in polarisation, rather than the low signal-to-noise case relevant to Planck. Low signal-to-noise introduces additional complexity to the foreground subtraction problem, nevertheless there are strong similarities between our approaches. Armitage-Caplan et al. focus on applying a spectral index prior to individual pixels to try and mitigate the foreground propagation into cleaned CMB maps, and again the work is similar in approach. We use a maximum-likelihood formalism, and use all the polarisation data available from Planck simulations in separating foregrounds and estimating errors. That the foregrounds can be approximated by power laws in frequency is a useful motivator for studies of this kind, and lend themselves well to the approach used here.

2.4.1 Motivation for Correlated Spectral Indices

The synchrotron spectral index β_s depends on cosmic ray properties, and varies with direction on the sky. As discussed in Section 2.1.3, observations from 408 MHz to 10 GHz have shown a spatial variation of β_s from -2.8 to -3.2. These studies have shown that whilst the exact morphology and variance is dependent on the implied assumptions about other components, the global behaviour is consistent with an index that varies on scales no smaller than about $5 - 10°$. This is also consistent with gamma ray observations which do not predict a strong spatial variation of the synchrotron spectral index, mostly due to the large interaction length of cosmic ray electrons [136].

The thermal dust emission is simulated by assuming that the two dust populations are well mixed spatially, and therefore both heated by the same radiation field. It is also assumed that the optical properties of the two populations are constant (i.e. fixed β_d and opacity). Given these assumptions, Finkbeiner, Davis & Schlegel [137] showed that the spatial variation in effective dust spectral index observed is only determined by the local strength of the interstellar radiation field, and the total dust column density. Thus for the map resolutions and simulations used in this study, imposing a spatial correlation of the spectral indices is motivated by the observation that we would not expect β_s or β_d to vary wildly in neighbouring pixels, something which could alias noise into other fitted components. In addition, the template maps used in the PSM simulations have been processed to exhibit a constant signal-to-noise across the sky, which results in a lower angular resolution (several

degrees) at higher Galactic latitudes than across the Galactic plane. The model itself is fit to the very large scale dust emission at 7°, even though variations of the dust properties are observed down to increasingly small scales in more recent data [138].

2.4.2 Method

The multifrequency sky signal is modelled as

$$\mathbf{d}_p = \mathbf{A}_p \mathbf{s}_p + \mathbf{n}_p, \tag{2.35}$$

where $\mathbf{d}_p$ is a vector containing the data from N_{freq} frequencies assumed to share a common angular resolution, $\mathbf{s}_p$ is a vector of N_{comp} signal amplitudes to be estimated, $\mathbf{A}_p \equiv \mathbf{A}_p(\beta)$ is a component mixing or frequency scaling matrix with a total of N_{spec} free spectral parameters β also to be estimated, and $\mathbf{n}_p$ is the noise level at each pixel p. We can write down a likelihood for the data of the form

$$-2 \ln \mathcal{L}_{data}(\mathbf{s}, \beta) = C + (\mathbf{d} - \mathbf{A}\,\mathbf{s})^t \, \mathbf{N}^{-1} \, (\mathbf{d} - \mathbf{A}\,\mathbf{s}), \tag{2.36}$$

where $\mathbf{N}$ is the noise covariance matrix of the data and we have now dropped the pixel index p. This likelihood reaches its maximum for the values of $\mathbf{s}$ and β that satisfy:

$$-(\mathbf{A}_{,\beta}\,\mathbf{s})^t \, \mathbf{N}^{-1} \, (\mathbf{d} - \mathbf{A}\,\mathbf{s}) = 0, \tag{2.37}$$

$$\mathbf{s} = \left(\mathbf{A}^t \, \mathbf{N}^{-1} \, \mathbf{A}\right)^{-1} \, \mathbf{A}^t \, \mathbf{N}^{-1} \, \mathbf{d}, \tag{2.38}$$

where $_{,\beta}$ denotes a partial derivative with respect to β_i. Under the assumption that the spectral parameters do not vary significantly over a region of the sky, corresponding to a physical assumption that the spectral parameters vary more slowly in space than the signal amplitudes do, we can substitute the generalised least squares solution Equation 2.38 into the likelihood Equation 2.36 eliminating the sky signals $\mathbf{s}$, in order to obtain a spectral index likelihood given by

$$-2 \ln \mathcal{L}_{spec}(\beta) = \mathrm{C} - (\mathbf{A}^t\mathbf{N}^{-1}\mathbf{d})^t(\mathbf{A}^t\mathbf{N}^{-1}\mathbf{A})^{-1}(\mathbf{A}^t\mathbf{N}^{-1}\mathbf{d}). \tag{2.39}$$

The spectral parameters that minimise Equation 2.39 can be found using numerical minimisation techniques, and then substituted into Equation 2.38 in order to calculate the corresponding signal amplitudes pixel by pixel. Finally, the noise covariance matrix describing the properties of the noise contained in the data $\mathbf{d}$, is propagated to the component estimates $\mathbf{s}$:

$$\mathbf{N_s} \equiv \left(\mathbf{A}^t\,\mathbf{N}^{-1}\,\mathbf{A}\right)^{-1}. \tag{2.40}$$

Once the spectral parameters have been determined from an analysis of the samples, the values are then substituted into Equations 2.38 and 2.40 in order to obtain the signal amplitudes and their covariance.

The sampling proceeds by initially performing a low-tolerance multidimensional downhill simplex routine before a Newton-Raphson minimisation (both codes developed using *Numerical Recipes in Fortran*). The step at each stage of the iteration is calculated as $\Delta x = -\mathbf{M}^{-1}\mathbf{R}$ where $\mathbf{M}$ is the matrix of second derivatives of the likelihood at the current trial point, and $\mathbf{R}$ is the vector of first derivatives. The tolerance for fractional change in action is set to achieve convergence for a high percentage of pixels, however for some pixels along the Galactic plane the large foreground amplitudes lead to a divergence of the chain. These pixels are excluded from the subsequent likelihood analysis as they fall well inside even the most conservative Galactic mask used.

2.4.3 Likelihood

We now review the calculations for the pixel and noise covariance matrices. The pixel covariance matrix calculation follows the formalism adopted in Tegmark et al. (2001) [139], and the noise covariance matrix for degraded resolution maps calculation follows that of Efstathiou et. al (2009) [140]

2.4.3.1 Pixel Covariance Matrix

Let the 3-dimensional vector X_i denote the three measurable quantities for T, Q and U in the i$^{\text{th}}$ pixel. The 3×3 covariance matrix between two such vectors at different points can be written

$$\langle \mathbf{x}_i \mathbf{x}_j^t \rangle = \mathbf{R}(\alpha_{ij})\mathbf{M}(\widehat{\mathbf{r}}_i \cdot \widehat{\mathbf{r}}_j)\mathbf{R}(\alpha_{ji})^t, \tag{2.41}$$

where $\mathbf{M}$ is the covariance using a (Q,U)-convention where the reference direction is the great circle connecting the two points, and the rotation matrices given by

$$\mathbf{R}(\alpha) \equiv \begin{pmatrix} 1 & 0 & 0 \\ 0 & \cos 2\alpha & \sin 2\alpha \\ 0 & -\sin 2\alpha & \cos 2\alpha \end{pmatrix} \tag{2.42}$$

accomplish a rotation into a global reference frame where the reference directions are meridians. The full $(3n) \times (3n)$ map covariance matrix is formed from the 3×3 blocks of Equation 2.41 by

looping over all pixel pairs.

Computing the magnitudes of the rotation angles α_{ij} is straightforward. The great circle connecting the two pixels has the unit normal vector

$$\widehat{\mathbf{r}}_{ij} \equiv \frac{\widehat{\mathbf{r}}_i \times \widehat{\mathbf{r}}_j}{|\widehat{\mathbf{r}}_i \times \widehat{\mathbf{r}}_j|}. \tag{2.43}$$

Similarly, the meridian passing though pixel i has the unit normal vector

$$\widehat{\mathbf{r}}_i^* \equiv \frac{\widehat{\mathbf{z}} \times \widehat{\mathbf{r}}_i}{|\widehat{\mathbf{z}} \times \widehat{\mathbf{r}}_i|}, \tag{2.44}$$

where $\widehat{\mathbf{z}} = (0, 0, 1)$ is the unit vector in the z-direction. The magnitude of α_{ij}, the rotation angle for pixel i, is simply the angle between these two great circles, so $\cos\alpha_{ij} = \widehat{\mathbf{r}}_{ij} \cdot \widehat{\mathbf{r}}_i^*$. The sign of α_{ij} is defined so that a positive angle corresponds to clockwise rotation at the pixel (at $\widehat{\mathbf{r}}_i$). We therefore compute the cross product of the two circle normals, which has the property that $\widehat{\mathbf{r}}_{ij} \times \widehat{\mathbf{r}}_i^* = \widehat{\mathbf{r}}_i \sin\alpha_{ij}$. We can then show that

$$\sin\alpha_{ij} = (\widehat{\mathbf{r}}_{ij} \times \widehat{\mathbf{r}}_i^*) \cdot \widehat{\mathbf{r}}_i \propto [(\widehat{\mathbf{r}}_i \times \widehat{\mathbf{r}}_j) \times (\widehat{\mathbf{r}}_i \times \widehat{\mathbf{z}})] \cdot \widehat{\mathbf{r}}_i = [(\widehat{\mathbf{r}}_i \times \widehat{\mathbf{r}}_j) \cdot \widehat{\mathbf{z}}]\, \widehat{\mathbf{r}}_i \cdot \widehat{\mathbf{r}}_i \propto \widehat{\mathbf{r}}_{ij} \cdot \widehat{\mathbf{z}},$$

where the omitted proportionality constants are positive. α_{ij} therefore has the same sign as the z-coordinate of $\widehat{\mathbf{r}}_{ij}$, and is given by

$$\alpha_{ij} = \begin{cases} +\cos^{-1}(\widehat{\mathbf{r}}_{ij} \cdot \widehat{\mathbf{r}}_i^*) & \text{if } \widehat{\mathbf{r}}_{ij} \cdot \widehat{\mathbf{z}} > 0, \\ -\cos^{-1}(\widehat{\mathbf{r}}_{ij} \cdot \widehat{\mathbf{r}}_i^*) & \text{if } \widehat{\mathbf{r}}_{ij} \cdot \widehat{\mathbf{z}} < 0. \end{cases} \tag{2.45}$$

For generic pairs of directions, Equation 2.45 gives the two rotation angles α_{ij} and α_{ji} needed for Equation 2.41. However, it fails when the two pixels are either identical or on exactly opposite sides of the sky. Hence any great circle through $\widehat{\mathbf{r}}_i$ will go through $\widehat{\mathbf{r}}_2$ as well. We can choose this circle to be the meridian, so no rotation is needed for this case. Indeed $\mathbf{M}$ comes out diagonal for this case by symmetry, with $\langle Q_i U_j \rangle = 0$ and $\langle Q_i Q_j \rangle = \langle U_i U_j \rangle$, so rotations have no effect. If $\widehat{\mathbf{r}}_i \times \widehat{\mathbf{z}} = \mathbf{0}$, then the pixel is at the north or south pole which makes the global (Q, U)-convention undefined.

The $\mathbf{M}$-matrix depends only on the angular separation between the two pixels. Following the formalism of Zaldarriaga [141], it is given by:

$$\mathbf{M}(\widehat{\mathbf{r}}_i \cdot \widehat{\mathbf{r}}_j) \equiv \begin{pmatrix} \langle T_i T_j \rangle & \langle T_i Q_j \rangle & \langle T_i U_j \rangle \\ \langle T_i Q_j \rangle & \langle Q_i Q_j \rangle & \langle Q_i U_j \rangle \\ \langle T_i U_j \rangle & \langle U_i Q_j \rangle & \langle U_i U_j \rangle \end{pmatrix}, \tag{2.46}$$

$$\langle T_i T_j \rangle \equiv \sum_\ell \left(\frac{2\ell+1}{4\pi} \right) P_\ell(z) C_\ell^T, \tag{2.47}$$

$$\langle T_i Q_j \rangle \equiv -\sum_\ell \left(\frac{2\ell+1}{4\pi} \right) F_\ell^{10}(z) C_\ell^{TE}, \tag{2.48}$$

$$\langle T_i U_j \rangle \equiv -\sum_\ell \left(\frac{2\ell+1}{4\pi} \right) F_\ell^{10}(z) C_\ell^{BT}, \tag{2.49}$$

$$\langle Q_i Q_j \rangle \equiv \sum_\ell \left(\frac{2\ell+1}{4\pi} \right) \left[F_\ell^{12}(z) C_\ell^E - F_\ell^{22}(z) C_\ell^B \right], \tag{2.50}$$

$$\langle U_i U_j \rangle \equiv \sum_\ell \left(\frac{2\ell+1}{4\pi} \right) \left[F_\ell^{12}(z) C_\ell^B - F_\ell^{22}(z) C_\ell^E \right], \tag{2.51}$$

$$\langle Q_i U_j \rangle \equiv \sum_\ell \left(\frac{2\ell+1}{4\pi} \right) \left[F_\ell^{12}(z) + F_\ell^{22}(z) \right] C_\ell^{EB}, \tag{2.52}$$

where $\mathbf{z} = \widehat{\mathbf{r}}_i \cdot \widehat{\mathbf{r}}_j$ is the cosine of the angle between the two pixels under consideration. P_ℓ denotes a Legendre polynomial, and the functions F^{10}, F^{12} and F^{22} are given by

$$F^{10}(z) = 2 \frac{\frac{\ell z}{(1-z^2)} P_{\ell-1}(z) - \left(\frac{\ell}{1-z^2} + \frac{\ell(\ell-1)}{2} \right) P_\ell(z)}{[(\ell-1)\ell(\ell+1)(\ell+2)]^{1/2}} \tag{2.53}$$

$$F^{12}(z) = 2 \frac{\frac{(\ell+2)z}{(1-z^2)} P_{\ell-1}^2(z) - \left(\frac{\ell-4}{1-z^2} + \frac{\ell(\ell-1)}{2} \right) P_\ell^2(z)}{(\ell-1)\ell(\ell+1)(\ell+2)} \tag{2.54}$$

$$F^{22}(z) = 4 \frac{(\ell+2) P_{\ell-1}^2(z) - (\ell-1) z P_\ell^2(z)}{(\ell-1)\ell(\ell+1)(\ell+2)(1-z^2)} \tag{2.55}$$

Here P_ℓ and P_ℓ^2 denote Legendre polynomials P_ℓ^m for the cases $m = 0$ and $m = 2$, respectively, which are computed using the recursion relations

$$P_\ell(z) = \begin{cases} 1 & \text{for } \ell = 0, \\ z & \text{for } \ell = 1, \\ \frac{(2\ell-1) z P_{\ell-1}(z) - (\ell-1) P_{\ell-2}(z)}{\ell} & \text{for } \ell \geq 2, \end{cases} \tag{2.56}$$

$$P_\ell^2(z) = \begin{cases} 3(1-z^2) & \text{for } \ell = 2, \\ 5zP_2^2 & \text{for } \ell = 3, \\ \frac{(2\ell-1)zP_{\ell-1}^2(z) - (\ell+1)P_{\ell-2}^2(z)}{\ell-2} & \text{for } \ell \geq 4. \end{cases} \tag{2.57}$$

The division by $(1-z^2)$ causes expressions (2.53)−(2.55) to blow up numerically when $z = \pm 1$, i.e, at zero separation or between opposite pixels in the sky. Taking the appropriate limits for these cases gives

$$F_\ell^{10}(z) = 0 \text{ if } |z| = 1, \tag{2.58}$$

$$F_\ell^{12}(z) = \begin{cases} \frac{1}{2} \text{ if } z = 1, \\ \frac{1}{2}(-1)^\ell \text{ if } z = -1, \end{cases} \tag{2.59}$$

$$F_\ell^{22}(z) = \begin{cases} -\frac{1}{2} \text{ if } z = 1, \\ \frac{1}{2}(-1)^\ell \text{ if } z = -1. \end{cases} \tag{2.60}$$

2.4.3.2 Noise Covariance Matrix for Degraded Resolution Maps

Let x_i denote the pixel value in the high resolution map and X_i denote the pixel value in the low resolution map. The harmonic coefficients computed from the high resolution map are

$$a_{\ell m} = \sum_i x_i \Omega_i Y_{\ell m}^*(\theta_i), \tag{2.61}$$

where Ω_i is the solid angle of a high resolution map pixel. So, the pixel values in the degraded map are

$$X_i = \sum_{\ell m} a_{\ell m} Y_{\ell m}(\theta_i) f_\ell(\theta_s), \tag{2.62}$$

where $f_\ell(\theta_s)$ is the smoothing function applied to the high resolution map. In terms of the pixel values of the high resolution map

$$X_i = \sum_{\ell m p} x_p \Omega_p Y_{\ell m}^*(\theta_p) Y_{\ell m}(\theta_i) f_\ell(\theta_s). \tag{2.63}$$

Using the addition theorem for spherical harmonics, the pixel noise covariance of the low resolution map is

$$\langle X_i X_j \rangle = \sum_{\ell_1 \ell_2} \langle x_p x_q \rangle \frac{(2\ell_1+1)}{4\pi} \frac{(2\ell_2+1)}{4\pi} \Omega_p \Omega_q P_{\ell_1}(\cos\theta_{ip}) P_{\ell_2}(\cos\theta_{jq}) f_{\ell_1} f_{\ell_2}.$$

This expression is time-consuming to evaluate, but it simplifies significantly if the noise is diagonal $\langle x_p x_q \rangle = \sigma_p^2 \delta_{pq}$ and if we assume small angles. In this case, for a Gaussian smoothing function, this simplifies to

$$\langle X_i X_j \rangle \approx \frac{1}{\theta_s^4} \frac{1}{2\pi^2} \sum_p \sigma_p^2 \Omega_p^2 \exp\left(-\frac{\theta_{ip}^2}{2\theta_s^2}\right) \exp\left(-\frac{\theta_{jp}^2}{2\theta_s^2}\right). \tag{2.64}$$

In the case of diagonal pixel noise at high resolution, and for small angles, the polarisation covariance matrices $\langle Q_i Q_p \rangle$ for the degraded resolution maps can be approximated by equation 2.64. Consider a degraded resolution Q map. The equivalent to Equation 2.63 is

$$Q_i = \frac{1}{2} \sum_{\ell m} \sum_p (q_p \left[{}_2Y^*(p) {}_2Y(i) + {}_{-2}Y^*(p) {}_{-2}Y(i) \right] + i u_p \left[{}_2Y^*(p) {}_2Y(i) - {}_{-2}Y^*(p) {}_{-2}Y(i) \right]) \Omega_p f_\ell. \tag{2.65}$$

The addition theorem for the tensorial harmonics is

$$\sum_m {}_{s_1}Y^*_{\ell -m}(\theta_1, \phi_1) \, {}_{s_2}Y_{\ell -m}(\theta_2, \phi_2) = (-1)^{s_1} \left(\frac{2\ell+1}{4\pi}\right)^{1/2} {}_{-s_1}Y_{\ell s_2}(\beta, \alpha) \mathrm{e}^{i s_1 \gamma}, \tag{2.66}$$

Applying the addition theorem to Equation 2.65 gives

$$Q_i = \sum_{\ell p} \frac{1}{2} \left(\frac{2\ell+1}{4\pi}\right)^{1/2} \Big(q_p \left[{}_{-2}Y_{\ell 2} \mathrm{e}^{i2\gamma} + {}_2Y_{\ell -2} \mathrm{e}^{-i2\gamma} \right] + i u_p \left[{}_{-2}Y_{\ell 2} \mathrm{e}^{i2\gamma} - {}_2Y_{\ell -2} \mathrm{e}^{-i2\gamma} \right] \Big) \Omega_p f_\ell.$$

Now we can write

$${}_2Y_{\ell m} = 2\sqrt{2} N_\ell A_\ell^m (G^+ - G^-) \mathrm{e}^{im\phi} \tag{2.67}$$

$${}_{-2}Y_{\ell m} = 2\sqrt{2} N_\ell A_\ell^m (G^+ + G^-) \mathrm{e}^{im\phi} \tag{2.68}$$

and so

$$Q_i = \sum_{\ell p} \frac{1}{2} \left(\frac{2\ell+1}{4\pi}\right)^{1/2} 2\sqrt{2} N_\ell A_\ell^2 (G^+ + G^-) \Omega_p f_\ell \left[q_p \cos(2\alpha + 2\gamma) - u_p \sin(2\alpha + 2\gamma) \right]. \tag{2.69}$$

In the limit $\ell \to \infty$, the prefactor in Equation 2.69, tends to

$$\left(\frac{2\ell+1}{4\pi}\right)^{1/2} \sqrt{2} N_\ell A_\ell^2 \to \left(\frac{2\ell+1}{2\pi}\right) \frac{1}{\ell^4}, \tag{2.70}$$

and

$$G^{\pm}_{\ell m}(s) \to \frac{1}{4} \ell^4 (J_0(s) \pm J_4(s)), \tag{2.71}$$

and so Equation 2.69 becomes

$$Q_i \approx \sum_{\ell p} \left(\frac{2\ell+1}{4\pi}\right) J_0\left((2\ell+1)\sin\beta/2\right) \Omega_p f_\ell \left[q_p \cos(2\alpha + 2\gamma) - u_p \sin(2\alpha + 2\gamma) \right]. \tag{2.72}$$

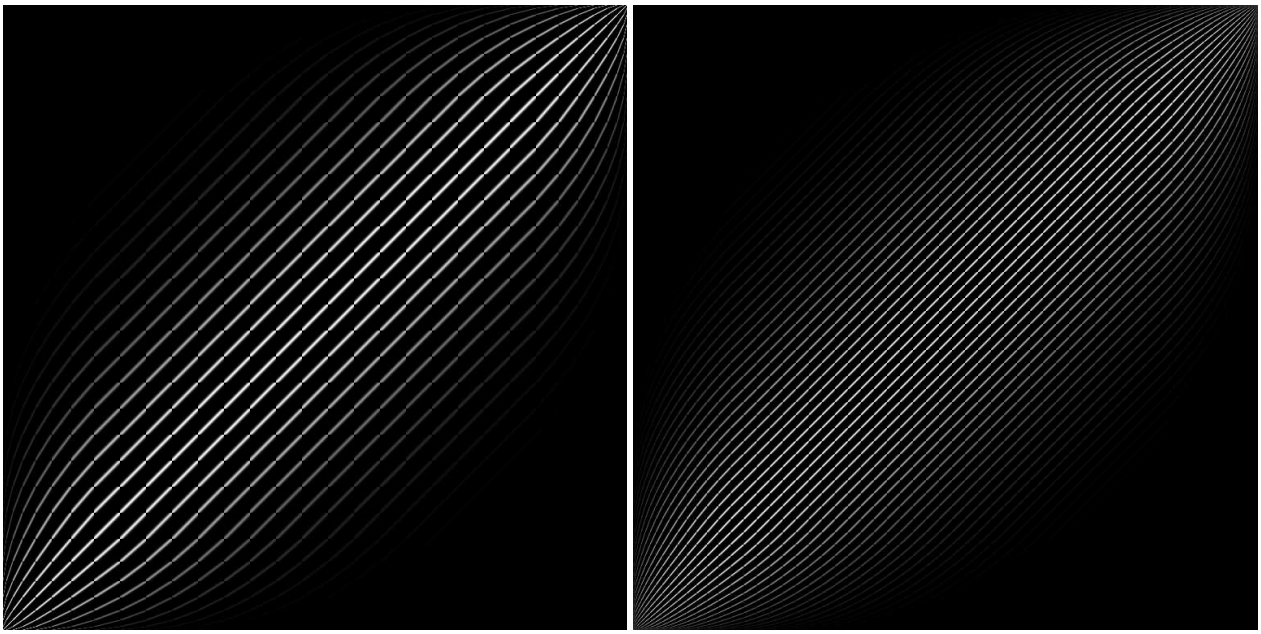

Figure 2.12: Normalised low-resolution noise covariance matrices calculated at $N_{side} = 8$ (left) and $N_{side} = 16$ (right) in the HEALPix ring format. Central pixel rings contain more pixels, contributing to the bowing effect seen towards the edges.

Summing over ℓ,

$$Q_i \approx \frac{\Omega_p}{\theta_2^2}\frac{1}{2\pi}\sum_p \left[q_p \cos(2\alpha + 2\gamma) - u_p \sin(2\alpha + 2\gamma)\right] \exp\left(-\frac{\theta_{ip}^2}{2\theta_s^2}\right), \tag{2.73}$$

for Gaussian smoothing. Thus, if q_p and u_p are uncorrelated between pixels and are uncorrelated with each other, and for small angular separations, it is possible to show that this gives exactly the same covariance matrix as the scalar result of Equation 2.64

$$\langle Q_i Q_j \rangle \approx \frac{1}{\theta_s^4}\frac{1}{2\pi^2}\sum_p \sigma_p^2 \Omega_p^2 \exp\left(-\frac{\theta_{ip}^2}{2\theta_s^2}\right)\exp\left(-\frac{\theta_{jp}^2}{2\theta_s^2}\right). \tag{2.74}$$

An analogous derivation applies for the covariance matrix $\langle U_i U_j \rangle$ (note that $\langle Q_i U_j \rangle \approx 0$). The scalar approximation of Equation 2.74 is a good approximation and is perfectly adequate for the smoothing scales adopted in this work. Normalised noise covariance matrices are shown in Figure 2.12 for two low resolution maps at $N_{side} = 8$ and $N_{side} = 16$ in the HEALPix ring format.

Using the pixel and noise covariance matrices derived in Section 2.4.3, we can construct a pixel-based likelihood expression for a given value of the tensor-to-scalar ratio (or any other parameters) and calculate the likelihood for different values of r to build up a posterior distribution from which the maximum likelihood value can be read. The individual pixel likelihood is modified by the

inclusion of prior assumptions about the distribution of the foreground spectral indices as:

$$-2\ln(\mathcal{L}) = \chi^2 + c \tag{2.75}$$

with

$$\chi^2 = \frac{1}{2}(d_i - s_i)^T N^{-1}(d_i - s_i) + \frac{(\beta_{s,i} - \bar{\beta}_s)^2}{2\Delta\beta_s^2} + \frac{(\beta_{d,i} - \bar{\beta}_d)^2}{2\Delta\beta_d^2}, \tag{2.76}$$

which can straightforwardly be extended to incorporate a spatial correlation of the spectral indices β_s and β_d by the modification of the spectral indices terms to:

$$\frac{1}{2}(\beta_c - \bar{\beta}_c)^T \mathbf{C}_{\beta_c}^{-1}(\beta_c - \bar{\beta}_c) \tag{2.77}$$

for each foreground component. Here $\mathbf{C}_{\beta_s}$ and $\mathbf{C}_{\beta_d}$ are the covariance matrices for the synchrotron and dust spectral indices, and are calculated similarly to the noise covariance matrix for the degraded-resolution maps. The correlation falls with pixel separation as:

$$\mathbf{C}(\theta_{ij}) = \frac{1}{\sigma^2}\left[\exp\left(-\frac{\theta_{ij}^2}{2\theta_s^2}\right)\right], \tag{2.78}$$

where θ_{ij} is the angular separation of the pixels, θ_s is the correlation angle, and σ is the standard deviation for the index across the sky. For fitting synchrotron emission we impose a spatial correlation of 5° with a mean of -2.9 and variance 0.3^2, and for dust we again impose a 5° correlation angle, but with a mean of 1.5 and a variance 0.5^2.
We fix all parameters except r at their WMAP 7-year concordance values, and calculate the likelihood at varying values of r. We show in Section 2.5 that by including the spatial correlation of the foreground spectral indices, the spread of likelihood peaks averaged over simulations is reduced at higher N_{side} due to the mitigation of noise propagation into the final cleaned CMB maps. This is a good motivator for using such methods as a more reliable estimator for a B-mode contribution at $N_{side} = 16, 32$, and utilises prior knowledge about the degree of variability of the synchrotron and dust spectral indices across the sky.

2.5 Results

Before analysing the effect of foreground propagation into cleaned CMB maps, it is important to test for any potential biasing of a B-mode signal by the likelihood sampling code. We first check that for a number of known test cases the separation algorithm gives the expected result at low-ℓ. We then analyse the effect of foreground cleaning for the uncorrelated case by checking for any introduced bias in r, and exploring the spread of the distribution over a number of noise and CMB realisations. We then compare the propagated noise level to the residuals generated for three pixellisations at $N_{side} = 8, 16$, and 32. Next we incorporate correlation of the foreground

spectral indices into our likelihood, and again check for any potential biasing. We finally show that including the spectral correlation leads to increased stability of the posteriors in r over realisations at higher resolutions and again examine the residuals and propagated noise levels.

2.5.1 Testing for Bias: Foreground-Free Simulations

In this section we analyse our sampling code to show that it produces morphologically correct CMB polarisation maps in the absence of foregrounds and with simple diagonal (white) noise. We use the resultant maps as input to a likelihood analysis, focussed on constraining the value of r at low-ℓ. We show that the input and output values of r agree well in all cases, and converge to the input value over many realisations.

In Figure 2.13 we show the input and marginalised output Q and U polarisation maps (using a Molleweide HEALPix projection) with a noisy CMB realisation at 30 GHz. Both input and output Q/U maps are plotted with the same temperature scale for comparison, and agree well. Planck-level noise is dominant over the polarised CMB over the entire 30-353 GHz frequency range, and the noisy CMB plots are shown with extended temperature scales to reflect the larger range as a result of the addition of Gaussian noise. This test also serves as a useful demonstration that the signal-to-noise attainable with Planck (if the noise can be approximated to be white) is sufficient to extract morphological features in the CMB polarisation maps.

We simulate 10 realisations of noisy CMB and use the marginalised Q/U maps as input to a likelihood calculation sampling r. The posterior distributions are shown in Figure 2.14. The average likelihood distribution can be obtained by calculating the sum of the individual log-likelihoods ($\sum_{i=1}^{N_{sim}} -2\ln\mathcal{L}_i$), and we find that for the foreground-free case our result is consistent with the input value of $r = 0.1$ at 1.1σ. Figure 2.15 shows the pixel residual distribution ($Q_{in} - Q_{out}$) for one of the ten simulations. The pixel residuals are consistent with a zero-mean distribution with $\Delta T_{rms} = 0.28$ μK for Q and U. Similar results are obtained for additional realisations.

2.5.2 Foreground Separation

In this section we apply the above formalism to simulations that include foregrounds and Planck-level noise. We generate noisy CMB simulations with synchrotron and dust models as described in Section 2.3, assuming the noise to be white and uncorrelated. It is possible to extend the analysis to allow for a realistic scanning strategy with correlated noise, given an appropriate model and corresponding covariance matrix for the noise N_{ij}, however it is assumed that the correlated errors are small for Planck and we therefore ignore this extension. Provided the covariance matrix is estimated accurately, there should be no significant change in results, and the methodology is identical. However, errors in the covariance matrices could produce biases in the power spectrum. We perform the full component separation described in Section 2.4 imposing a spatial correlation of

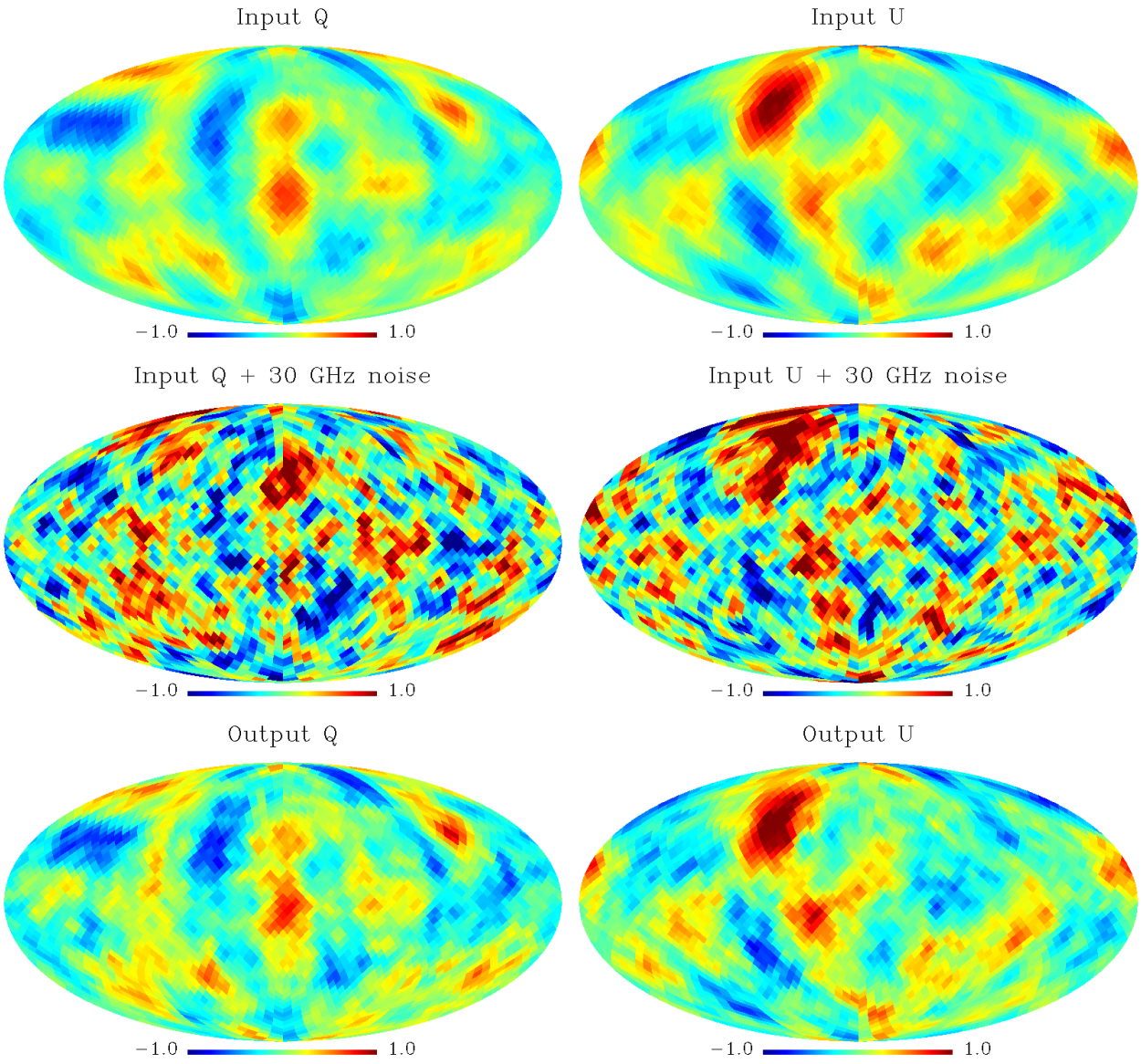

Figure 2.13: Top: Input Q and U CMB-only polarisation maps for a single simulation generated with $r = 0.1$, at a resolution $N_{side} = 16$ with 3072 pixels and $\ell_{max} = 2N_{side}$. Centre: CMB with a noise realisation generated to the Planck noise specification at 30 GHz. Bottom: Output foreground-cleaned CMB maps with good recovery of anisotropies at low ℓ. Units are μK.

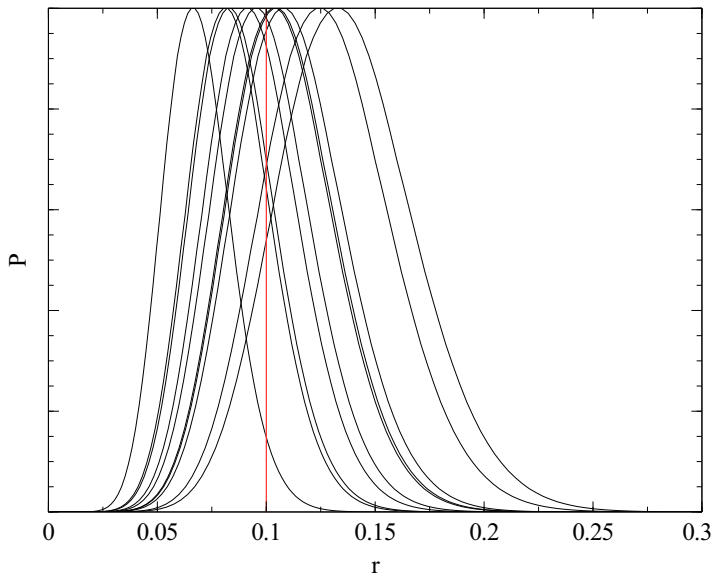

Figure 2.14: Posterior likelihood distributions for 10 r=0.1 foreground-free simulations at N_{side} = 16. The red line shows the prior input value.

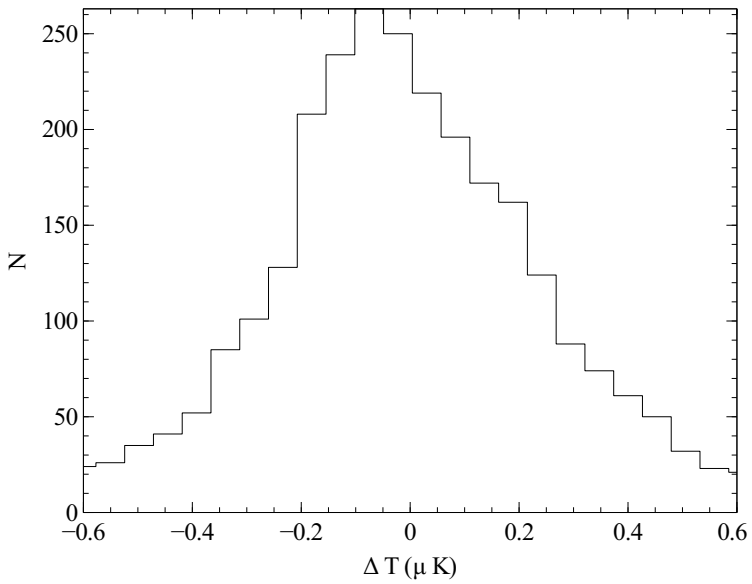

Figure 2.15: Pixel residual distribution (input-output) for Q for one simulation at N_{side} = 16. Residuals are consistent with a zero-mean distribution and show no significant bias.

the spectral indices over a patch of sky 5° across. The synchrotron variation is set at $\beta_s = -2.9 \pm 0.3$ and the dust variation is set at $\beta_d = 1.5 \pm 0.5$. Imposing the correlation has the effect of mitigating the influence of noise in neighbouring pixels, and producing a less visually 'noisy' cleaned CMB polarisation map. Especially noisy pixels separated by a small angle on the sky can drive β_s/β_d to more extreme values, so forcing a patch of sky to take similar values limits the propagation of this effect into the resultant cleaned maps. Regions close to the Galactic plane where the foreground signal-to-noise is higher are less driven by the prior, whereas regions away from the Galactic plane with lower foreground signal-to-noise tend to take values closer to the prior. Figure 2.16 shows the input and output Q and U CMB maps, the residual maps ($Q_{input} - Q_{output}$), and the propagated marginalised error maps for the CMB, plotted at the same temperature scale for comparison. The highest residuals are found along the Galactic plane where the foreground signal is high, and this is reflected in the error maps, which correlate highly with the residuals. There is a clear bias in the recovered Q image along the plane, which is mainly due to the synchrotron morphology. The orientation of the field is such that the synchrotron Q emission is much stronger than for U along the plane, and this bright region causes an overestimation of the foreground emission and an underestimation of the CMB. This effect persists over different CMB and noise realisations.

Figures 2.17 and 2.18 shows the input and recovered foreground maps for one simulation. The synchrotron and dust amplitudes are morphologically very similar with the exception of a few particularly noisy pixels near the Galactic plane. The residual plots show a slight excess along the Galactic plane, but are otherwise direction-independent. The Fisher information is calculated as the inverse of the second derivative matrix with respect to the variables C, A_s, β_s, A_d, β_d (the five fitted components in the model). The errors for each component can then be read as the diagonals of F^{-1}.

A useful consistency check is to compare the residual pixel levels with the achievable level given the noise characteristics of Planck. Since the CMB is constant over all frequency channels (in thermodynamic units), the limiting residual level can be calculated as $1/\sigma^2 = \sum 1/\sigma_i^2$, which for equivalent noise levels at $N_{side} = 16$ gives $\sigma = 0.241$ μK. The pixel distribution with latitude is shown in Figure 2.19. At high Galactic latitude, the recovered tolerance is consistent with the achievable level. The effect of noise is also mitigated by the smoothing during map preparation before component separation. Closer to the Galactic plane the residual level rises sharply well above the noise tolerance, particularly in Q, for which the synchrotron and dust emission is much stronger than for U.

We now generate 100 $N_{side} = 2048$ CMB and noise realisations and form full-sky maps with the same foreground model, before repixellising at $N_{side} = 16$ as before. The CMB is parametrically fit for each realisation and the errors calculated as before. The average Fisher and rms errors for Q and U are shown in Figure 2.20. As more simulations are added, the average of the residuals will approach zero for any particular pixel (with the exception of some along the Galactic plane which are always overestimated). The rms errors trace the average Fisher errors well, exhibiting a noisier

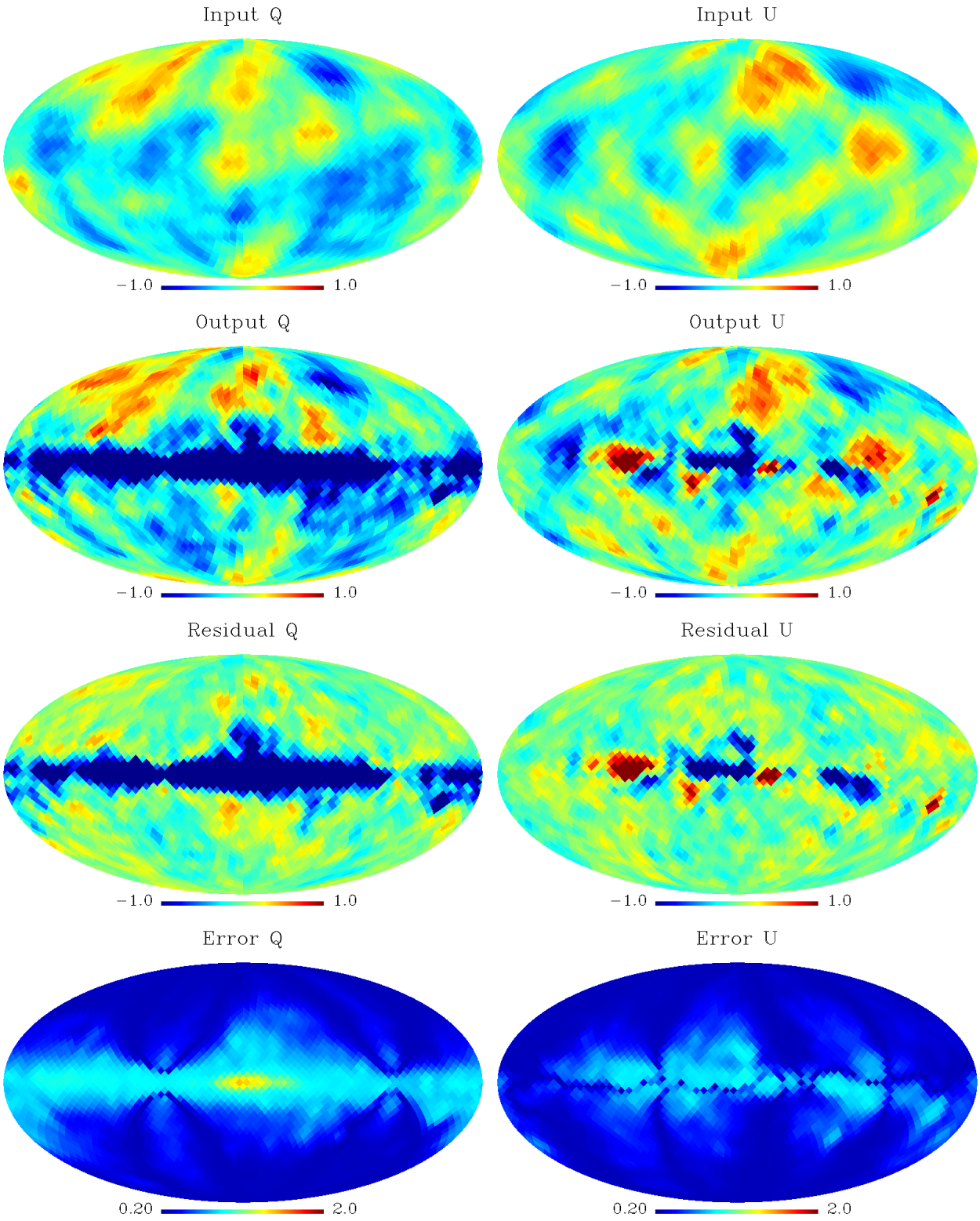

Figure 2.16: Foreground separated CMB maps including spectral correlation. First panels show input CMB Q/U, second panels show output CMB Q/U, third panels show residuals ($Q_{input} - Q_{output}$, $U_{input} - U_{output}$), and fourth panels show the propagated noise estimated for Q/U. All plots are at $N_{side} = 16$, and units are μK.

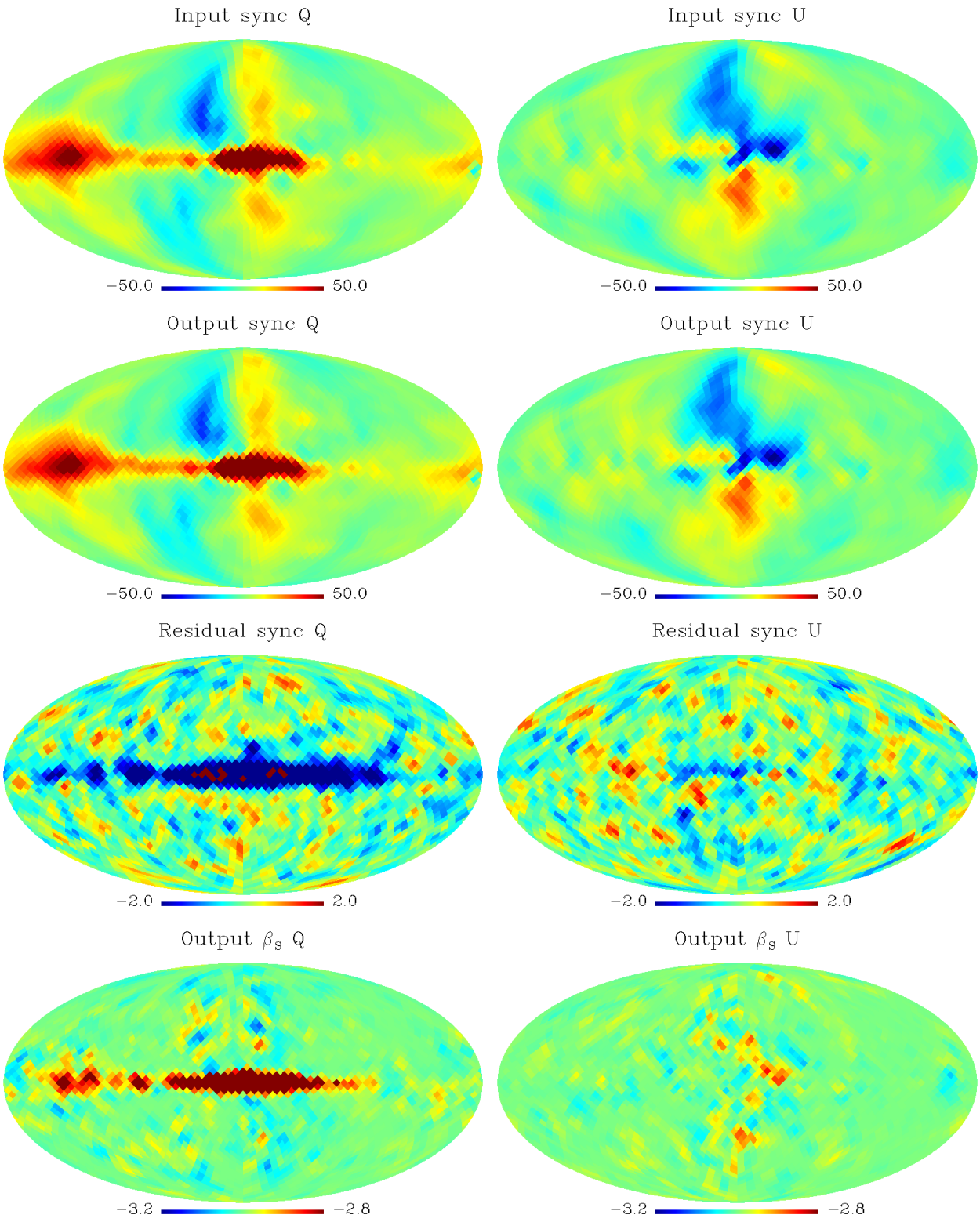

Figure 2.17: Recovered synchrotron foreground maps at $N_{side} = 16$. Top: Input amplitude at 30 GHz. Upper: Recovered synchrotron at 30 GHz. Lower: Pixel residual distribution. Units are μK. Bottom: Recovered β_s. Away from the Galactic plane the spectral index is driven to the prior value.

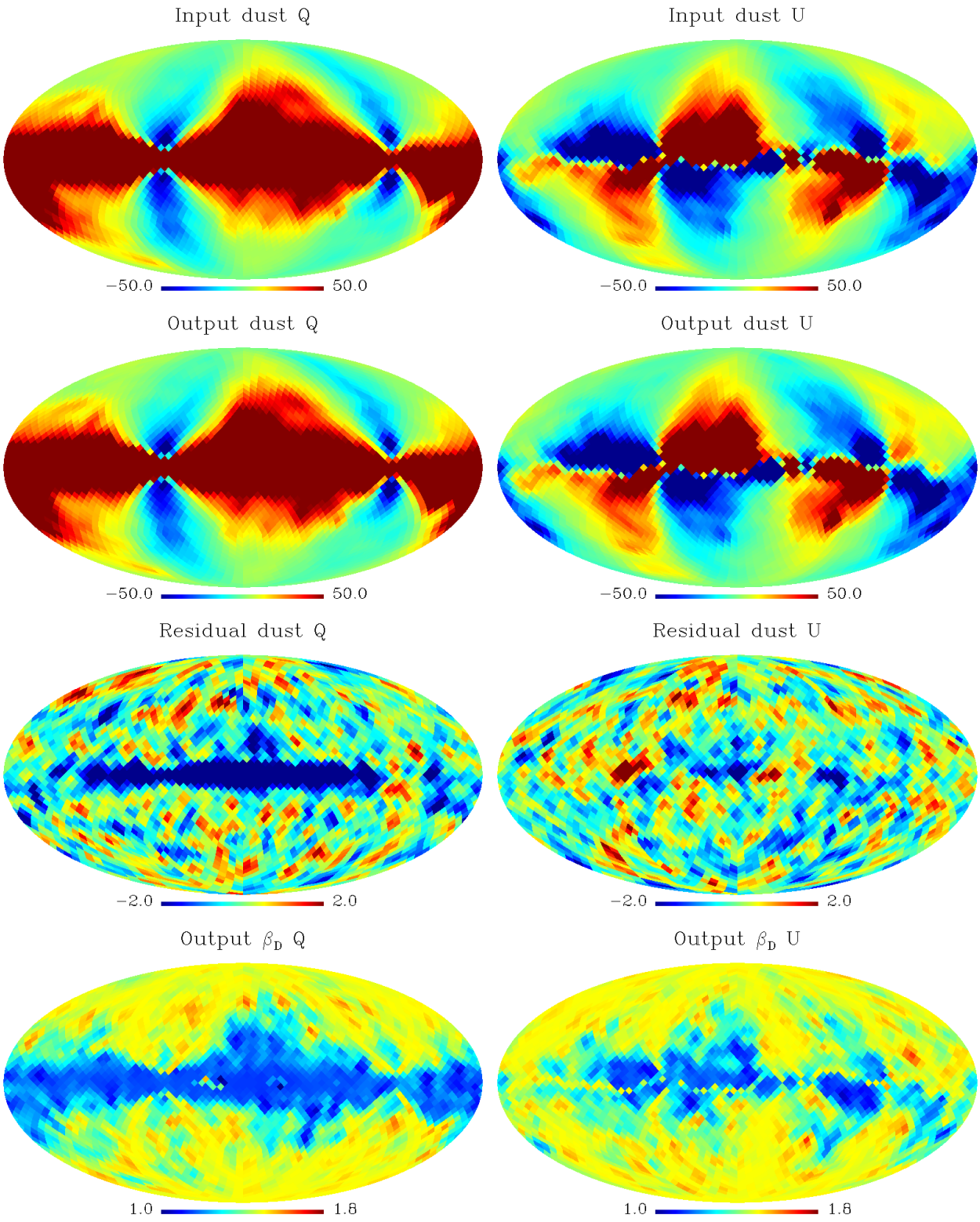

Figure 2.18: Recovered thermal dust foreground maps at $N_{side} = 16$. Top: Input amplitude at 353 GHz. Upper: Recovered amplitude at 353 GHz. Lower: Pixel residual distribution. Units are μK. Bottom: Recovered β_d. Away from the Galactic plane the spectral index is driven to the prior value.

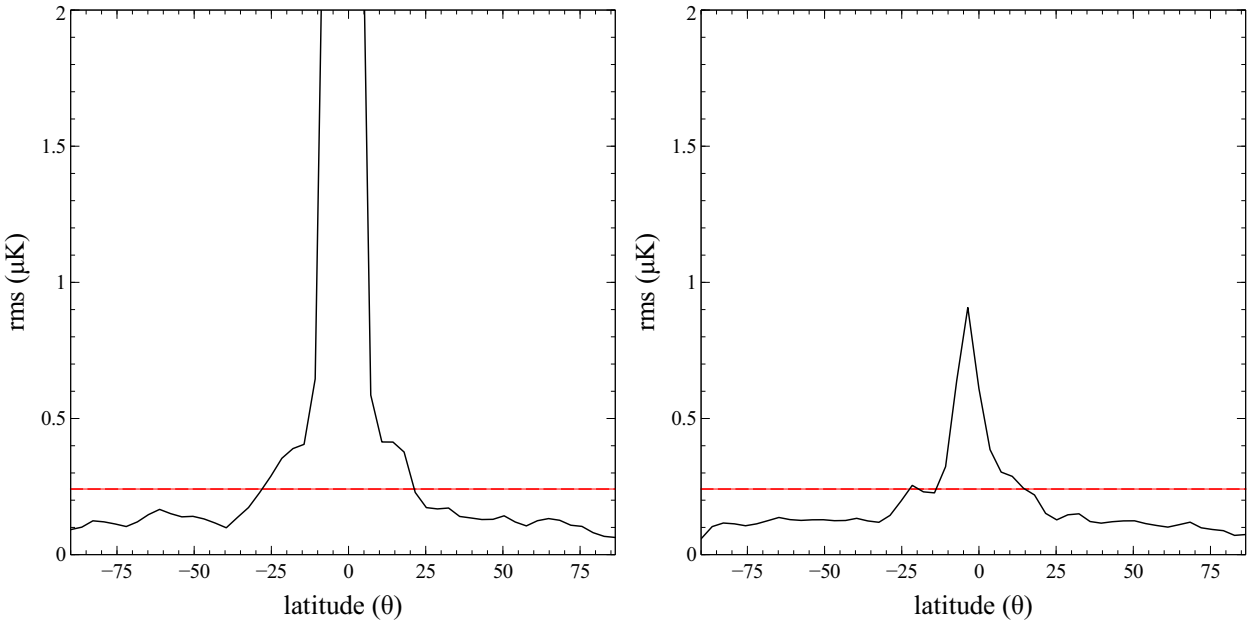

Figure 2.19: Pixel residuals for one simulation at $N_{side} = 16$ plotted against Galactic latitude. The dashed red line shows the equivalent noise level for all seven Planck channels at this resolution. Fewer pixels contribute to the bins at more extreme latitudes.

distribution while tracing the foreground brightness.

2.5.3 Likelihoods

The structure of the foreground is similar at each of these frequencies, and so for the calculation of the likelihood we use the 30 and 353 GHz maps to define a polarisation mask by simply applying a threshold to each of the Q and U maps. An internal mask is then defined as the union of the two Q and U masks at both frequencies. For the tests and maps described in this section we use a fairly conservative mask which removes about 37% of the sky. A masked simulation is shown in Figure 2.21.

The upper panels of the Figure show the noise-free CMB-only simulation for Q and U, with $r = 0.1$ outside the Galactic mask. The second panels show the foreground-subtracted noisy reconstruction following the above procedure. The correspondence between the two maps is evident. The third panels show the B-mode contribution to the input simulation Q and U maps, and the lowest panels show the foreground-separated noisy reconstruction of the B-mode contribution. Again there is reasonable correspondence, but noise is much more dominant than for the total Q and U recovery, and close to the Galactic plane the recovered B-mode signal is significantly noisy.

We generate simulations at three resolution parameters $N_{side} = 8, 16, 32$ and run our likelihood code to evaluate the stability of r-estimation over ten random simulations. We look at the spread in recovered maximum-likelihood estimates for the three resolutions both with and without including

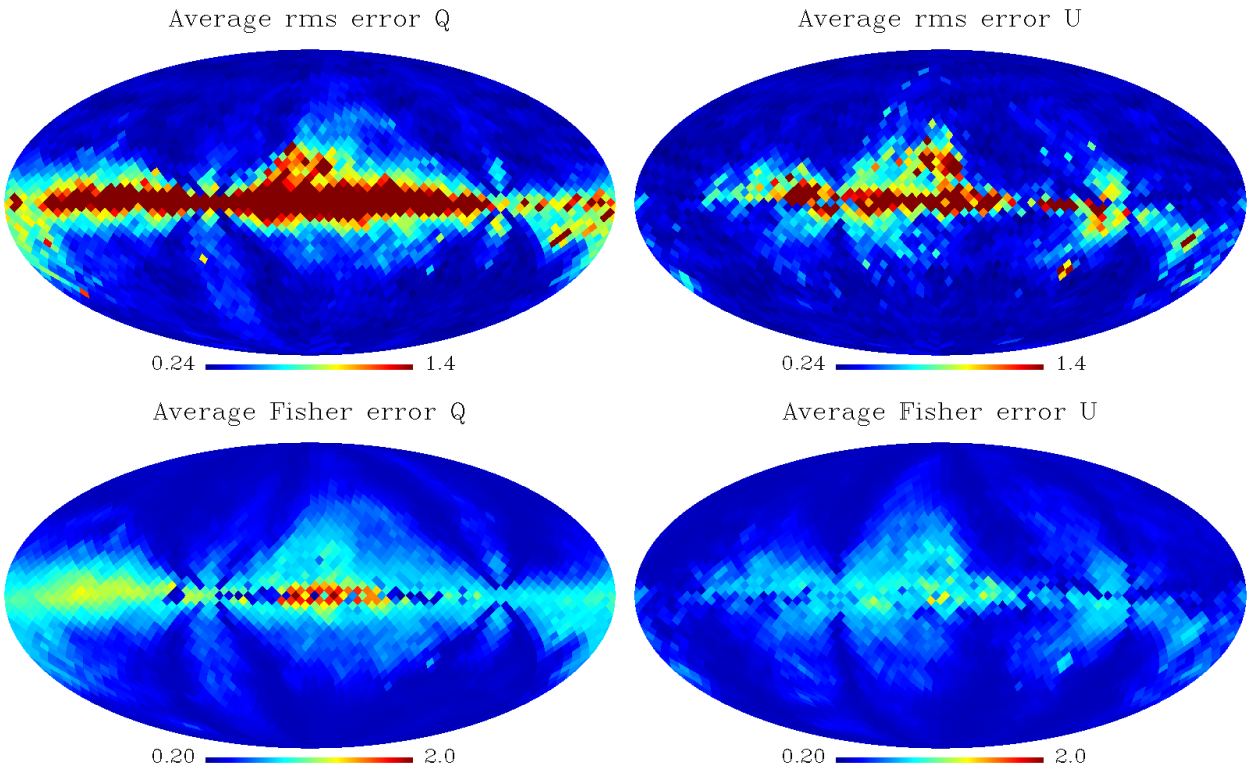

Figure 2.20: Q/U rms pixel residuals and CMB Fisher errors averaged over 100 simulations of CMB and noise at $N_{side} = 16$. The same foreground model is used in each run. Units are μK.

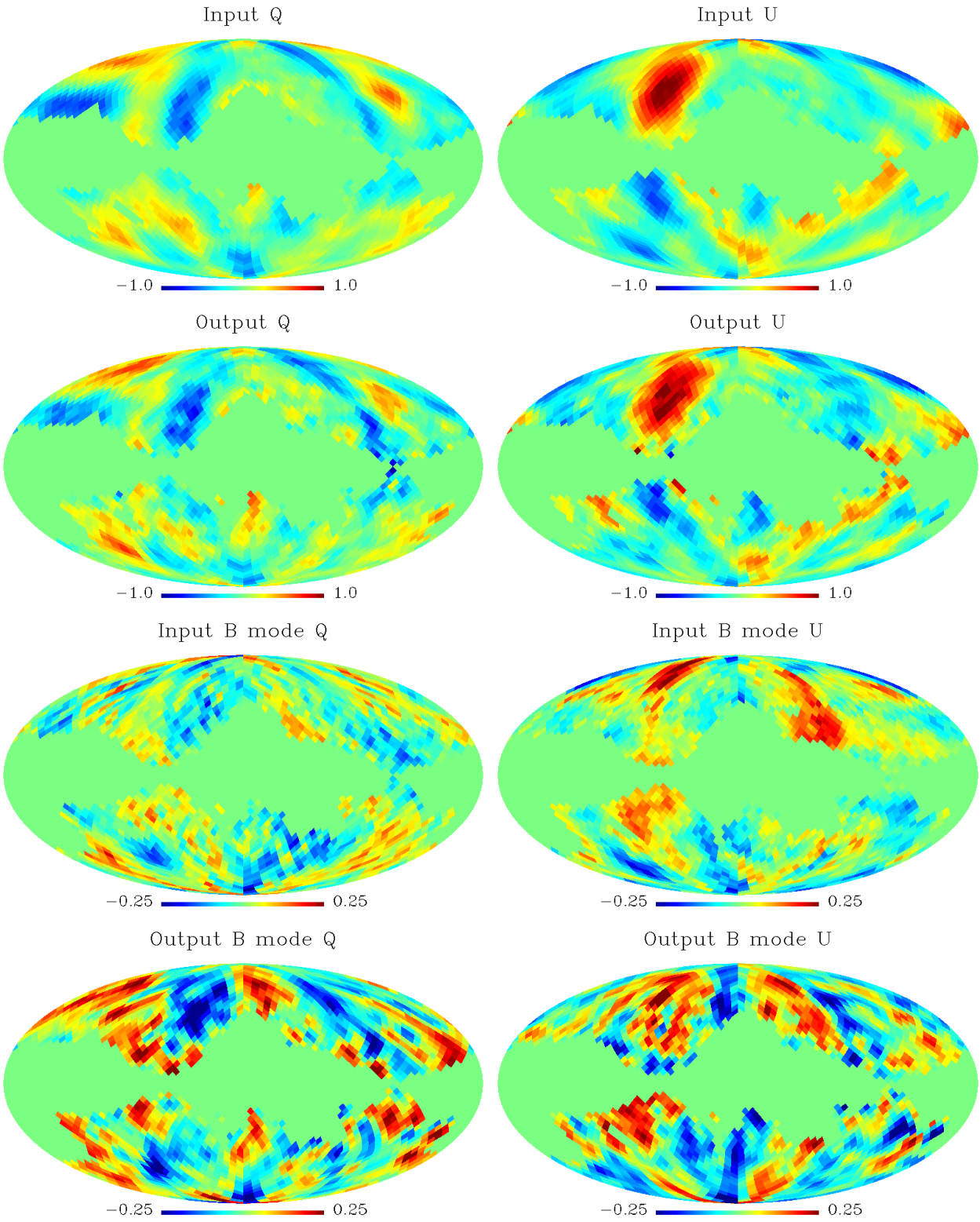

Figure 2.21: Q and U maps: Upper panels show the noise-free CMB simulations with $r = 0.1$ for regions outside the union mask. The second panels show the foreground subtracted noisy reconstructions computed as described in the text. The third panels show the B-mode contribution to the noise-free CMB maps. The lowest panels show the noisy foreground-subtracted reconstruction of the B-mode signal. Note the differing colour scale between the total and B-only maps. Units are μK.

Table 2.2: Averaged maximum-likelihood recovered r values and deviations over ten simulations at three resolutions. Upper results use maps separated using individual pixel priors, lower results use maps that incorporate a spatial correlation (denoted by c) of the foreground spectral indices. The stability of r over simulations is increased by utilising prior information about the spatial correlation of β_s, β_d.

N_{side}	$\bar{r}$	σ_r
8	0.116	0.018
16	0.10761	0.050
32	0.222	0.123
8(c)	0.122	0.019
16(c)	0.129	0.022
32(c)	0.103	0.030

correlated spectral indices. For the non-correlated case, the stability of solutions breaks down when run at the higher resolution $N_{side} = 32$. Some simulations for which most of the input B-mode signal is inside the internal mask, and for which the recovered B-mode signal is spuriously strong outside the mask (due to noise), generate a high estimation of r. When we include the correlated indices, the spread of recovered r-values remains reasonably stable across the resolution range, increasing slightly at each N_{side}. The recovered likelihoods are plotted in Figure 2.22 and the increase in stability can clearly be seen whereas with no correlation, the stability of the recovered $r = 0.1$ mode is lower.

Although we have not extended this calculation for higher resolutions beyond $N_{side} = 32$ (the numerical calculation becomes prohibitively expensive), it is clear that as resolution increases, the variance of the recovered r values will increase significantly due to the noise and propagation of foregrounds into cleaned CMB maps. Imposing the correlation helps to limit the effect of the noise propagation into the final maps. Table 2.2 shows the average maximum-likelihood estimation along with the spread for the ten simulations at each resolution. These results are complementary to those of Armitage-Caplan et.al [113] in that they show that the broadening of the posteriors in r at higher resolutions caused by foreground-subtraction errors can be mitigated by utilising a correlation length for the spectral indices. Our results are similarly limited by our simplified noise and data models, but the improved stability of the posteriors in r at higher resolution demonstrates that this approach is a useful extension.

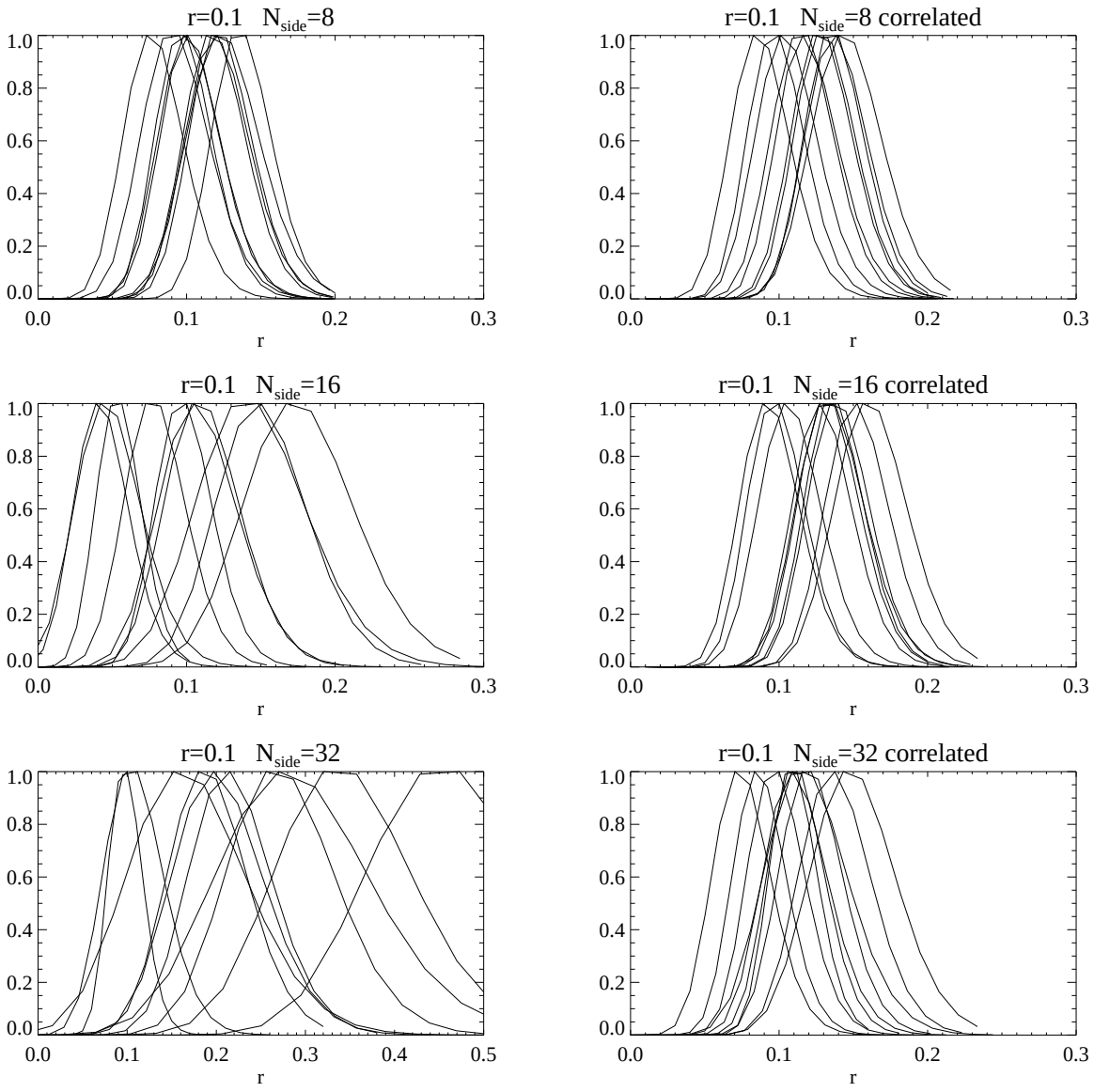

Figure 2.22: Posterior likelihood distributions for 10 $r = 0.1$ recovered foreground-separated CMB simulations. Left panels show the increasing spread in the maximum likelihood as N_{side} is increased. Right panels show the stabilisation produced by imposing a spatial correlation on β_s and β_d.

2.6 Conclusion

In this chapter we have explored various methods used to simulate the diffuse polarised foreground emission, and referenced these to the underlying emission theory. We then looked at the main methods used to separate such emission and recover the polarised CMB. We explained how a simple template-fitting routine could be extended to an ILC algorithm, and how this compares to a parametric fitting framework.

By generating full sky polarised simulations with Planck-level noise and repixellising to a lower resolution, we have tested a parametric fitting routine to recover a r=0.1 B-mode signal from the multifrequency sky maps. This work builds on that of Armitage et al. [113] by improving the foreground fitting and utilising a spatial correlation of the foreground spectral indices. This modification improves the reliability of recovery of the B-mode signal when taken to higher resolution, and this method is important for testing the Planck polarisation maps (See Chapter 4). An important assumption is that the foreground indices vary on a scale smaller than the amplitudes do, and from the recent body of evaluative work on diffuse emission, and the initial release Planck papers, this seems a reasonable assumption (in temperature at least). Given the foregrounds are not significantly more complicated than these models assume, parametric fitting will be one of the most useful separation routines at low resolution, particularly for studies hunting the low-ℓ B-mode bump. Armitage-Caplan et. al conclude that foreground subtraction errors cause a broadening in the posteriors in r, but this is not quite true if the spectral indices are strongly correlated (i.e. have a large coherence scale). Our procedure leads to stable results (weakly dependent on N_{side} in this case).

We have shown that:

- Synchrotron and dust templates can be used to generate full-sky noisy realisations of the Planck sky (Section 2.3).
- Parametric fitting is very effective at recovering a polarised CMB signal at low-ℓ provided foreground knowledge is sound (Section 2.4).
- With diagonal noise parametric fitting recovers an input CMB to a few percent, and reliably recovers an input B-mode (Section 2.4.3).
- Modifying the likelihood to incorporate spectral index priors increases the reliability of a recovered B-mode for higher resolution simulations (Section 2.5.3).

In Chapter 3 we check directly whether these simple models are indeed reflected in the Planck polarisation data. These methods will also be fruitful for studies of the diffuse emission itself, as well as noise propagation into the final cleaned maps. The frequency dependence of the polarised foregrounds is poorly constrained, and Planck's large frequency coverage will give us a long lever-arm for estimating foreground models. Should further satellite missions be launched to measure the

polarisation in more detail (e.g. COrE) [142], foreground characterisation will remain the ultimate limit with which a potential B-mode can be extracted.

Faber est suae quisque fortunae
- The Francians

Chapter 3

Comparing Planck Data to the Sky Model

An important consideration when analysing results based on simulations (as we have done in Chapter 2) is whether the simulations resemble what we see in real data. Whether the foregrounds can be appropriately characterised with enough complexity using the basic models described in Chapter 2 is a useful test to perform. If the foregrounds exhibit a more complex emission spectrum than is assumed in the Planck Sky Model (PSM), or a more subtle scaling with Galactic latitude, then more sophisticated methods will be needed to separate the polarised CMB to a precision high enough to detect an inflationary B-mode, even at the $r = 0.1$ level [143]. If however the real data can be fit with a simplistic model such as in the PSM, then such separation schemes will work well and instrumental noise will become the limiting factor in B-mode estimation. Since foregrounds represent the ultimate uncertainty (at least for low-resolution studies) on the polarised CMB, it is instructive to parameterise the discrepancy between the assumed emission in the PSM and the full-sky nominal mission Planck data. The actual level of polarisation in the PSM is an issue of uncertainty, and correlation with the real data will aid in understanding whether the assumptions are correct. In this section we first look at a comparison of the polarisation fraction across the frequency bands, and relate this to the underlying foreground distribution. We can then compare this to the input level of the PSM models. We then look at a comparison of high-resolution power spectra with the fiducial model for a variety of Galactic maskings, and analyse the effect that the Galactic plane has on the behaviour of the spectra.

We look at the synchrotron emission at the lowest Planck frequencies, and quantify the level of polarisation both globally and as a function of Galactic latitude, and examine whether the morphology in the PSM-assumed polarisation is reproduced using low-resolution maps. We then use combinations of maps to estimate the synchrotron spectral index both in temperature and for polarisation, and compare the global distribution of β_s to the templates used in the PSM. One feature of the PSM is that some models use the same β_s maps for temperature and polarisation.

We can test this assumption using the Planck data, and check whether this holds both in the Galactic plane and at high latitudes. Given Planck's large frequency coverage, we can examine the spectral index shift from synchrotron to dust as we increase in frequency, and also form multiple maps of the indices using alternate combinations of datasets. We first briefly review the simulation in the PSM and detail the Planck data maps used in the analyses.

3.1 Introduction/PSM Overview

The foreground model for synchrotron used in Chapter 2 of this thesis is based on the WMAP 23 GHz data, scaled to the Planck observing frequencies using a spectral index template given in Equation 2.12. There are multiple methods used to calculate the spectral index map, using complementary synchrotron data between 408 MHz and 23 GHz. The first spectral index map is formed from multiple observations at 408 MHz, 1420 MHz and 2326 MHz, and by padding the unobserved area around the south pole with the mean spectral index, at a resolution (FWHM) of 10°. The index varies from -2.5 in the Galactic plane, to isolated regions with a steeper spectrum of -3.2 out of the plane in the Galactic spur, and at about $(\theta, \phi) = (90, 20)$ from the Galactic centre. The second model is calculated in a similar manner, but instead uses a direct scaling between 408 MHz and 23 GHz, and estimates for the reduction factor and the fractional polarisation. The level of polarisation is highly dependent on modelling considerations, particularly on whether an anomalous dust component is included [144]. For the favoured model including an anomalous unpolarised dust component, an average level of polarisation $f_{pol} \approx 0.3$ is found, with a maximum around the Galactic spur region of $f_{pol} \approx 0.45$. This estimate would be modified if the anomalous component has a non-negligible polarisation fraction. Knowing the electron energy distribution, one can calculate the theoretical polarisation fraction as described in Chapter 2. This calculation however is only correct for a uniform magnetic field, and does not take into account depolarisation, which is particularly important at low Galactic latitudes [145]. The polarisation fraction f_s is estimated as $(3|\beta_s| - 3)/3(|\beta_s| - 1)$ so that regions with a steeper index give rise to higher levels of polarisation. The resulting f_{pol} map varies between 69% and 77%, with mean 72%. The map is normalised to give a mean fractional polarisation of 30%, and a span from 5-70%.

The dust polarisation model scales a 100 μm full-sky intensity map in frequency, modulated for Q and U by a logarithmic spiral-arm model for the polarisation angle, and a global polarisation fraction of 5%. The dust model is scaled to the Planck frequencies by a calculation of the emission based on a two-temperature component black-body model, and has an effective global spectral index of $\beta_d = 1.5$ (again see Chapter 2 for full details). Given that the dust model in polarisation is based only on temperature data, and the synchrotron data is modelled directly from the WMAP polarisation data, one would expect the real data at highest frequencies (i.e. primarily sensitive to dust) to be less correlated with the simulations than for the synchrotron data, and expect the spectral index to reflect more structure than is assumed by a global value. We now look at the level

of polarisation present in the lowest and highest frequency maps and compare this to the input percentage level in the PSM, both in temperature and polarisation.

3.2 Level of Polarisation

The Planck data which we use for comparison in this section are the dx8 exchange full-sky maps released in mid-2012, including the bandbass-correction for the 30, 44, and 70 GHz channels (see Chapter 4 for details on application of the bandpass correction and its effect on the polarisation data). The maps are formed from five complete sky surveys over 30 months of data collection, and are similar to the publically released data in temperature. We calculate the fractional polarisation of the sky maps at each frequency as

$$f_\nu = \frac{(Q_\nu^2 + U_\nu^2)^{0.5}}{I_\nu}, \tag{3.1}$$

and can also calculate a relative amplitude factor for Q and U as

$$A_{rel} = \frac{A_{PSM}}{A_{dx8}} \tag{3.2}$$

at each frequency. Simulations for synchrotron and dust polarised emission can be modified by the inclusion of a geometric depolarisation factor. Geometric depolarisation arises due to variation along the line-of-sight of the angle between the magnetic field orientation and the line-of-sight direction. The magnetic field orientation depends on the spiral structure of the large-scale Galactic magnetic field, and on turbulent behaviour of the magnetic field on a local scale. The depolarisation effect is implemented as a simple multiplicative mask in the simulations described in this work, and reduces the polarisation percentage by between 10 and 50%, with a different morphology for synchrotron and dust (see Chapter 2 for more details on the modelling). Of course the CMB istelf acts as a contaminant for foreground analyses, but is small on large scales at all frequencies; the 30 and 353 GHz channels are dominated by dust and sunchrotron emission and although the contribution increases at intermediate frequencies, the data are still foreground-dominated.

3.2.1 Synchrotron

The lowest LFI channels are most sensitive to synchrotron emission which dominates at all LFI channels. We analyse the 30 and 44 GHz channels as indicators of polarised synchrotron behaviour and compare the polarised fractions to the simulations. Figure 3.1 shows the polarisation fraction for the two lowest channels at a resolution of $N_{side} = 16$.

At higher resolutions, the signal-to-noise ratio drops sharply, and the off-plane f_ν calculated rises

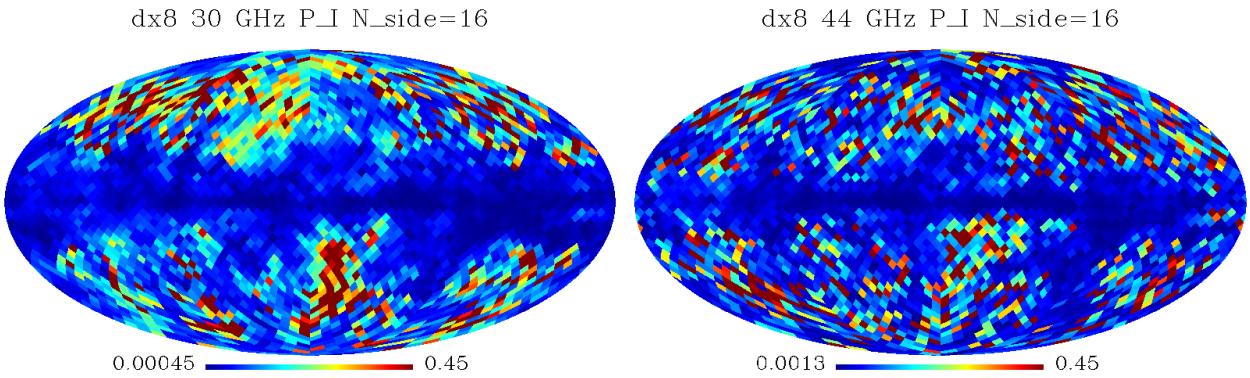

Figure 3.1: Fractional polarisation for LFI 30 (left) and 44 GHz (right) at a resolution of $N_{side} = 16$ (pixel rebinned), using bandpass-corrected dx8 maps. Highest signal-to-noise regions are found in the Galactic plane, with a typical polarisation of $5 - 10\%$. Regions away from the Galactic plane exhibit some residual noise contamination, an artefact which becomes more pronounced at higher resolutions.

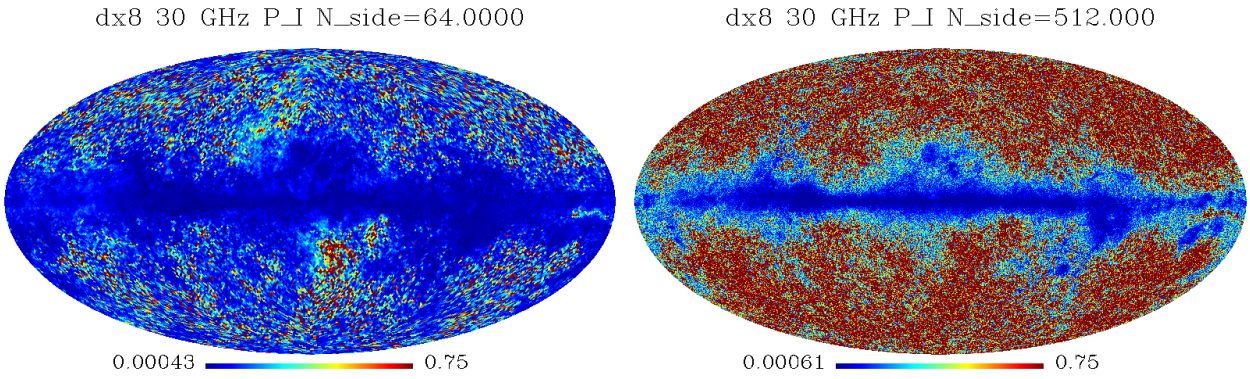

Figure 3.2: Fractional polarisation for LFI 30 GHz at a resolution of $N_{side} = 64$ (left) and $N_{side} = 512$ (right), using bandpass-corrected dx8 maps. The signal-to-noise ratio drops sharply at higher resolutions away from the Galactic plane. Even at lower resolutions regions away from the Galactic plane exhibit some residual noise contamination, but the effect is lessened.

sharply and saturates the sky maps, leaving only a thin central Galactic slice where meaningful information may be extracted. This is shown in Figure 3.2 where at the higher $N_{side} = 512$ resolution, f_{30} saturates the colour scale at the maximum value of 0.75.

As we lower the resolution, we increase the signal-to-noise ratio but also lose information on smaller angular scales. At a resolution of $N_{side} = 16$ a small fraction of the pixels off-plane are noisy, and we retain detail on angular scales of a few degrees. Figure 3.3 shows the polarised fraction at 30 GHz plotted with Galactic latitude.

The synchrotron emission at 30 GHz in the Galactic plane is polarised at 10-12%, where the depolarisation effect is strongest. Away from the plane this rises to 15%-20%, with a maximum polarisation of 35% in an isolated region at Galactic coordinates $(5°, -45°)$. For the whole sky,

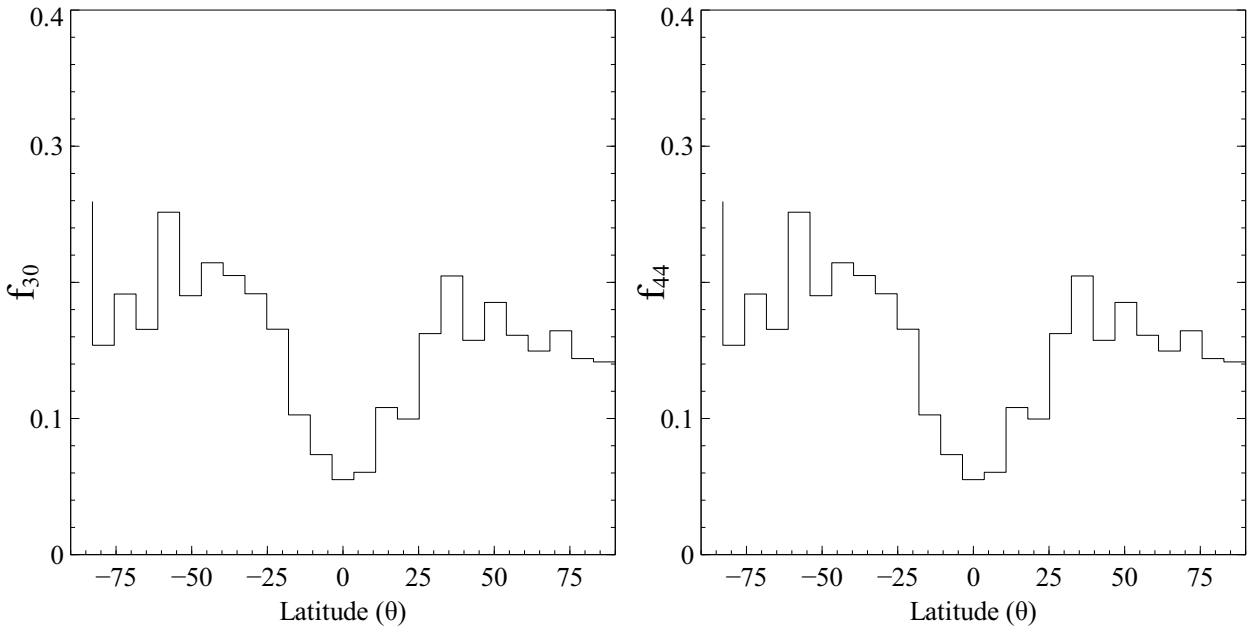

Figure 3.3: Fractional polarisation for LFI 30 (left) and 44 GHz (right) against Galactic latitude for the maps shown in Figure 3.1 The depolarisation effect is strongest in the Galactic plane, where the lowest levels of polarisation are found. The bin size is 8°. Due to the pixellisation of the maps, more pixels contribute to lower Galactic latitude bins than higher latitude bins.

the mean polarisation is 14.7% with a variance of 4.1%. At 44 GHz, visually the overall level of polarisation drops slightly but appears noisier, consistent with a lessening polarised synchrotron component at higher frequencies. The central polarisation drops to 7-9%, and the typical off-plane level remains about 15-20%. The polarisation in the isolated region at Galactic coordinates $(5°, -45°)$ also falls to about 25%. For the full sky at 30 GHz, the mean polarisation is 15.1% with a variance of 5.1%.

Figure 3.4 shows the polarised fraction for the simulated synchrotron emission with and without the geometric depolarisation factor. The uncorrected map shows a large excess of polarised emission across a large part of the sky, and the isolated region at $(5°, -45°)$ is reproduced, but the polarisation fraction is overestimated by a factor of 2.5. Also shown is the residual error in the estimated synchrotron polarisation fraction calculated as $P_I^{PSM} - P_I^{dx8}$, which gives a handle on by how much the PSM is under/overestimating the polarisation level. Without depolarisation, the simulation overestimates the Galactic plane $(-10°, +10°)$ by on average 11.7%, and off-plane by 8.4% (absolute values). The southern Galactic hemisphere is overestimated by 11.1% and the northern Galactic hemisphere by 5.6%. Globally the average error is 9.3% (mean) and 24.6% (rms). Including the depolarisation greatly improves the correlation between the PSM and the real data. The rms average error on the Galactic plane is now 0.5%, and the average off-plane error is now 5.0%, with the southern and northern Galactic hemispheres incorrect by 2.2% and 7.8% (rms) respectively. There is also more small-scale structure in P_I apparent in the dx8 maps across the whole sky compared to the simulations. This is particularly apparent when comparing the Galactic plane

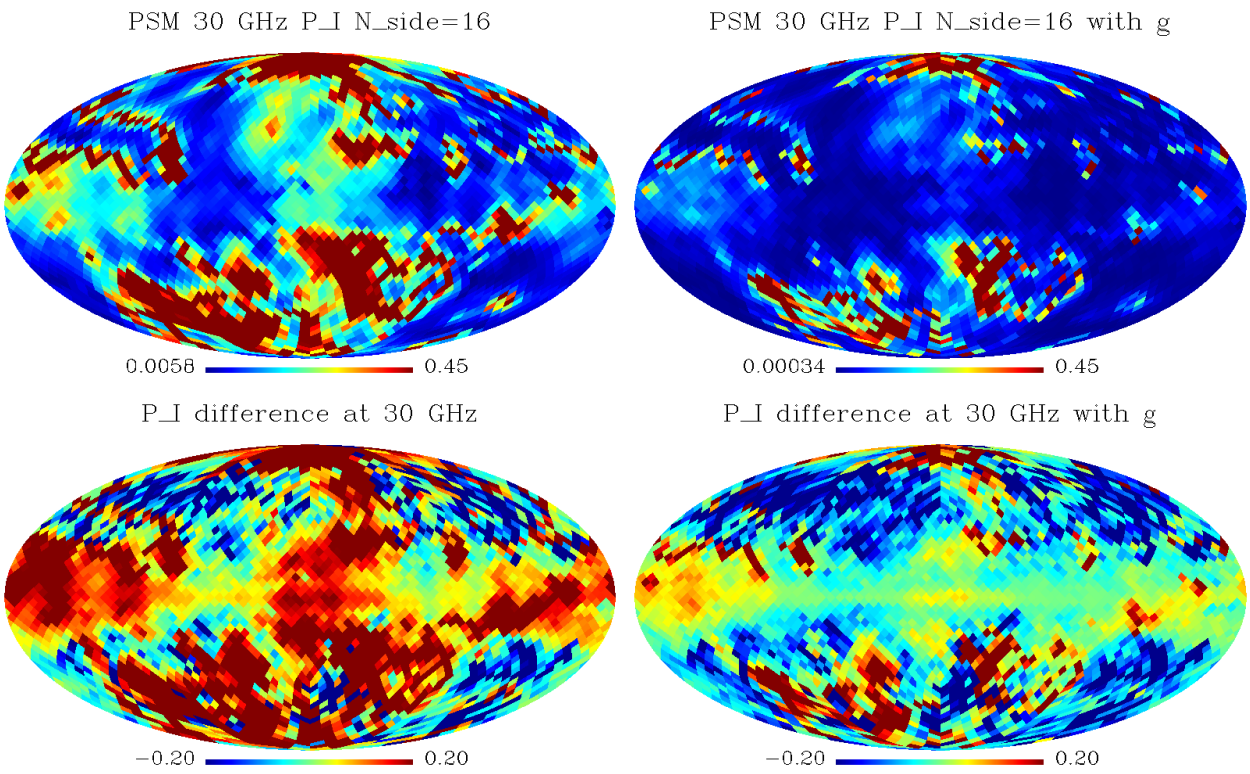

Figure 3.4: Fractional polarisation for the 30 GHz simulation in the PSM without (upper left) and with (upper right) the geometric depolarisation factor, which reduces the WMAP-assumed polarisation fraction by about 20% (absolute) across the off-plane sky, and by about 30% (absolute) in the Galactic plane. Also shown is the difference in polarisation fraction $P_I^{dx8} - P_I^{PSM}$ between the real data and the PSM without (lower left) and with (lower right) the geometric depolarisation factor. The polarisation level observed in the dx8 maps is much more consistent with the depolarised maps across the full sky, and particularly across the Galactic plane.

regions, where the dx8 signal-to-noise ratio is the highest. This discrepency is partly due to the way that the synchrotron is modelled in the simulations using the WMAP 23 GHz data, but could hint at more structure in the spectral index than is assumed in the simple PSM models.

3.2.2 Dust

The four highest Planck frequency channels 217, 353, 545, and 857 GHz are sensitive to thermal dust emission, which increases in intensity at higher frequencies. From these, only the 217 and 353 GHz channels are polarisation-sensitive, hence we can use these as a tracer of the polarised dust emission and examine the polarisation level present in the data. At the time of writing, there were no bandpass correction maps available for HFI channels, so we use the uncorrected dx8 maps and degrade in resolution to $N_{side} = 16$. An assumption in the simulation is that the synchrotron and thermal dust polarised emission are influenced by the same Galactic magnetic field and that their geometric depolarisation maps should be correlated. In the simulations g_s and g_d are based on

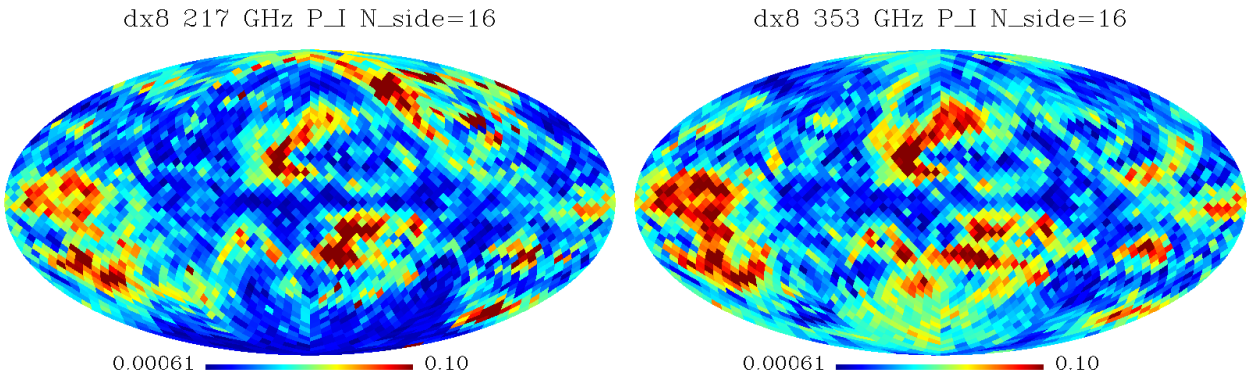

Figure 3.5: Fractional polarisation for HFI 217 (left) and 353 GHz (right) at a resolution of $N_{side} = 16$ (pixel rebinned), using uncorrected dx8 maps. Highest signal-to-noise regions are found in the Galactic plane, with a typical polarisation of $5 - 10\%$. Regions away from the Galactic plane exhibit some residual noise contamination, an artifact which becomes more pronounced at higher resolutions.

equivalent maps estimated for the synchrotron emission using the WMAP 23 GHz and the Haslam 408 MHz data. See Chapter 2 for more information on the difference between g_s and g_d.

Few observational datasets are currently available to accurately model polarised thermal dust emission. Available dust polarisation measurements have concentrated on specific regions of the sky, with the exception of the Archeops balloon-borne experiment (Benoit et al., 2004), which has mapped the emission at 353 GHz over about 17% of the sky, measuring a polarisation fraction around 4 - 5% in the Galactic plane, and up to 10 - 20% in some clouds. Recently, polarisation of dust emission at 100 and 150 GHz has been observed by BICEP over a smaller region of the Galactic plane (Matsumura et al., 2010) and by QUaD (Culverhouse et al., 2010). We can perform some simple tests to check whether the dx8 maps are in agreement with these surveys.

Figure 3.5 shows the polarisation fraction for the two highest polarised channels at 217 and 353 GHz at $N_{side} = 16$. The polarisation fraction is typically higher in the 353 GHz map, both across the sky, and in the isolated regions, or 'clouds' of higher polarisation.

The structure is morphologically very different to the synchrotron polarisation maps. The synchrotron maps exhibit a consistent level of polarisation across the Galactic plane, where the signal-to-noise ratio is highest. Away from the plane, f_{30} and f_{44} increase slightly and peak at at about $\pm 40°$ before dropping away slightly at higher Galactic latitudes. The dust polarisation is instead grouped into distinct 'clouds' of higher polarisation up to 10-15%, with a visible background polarisation of about 2-3%. Figure 3.6 shows the behaviour with Galactic latitude, and shows the distinctly different behaviour to the synchrotron emission in Figure 3.3.

At 217 GHz, the mean polarisation percentage along the Galactic plane is 3.5%, where again the signal-to-noise ratio is highest. Away from the more highly-polarised clouds seen in Figure 3.5 this level remains consistent across most of the sky, with a large patch in the southern Galactic

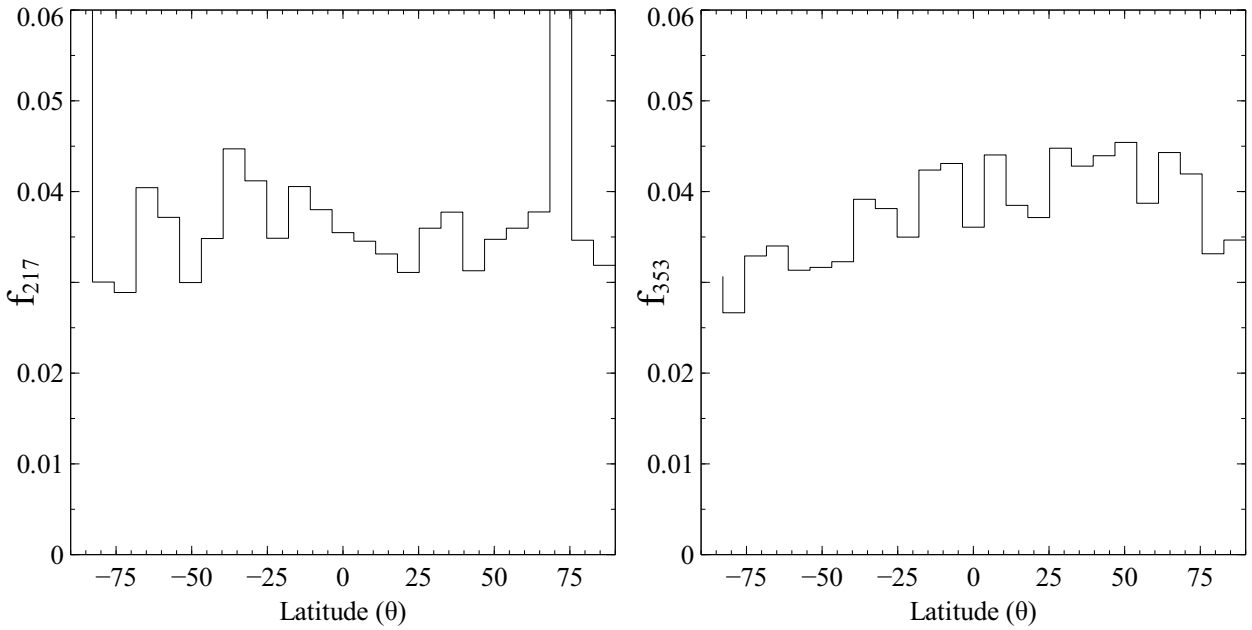

Figure 3.6: Fractional dust polarisation for HFI 217 (left) and 353 GHz (right) against Galactic latitude for the maps shown in Figure 3.5. The bin size is 8°. Due to the pixellisation of the maps, more pixels contribute to lower Galactic latitude bins than higher latitude bins.

hemisphere centred on $l, b = (267, -60)$ exhibiting sub-percentage level polarisation. At 353 GHz where the dust emission is more intense, the typical Galactic polarisation rises slightly to 3.9%, and is less consistent away from the clouds across the sky, with the background level rising to 3.8%, and the region in the southern Galactic hemisphere rising from sub-percentage level to 2.0%. Table 3.1 shows the polarisation percentage levels for 7 high-polarisation clouds identified in the maps. The regions of strong emission were selected from the Healpix maps and the mean and standard error were calculated for both 217 and 353 GHz maps, along with the centres of the clouds in Galactic coordinates. The Healpix routine query_polygon was used to sample the pixels associated with each region of high emission. Much higher levels of polarisation are present in many of the cloud regions, with the strongest regions of emission (Cloud 1 and 7) polarised at about 13%. The average polarisation across all 7 of the selected clouds is 9.9%. For the whole sky at 217 GHz the mean level of polarisation is 3.6% with a variance of 0.01% and at 353 GHz, the mean level is 3.9% with a variance of 0.05%.

The dust simulation in the PSM relies on an estimated magnetic field orientation and polarisation angles to calculate Q and U maps, hence we should expect the Q and U dust simulations to bear less similarity to the real data than the synchrotron simulations (the synchrotron maps are based on real WMAP data at 23 GHz). The dust polarisation fraction used is based on previous measurements of small regions of the sky, so we could expect this quantity to be comparable. Figure 3.7 shows the PSM simulation at 353 GHz with and without the geometric depolarisation factor as described earlier in the text, and difference maps showing $P_I^{PSM} - P_I^{dx8}$.

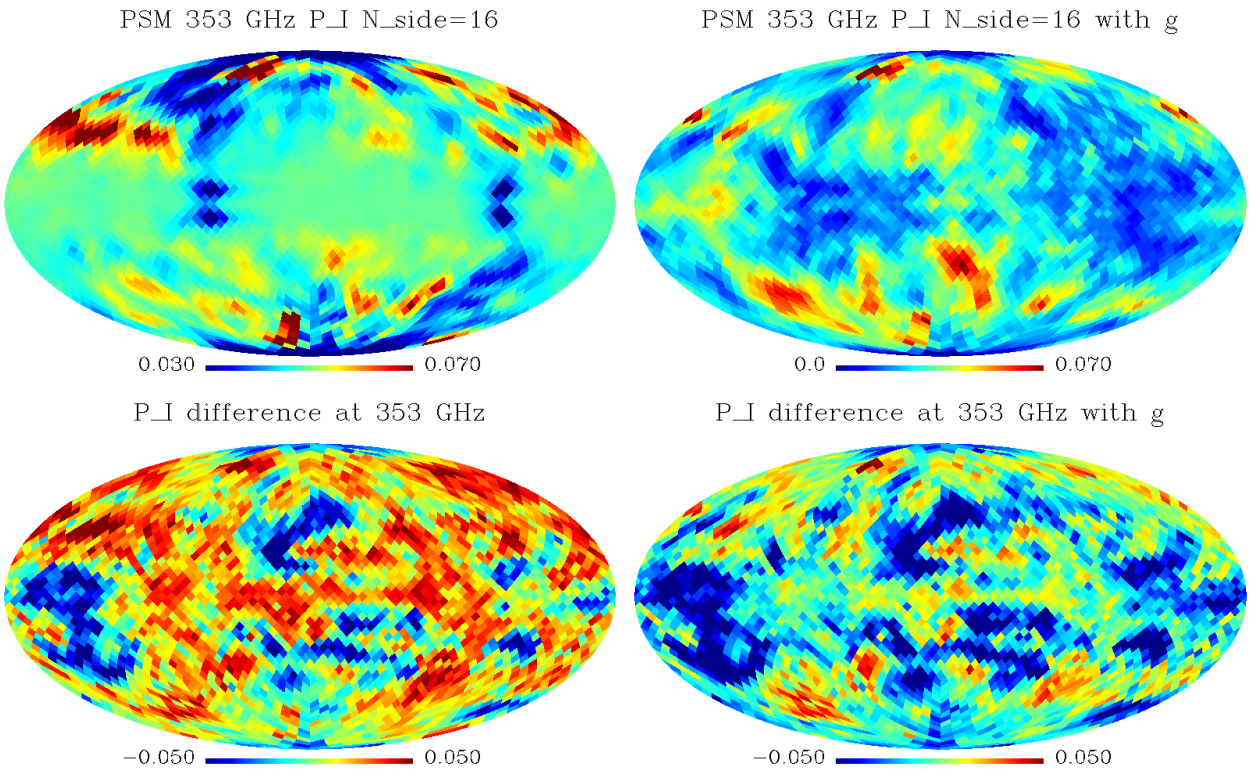

Figure 3.7: Fractional polarisation for the 353 GHz simulation in the PSM without (upper left) and with (upper right) the geometric depolarisation factor, which reduces the polarisation fraction by about 60% across the off-plane sky, and by about 80% in the Galactic plane. Note the different colour scale used to emphasize detail in the depolarised map. Also shown is the difference in polarisation fraction $P_I^{PSM} - P_I^{dx8}$ between the real data and the PSM without (lower left) and with (lower right) the geometric depolarisation factor.

Cloud index	l	b	N_{pix}	$p^{217}(\%)$	$p^{353}(\%)$
1	292	58	23	13.0 ± 2.2	
2	20	21	26	8.5 ± 0.3	9.8 ± 0.4
3	146	3	55	7.5 ± 0.2	9.0 ± 0.2
4	337	-16	30	11.2 ± 0.6	8.5 ± 0.4
5	142	-32	40	8.4 ± 0.4	8.4 ± 0.3
6	225	-27	10	7.8 ± 0.9	6.9 ± 0.6
7	207	-56	22	12.8 ± 3.4	5.8 ± 0.5

Table 3.1: Galactic coordinates and average polarisation percentages of the clouds in the 217 and 353 GHz dust maps quoted with standard errors. Also given are the number of pixels that the Healpix polygon for the cloud encompasses at a resolution of $N_{side} = 16$. Note that the cloud with index 1 only appears in the 217 GHz data. Typical background polarisation is 2-3% at 217 GHz, and 3-4% at 353 GHz.

Unlike for the synchrotron case where the most accurate simulation was along the Galactic plane, the typical error for dust (PSM-dx8) is consistent across the sky for both uncorrected and depolarised cases. Isolated regions are overestimated by up to 7%, and underestimated by up to 6%. The region of strongest dust emission towards the Galactic centre is reflected more accurately with the depolarisation mask included, as the absolute polarisation level has dropped, with errors typically less than 0.5%. The overall level of polarisation in the simulation without depolarisation is about 1% higher than observed in the real data. The raw mean error is -1.1%, with an rms error of 2.6%. Including the depolarisation factor not only drops the polarisation fraction but also changes the morphology of the P_I map, with the largest depolarisation along the Galactic plane. The raw mean error now drops to 0.9% with an rms error of 2.6%. This effect is illustrated in Figure 3.8.

The off-plane difference in dust drops for the depolarised map, but the Galactic plane region on average is now underestimated in the simulations. We note that this effect is numerically magnified by the particularly underestimated region at Galactic coordinates (130,-5), as visually the plane appears more accurately estimated in Figure 3.7.

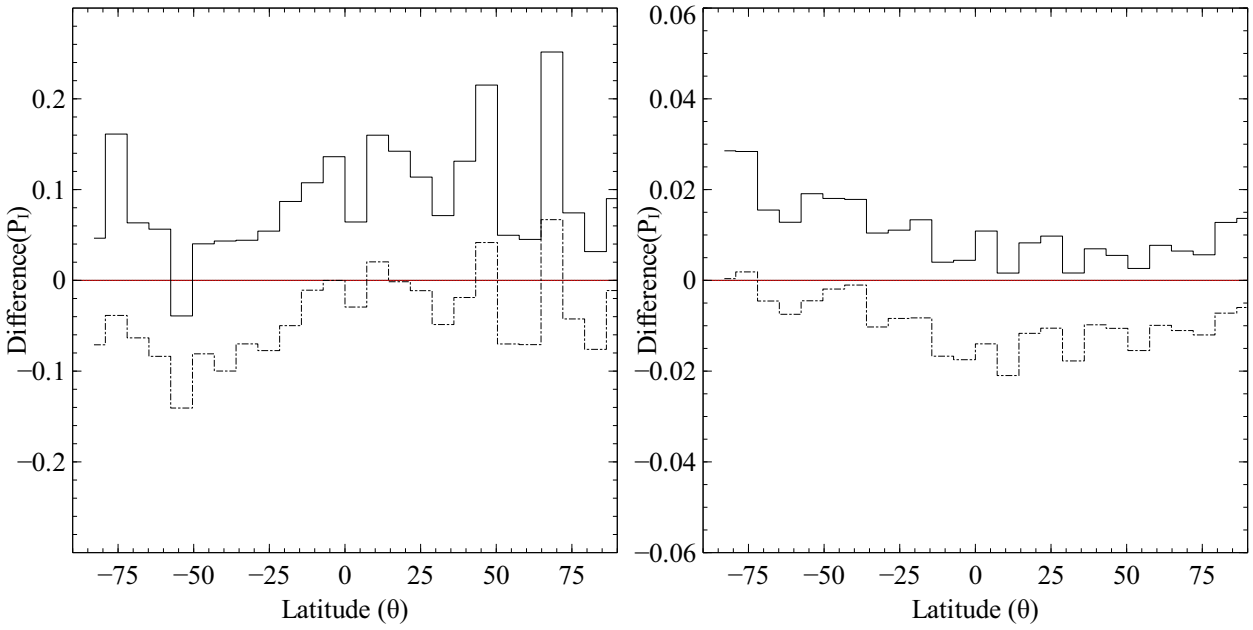

Figure 3.8: The difference in fractional polarisation between the dx8 maps and simulations with and without the depolarisation mask. The left pane shows the difference with latitude for the 30 GHz map and the right pane shows the difference for the 353 GHz map. In both plots the solid line shows the difference using the uncorrected simulation maps, and the dashed line shows the difference with the depolarisation factor applied to the simulations. The red dashed line shows a zero difference. For synchrotron, the depolarisation improves the match, whereas for dust the overall difference is negligible.

3.3 Amplitude and Polarisation angle

While the polarisation percentage is a useful handle on the physics of the Galactic emission, it is also useful to check the absolute calibration of the PSM simulations for Q and U both in the Galactic plane and at higher latitudes. Given that the synchrotron model is based on WMAP observations of emission at 23 GHz, a useful check of consistency is to analyse the difference in the calibration along the plane and in regions of lower emission. The synchrotron emission is weaker at LFI frequencies than at 23GHz (WMAP K-band), therefore it is unwise to assume that the scaling in frequency will be identical across the entire sky. Similarly for dust emission, the highest polarised HFI channels may not agree with simulations based on temperature data alone, and may not scale in the same manner as has been assumed in the PSM. In this section we look at the Q and U maps and check the calibration against the simulations.

3.3.1 Synchrotron

The 30 GHz channel is primarily synchrotron emission, so we first compare the raw bandpass-corrected dx8 maps with the simulations. The maps are degraded to $N_{side} = 16$ via a HEALPix rebinning with no smoothing applied. We compare this with the input synchrotron simulation with no CMB or noise added. Figure 3.9 shows the dx8 30 GHz Q and U maps, the input synchrotron simulation at 30 GHz (without geometric depolarisation), the residual, and the fractional residual (as a fraction of the input PSM).

The global morphology is reproduced well for Q and U, as expected since the simulations are based on WMAP polarisation measurements. The strong emission along the Galactic plane is traced well, with fractional differences typically 10-15%, however the off-plane emission is somewhat over-estimated (visible in the frational difference plot), with some regions overestimated by as much as 300%. These regions are small however, and could suggest that either high-intensity synchrotron emitting regions increase in polarisation intensity at frequencies higher than the WMAP template, or the signal-to-noise ratio is too low off the plane to give reliable results for polarisation. These regions persist at 44 GHz which implies that they are genuine features of the synchrotron polarisation map.

Imposing a cap on the fractional difference at 10 to limit the effect of spuriously noisy pixels in the dx8 maps, the mean pixel residual is 1.15 and 1.01 μK for Q and U respectively, and for the fractional difference the mean is 0.51 and 0.32. Regions of low emission are modelled most inaccurately, and subsequently push the mean residual up. A best-fitting global multiplicative factor for Q and U is found by simply minimising $\overline{(f * PSM - dx8)}$. The minimum is found for $f_Q = 0.93$ and $f_U = 0.99$ One feature of note in the residual maps is the appearance of the 'scanning systematic' that has also been observed in foreground-cleaned maps (See Chapter 3), with the Planck orbital poles centred on (100,30) and (280,-30). These are the most frequently-sampled

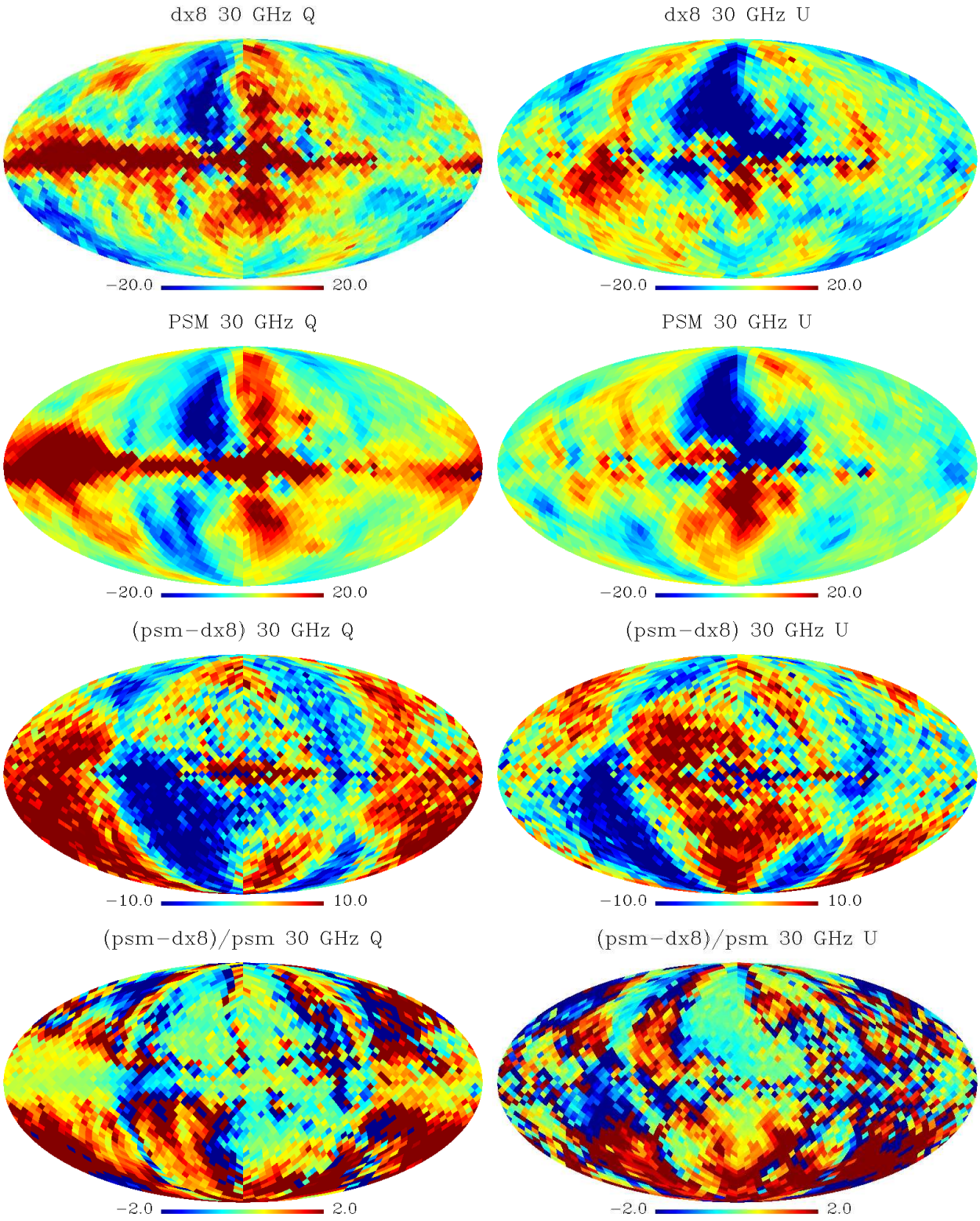

Figure 3.9: Bandpass corrected pixel-rebinned dx8 30 GHz Q and U maps (top) at $N_{side} = 16$, input synchrotron Q/U simulations without geometric depolarisation factor (second from top), residual Q and U maps formed as the difference between the data and simulations (second from bottom), and the fractional residual (as a fraction of the input PSM simulation (PSM-dx8)/PSM.

regions of the sky. A systematic structure is visible in both Q and U maps, and is morphologically similar to the foreground-cleaned dx8 polarisation maps. As mentioned before, this systematic has yet to be fully understood and characterised, but should be modelled for precise polarisation analyses. Bandpass correction maps and analog-to-digital (ADC) nonlinearity models for the HFI may to some degree address these problems, but corrections were not available during the period of this work.

3.3.2 Dust

The 353 GHz channel is primarily sensitive to thermal dust emission, so we now compare the raw dx8 maps with the simulations. The maps are degraded to $N_{side} = 16$ via a Healpix rebinning with no smoothing applied. We compare this with the input thermal dust simulation with no CMB or noise added. Figure 3.10 shows the dx8 353 GHz Q and U maps, the input thermal dust simulation at 353 GHz (without geometric depolarisation), the residual, and the fractional residual (as a fraction of the input PSM simulation).

Some noise is evident in the dx8 maps, but the global morphology is largely reproduced in the simulations. The most accurate regions are found along the Galactic plane with some off-plane regions incorrectly modelled by a factor of 3-4. Note the lack of the systematic 'scanning' artifact in the residuals, either masked by the high discrepancy or not present at 353 GHz. The correlation between the basic simulations and the data is now much lower, particularly for the U map, which seems even to anticorrelate in places. Limiting the differences to 20 μK to mitigate the effect of spuriously noisy pixels particularly along the plane, the mean fractional difference is 0.21 and 1.01 for Q and U respectively. For the raw residual map, the mean is -5.90 μK and 5.05 μK for Q and U respectively. The mismatch between simulation and data is severe, particularly in U along the Galactic plane where the emission is strongest. For Q the reverse is true, with regions of highest correlation found along the plane. The northern Galactic 'spur' region is also poorly modelled, with a large residual value, up to 200 μK in places. A best-fitting global multiplicative factor for Q and U is found by simply minimising $\overline{(f * psm - dx8)}$. The minimum is found for $f_Q = 0.72$ and $f_U = 0.90$, indicating a significantly poorer fit than for synchrotron, as expected. More complicated models of the magnetic field involving modifications to the 23 GHz polarisation angle now exist in the PSM which may address some of these dust mismatch issues. Of note is the reduced level of visible systematics in the 353 GHz residuals compared to 30 GHz residuals (seen in the plot in Figure 3.9). Either the systematics observed at 30 GHz are below the level of the residuals at 353 GHz (indicating the 353 GHz residuals are larger than the 30 GHz model), or the systematic is not present at 353 GHz and may be an artifact of just the LFI data processing/mapmaking. Foreground cleaning with templates as explored in Chapter 4 examines this issue in more detail by analysing residual plots across the entire frequency range and examining persistent systematic patterns.

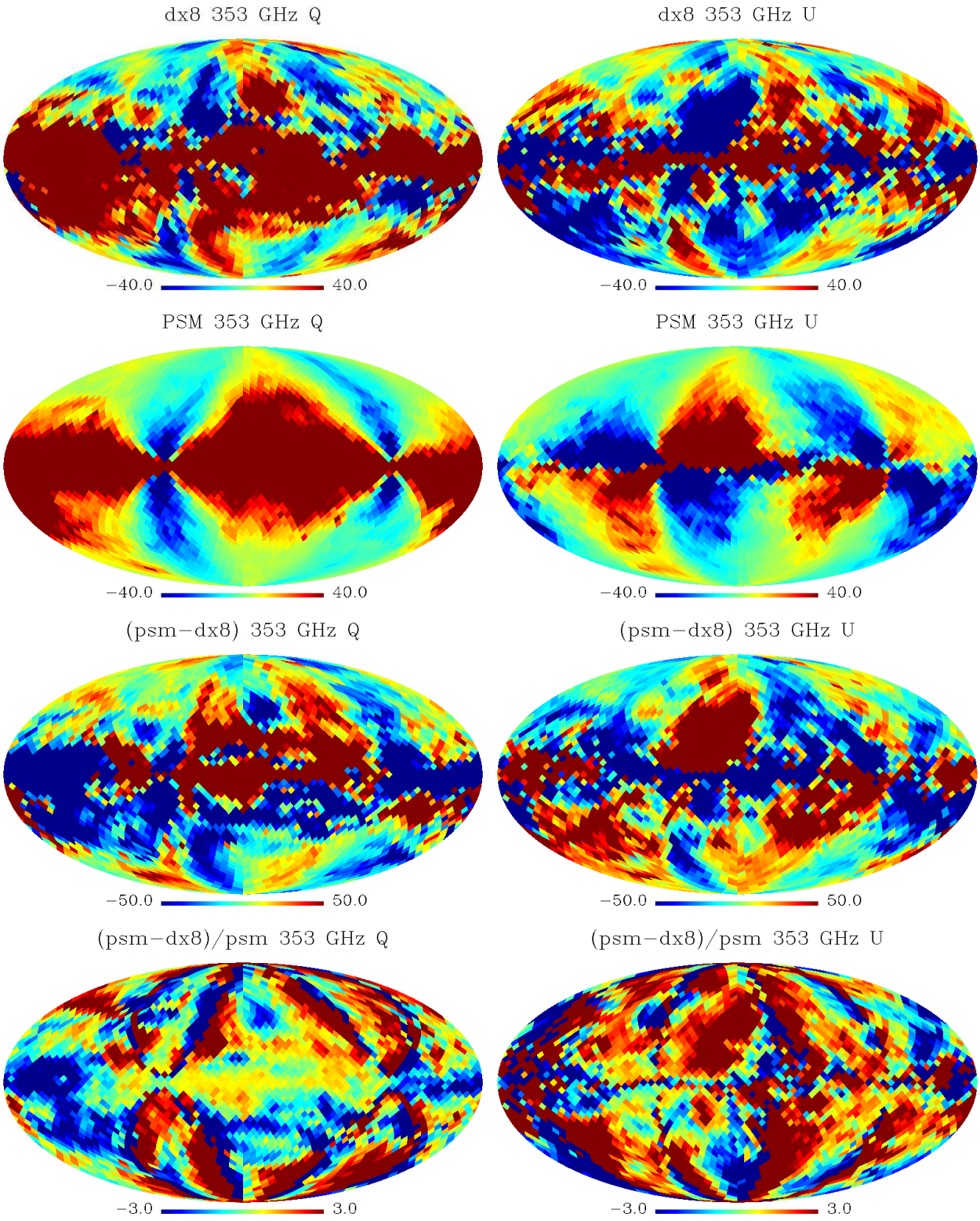

Figure 3.10: Pixel-rebinned dx8 353GHz Q and U maps (top) at $N_{side} = 16$, input thermal dust Q/U simulations based on a model of the Galactic magnetic field, without geometric depolarisation factor (second from top), residual Q and U maps formed from the difference between the data and simulations (second from bottom), and the fractional residual (as a fraction of the input PSM simulation (PSM-dx8)/PSM.

The PSM uses the WMAP 5-year 23 GHz polarisation maps to produce a template of the Galactic polarisation angle. This map is then used to construct the Q and U synchrotron simulation maps at the desired frequency by assuming that the emission at the Planck frequencies follows the same magnetic field as at 23 GHz. For thermal dust emission, a theoretical model of the magnetic field is used to create an artificial map of the polarisation angle with input properties of the spiral arm structure of the Milky Way. More recent models incorporate the synchrotron polarisation angle into the dust models by assuming that both dust and electrons follow the same magnetic field and thus the polarisation angle should correlate [146]. Given that the simulations explored in this work for thermal dust utilise only a theoretical spiral arm model, we should expect the data for the synchrotron polarisation angle to more closely resemble the simulations than for thermal dust.

Figure 3.11 shows the polarisation angle calculated as

$$\phi_\nu = \frac{1}{2} \arctan \frac{Q_\nu}{U_\nu}. \tag{3.3}$$

The simulated synchrotron polarisation angle at 30 GHz reproduces the global morphology seen in the data well. The ϕ distribution is much noisier than the simulation as expected, but the tightness of the spiral arm correlates well between the two maps. Some regions along the Galactic plane are incorrectly modelled with a much higher angle than is found in the data. Regions of stronger synchrotron emission correlate with regions of higher accuracy for ϕ.

For thermal dust emission, the simulated spiral arm structure does not correlate well with the data, as much more structure is evident along the Galactic plane and at high latitude. The ϕ distribution for dust also appears to be significantly noisier than for synchrotron. The thermal dust ϕ does not correlate strongly with the synchrotron ϕ, as assumed in some models of dust polarisation in the PSM.

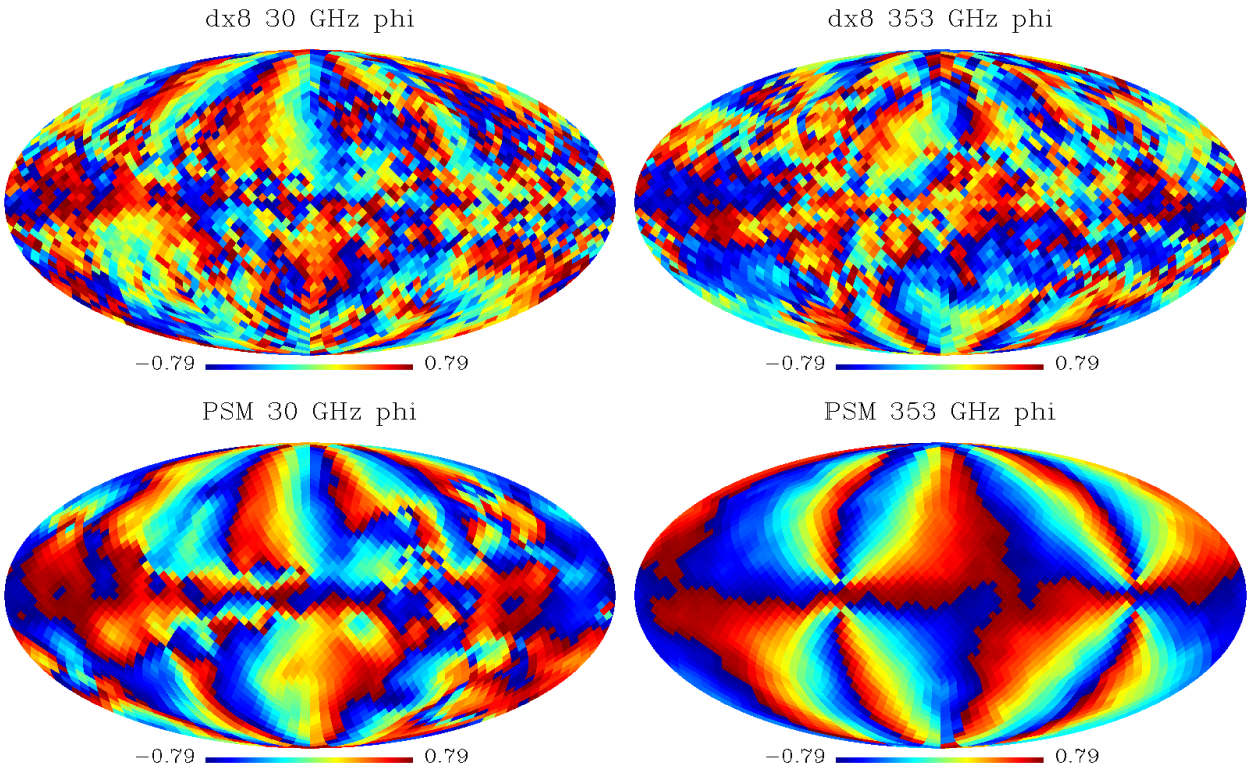

Figure 3.11: Polarisation angle ϕ calculated for bandpass-corrected dx8 30 GHz (top left), and 353 GHz (top right). Lower panels show corresponding simulations for 30 GHz (lower left), based on the WMAP 23 GHz polarisation data to estimate the magnetic field, and for 353 GHz (lower right), based on a theoretical spiral-arm model for the Milky Way. The large-scale correlation between simulation and data for 30 GHz synchrotron is reasonable but much less accurate for thermal dust at 353 GHz.

3.4 Spectral Index Models

We now look at the spectral index behaviour across the lowest and highest channels and compare this to the input models available. We calculate β_s for both the polarised intensity $\sqrt{Q^2+U^2}$ as well as for the temperature maps. Differences between plane regions and off-plane regions are also examined, and the correlation between polarisation and temperature data explored. As the maps we are using are in units of equivalent thermodynamic temperature, we must first convert from antenna temperature. The instruments first convert a flux into antenna temperature via

$$T_A = S\frac{\lambda^2}{2k_B\Omega}, \tag{3.4}$$

where k_B is Boltzmann's constant, λ is the wavelength and Ω is the effective beam size of the HFI/LFI instrument. The Antenna temperature is related to the thermodynamic temperature by the relation

$$T_A = \frac{x}{\exp(x)-1}T_T, \tag{3.5}$$

where we have defined $x = h\nu/kT$. Small fluctuations in the antenna temperature can be converted into the effective thermodynamic temperature fluctuations via

$$T_A = \frac{x^2\exp(x)}{(\exp(x)-1)^2}. \tag{3.6}$$

This conversion is necessary at each frequency as the spectral index is defined in antenna temperature. The conversion factor for the Planck channels is given in Table 3.2. The spectral index is calculated with $A \propto \nu^\beta$ in antenna temperature for temperature and polarisation.

Frequency (GHz)	30	44	70	100	143	217	353
Wavelength (mm)	10	6.8	4.2	3	2.1	1.4	0.85
$\Delta T_A/\Delta T_T$	1.02	1.05	1.13	1.29	1.65	2.99	12.92

Table 3.2: Conversion factors between antenna temperature and thermodynamic temperature computed at the Planck LFI and HFI observing frequencies.

3.4.1 Synchrotron

Figures 3.12 and 3.13 show the calculated spectral index for the temperature maps and the squared polarisation amplitude $Q^2 + U^2$, with and without smoothing with a 10° Gaussian beam, for three pairs of maps; 30 and 44 GHz, 30 and 70 GHz, and 30 and 44 GHz. The best estimate of the synchrotron spectral index will come from the first plot, calculated between 30 and 44 GHz,

as the synchrotron emission is most dominant at the lowest frequencies. The temperature and polarisation plots show a significantly different morphology and average polarisation level, across all three combinations of maps. For the 30-44 GHz map, $\beta_s \approx -2.8$, steepening and shallowing off-plane with some regions e.g. centred around (110,45) as low as -6 and as other regions e.g. (250,-60) as high as -0.5. The Galactic plane signal-to-noise is highest and for temperature β_s agrees well with simulation estimates of β_s between -3.1 and -2.7. Off-plane regions do not agree with simulation estimates, which typically predict $\beta_s = -3.0$. The polarisation map does not reproduce the consistent Galactic plane region seen in the temperature plot, with the Galactic anti-centre exhibiting a much higher spectral index than surrounding regions,and for some Galactic pole regions β_s is calculated as below -6. Some of this behaviour is partially due to the smoothing applied to the map, and the offending pixels can be easily seen in the unsmoothed maps. These regions of weak emission however fall outside even the widest Galactic masks where the signal to noise ratio is low. All dx8 map combinations show a much higher variance away from the strong central emission. It should be noted that subsequent dx9+ data exchanges may alter the polarisation maps significantly so this situation may change with time.

As expected, using the 70 GHz map in combination with either the 30 or 44 GHz map raises the spectral index, as at 70 GHz the synchrotron contribution is much less than at 30 GHz, and there is a higher CMB contamination at 70 GHz. The global morphology remains consistent with the 30-44 combination, albeit raised by on average 1.2 to $\beta = -1.5$. This is shown more clearly in Figure 3.14 which illustrates the behaviour with Galactic latitude and histogram plots of the distribution for each combination. The 30-70 GHz combination map also shows the clear difference in morphology of β across the sky, where again there is a large variation across the Galactic plane but for temperature the plane remains roughly constant. The statistics of the plane/off-plane regions are shown in Table 3.3. Given the current quality of the polarisation data, we should be careful not to interpret these results too literally, especially away from the plane, where the signal-to-noise ratio is significantly lower than the for the strong emission at low latitudes.

For the 40-70 GHz combination, the index rises significantly with a mean of -1.37 ± 0.02 for temperature, and -0.18 ± 0.06 for polarisation in the plane. The dust intensity is much higher at 70 GHz, and by 100 GHz the synchrotron and dust emission are approximately of equal intensity. Hence we observe a transition from the $\beta_s = -3$ regime to the $\beta_d = 1.5$ regime. Again the behaviour off-plane is different for polarisation than for temperature, with the polarisation exhibiting a much larger variance.

3.4.2 Dust

Figures 3.15 and 3.16 show the calculated spectral index for the temperature maps and the squared polarisation amplitude $Q^2 + U^2$, with and without smoothing with a 10° Gaussian beam, for three

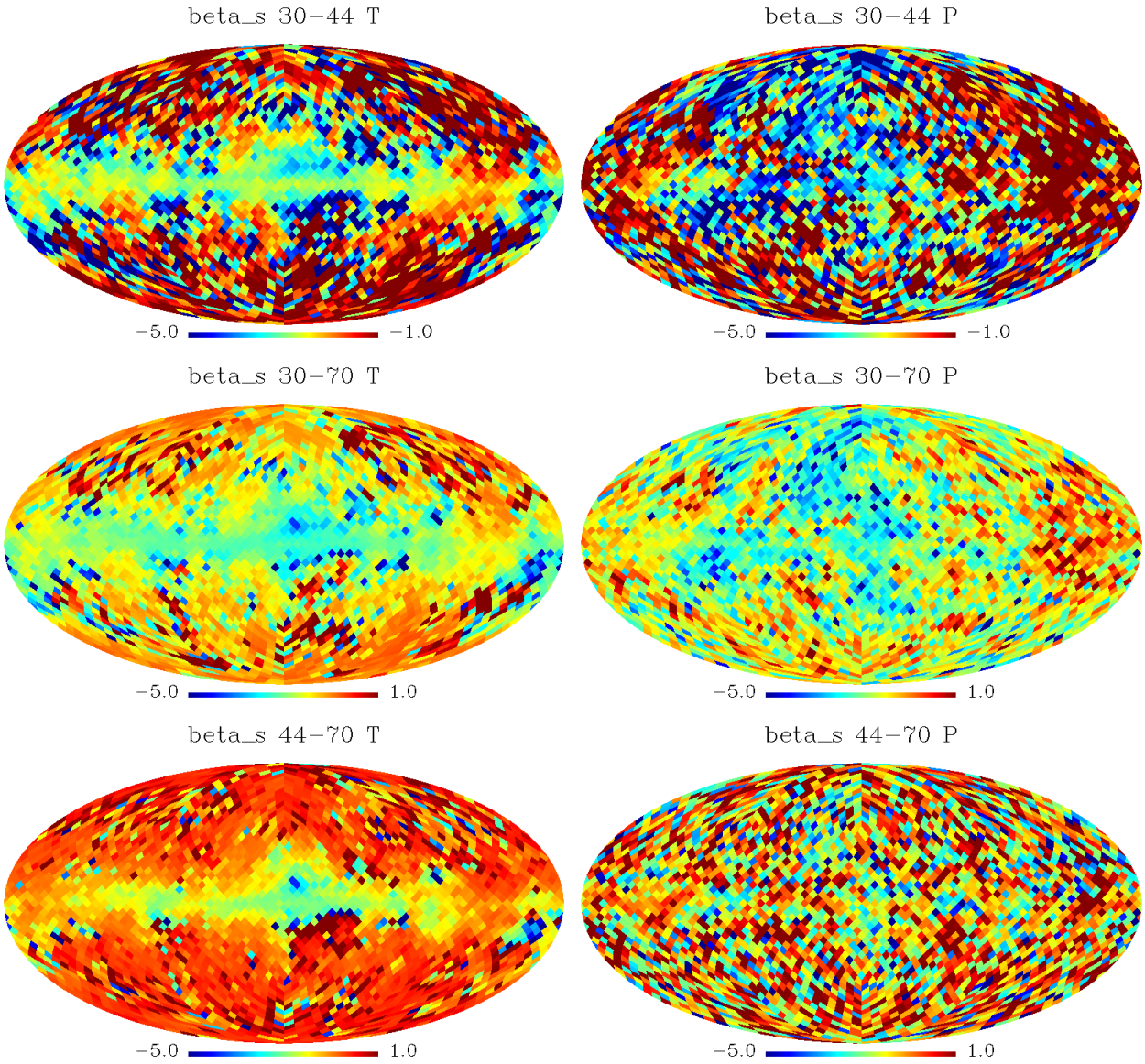

Figure 3.12: Spectral index maps for synchrotron emission estimated from the raw bandpass-corrected dx8 maps, at a resolution of $N_{side} = 16$. By pixel rebinning at this resolution, the signal-to-noise rises significantly allowing for easier visualisation of large-scale structure, but retains sufficient detail on angular scales of a few degrees. Top images show estimates using 30 and 44 GHz, the primary synchrotron combination, middle images show estimates using 30-70 GHz maps, and lower images show the estimates from 44 and 70 GHz. The left panels show temperature and the right panels show polarisation.

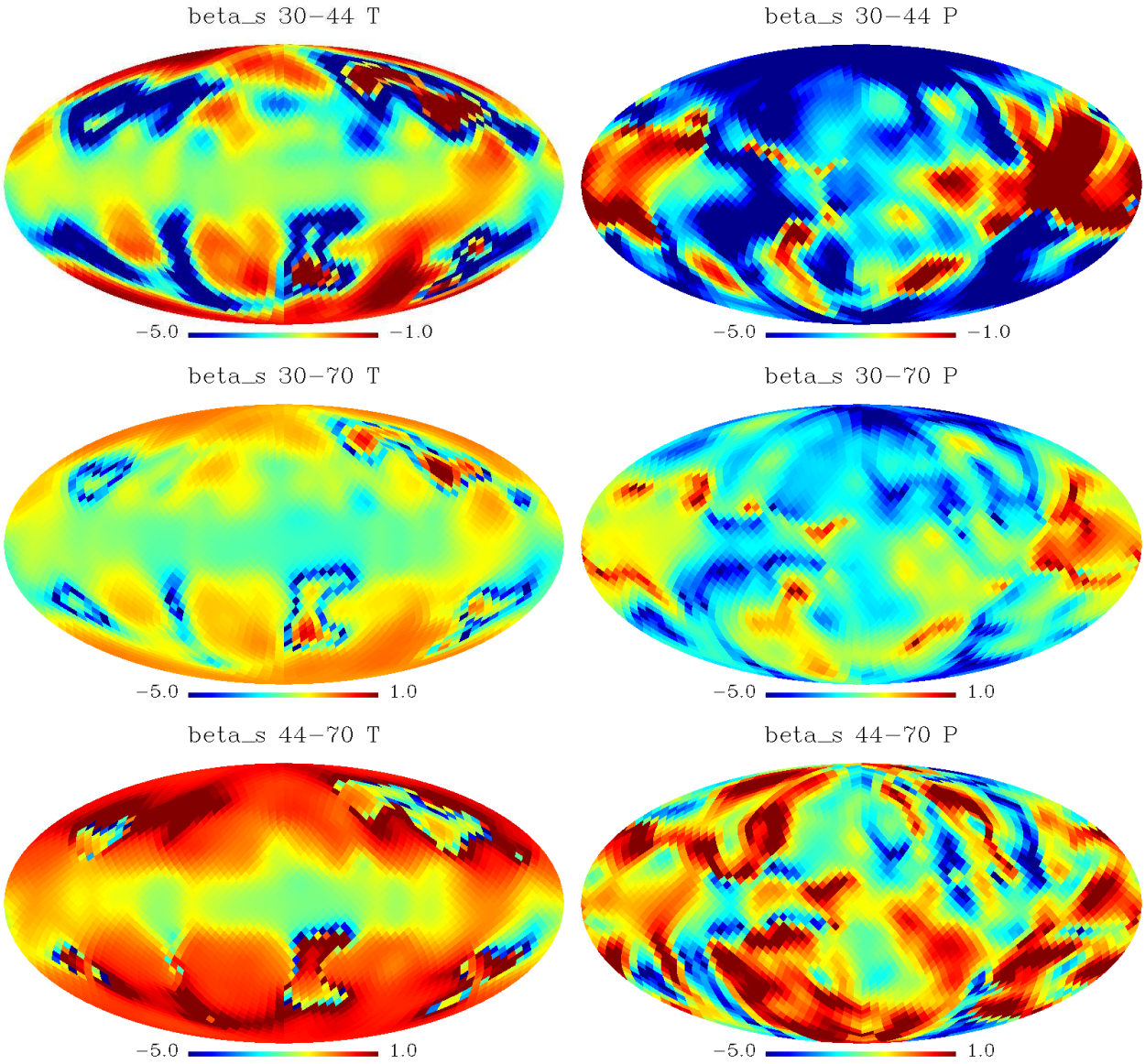

Figure 3.13: Spectral index maps for synchrotron emission estimated from the raw bandpass-corrected dx8 maps, at a resolution of $N_{side} = 16$ and then smoothed with a Gaussian beam with FWHM=10°. By pixel rebinning at this resolution, the signal-to-noise rises significantly allowing for easier visualisation of large-scale structure, but retains sufficient detail on angular scales of a few degrees. Top images show estimates using 30 and 44 GHz, the primary synchrotron combination, middle images show estimates using 30-70 GHz maps, and lower images show the estimates from 44 and 70 GHz. The left panels show temperature and the right panels show polarisation.

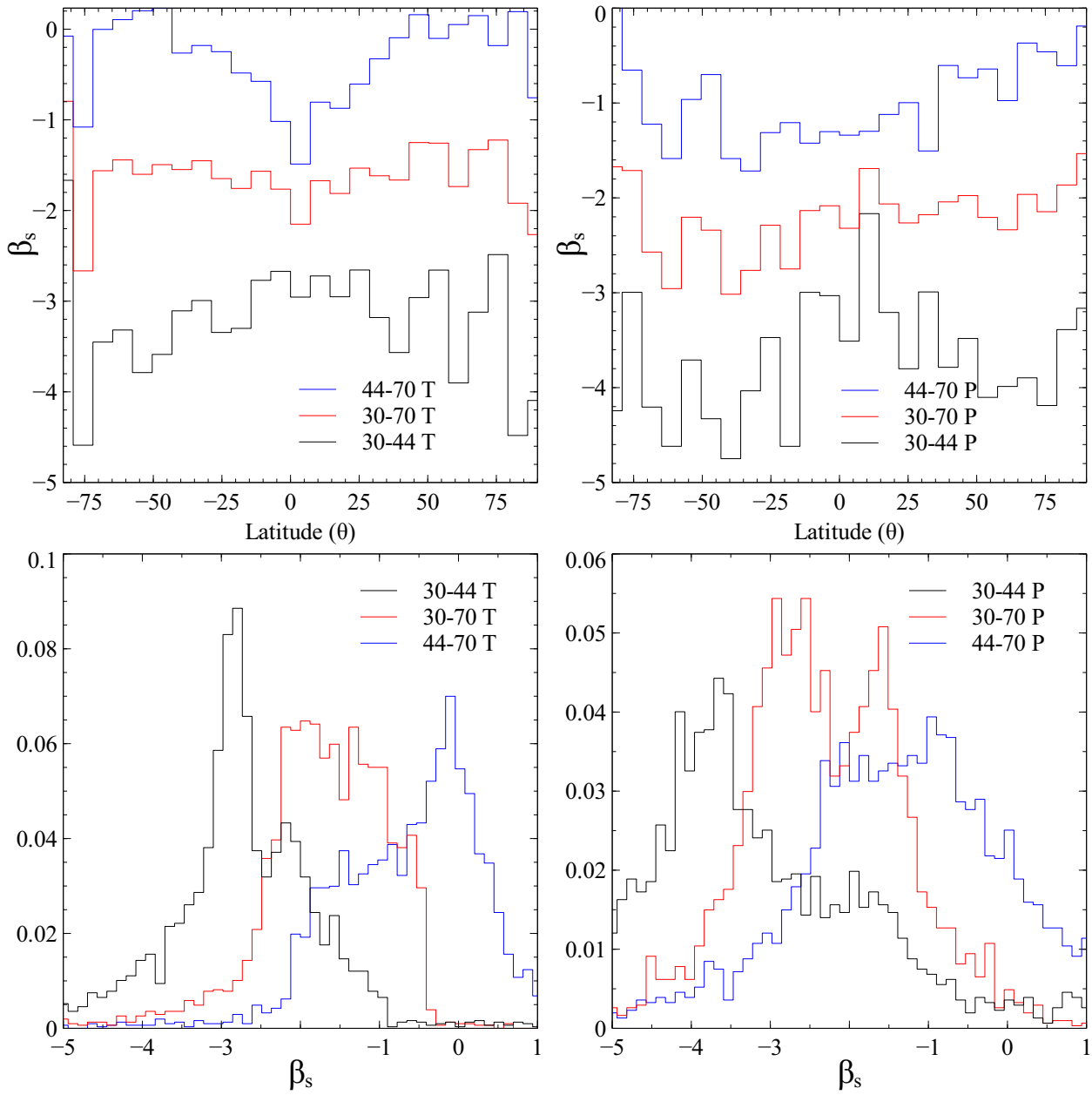

Figure 3.14: Synchrotron spectral index behaviour with Galactic latitude for temperature (top left) and polarisation amplitude (top right), and histogram plots for temperature (bottom left) and polarisation amplitude (bottom right). Regions closest to the Galactic plane have the highest signal-to-noise. In each plot three map combinations are shown, 30 & 44 GHz, 30 & 70 GHz, and 44 & 70 GHz. The spectral index increases with frequency.

Map combination	T_{plane}	P_{plane}	$T_{off-plane}$	$P_{off-plane}$
$30-44$	-2.73 ± 0.01	-2.45 ± 0.06	-3.20 ± 0.09	-3.92 ± 0.09
$30-70$	-1.98 ± 0.01	-1.79 ± 0.04	-1.55 ± 0.04	-2.37 ± 0.04
$44-70$	-1.37 ± 0.02	-1.24 ± 0.05	-0.18 ± 0.06	-1.10 ± 0.07

Table 3.3: Average spectral indices for the map combinations 30-44, 30-70, 44-70 GHz, calculated on-plane and off-plane (outside $\sim 10^\circ$ mask above/below the Galactic plane). Maps are as in the text at $N_{side} = 16$ and smoothed with 10° beam. Off-plane regions for temperature are higher than in the plane, whereas for polarisation on-plane regions are higher except for 44-70 GHz.

pairs of maps; 353 and 217 GHz, 353 and 143 GHz, and 217 and 143 GHz. The best estimate of the dust spectral index will come from the first plot, calculated between 353 and 217 GHz, as the dust emission is strongest at the highest frequencies. As is clear from the unsmoothed maps, even at this low resolution noise becomes more apparent for the lower frequency combinations, particularly off-plane for the 217-143 GHz combination. In all three however, the Galactic plane appears coherent, although for polarisation the noise is more apparent. For the 353-217 GHz combination, there is again more variance in polarisation than temperature, particularly at low latitudes. Regions of high polarisation fraction (as discussed previously) appear visibly less noisy and for these regions typically $\beta_d = 1.3$. Given that these regions have the strongest polarisation, the calculated β_d will be more reliable than low-polarisation regions. At extreme latitudes for the 353-217 GHz combination, regions of $\beta_d = -1$ and $\beta_d = 3.5$ are found. These regions do not persist in the other combinations with nearby frequencies or for the temperature maps so they are unlikely to be genuine features, and are most likely artifacts. At 353-143 GHz, the spectral index appears noisier off the plane but with a lower variance across the sky, with the same regions of high polarisation showing a consistent value of $\beta_d = 1.3$. For the 217-143 GHz combination these regions are also present however increase slightly due partly to noise. The means of the plane/off-plane regions are shown in Table 3.4.

Map combination	T_{plane}	P_{plane}	$T_{off-plane}$	$P_{off-plane}$
$353-217$	1.00 ± 0.007	1.28 ± 0.03	0.66 ± 0.03	0.95 ± 0.06
$353-143$	1.21 ± 0.006	1.20 ± 0.02	0.83 ± 0.02	1.03 ± 0.03
$217-143$	1.46 ± 0.010	0.93 ± 0.03	1.08 ± 0.03	1.10 ± 0.06

Table 3.4: Average spectral indices for the map combinations 353-217, 353-143, 217-143 GHz, calculated on-plane and off-plane (more than 10° above/below the Galactic plane). Maps are as in the text at $N_{side} = 16$ and smoothed with 10° beam. Off-plane regions for temperature are lower than in the plane, and for polarisation on-plane regions are higher except for 217-143 GHz.

The smoothed maps in Figure 3.16 allow for easier visualisation of the typical level of polarisation, but also introduce some localised aliasing effects due to the effect of particularly noisy pixels in the unsmoothed maps. This effect is more pronounced if higher resolution maps are used. Unlike for the synchrotron case in Figure 3.13, there is not a clear trend in increasing or decreasing β when analysing the Galactic plane in the series of map combinations. Instead it is useful to look at the regions of high polarisation fraction, where the index decreases slightly at the higher frequency

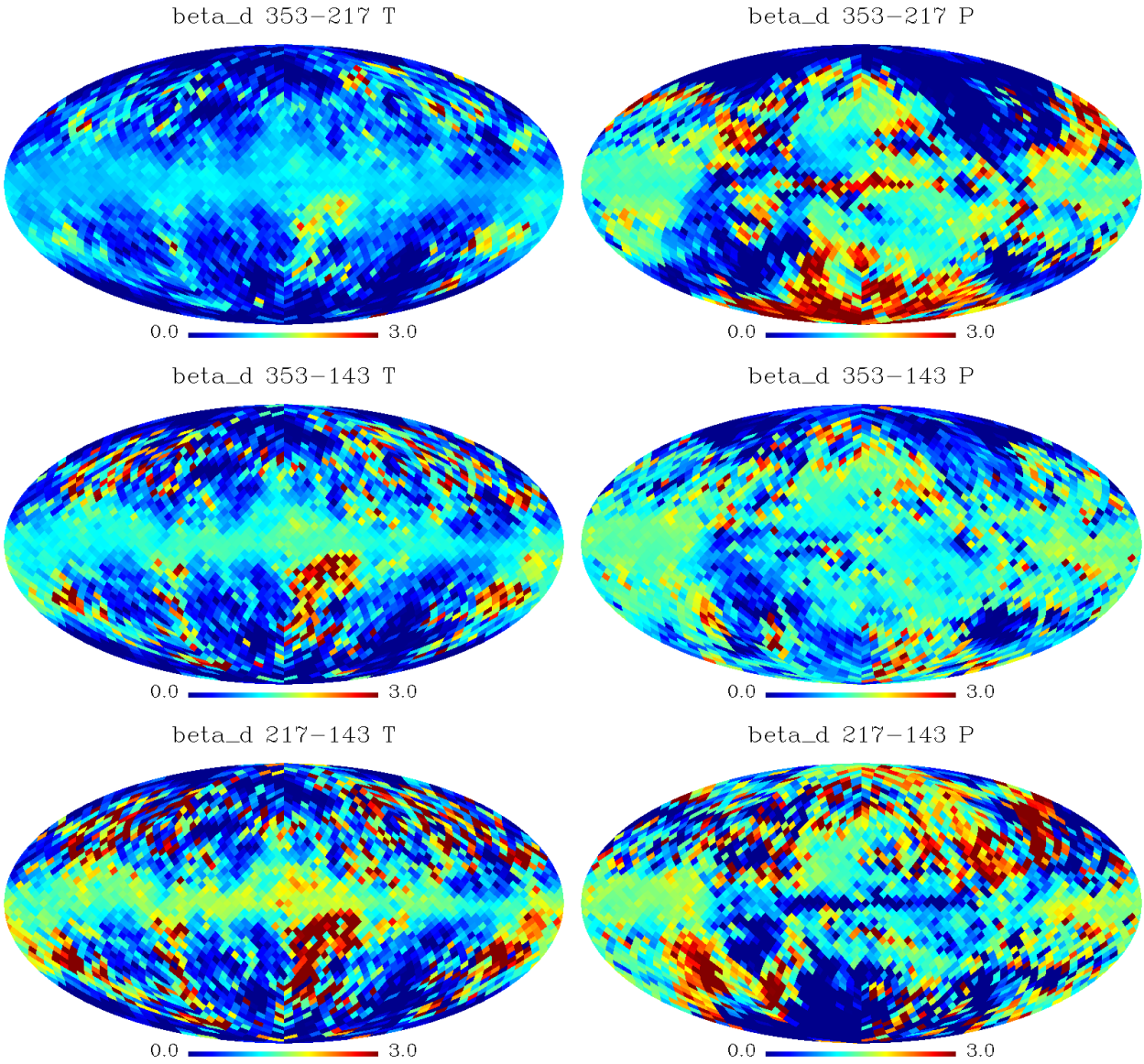

Figure 3.15: Spectral index maps for dust emission estimated from the raw dx8 maps, at a resolution of $N_{side} = 16$. By pixel rebinning at this resolution, the signal-to-noise rises significantly allowing for easier visualisation of large-scale structure, but retains sufficient detail on angular scales of a few degrees. Top images show estimates using 353 and 217 GHz, the primary dust polarisation combination, middle images show estimates using 353-143 GHz maps, and lower images show the estimates from 217 and 143 GHz. The left panels show temperature and the right panels show polarisation.

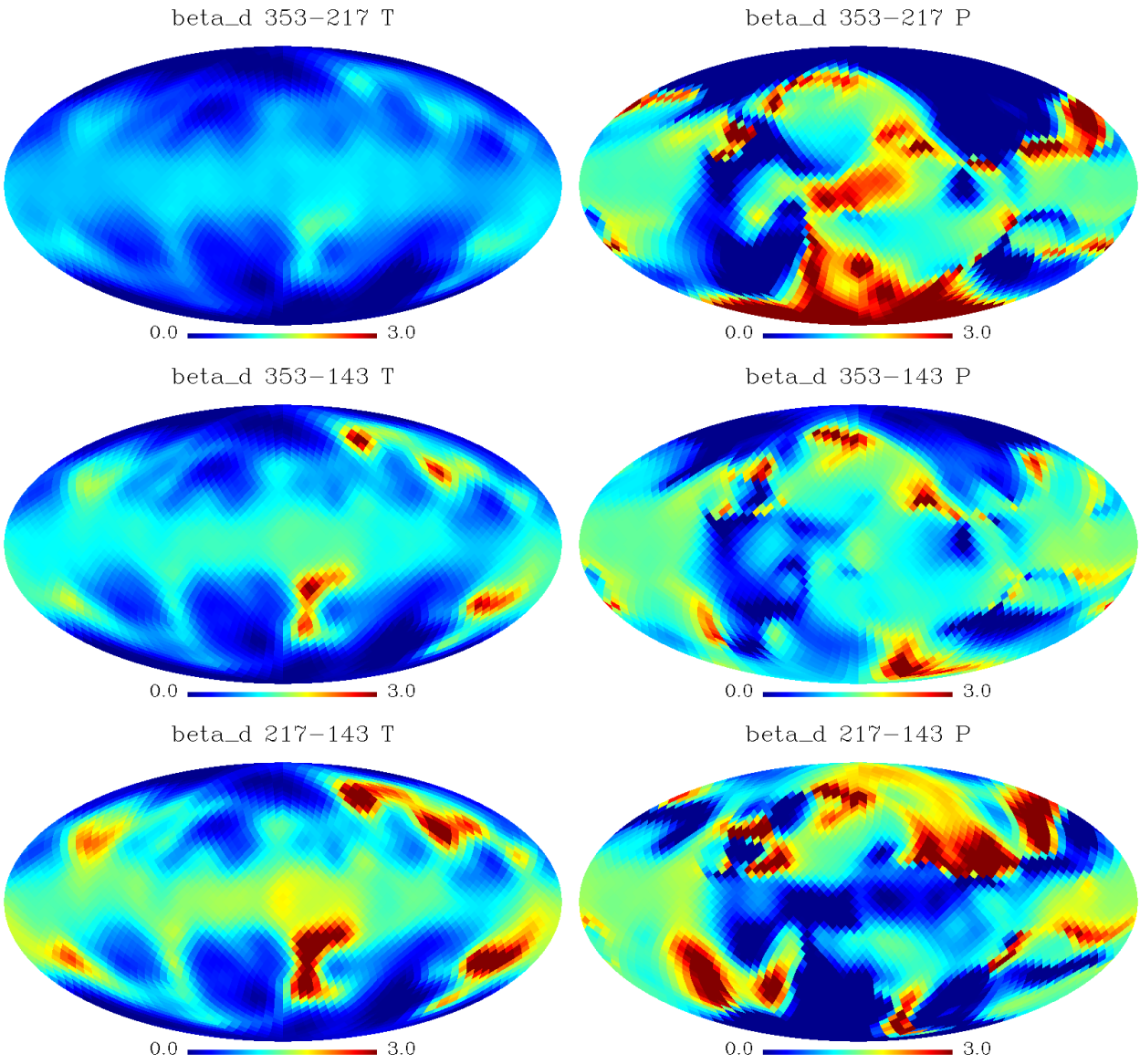

Figure 3.16: Spectral index maps for dust emission estimated from the raw dx8 maps, at a resolution of $N_{side} = 16$ and then smoothed with a Gaussian beam with FWHM=10°. By pixel rebinning at this resolution, the signal-to-noise rises significantly allowing for easier visualisation of large-scale structure, but retains sufficient detail on angular scales of a few degrees. Top images show estimates using 353 and 217 GHz, the primary dust polarisation combination, middle images show estimates using 353-143 GHz maps, and lower images show the estimates from 217 and 143 GHz. The left panels show temperature and the right panels show polarisation.

combinations from ∼1.5 at 217-143 GHz to ∼1.4 at 353-143 GHz, to ∼1.3 at 353-217 GHz, the exact value varying with the region chosen.

The global average spectral index for polarisation in the plane (within 10° of $\theta = \pi/2$) rises from 0.93 ± 0.03 at 217-143 GHz to 1.20 ± 0.02 at 353-143 GHz, to 1.28 ± 0.03 at 353-217. The standard simulation globally estimates the Q/U dust spectral index at ≈ 1.5, 0.2 higher than the observed dx8 β_s. Off the plane the opposite trend occurs, with β_s dropping from 1.10 ± 0.06 at 143-217 GHz, to 1.03 ± 0.03 at 353-143 GHz, to 0.95 ± 0.06 at 353-217 GHz. This is again lower than the globally assumed 1.5 found in the simulations. The distribution with latitude is shown in Figure 3.17.

Histograms for β_d produced with different combinations of maps show the distinct difference between temperature and polarisation. The distribution broadens and shifts up with frequency for temperature, whereas for polarisation very little difference can be seen with the peak of the distribution remaining at 1.5 for all combinations.

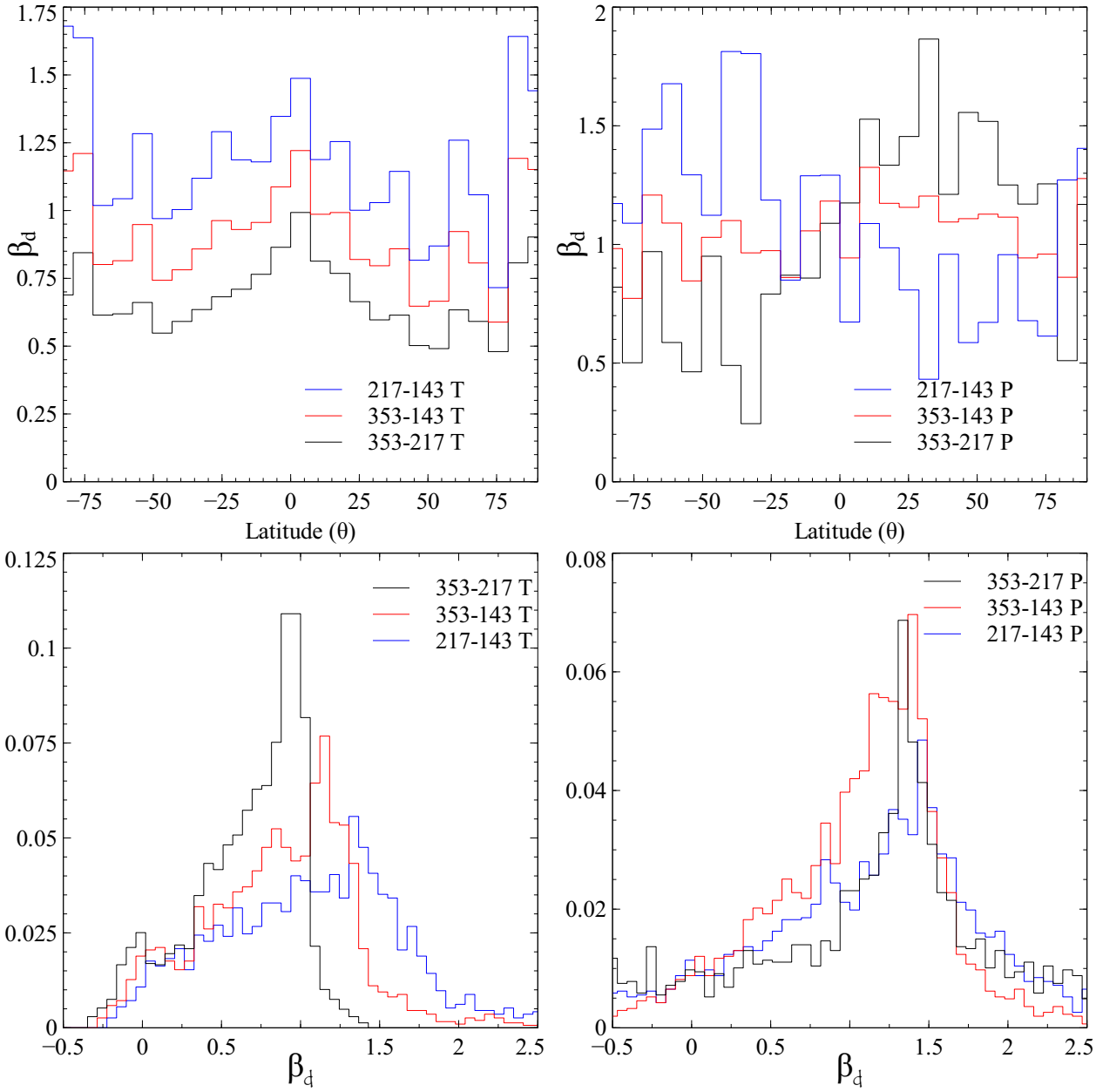

Figure 3.17: Dust spectral index behaviour with Galactic latitude for temperature (top left) and polarisation amplitude (top right), and histogram plots for temperature (bottom left) and polarisation amplitude (bottom right). Regions closest to the Galactic plane have highest signal-to-noise. In each plot three map combinations are shown, 353 & 217 GHz, 353 & 143 GHz, and 217 & 143 GHz.

3.5 Behaviour with Frequency

A simple way of visualising the foregrounds changing with frequency is to analyse the shift from synchrotron to dust in the spectral indices of the dx8 polarisation maps. Synchrotron intensity drops to a similar level to dust at around 70 GHz, and the spectral index will shift from ≈ -3 to $\approx +1$ from 30-353 GHz. Figure 3.18 shows the average spectral index for T, Q, U, and P both inside and outside a Galactic mask preserving 74% of the sky. The mask is formed from the Q/U union of the thresholded 30 and 353 GHz dx8 maps detailed earlier in this chapter. The stronger foreground signal inside the mask will increase reliability of the estimates, given the higher signal-to-noise ratio. Dashed lines show the value for the pixels outside the mask for comparison. As seen before, at the lowest frequency combination, the synchrotron temperature spectral index is lower than for either Q, U, or P, but this difference drops when moving to higher frequency pairs. Averages calculated outside the mask exhibit a lower variation, and lower absolute values, particularly at the 70-100 GHz combination. At the primary dust frequencies, the polarisation spectral index is higher than for temperature by at least 0.2.

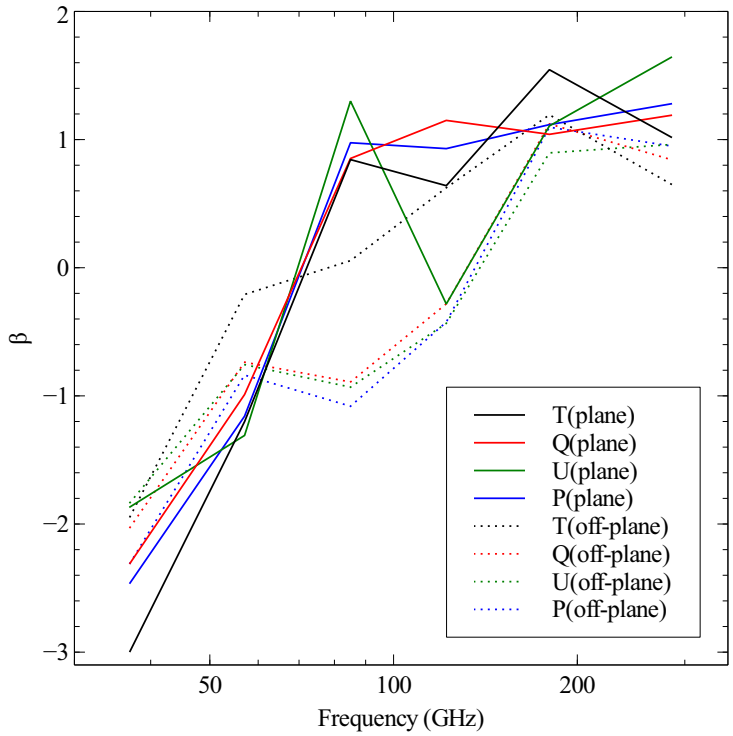

Figure 3.18: Average spectral index calculated between adjacent frequencies plotted against the frequency midpoint for temperature, polarisation, and polarised intensity. Solid lines show averages inside a Galactic mask preserving 74% of the sky. Dashed lines show the average outside the mask.

3.6 CAM-SPEC Spectra

In this section we look at the effect of masking on the polarisation power spectra. We use a series of foreground masks and calculate the TE cross and EE auto spectra using the CAM-SPEC package. The aim is to analyse the effect on the accuracy of the spectra as the mask size decreases, and more foreground power is aliased into the CMB spectra. With CMB-conservative (i.e. small) masks, a large amount of foreground power is present at low latitudes, and with less CMB-conservative (i.e. larger) masks the correspondence of the calculated spectra with the fiducial model will drop with the number of remaining unmasked modes contributing to the power spectra. The purpose of this section is then to determine how much of the sky can be used safely for polarisation analysis.

3.6.1 CAM-SPEC

The CAM-SPEC package is a complete package for cross-spectra and likelihood analysis that can be applied to a large number of independent Planck maps. The analysis corrects for departures from white noise, arbitrary map weighting, and differing beam transfer functions for each map. For a particular masked sky and weighting scheme, we can compute the pseudo-spectra

$$\tilde{\mathbf{C}} = \begin{pmatrix} \tilde{C}^{T_iT_j} & \tilde{C}^{T_iE_j} & \tilde{C}^{T_iB_j} \\ \tilde{C}^{E_iT_j} & \tilde{C}^{E_iE_j} & \tilde{C}^{E_iB_j} \\ \tilde{C}^{B_iT_j} & \tilde{C}^{B_iE_j} & \tilde{C}^{B_iB_j} \end{pmatrix}, \tag{3.7}$$

which are related to the deconvolved spectra ($\hat{C}^T$, $\hat{C}^{TE}$, etc) via a set of couping matrices as $\hat{\mathbf{C}} = M^{-1}\tilde{\mathbf{C}}$ as defined in the Planck likelihood paper [147]. If we have N_{map} independent maps, then we require $\frac{5}{2}N_{map}(N_{map}+1)$ coupling matrices (if all maps contain polarisation data). A more difficult task is to compute the covariances of the pseudo-spectra $\mathrm{Cov}(C^{T_{ij}}C^{T_{pq}})$ (for temperature), which involves computing N_{map}^4 coupling matrices, and the problem rapidly becomes intractable even for relatively low values of N_{map}. Let $\tilde{\mathbf{X}} = \mathrm{Vec}(\tilde{\mathbf{C}})$ denote a column vector composed of ordered elements of $\tilde{\mathbf{C}}$. The index p of an element X_p denotes the map combination (i, j), multipole ℓ, and spectrum (T, TE, etc). The covariance of this vector is $\tilde{\mathcal{M}} = (\tilde{\mathbf{X}} - \langle\tilde{\mathbf{X}}\rangle)(\tilde{\mathbf{X}} - \langle\tilde{\mathbf{X}}\rangle)^T$. For Planck, this vector and associated covariance matrix are very large. The high-ℓ computation is simplified by compressing the vector containing the cross-spectra estimates into a linear combination of the various cross-spectra,

$$\hat{C}_\ell^T = \left(\sum_{i,j,i\neq j} \frac{\alpha_\ell^{TT_{ij}} c_i c_j \hat{C}_\ell^{T_{ij}}}{(b_\ell^{T_{ij}})^2 (p_\ell^T)^2} \Big/ \sum_{i,j,i\neq j} \alpha_\ell^{TT_{ij}} \right), \tag{3.8}$$

where $b_\ell^{T_{ij}}$ is the fiducial isotropised beam function for map i at multipole ℓ, p_ℓ is the pixel window function, and c_i quantify calibration errors. HFI calibration is important, and relative calibration is demonstrated to be accurate to $\sim 0.1 - 0.2\%$ [148]. Relative calibration errors are computed by comparing the cross-spectra before forming the linear combination. CAM-SPEC determines the optimal combination of coefficients α_{ij} by weighting each estimate by the diagonal component of the relevant covariance matrix, as at high-ℓ, these are nearly diagonal and have similar structure. This assigns each cross-spectra equal weight in the signal-dominated regime, and inverse variance weighting in the noise dominated regime. With this approxiation, the combined estimates can be computed rapidly. Since the combined estimates are just linear combinations of the pseudo-C_ℓ estimates, their covariances are given by e.g.

$$\mathrm{Cov}(\hat{C}_\ell^T C_{\ell'}^T) = \sum \alpha_\ell^{TT_{ij}} \alpha_{\ell'}^{TT_{pq}} \mathrm{Cov}(\hat{C}_\ell^{T_{ij}} \hat{C}_{\ell'}^{T_{pq}}). \tag{3.9}$$

As mentioned above, the number of coupling matrices required to compute these spectra becomes prohibitively expensive as N_{map} increases. However, most of these coupling matrices are very similar, differing primarily in the amplitude of the noise levels and in minor respects such as missing pixels. CAM-SPEC adopts the same masks and weightings for groups of cross-spectra, and computes coupling matrices only for distinct combinations, which dramatically reduces the computational burden at the expense of complicating the indexing.

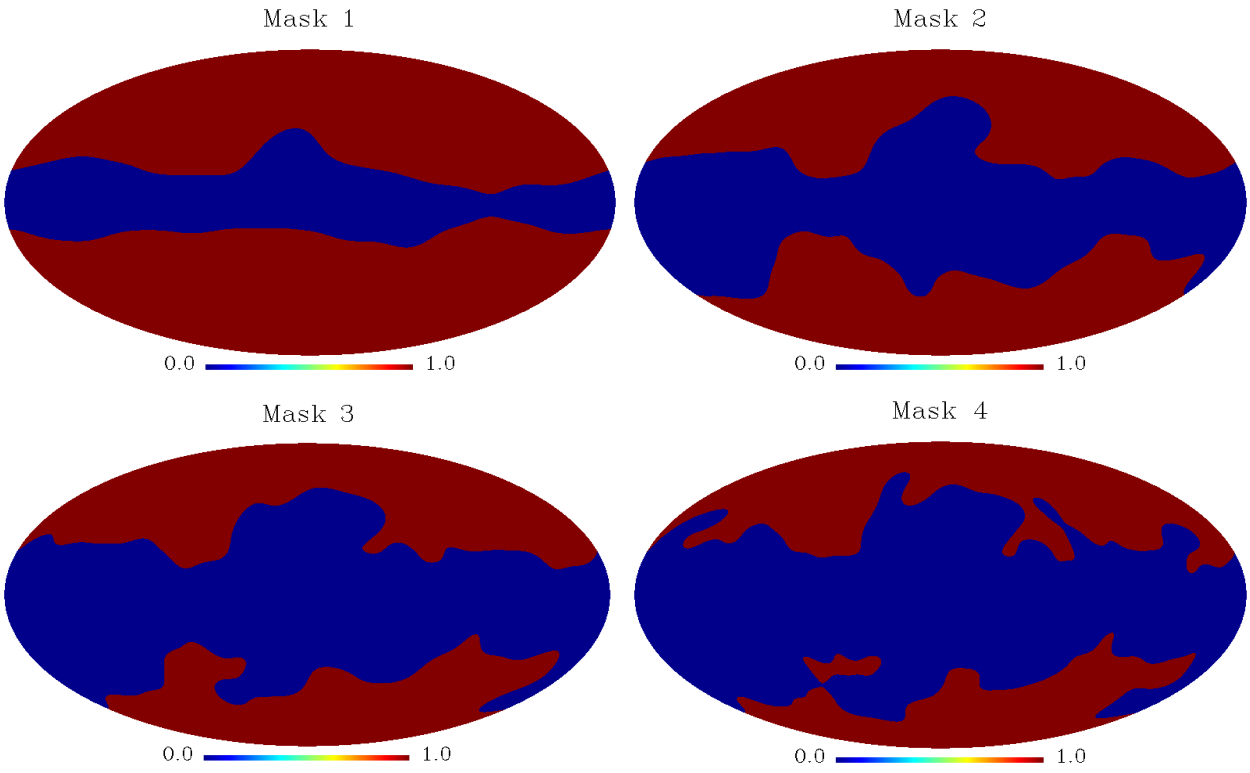

Figure 3.19: Polarisation masks at the native Planck resolution $N_{side} = 2048$ formed from thresholding and smoothing the union of the Q and U data at 30 and 353 GHz. The percentage of the sky masked in each of the 4 masks is 26%, 46%, 54%, and 62% respectively, and for the temperature mask which remains unchanged is 63%

The masks are assumed to be different for temperature and polarisation. We create a series of polarisation masks which remove increasing amounts of the sky. The masks are formed by thresholding the 30 and 353 GHz polarisation maps at increasing absolute levels, as tracers of the morphologically different foreground emission. The union of Q and U is taken at both frequencies, followed by smoothing the union of the 30 and 353 GHz masks. Four masks are formed at $N_{side} = 2048$, and are shown in Figure 3.19, and then coadded with a point source mask. The percentage of the sky masked in each of the 4 masks is 26%, 46%, 54%, and 62% respectively. The temperature mask is formed from the 30 and 353 GHz temperature data, and remains unchanged for the four analyses. The percentage of the sky masked in the temperature mask is 63%.

The transfer function, or the *beam window function* relates the true angular power spectrum C_ℓ to the observed angular power spectrum, and we note that in some studies the notation $W_\ell^{T_{ij}} \equiv (b_\ell^{T_{ij}})^2$ is used interchangeably. The beam transfer functions for different polarisations will in general be very slightly different, but we use the temperature transfer functions only, even for TE/E modes. This is all that is available, or likely to be available for Planck. Figure 3.20 shows the beam transfer functions for the HFI 100, 143, and 217 GHz channels, with fiducial Gaussian beams at $9.47'$, $7.04'$, and $4.68'$ FWHM for comparison. We also correct for a HEALPix pixel window function at the

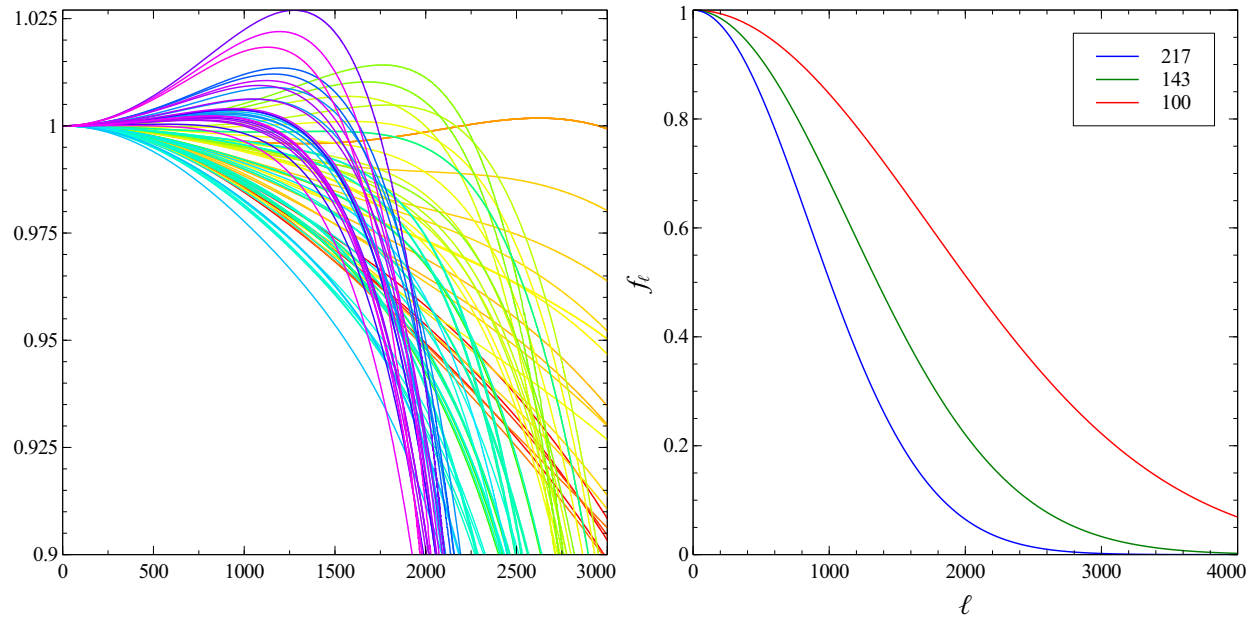

Figure 3.20: Left: 91 beam transfer functions for detector pairs at 100, 143, and 217 GHz. Right: Idealised fiducial Gaussian beams at 9.47′, 7.04′, and 4.68′ FWHM.

native resolution of the maps.

We use the CAM-SPEC package to calculate polarisation spectra, however the covariance matrix part of the code for polarisation is still under development, and so we do not show errors at this stage (although estimated covariance matrices are used in the calculation, which will produce a sub-optimal weighting of $C_{\ell\ell'}$). The TE and EE angular power spectra are calculated for the 143 GHz and 217 GHz channel for each of the 4 masks described earlier, averaged over all detector combinations for each frequency band. Planck is equipped with eight 143 GHz detectors, four of which form polarisation-sensitive pairs, giving two polarisation-sensitive sets. There are therefore more detector contributions to the TE cross power spectrum than for the EE spectrum. The TE cross spectra are shown in Figure 3.21, and the EE spectra are shown in Figure 3.22.

The calculated TE spectra are consistent with the fiducial model at both 143 and 217 GHz up to $\ell \sim 2000$ beyond which the noise drives the residuals to increasingly large values. At 217 GHz the estimated spectra are more consistent with the fiducial model (the residuals are markedly lower) to higher multipoles $\ell \sim 2500$. In both cases we find that the more conservative masks lead to higher residuals at lower ℓ as a result of foreground leakage, but at higher ℓ where noise is the dominant factor there is little difference between the 4 maskings. Mask 4 removes about 62% of the sky, and at high ℓ the residuals are consistent with the residuals for mask 1, which removes only 26% of the sky.

The EE spectrum is much more noise-dominated, due both to the lower number of detectors and therefore smaller amount of data, and the smaller signal itself. The residuals diverge much earlier

for our binning of $\Delta\ell = 20$ around $\ell \sim 1500$, and the 143 GHz residuals are lower across the entire ℓ range. At 217 GHz with the most conservative mask 1 a large excess of power is seen at all multipoles, which is most likely foreground dust power aliased into the power spectrum. At higher ℓ this excess foreground power is indistinguishable from the increasing noise level. The difference in spectra between masks 1, 2, and 3 is very small, but reducing the size of the mask below 45% (the level of mask 2) will introduce foreground contamination as seen with mask 1, and the excess is seen at both large and small scales. If we examine the difference in spectra between mask 1 and mask 2, shown in Figure 3.23 on a logarithmic scale, we see that the dust spectrum falls off significantly less steeply in polarisation than in temperature (in temperature, $C_\ell^{dust} \propto \ell^{-2.6}$), and this is an important conclusion.

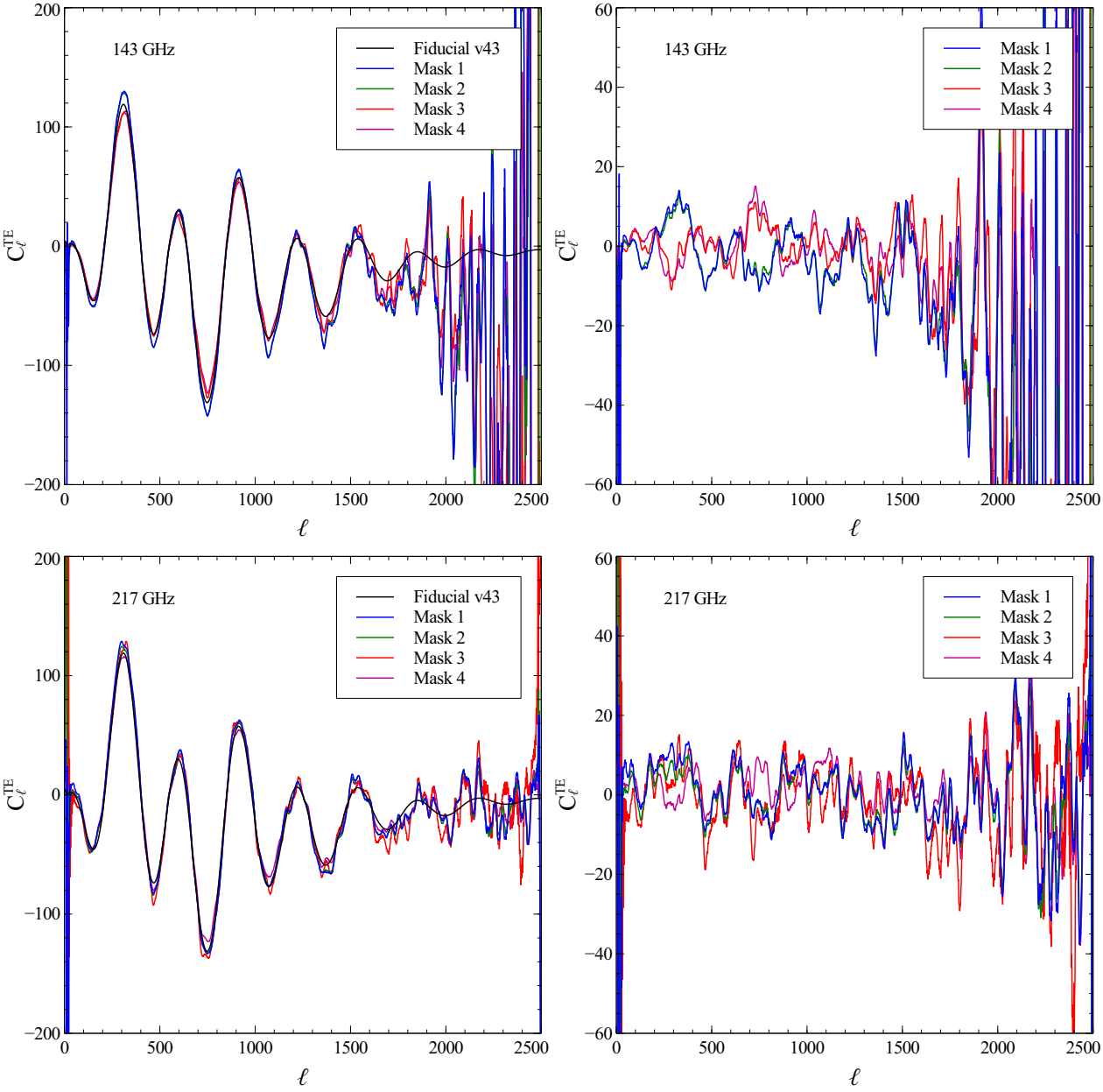

Figure 3.21: Left: TE cross spectra calculated at 143 and 217 GHz averaged over detectors, binned at $\Delta\ell = 20$ using nominal mission beam transfer functions for each detector pairing, for each mask as described in the text. The v43 maximum-likelihood fiducial spectrum (computed from the temperature data) is shown in black. Right: Residuals calculated between the CAM-SPEC spectra and the fiducial model.

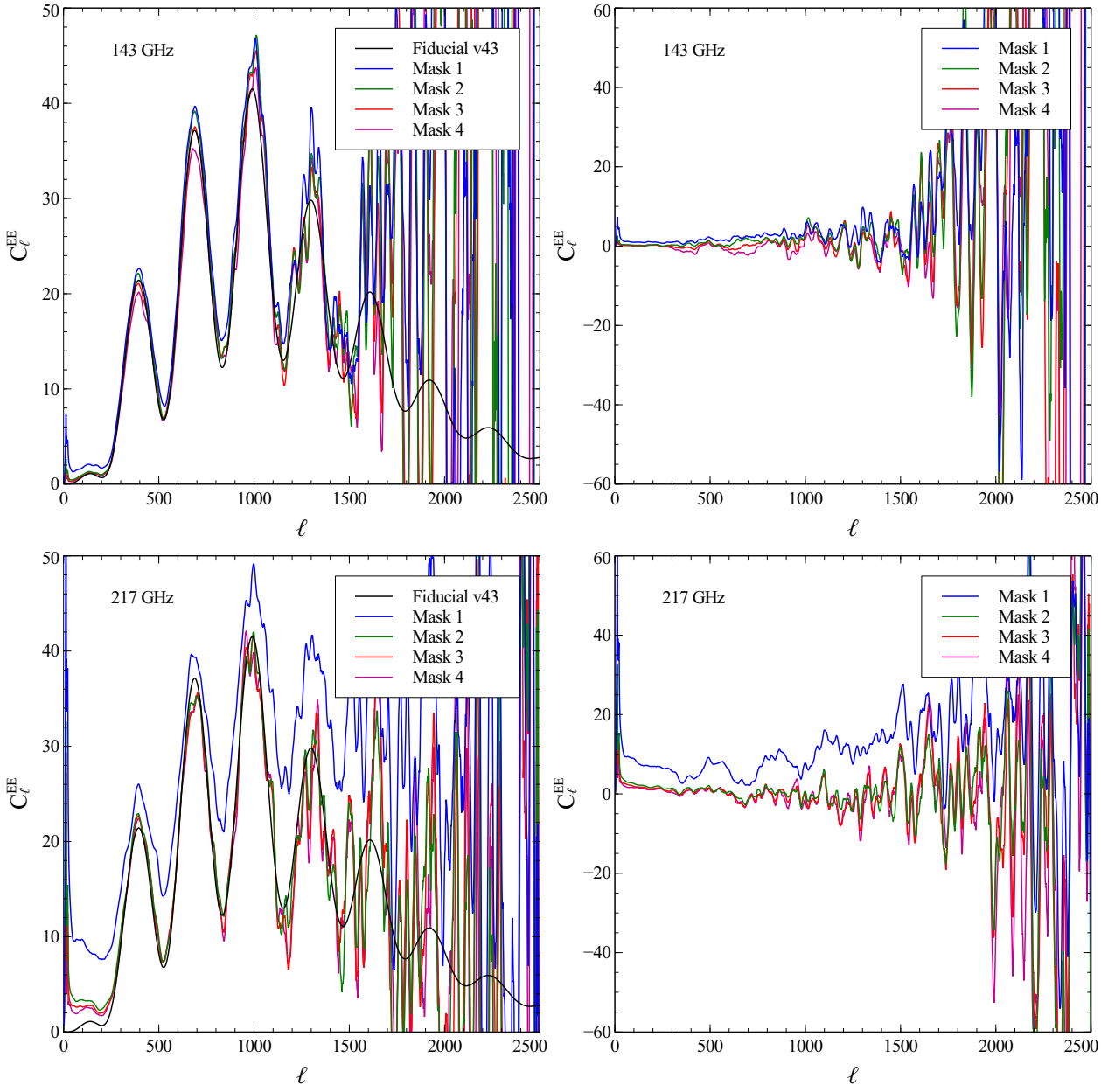

Figure 3.22: Left: EE spectra calculated at 143 and 217 GHz averaged over detectors, binned at $\Delta\ell = 20$ using nominal mission beam transfer functions for each detector pairing, for each mask as described in the text. The v43 maximum-likelihood fiducial spectrum is shown in black. Right: Residuals calculated between the CAM-SPEC spectra and the fiducial model.

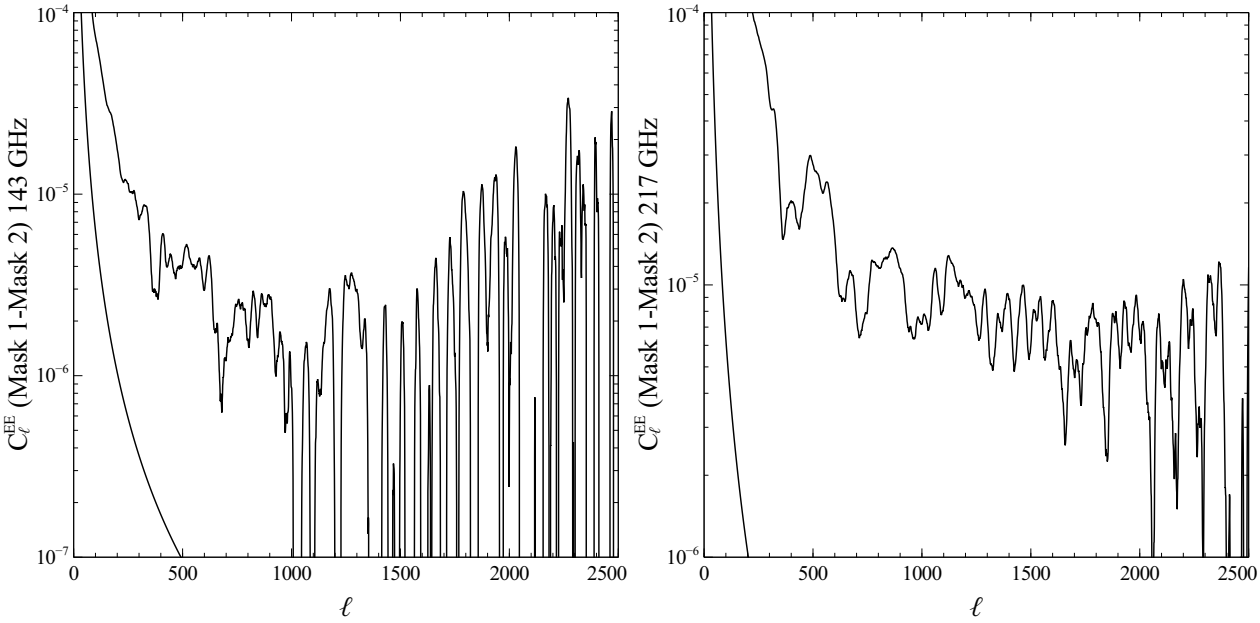

Figure 3.23: Left: Difference in EE spectra calculated at 143 GHz averaged over detectors between mask 1 and mask 2 described in the text, binned at $\Delta\ell = 20$ using nominal mission beam transfer functions for each detector pairing. Right: Same residuals calculated at 217 GHz for EE. Also plotted on both figures is the fit to the dust temperature spectrum. Clearly the dust spectrum falls off significantly less steeply in polarisation than in temperature ($C_\ell^{dust} \propto \ell^{-2.6}$ for T).

3.7 Conclusion

In this chapter we have looked at how the sky seen by Planck differs from the simulations in the PSM and simulations based on fiducial models. We began by analysing the level of polarisation in the foreground-sensitive channels, 30 and 353 GHz. The synchrotron emission at 30 GHz in $N_{side} = 16$ maps was found to be polarised at 10-12%, as expected given the depolarisation effect. Moving away from the plane, the synchrotron polarisation rises to 15-20% with a small number of isolated regions polarised at up to 40%. We have shown that the PSM is accurate for synchrotron polarisation at low Galactic latitude where the emission is strongest. We should expect this, as the synchrotron model we have used is based on WMAP data, with low signal-to-noise at higher Galactic latitudes. At higher latitudes however, the structure seen is somewhat different to the PSM simulations, with isolated regions incorrect by up to 20%. Some of these regions do not persist between neighbouring frequencies suggesting they are artifacts, however some regions are consistent over several frequencies and therefore suggest that the model of polarised emission is incorrect.

The dust polarisation is much less accurate, given the PSM dust models are themselves based on temperature-only data, and models of the polarised emission. At 353 GHz, we find the mean dust polarisation along the Galactic plane to be 3.9%, rising to around 10% in isolated regions at higher latitude. At 217 GHz, the mean drops slightly to 3.5%. Basic models in the PSM assume a 5% global polarisation. Including the geometric depolarisation factor, the PSM model typically overestimates the dust polarisation by about 1% along the Galactic plane.

With a small gain adjustment, the dx8 synchrotron morphology is found to correlate well with the PSM simulations, with residual maps exhibiting a similar banding structure to foreground-cleaned CMB maps. The dust simulations however bear little resemblance to the dx8 high frequency data, with the data pointing towards a more complicated magnetic field model than is assumed in the PSM. The dust is typically under/overestimated even in the Galactic plane by a factor of 2-3, suggesting more work should be invested in characterising dust polarisation models. Indeed the Planck high frequency data have given us the first all-sky dust polarisation survey between 143 and 353 GHz, and future models built with this data will help to further characterise the morphology in polarisation.

The synchrotron spectral index is found to be higher in polarisation than for temperature, both on and off the plane, and this is also seen in the dust polarisation at higher frequencies. At $N_{side} = 16$ resolution which we have used in this Chapter, the dust and synchrotron spectral index is shown to have a much larger variation than is assumed in the PSM. This variation could be incorporated into the PSM by further calculation of the spread across the sky, and using the Planck low and high frequency channels as spectral index templates for foreground separation studies.

We then looked at the comparison between the CAM-SPEC calculated TE and EE angular power spectra for a series of Galactic plane maskings. The choice of Galactic mask has a large effect

on the calculation of the power spectra. If the mask is too conservative, foreground leakage will contaminate the calculated spectra. If the mask is too aggressive and the sampled area of sky decreases, the number of modes decreases and the reliability of calculated spectra drops. We find that at a 46% masking, the residuals calculated between the CAM-SPEC spectra and the fiducial model do not diverge significantly for TE and EE, and in fact even a 26% masked sky gives similar results to a much less conservative 62% masking. For the EE power, at 26% masking, the foreground leakage significantly increases the power spectrum at 217 GHz at all angular scales due to the dust polarisation, however at 143 GHz this effect is not seen, suggesting that at 143 GHz a conservative mask can be used to retain a significant part of the sky with minimal impact on the spectra. We look at the difference between mask 1 and mask 2 on a logarithmic scale and find that the dust spectrum falls off much less steeply in polarisation than in temperature, suggesting that more complicated models of the dust polarisation will be required than basic models built using temperature data.

We have shown that for the dx8 exchange data:

- Synchrotron is polarised at $\sim 10 - 12\%$, and dust at $\sim 4 - 10\%$ in the plane (Section 3.3).
- Synchrotron emission is well modelled in the plane and still reasonably accurate at high latitudes however dust emission is inaccurate across most of the sky and should be remodelled (Section 3.3.2).
- Foreground spectral indices for temperature cannot be used for polarisation as they are significantly higher and have a larger variance across the sky (Section 3.4).
- For polarisation power spectra, at 143 GHz a conservative mask can be used, but at 217 GHz a larger mask is needed to remove strong dust emission (Section 3.6).
- The dust spectrum falls off much less steeply in polarisation than for temperature, a more sophisticated model of dust polarisation will be needed (Section 3.6.1).

In this Chapter we have not looked at high resolution images of dust and synchrotron polarisation on small angular scales. This is an area which will become increasingly important for future ground-based experiments targeting small regions of the sky. With the Planck data we can now modify the PSM to more accurately simulate the small-scale structure at any observing frequency which is an invaluable tool for hunting regions of low foreground polarisation or characterising the small-scale foreground power. The PSM does a reasonable job of estimating the synchrotron polarisation, but the dust polarisation as seen by Planck appears very different to the simulations, and further work is needed to develop a comprehensive and accurate model of the microwave sky as seen by Planck.

If you wish to make an apple pie from scratch, you must first invent the Universe
Carl Sagan

Chapter 4

Probing Planck dx8 Polarisation maps

In this chapter we look at the full mission Planck data and analyse the sky maps for a number of interesting polarisation features. We first apply the bandpass correction to the LFI dx8 maps (see later for description), and analyse the effect this has on the maps before performing a simple template fitting scheme to blindly remove foregrounds. Although this method of foreground removal is very simple, it is useful for checking residual instrumental systematics that almost certainly affect the Planck polarisation data. We use the 353 GHz Planck channel as a tracer of dust, and the 23 GHz WMAP data as a tracer of synchrotron emission. The central Planck channel is varied from 70 GHz to 143 GHz to examine the resultant CMB distribution. We also clean the WMAP 61 GHz channel and compare the cleaned map to the WMAP team's cleaned map. We analyse the composition of the maps at each frequency in terms of the relative contribution of dust and synchrotron, and compare the systematic level to the polarised foreground amplitudes. An important question is whether the systematics currently dominate over the foregrounds in the HFI channels, and whether the cleaned maps correlate between frequencies. We then look at the correlation between the foreground components at each frequency in temperature and polarisation and examine the match between the WMAP-derived, the WMAP+Planck-derived, and the Planck-derived CMB polarisation maps. As an additional motivation, at low multipoles the CMB polarised sky is foreground dominated, therefore it is important to investigate the behaviour of polarised component separation even in the presence of significant systematics. The systematics depend on frequency and multipole range, and at lower multipoles may be subdominant to the foreground emission. The parametric fitting described in the previous chapter is more sophisticated than either template fitting or ILC, however these component separation routines provide a useful check for the level of fundamental systematics and the behaviour of the data with differing foreground assumptions.

4.1 Preparing DX8 Maps

Planck data exchanges are released to the science teams in periodic iterations, with each release building on more extensive analysis and preparation. The maps used in this section are the dx8 maps, which are the first maps to be processed after the end of the mission in 2012. The Galactic and point source flags are built using masks derived from a previous DX5 release. Sky maps are produced for each bolometers' intensity map, I,Q,U maps per frequency channel, and I,Q,U maps per detector set. For each set, nominal-survey maps and combined all-survey maps, first/last rings maps, and combined full-ring maps are also produced. The photometric calibration at low frequency is via a template fitting method using the dipole (WMAP 5-year solar dipole and the Planck orbital dipole), and at high frequency with a Galactic calibration. The averaged maps are calculated using an inverse noise-weighing scheme, and are at a resolution of $N_{side} = 2048$, or $\sim 5 \times 10^7$ pixels in Galactic coordinates. For more complete information on the sky map preparation see the early release data processing reports [149] [150], and the 2013 data processing papers [151] [152] [153] [148]. We now describe the bandpass correction process for the LFI 30, 44, and 70 GHz channels.

4.1.1 Bandpass Correction

Planck is optimised to measure temperature anisotropies between 28 and 900 GHz. Polarization measurements are more intricate in that the Stokes parameters cannot be measured directly for each single detector. For intensity maps, it is sufficient to simply combine detector measurements, adjusting for the relative noise and systematic effects between bolometers. Each detector has a particular response to the received signal, so each of the bolometers measure a convolution of the spectrum on the sky with the bandpass of that particular bolometer. This bandpass effect only needs to be corrected in intensity when calibrating the output power photometrically with respect to the CMB dipole. In polarisation, this effect will introduce errors of order 1-3%, depending on which detector set is considered [154]. Therefore, the measured Stokes parameters can differ significantly from the true values across the sky. This effect is particularly pronounced in pixels where the CMB is not the dominant emission (i.e. along the Galactic plane). For temerature the effect is of order $\sim 0.1 - 0.5\%$, which is below the mission goal of calibration systematics $< 1\%$ [18]. In order to correct the Planck polarisation maps, combinations of detectors' spectral responses are calculated and combined into a common value for each pixel associated with each frequency band. There are two main issues with combining detectors in such a manner. Firstly, the detectors each have a different beam function. This can be dealt with by convolving the outputs to a commom beam response, since such a convolution combines information from different pixels. Secondly, each detector will measure a different set of integrated Stokes parameters

$$\mathbf{S} = \int h(\nu) s(\nu) d\nu, \qquad \text{with} \qquad \int h(\nu) d\nu = 1, \tag{4.1}$$

where $h(\nu)$ is the spectral response of the detector and $s(\nu)$ are the Stokes parameters at a single frequency. Each detector will measure a different set of integrated parameters. This second issue does not have a similar treatment. The result of integration across the band does not mesh signals from different pixels. Ultimately this issue is degenerate. For Planck, the correction estimates are based on a multi-frequency physical model of the bandpass mismatch effect, which involves two analysis steps: multi-frequency foreground modelling in temperature, and estimating the coupling of the bandpass mismatch effect from the raw data. The principle instrumental factor controlling bandpass leakage is the effective frequency mismatch between the two paired detectors, $a = (\nu_S - \nu_M)/2\nu_0$, which must be combined with estimates of the leakage amplitude of the foreground emission. Because the leakage amplitude relies on products from component separation, foreground leakage maps are available at no higher resolution than that of the 30GHz channel, and are most reliable at lower resolution. In principle the a-factors can be estimated from the bandpass profiles measured during the pre-flight calibration, but as anticipated more accurate values can be found from the flight data. A significant problem at present is accurate evaluation of the leakage amplitude, which requires not only excellent separation of CMB and foreground emission but also accurate estimates of the foreground spectral index within the detector's frequency band. This is comparable to the mean polarisation fraction along the Galactic plane, as quantified in the bandpass 'a-factors'. The first step has been updated by Leach et. al (Planck internal communication) for dx8 data. The second step still uses a-factors from a previous DX7 data release, which should in future be revised to use the full-survey data. To correct the survey frequency maps, the Healpix correction maps are added to the corresponding data map to correct for the bandpass mismatch. The secondary variance files give an estimate of the error variance per pixel that this correction introduces. The units of the correction maps are K_{CMB}; the units of the variance maps are K^2_{CMB}. Full-survey correction maps are added to the dx8 full survey maps (4 full-sky surveys). Correction estimates for all the individual sky surveys are also available, but not explored in this work. The 70 GHz correction estimates are at the sub μK level in Q and U at high Galactic latitude. As a caveat to this correction, it should be noted that it is not currently understood whether the bandpass correction estimates are really accurate to that level. Given these doubts, there are also additional correction map simulations which are based on extrapolating the 30 and 44 GHz foreground models and could be used for low resolution cosmological analyses. These additional correction models are less than 0.5 μK in polarised intensity at 70 GHz across most of the sky, so low resolution cosmological analyses of the 70 GHz maps could be performed without any bandpass correction applied. For each correction map, a projection map, P, is also calculated. The projection map gives the mapping of the bandpass mismatch leakage to the Stokes Q and U parameter maps. Given an estimate for the bandpass leakage L, where

$$L = \nu_0 \frac{\partial T_{CMB}}{\partial \nu}|_{\nu_0} \tag{4.2}$$

then the Q/U correction map, C, is given by

$$C = L \times P \tag{4.3}$$

The projection map depends on the particular survey pointing and leakage factor for each pixel. The bandpass correction maps added to the full survey maps are shown in Figure 4.1

4.1.2 Degrading Resolution

The bandpass correction and full survey maps are degraded to $N_{side} = 16$ resolution. The 353, 217, 143, and 100 GHz maps are in ring format, and the 30, 44, and 70 GHz are in nested format. The maps are degraded by averaging pixels into larger parent pixels in quadrature (allowing factors of 4 reduction in resolution). All sets of maps are output in ring format and shown in Figure 4.2.

The correction maps are added to the full survey maps, and are shown in Figures 4.3 and 4.4. The bandbass correction applies only for polarisation. The correction maps are at a resolution of $N_{side} = 1024$ giving $\sim 1 \times 10^7$ pixels per Q/U image. The Planck maps are first degraded to $N_{side} = 1024$ before correction, then the corrected maps are degraded to $N_{side} = 16$.

The bandpass correction is largest for the 30 GHz channel due to the increased synchrotron emission at lower frequencies. The Galactic plane exhibits the highest raw correction levels at 10-15 μK dropping to 3-5 μK off the plane (at $N_{side} = 16$). At 44 GHz, the correction in the plane drops to 2-3 μK, and off-plane typically below 0.3 μK. At 70 GHz only a thin Galactic slice $\pm 5^\circ$ exhibits a correction above 1 μK with the off-plane correction typically below 0.2 μK. The fractional correction $f_c^Q = C/Q_\nu$ and $f_c^U = C/U_\nu$ also drops at higher frequencies, but the morphology is distinct. At 30 GHz the highest f_c^Q is again along the plane typically 1-2 peaking at 4-5. Off-plane $f_c^Q = 0.3 - 0.5$. At 44 and 70 GHz f_c^Q varies between 0.05-0.1 across the full sky, with some isolated pixels rising to 0.5. For U the Galactic plane correction is higher, with f_c^U varying between 0.5-0.7, and off-plane f_c^U varies between 0.05-0.1, with a noisier distribution across the sky.

4.1.3 Creating Galactic Polarisation Masks

A set of temperature-based Galactic masks already exist for the dx8 data at various threshold levels, however these are not suitable for polarisation analyses. Given that the foreground emission is strongest at the lowest and highest frequency Planck channels for synchrotron and dust respectively, we make masks from the Q and U data at 30 and 353 GHz. We define a cutoff amplitude A_c, above which pixels are set to zero (similarly for $-A_c$). The effect of changing A_c on the amount of sky retained after the cut f_{sky} is shown in Figure 4.5. For the central channels, above about 10 μK_{CMB}, f_{sky} rises to almost 100% in all but the 217 GHz map (where the dust is now very strong along the plane and hence much of the sky is lost). At 30 and 353 GHz the threshold has to be set higher

to retain the same fraction of the sky, given the brighter foreground signal. A conservative balance between excising enough sky to mitigate the biasing effect of the galaxy, and retaining enough sky for interesting cosmological analysis is a 15% cut, which can be achieved with a threshold set at $A_s \approx 10$ μK for the 30 GHz channel, and $A_s \approx 200$ μK for the 353 GHz channel, illustrating the significantly brighter dust emission at 353 GHz along the plane.

Before the maps are thresholded and the union taken, a Gaussian smoothing is applied. This helps to minimise the noise artifacts in the final mask, and gives less fragmented masks. The 30 and 353 GHz maps are smoothed with a 14° beam before thresholding is applied. The union of Q and U is then taken. The resultant map is shown in Figure 4.6, at various f_{sky} levels, cutting increasing amounts from the sky up to almost 70% in the final image. For more agressive sky cuts, a larger smoothing radius is required to limit fragmentation of the mask, with a 25° beam required for the most agressive 70% sky cut. The 30 and 353 GHz channels are the most foreground-sensitive, and exhibit a higher signal-to-noise level for foregrounds than the central channels, justifying their use as mask templates.

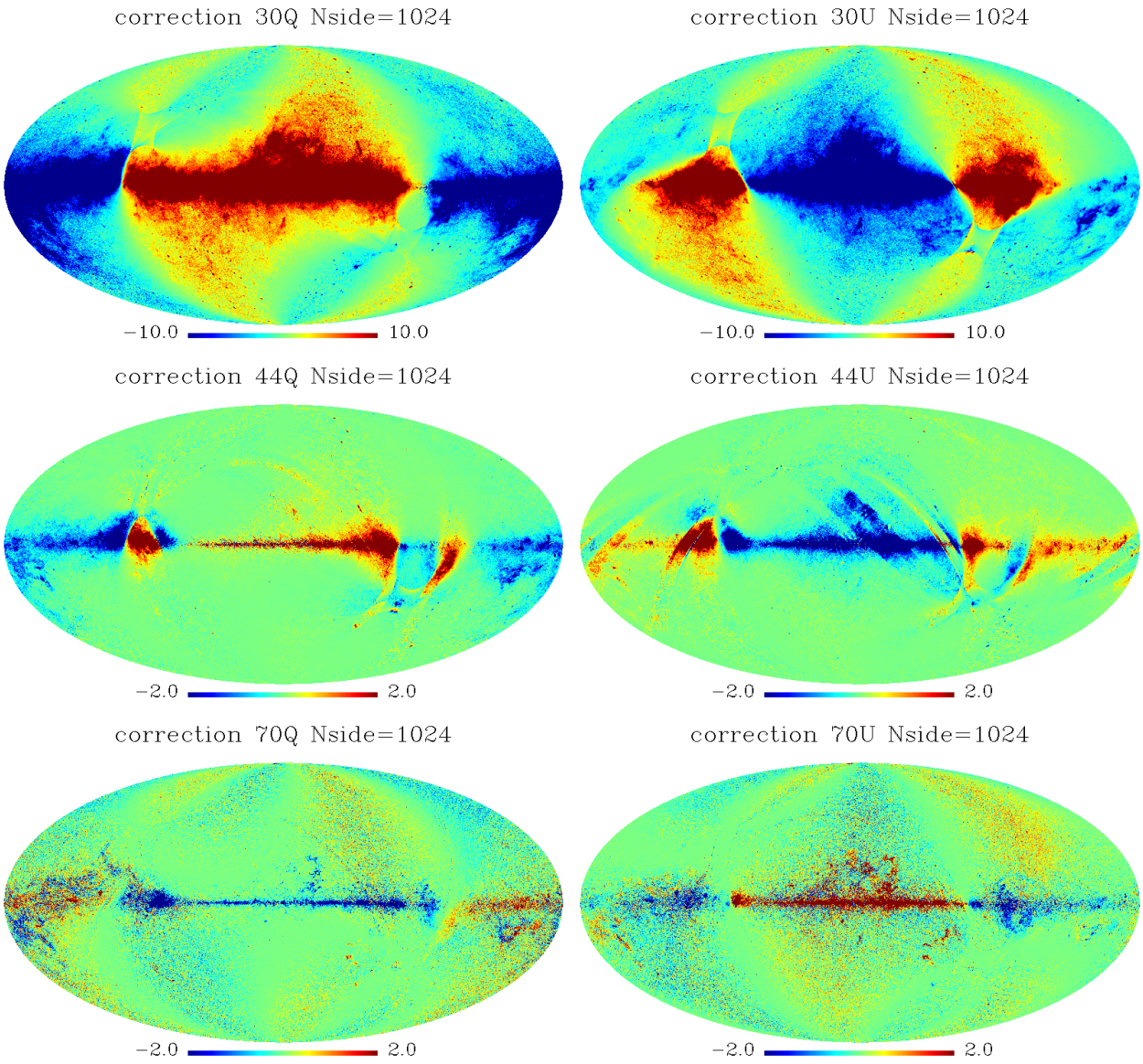

Figure 4.1: Correction maps for LFI channels at $N_{side} = 1024$ resolution, or $\sim 1 \times 10^7$ pixels. The 70 GHz correction is smallest due to the lower foreground amplitude. The correction factor across the Galactic plane for all three frequency channels is much larger than for high Galactic latitudes again reflecting the morphology. Structure from the Planck scanning strategy is clearly visible across all channels.

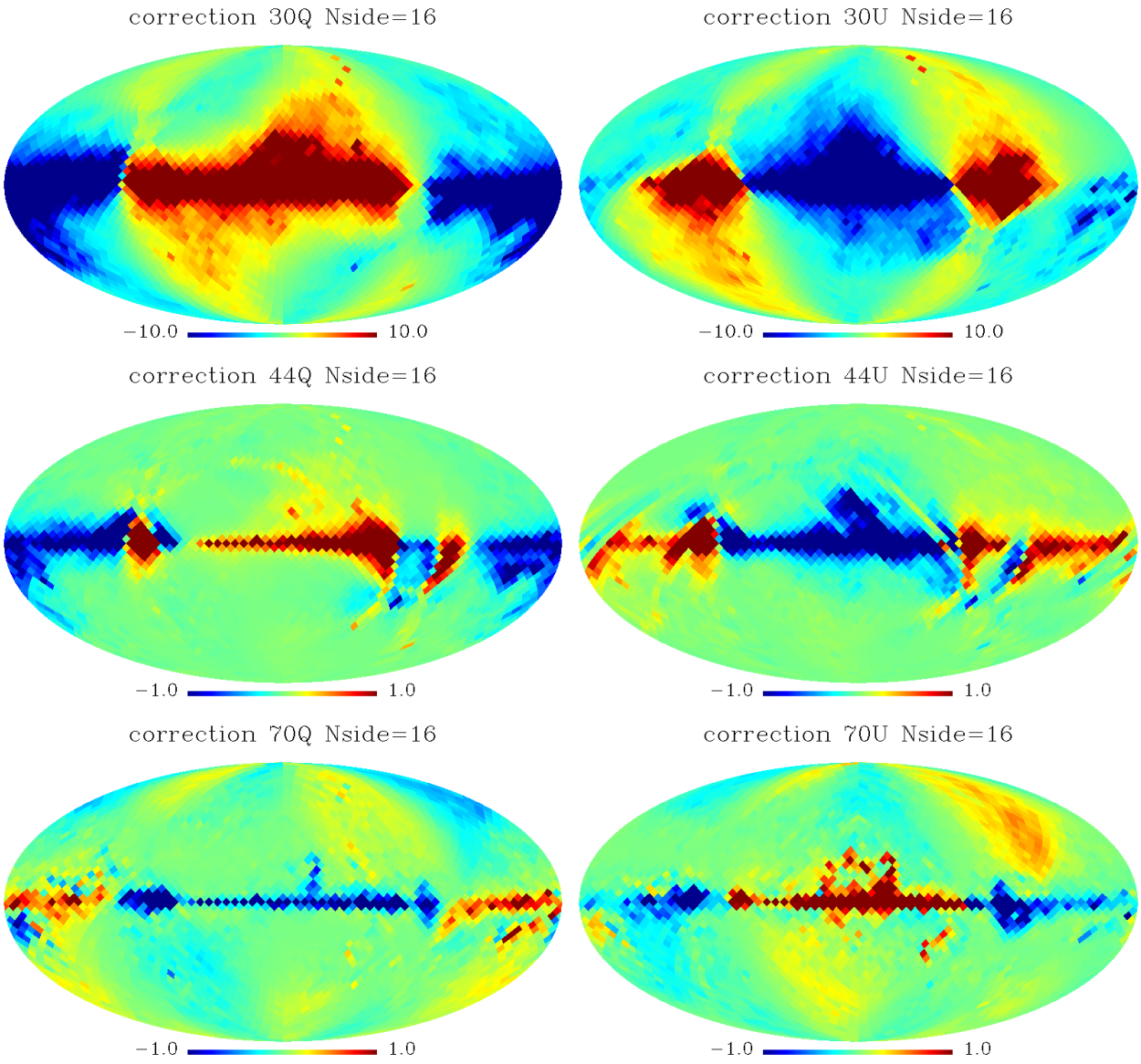

Figure 4.2: Correction maps for LFI channels degraded to $N_{side} = 16$ or 3072 pixels. Maps were degraded with the Healpix routine ud_grade, without harmonic smoothing. This avoids excessive shift of power away from the Galactic plane. The scanning structure is less evident than for high resolution maps in the previous figure but still present.

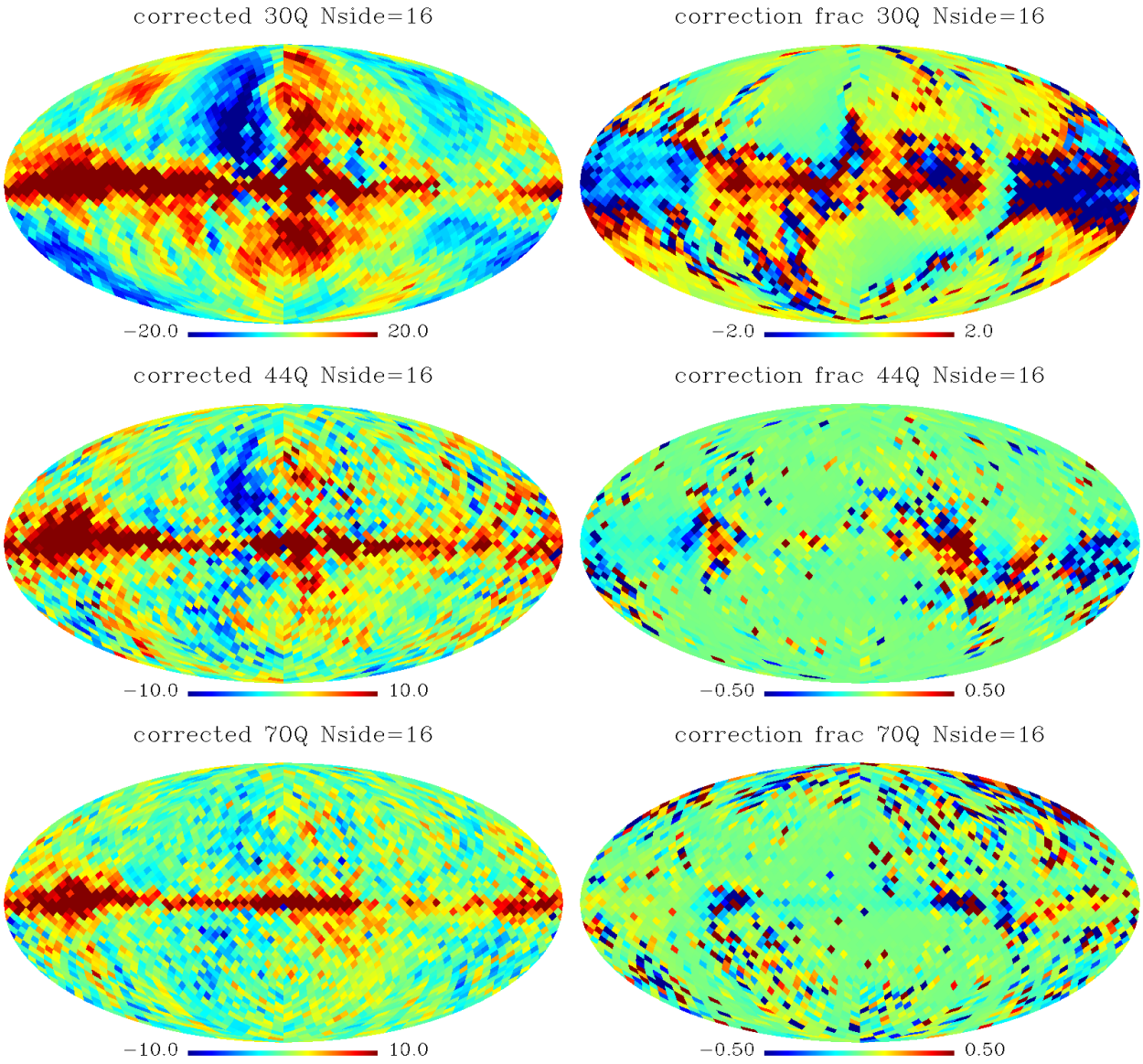

Figure 4.3: Corrected maps for LFI Q channels at $N_{side} = 16$ resolution, or 3072 pixels. The left panels show the corrected maps for Q, and the right panels show the correction fraction $f_c = C^Q/Q_\nu$. The correction factor across the Galactic plane is of the order 1-2 in places, while away from the Galactic plane drops well below unity in regions around the scanning poles. Note the different colour scale for 30 GHz. The largest correction fraction is for 30 GHz.

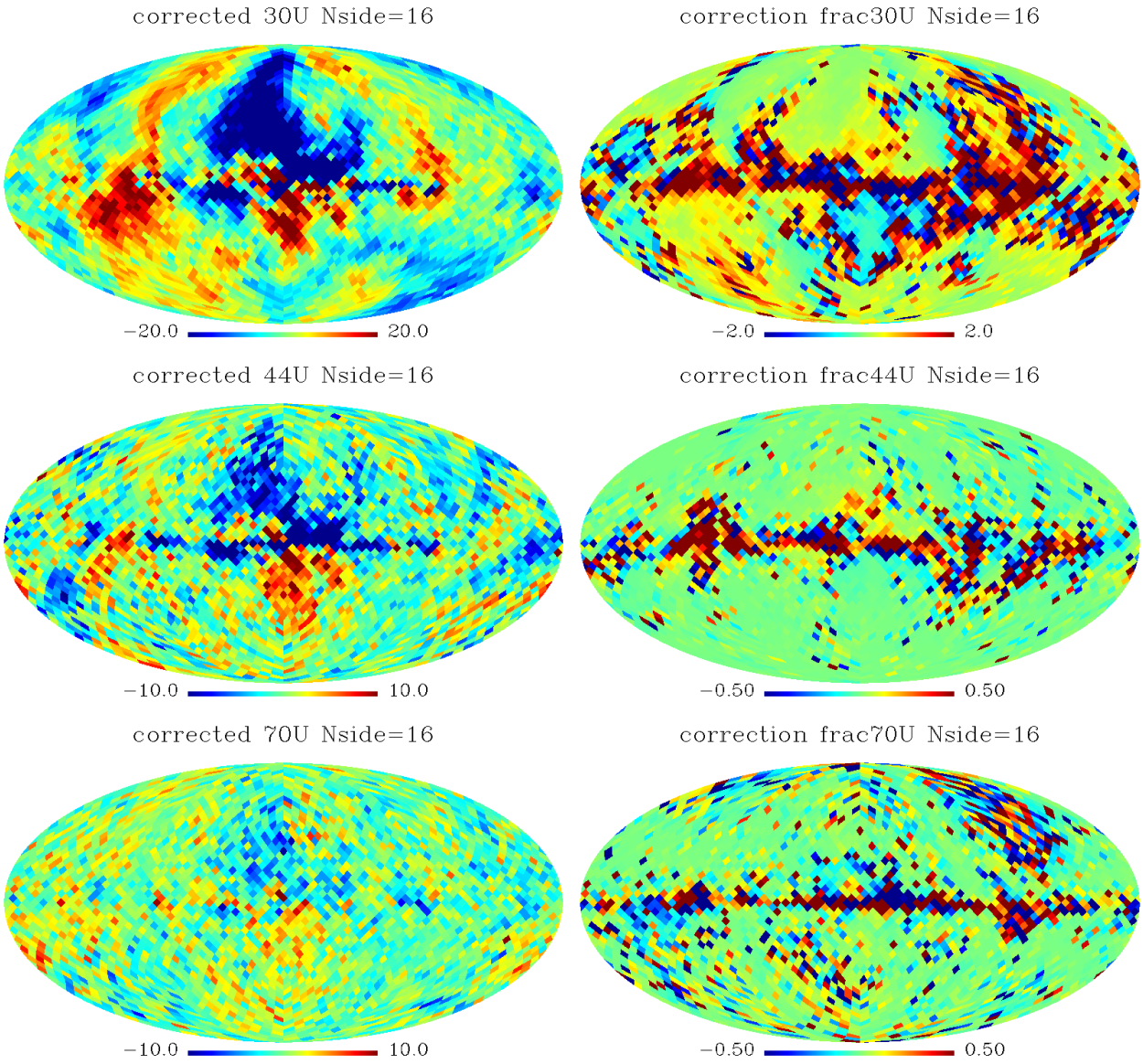

Figure 4.4: Corrected maps for LFI U channels at $N_{side} = 16$ resolution, or 3072 pixels. The left panels show the corrected maps for U, and the right panels show the correction fraction $f_c^U = C/U_\nu$. The correction factor across the Galactic plane is of the order 1-2 in places, while away from the Galactic plane drops well below unity in regions around the scanning poles. Note the different colour scale for 30 GHz. The largest correction fraction is for 30 GHz.

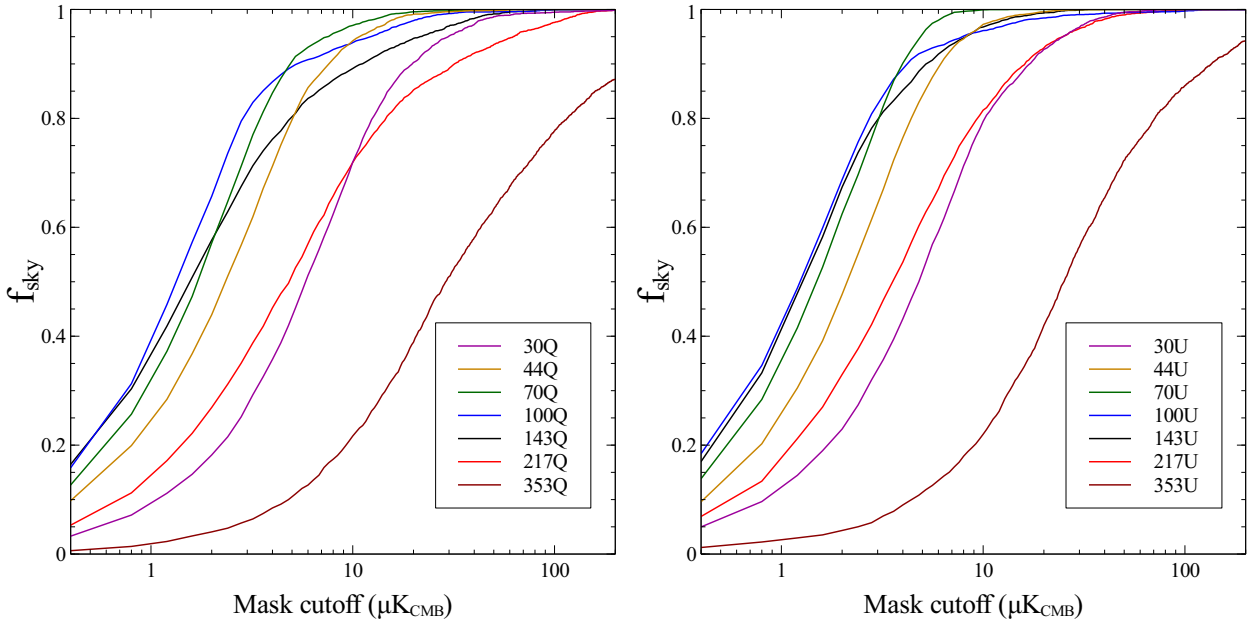

Figure 4.5: The fraction f_{sky} of the full-sky map remaining after removing all pixels with an absolute amplitude greater than the cutoff amplitude (in μK_{CMB}). The left panel shows the results for Q at 30, 44, 70, 100, 143, 217, and 353 GHz. The right panel shows the same for U. All plots are for maps at $N_{side} = 16$ resolution.

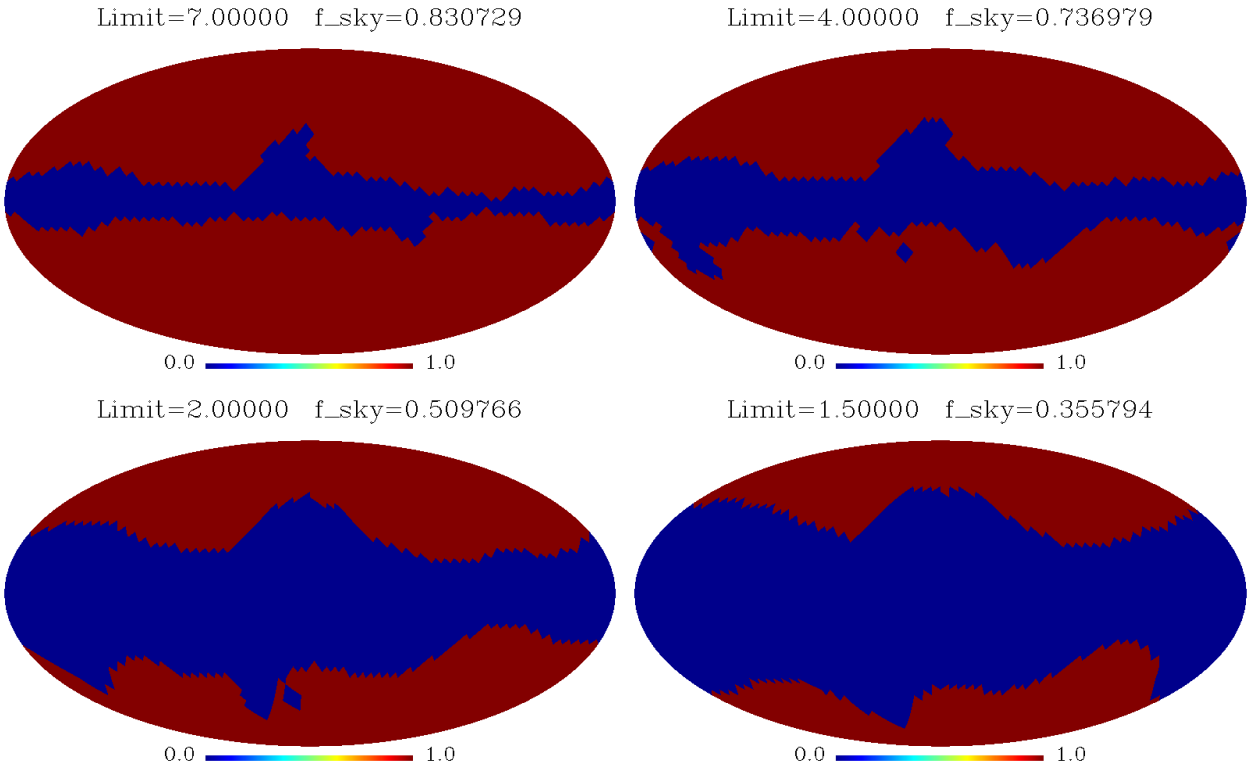

Figure 4.6: A selection of sky masks formed from the union of smoothed, thresholded dx8 30 and 353 GHz maps at a resolution of $N_{side} = 16$. The most conservative mask is smoothed with a 10° beam then thresholded at 7 μK, leaving 83% of the sky, and the most aggressive mask is smoothed with a 25° beam, thresholded at 1.5 μK and leaves only 36% of the sky.

4.2 Comparison with WMAP

It is instructive to analyse the correspondence between WMAP 61 GHz and LFI 70 GHz, not only to check the relative amplitudes for calibration, but also as an initial check for dominant systematics above the foreground level in the LFI 70 GHz data. As a check, both maps are repixellised to $N_{side} = 32$ and shown in Figure 4.7. The corrected maps at this resolution show little sign of the systematics evident in the foreground-cleaned maps. The top panels show WMAP 61 GHz at $N_{side} = 32$ and the second panels show LFI 70 GHz maps at the same resolution. The maps show a high degree of correlation, with slight excess emission in the WMAP 61 GHz data due to the higher synchrotron emission at 61 GHz. The difference maps $Q_{70} - Q_{61}$ and $U_{70} - U_{61}$ are shown in the third panels, and a slight excess from Galactic emission is evident along the plane. Across the full sky the difference maps are noise-dominated and peak at around 15-20 μK near the Galactic centre. Also shown is the absolute difference $A_d = |A^{70} - A^{61}|$ smoothed with a FWHM= 7° beam. The ecliptic plane excess is now much more evident than in the unsmoothed difference maps. The largest A_d values are found at the anti-centres of the Planck/WMAP ecliptic poles, consistent with higher noise levels in these regions, as they are covered less over sky surveys. The lowest absolute difference is found at the ecliptic poles with $A_d \sim 2$ μK. If the systematics have been completely removed, and we assume the WMAP systematics have also been removed, then A_d should resemble the synchrotron emission and noise which is still dominant at 70GHz, which it clearly does not. There is therefore some tension between the WMAP and Planck data at this central CMB-sensitive frequency range.

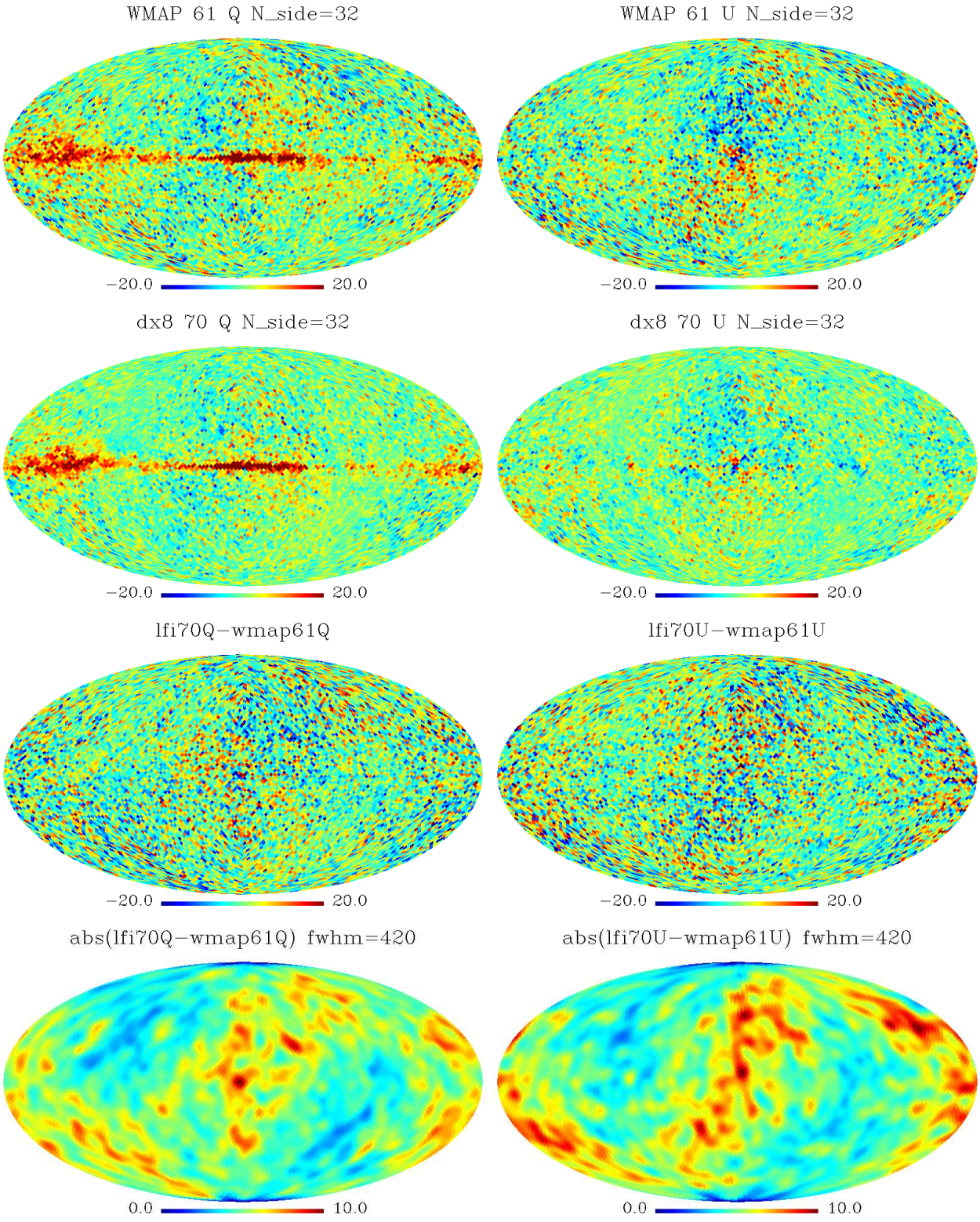

Figure 4.7: Top panels show WMAP 61 GHz channels Q and U at $N_{side} = 32$, second panels show LFI 70 GHz Q and U images, third panels show the difference LFI70-WMAP61 Q and U images. Fourth panels show the absolute difference |LFI70-WMAP61| smoothed with a FWHM=420′ beam.

4.3 Template Fitting

Planck's frequency coverage provides a large lever arm. We can utilise the highest polarisation-sensitive channel at 353 GHz combined with the lowest WMAP channel at 23 GHz, to remove foregrounds from central-channel polarisation maps using a simple template fitting method. One advantage of choosing a template fitting approach is that we can generate CMB polarisation maps at several frequencies, depending on our choice of central channel. This allows for consistency checks to verify whether any detected feature of the data appears throughout the LFI/HFI channels or is a feature of only one channel. Use of only internal (i.e. Planck) templates reduces any systematic effect related to WMAP, but also increases the noise, as the templates themselves are noisy, so subtracting them from data will increase the resultant noise. An overall calibration is unimportant since it just modifies the template coefficients (provided the primordial CMB contribution is small at the template frequencies). Using the low-frequency external WMAP template acts as a useful cross-check and calibration tool, and will provide a better low-resolution tracer of synchrotron emission than the LFI 30 GHz channel, which is a good reason to use it as a low frequency template.

The template subtraction method involves subtracting scaled versions of the 23 GHz and the 353 GHz channel polarisation maps from a central channel while minimizing the variance to leave the CMB+noise signal. The resultant map is then scaled to give a unity response to the CMB by a corrective multiplication (as subtracting some percentage of the 353 and 23 GHz maps will also subtract some CMB). The multiplicative factor with which to subtract the template maps will be of order a few %.

The template-fitting CMB estimator is defined as the subtraction of a linear combination of templates t_i from the original map at frequency ν:

$$\hat{T}_{CMB}(\nu, p) = T(\nu, p) - \sum_{i=1}^{N_t} \beta_i^\nu t_i(p), \tag{4.4}$$

where β_i^ν are the coefficients of each template. The coefficients are found by minimising the variance of $\hat{T}_{CMB}$:

$$E(\nu) = \sum_p \left(T(\nu, p) - \sum_{i=1}^{N_t} \beta_i^\nu t_i(p) \right)^2 . \tag{4.5}$$

In thermodynamic units, the CMB response is unity in each frequency channel, therefore a suitable multiplicative factor applied to the cleaned map will restore a unity response to the CMB as $T_{CMB} = D\hat{T}_{CMB}$. We first clean the WMAP data with the Planck high-frequency dust map before cleaning the central Planck channels.

4.3.1 WMAP23-WMAP61-HFI353 Results

We set the low frequency template as the WMAP 7-year 23 GHz full-sky map. WMAP 7-year data maps are calculated as a pixel-by-pixel mean of the seven single year maps weighted with N_{obs}. The maps have also been smoothed to 1° resolution. The 23 GHz map is repixellised to $N_{side} = 16$ and the weights β are found. The plot of the distribution in βs is shown in Figure 4.9, and the weights are given in Table 4.1. The slight degeneracy in $\beta_{23} - \beta_{353}$ is more evident for Q than for U, due to the stronger signal across the Galactic plane originating both from synchrotron and dust emission. The U distribution map is less degenerate as there is less emission across the Galactic plane, and less similarity between the dust and synchrotron emission.

Map combination	β^Q_{23}	β^Q_{353}	β^U_{23}	β^U_{353}
WMAP23-WMAP61-HFI353	0.053	0.006	0.062	0.0072
-Unmasked	0.049	0.0074	0.062	0.004
WMAP23-LFI70-HFI353	0.029	0.0004	0.041	0.0076
-Unmasked	0.041	0.0082	0.045	0.0042
WMAP23-HFI100-HFI353	0.023	0.0164	0.013	0.0178
-Unmasked	0.094	0.0158	0.000	0.0198
WMAP23-HFI143-HFI353	0.000	0.0375	0.000	0.040
-Unmasked	0.038	0.037	0.038	0.008

Table 4.1: Template fitting coefficients for various combinations of WMAP and Planck full-sky maps in Q and U. The mask used is the 30 and 353 GHz union described in the text. Template fitting without a Galactic mask significantly alters the template coefficients due to the increased emission along the plane for both synchrotron and dust.

The template cleaned maps are shown in Figure 4.9. Both Q and U maps show significant reduction in the foreground power and particularly for Q strong emission around the Galactic plane is mostly removed. More power across the plane remains in U, however the strong Galactic spur region remains somewhat contaminated. Maps smoothed with HEALPix i_smoothing are also shown, with a FWHM= $420'$ beam. The smoothing lessens the visual impact of the residual noise in the maps and allows for easier identification of systematics. The difference between the WMAP 61 GHz and the cleaned 61 GHz maps is highly evident. It is instructive to compare the WMAP foreground-cleaned Q/U maps to the cleaned maps obtained with the 23-353 GHz template cleaning method. This template cleaning method is very fast, taking a couple of seconds on LEDA (a high-performance development cluster), and could easily be performed quickly on the full resolution WMAP data, at $N_{side} = 512$. The advantage of degrading is clear in the mitigation of noise, which is still very apparent in both WMAP and HFI maps.

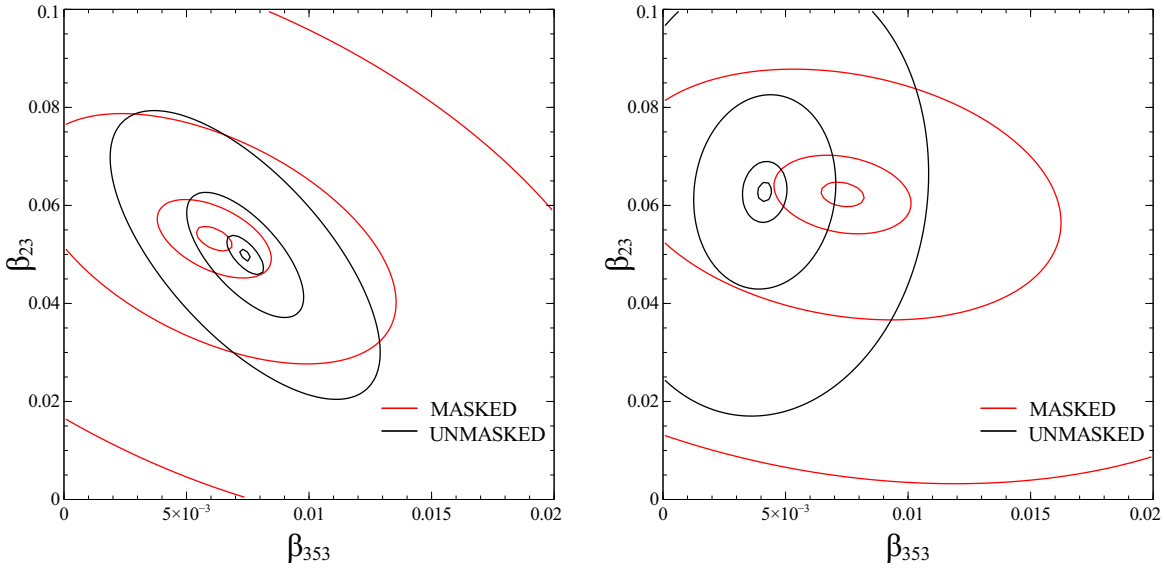

Figure 4.8: Template cleaning with WMAP 23, WMAP 61, HFI 353 GHz: 1) Calculated 2D distribution for template subtraction plotting β_i^{353} against β_i^{23}. Contours are 1%, 0.1%, 0.05% and 0.001% percentage differences in rms. Left panel is for Q and right panel is for U. The minimum distribution is shown in Table 4.1.

4.3.2 WMAP23-LFI70-HFI353

The central CMB channel is now switched from the WMAP 61 GHz channel to the LFI 70 GHz channel. Given that we are now using LFI data as our primary CMB source, the cleaned template can be correlated with the WMAP-estimated CMB, and the correlation information is given in Table 4.2. The correlation is consistent with zero, and illustrates a worrying mismatch between the Planck data at 70 GHz and the WMAP-cleaned data. At 70 GHz, the synchrotron emission is still the dominant emission mechanism and we should expect that the actual contribution from the 23 GHz channel will be stronger, both in the plane and across the sky. With masking, for Q 2.9% of the synchrotron and 0.04% of the dust templates are subtracted, and for U, 4.1% and 0.7% respectively. The difference in Q and U coefficients is large, and this arises from the stronger emission in the Q data for synchrotron and dust. Omitting the Galactic mask increases all the template factors, due to the higher foreground emission along the Galactic plane.

4.3.3 WMAP23-HFI100-HFI353 Results

We now switch the central CMB channel to HFI 100 GHz. The minimum distribution is found as before, and the multiplicative factors are again detailed in Table 4.1 At 100 GHz, the dust emission is much stronger than at either 61 GHz or 70 GHz, while the synchrotron emission has dropped sharply. For Q, 2.3% and 1.6% of the 23 and 353 GHz map are subtracted respectively, and for U 1.3% and 1.7%. When the subtraction is calculated without a Galactic mask, β_{23}^U drops to zero, indicating that the best fit is achieved only subtracting dust emission. This is due to

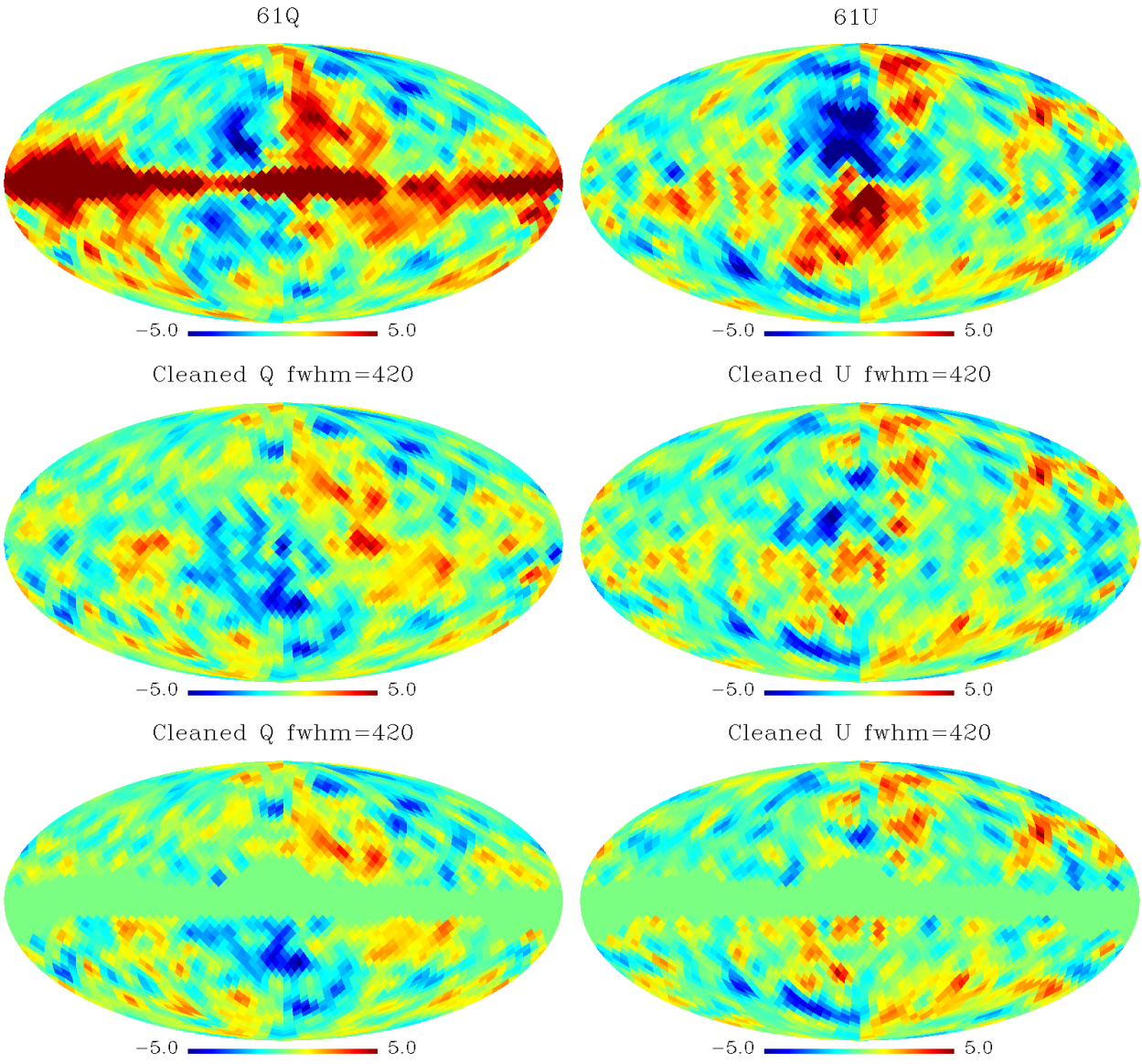

Figure 4.9: Template cleaning with WMAP 23, WMAP 61, HFI 353 GHz: 1)WMAP 61 GHz channels Q and U, 2) Template subtracted Q and U images without masking, 3) Masked template subtracted Q/U, smoothed with a fwhm of 7°.

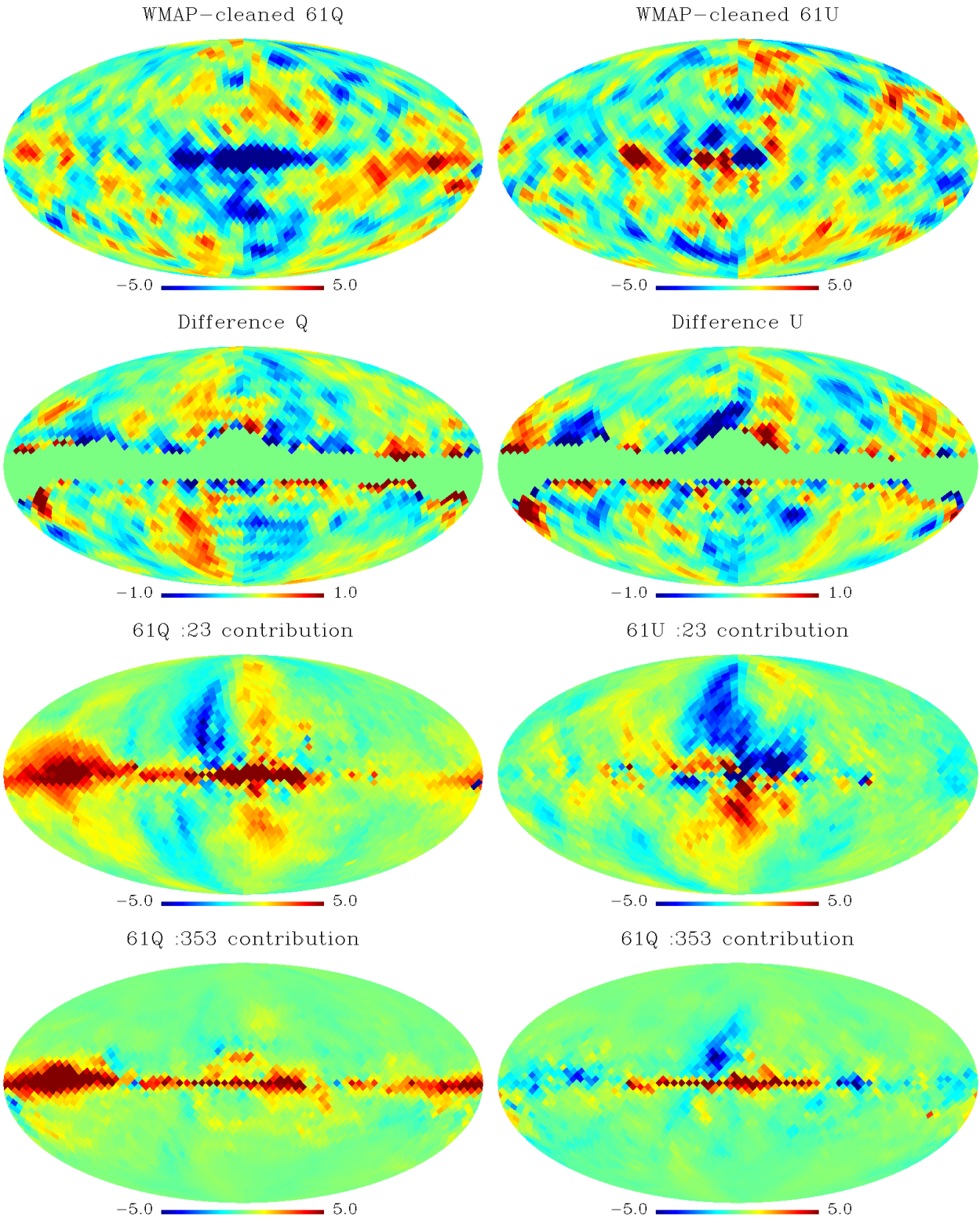

Figure 4.10: Template cleaning with 23, 61, and 353 GHz: Contributions from 23/353 maps into 61 GHz calculated from template fitting. Top panels show the cleaned 61 GHz Q and U, second panels show the difference between the cleaned maps and the WMAP-cleaned maps, third panels show the 23 GHz contribution, and bottom panels show 353 GHz contribution.

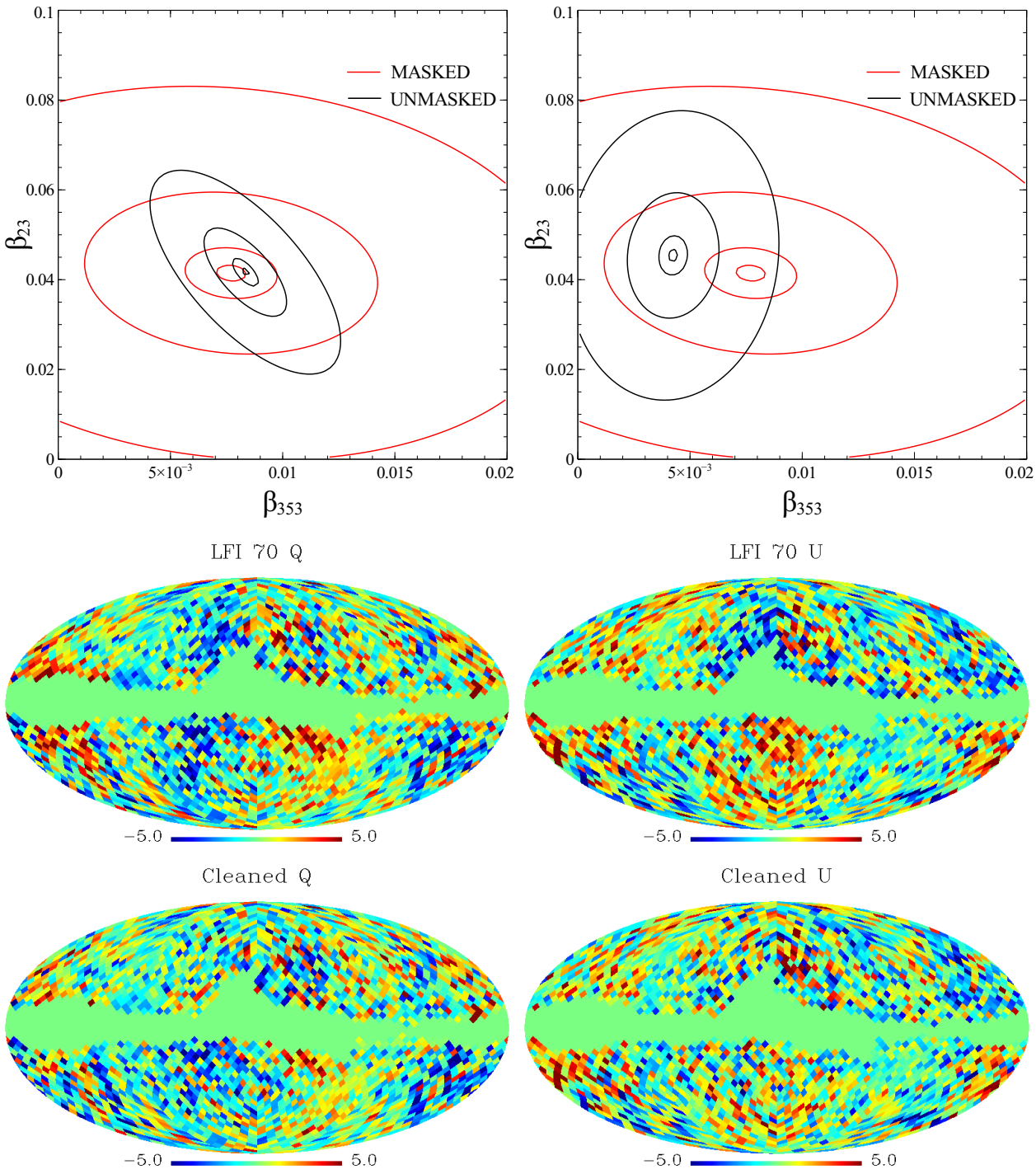

Figure 4.11: Template cleaning with WMAP 23 GHz, LFI 70 GHz, and HFI 353 GHz: Top panels show the calculated 2D distribution for template subtraction plotting β_i^{353} against β_i^{23}. Contours are 1%, 0.1%, 0.05% and 0.001% percentage differences in rms. Left panel is for Q and right panel is for U. The minimum distribution is shown in Table 4.1. Second panels show LFI 70 GHz Q and U, and third panels show the template cleaned CMB estimation.

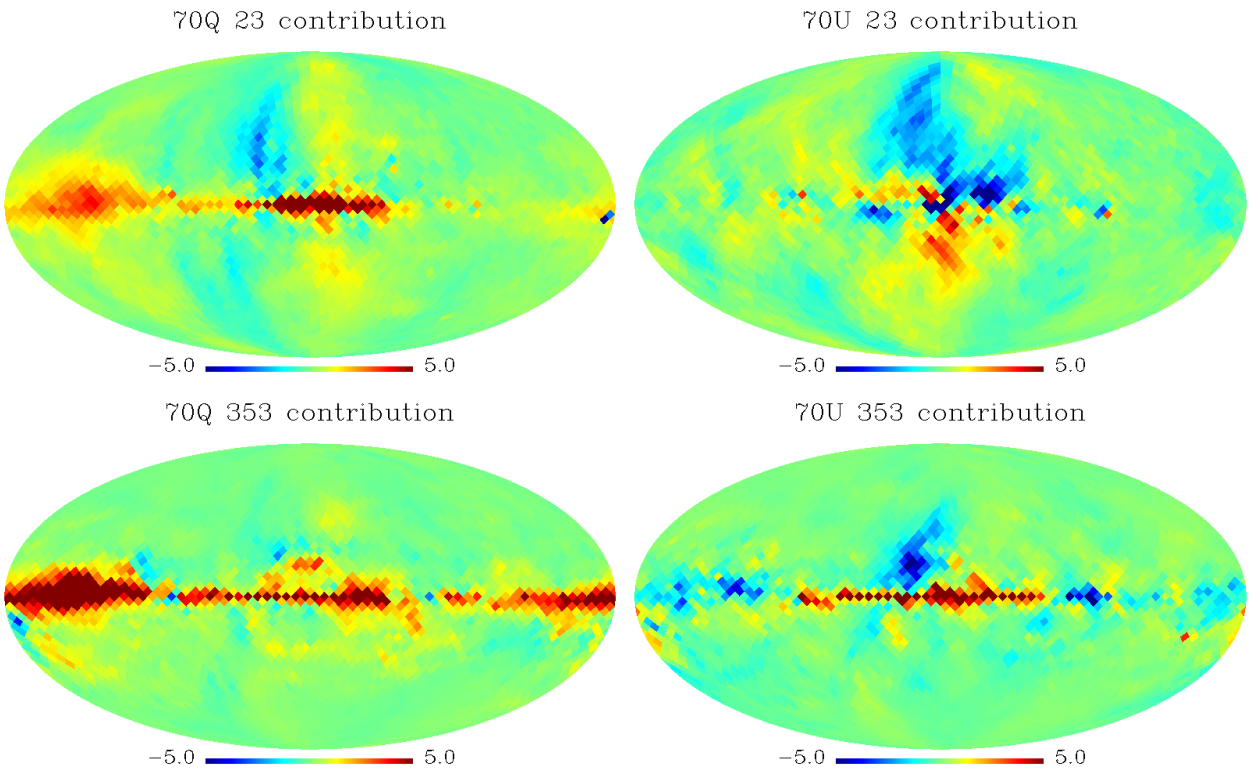

Figure 4.12: Template cleaning with WMAP 23 GHz, LFI 70 GHz, and HFI 353 GHz. Upper panels show the contribution from 23 GHz Q and U, and bottom panels show contribution from 353 GHz Q and U.

the increased emission along the Galactic plane being dominated by the sharp increase in dust emission, which drives the solution towards a dust-only separation. If masking is not applied, the foreground-dominated galactic plane has high weight. The shift in subtraction factors due to the masking is significant and the resultant CMB maps look markedly different to the unmasked case. In either case there appears to still be some contamination from systematics, and the Q and U maps appear somewhat correlated (particularly in the lower Galactic hemisphere). HFI correction maps will later become available which can be used to correct for leakage in 100, 143, 217, and 353 GHz which will be useful for these subctraction studies.

4.3.4 WMAP23-HFI143-HFI353

Using the same masking as before, we switch the central channel to 143 GHz. The subtraction factors are found as before and displayed in Table 4.1. For the masked maps, there is no contribution from 23 GHz and a 3.75 and 4.0% contribution from the 353 GHz Q and U map respectively. However when we clean the unmasked maps, the contribution from 23 GHz rises to 3.8% for both Q and U. β^Q_{353} drops slightly to 3.7% and β^U_{353} drops to 0.8%. This is due to picking up a synchrotron contribution in the galactic plane which is otherwise inside the masked region.

We now have template-cleaned CMB maps at 70, 100, and 143 GHz that we can compare to the WMAP polarisation maps in V and W bands, 70 and 90 GHz respectively. The WMAP team provide foreground-cleaned maps as part of the LAMBDA archive. WMAP foreground-reduced maps have been produced by removing a foreground model from the seven-year maps using the foreground template model discussed in Hinshaw et.al. [155] and Page et.al. [156]. Synchrotron, free-free, and dust emission templates were modelled and then subtracted from the seven-year data. The WMAP team claim that that the set of maps with the foreground removed retain WMAP's noise characteristics. It is useful to characterise the level of WMAP-Planck agreement in the cleaned maps, and this can be achieved with a simple correlation coefficient. A joint mask is produced from the union of the WMAP mask and the HFI-derived mask described earlier, and both sets of maps are smoothed with a 7° beam. Concatenated vectors $A_{\rm WMAP}$ and $A_{\rm TC}$ are produced for the points in the WMAP-cleaned and Planck foreground-cleaned datasets outside the joint mask. These vectors are then correlated using the linear Pearson correlation coefficient. The correlations are shown for the cleaned maps in Q and U in Table 4.2.

The strongest correlation is found for the 23-61-353 GHz combination with $P_Q = 0.61$ and $P_U = 0.75$ for the WMAP V channel. This is not surprising, as the same synchrotron template has been used as in the WMAP team's analysis, but with a Planck dust template. The WMAP analysis uses a theoretical model for the Galactic magnetic field which does not reflect the true distribution of the dust emission. The discrepancy between the two datasets should therefore be described by the difference between the 353 GHz dust emission and the FDS dust model used by the WMAP team, plus noise and systematics. The Planck 353 GHz channel will act as a better tracer of the dust

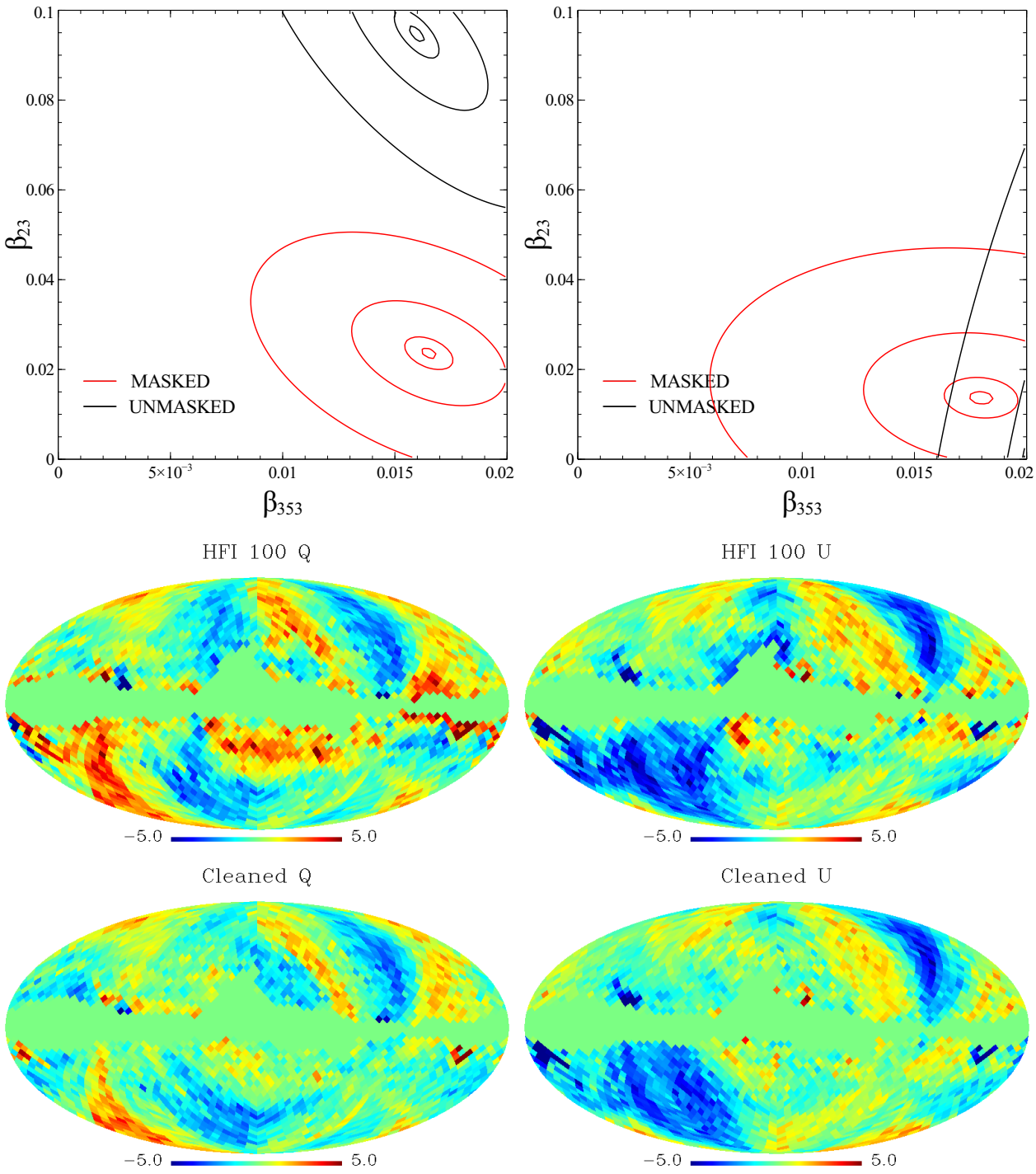

Figure 4.13: Template cleaning with WMAP 23 GHz, HFI 100 GHz, and HFI 353 GHz: Top panels show calculated 2D distribution for template subtraction plotting β_i^{353} against β_i^{23}. Contours are 1%, 0.1%, 0.05% and 0.001% percentage differences in rms. Left panel is for Q and right panel is for U. The minimum distribution is shown in Table 4.1. Second panels show HFI 100 GHz channels Q and U, third panels show the template cleaned CMB estimation.

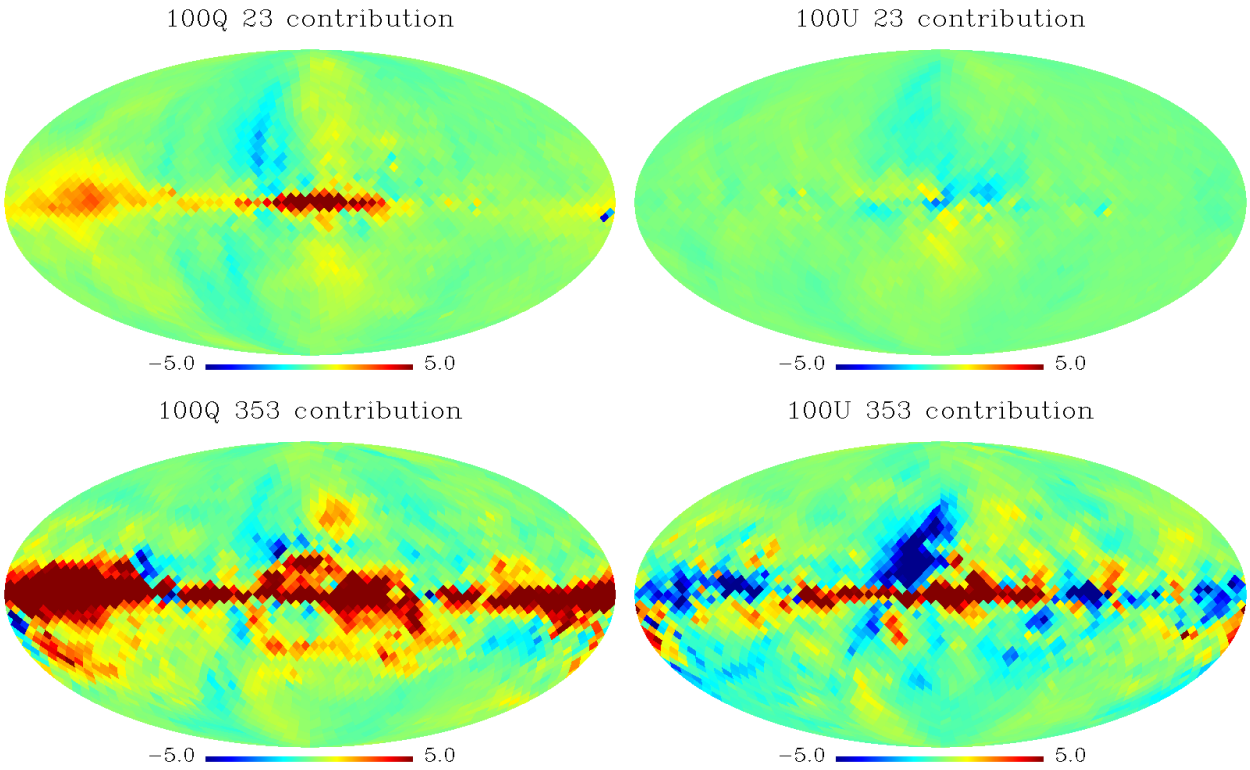

Figure 4.14: Template cleaning with WMAP 23 GHz, HFI 100 GHz, and HFI 353 GHz. Upper panels show the contribution from 23 GHz Q and U, and bottom panels show contribution from 353 GHz Q and U.

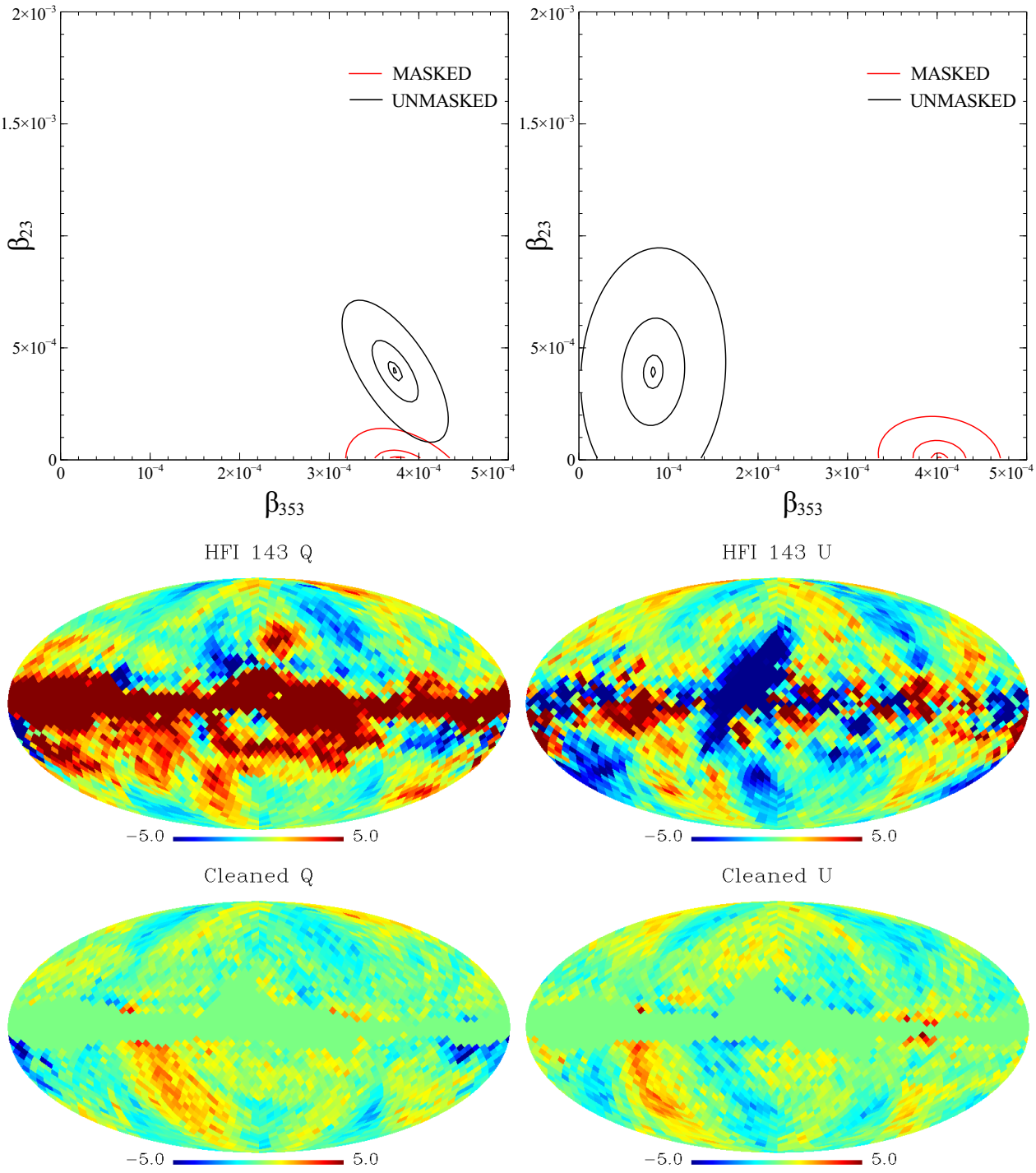

Figure 4.15: Template cleaning with WMAP 23 GHz, HFI 143 GHz, and HFI 353 GHz: Top panels show calculated 2D distribution for template subtraction plotting β_i^{353} against β_i^{23}. Contours are 1%, 0.1%, 0.05% and 0.001% percentage differences in rms. Left panel is for Q and right panel is for U. The minimum distribution is shown in Table 4.1. Second panels show HFI 143 GHz channels Q and U, third panels show the template cleaned CMB estimation.

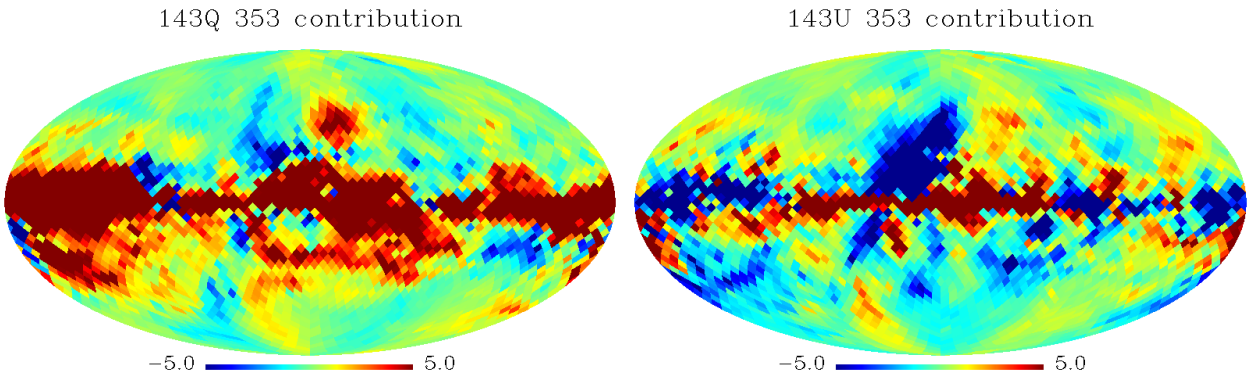

Figure 4.16: Template cleaning with WMAP 23 GHz, HFI 143 GHz, and HFI 353 GHz, showing contribution from 353 GHz Q and U. There is no contribution from 23 GHz so the zero plot has been omitted.

emission and so this estimate of the CMB should be more reliable than the WMAP-only cleaned CMB. Using the same dust model to clean the LFI 70 GHz data would give a useful handle on the residuals between the two datasets without the propagation of dust mismatch.

The correlation between the 23-70-353 GHz combination and the WMAP data is very low, and in fact for U shows a small amount of anti-correlation of 10%. This implies a problem either with the WMAP/Planck cleaned data or a mismatch between the fitted dust model with noise. Even at $N_{side} = 16$ noise is a significant component, and the residuals between the datasets are very noisy. With 100 GHz as the central channel, the two datasets are consistent with no correlation for Q or U, again suggesting that either the WMAP-fitted dust model is very wrong or the HFI systematics and noise dominate over the CMB. At 143 GHz, the correlation rises to about 30% for Q with the V channel, and 10% for the W channel, which is the highest correlation for a Planck-cleaned map. All correlation factors are calculated outside the mask and would increase if no mask is used due to the residual Galactic emission correlating between WMAP and Planck. The Planck data at low resolution are currently dominated by systematics - in the case of HFI, potentially dipole leakage from gain errors. We can infer that these are from the Planck data due to the large differences between 70-143 GHz. We therefore have to conclude that the Planck data are not currently suitable for such analyses. The next section helps to demonstrate that it is also unlikely to be a problem caused by the simplicity of the foreground subtraction.

Correlated maps	WMAP V Q	WMAP V U	WMAP W Q	WMAP W U
WMAP V Q	0.610	-	0.510	-
WMAP V U	-	0.750	-	0.660
LFI 70 Q	-0.023	-	-0.030	-
LFI 70 U	-	-0.092	-	-0.110
HFI 100 Q	0.005	-	0.006	-
HFI 100 U	-	-0.016	-	-0.014
HFI 143 Q	0.296	-	0.332	-
HFI 143 U	-	0.096	-	0.120

Table 4.2: Pearson correlation coefficients between Planck-cleaned and WMAP-cleaned CMB maps. WMAP V/W are the WMAP 61 and 90 GHz seven-year data. Maps are smoothed with a 7° beam, and a joint mask created as the union of the WMAP and HFI masks described in the text. The highest correlation with the WMAP data is for 61 GHz cleaned with 353 GHz and 23 GHz.

4.4 Comparison with ILC

The standard method to produce a so-called internal linear combination map (ILC) assumes nothing about the particular frequency dependencies or morphologies of the foregrounds. Instead, a CMB map is reconstructed by co-adding the data at multiple frequencies (convolved to a common angular resolution) with a set of weights that minimises the final variance of the map. The ILC method as defined by Bennet 2003 [44] is based on a simple premise: suppose there are k observed CMB maps at different frequencies (but with identical beams), and the aim is to suppress foregrounds and noise. Each of the k maps may be written (in thermodynamic temperature) in the form $T(\nu_k) = T_{\rm CMB} + T_{\rm residual}(\nu_k)$, where $T_{\rm CMB}$ and $T_{\rm residual}(\nu_k)$ are statistically independent. Therefore, if we now form the linear combination

$$T = \sum_{i=1}^{k} w_i T(\nu_i), \tag{4.6}$$

and require that

$$\sum_{i=1}^{k} w_i = 1, \tag{4.7}$$

the resulting map may be written as

$$T = T_{\rm CMB} + \sum_{i=1}^{k} w_i T_{\rm residual}(\nu_i). \tag{4.8}$$

Thus, the response to the CMB signal is always equal to unity since it is independent of the frequency, and the $k-1$ free weights may be chosen to minimise the impact of the residuals. Assuming the CMB component is statistically independent of the foregrounds and the noise, one convenient measure for this is simply the variance of T,

$$\mathrm{Var}(T) = \mathrm{Var}(T_{\rm CMB}) + \mathrm{Var}\left(\sum_{i=1}^{k} w_i T_{\rm residual}(\nu_i)\right). \tag{4.9}$$

The internal linear combination method may now be defined succinctly in terms of Equations 4.6 and 4.7, where the weights are determined by minimising the variance in Equation 4.9.

We compute the weights with the downhill minimisation routine amoeba, which uses a simplex-stepping algorithm to move around the k-dimensional weight space and find the optimum weighting. It is also important with such methods to factor in Galactic masking, which can have a large effect on the resultant cleaned CMB map. If the Galactic plane is heavily contaminated with foreground emission, the combination procedure will over-subtract maps where this emission is strongest, to minimise the global variance. We apply the first polarisation mask shown in Figure 4.6 before solving for the weights.

4.4.1 ILC Results

The results of the ILC procedure are shown in Table 4.3. We use different combinations of maps to explore the effect this has on the fitting coefficients. We first fit using all seven Planck channels, which should produce the optimum foreground-free CMB estimation for Q and U. We can also form individual fits for just the LFI channels, just the HFI channels, and just the central CMB channels i.e. 70, 100, and 143 GHz. We then compute the correlation between the ILC solutions and the WMAP-cleaned CMB estimations, also shown in Table 4.3. It is also of interest to examine the pure-LFI and pure-HFI ILC solutions for differences in the visual level of systematics, since the LFI and HFI operate with different detector technology, beams, and readout electronics, and will therefore have different systematic errors.

The full Planck ILC solution places the largest weight on the 143 GHz channel at 58% for Q and 69% for U respectively, with the next largest weight on the 100 GHz channel at 40% for Q and 27% for U. The remaining frequency channels essentially act as high and low-frequency foreground templates. All the weights are smaller than unity and so the instrument noise is not stongly amplified in the ILC map. As expected, the pure-LFI solution weights the 70 GHz channel with almost unity weight, with the 30 and 44 GHz channel providing a synchrotron template at the

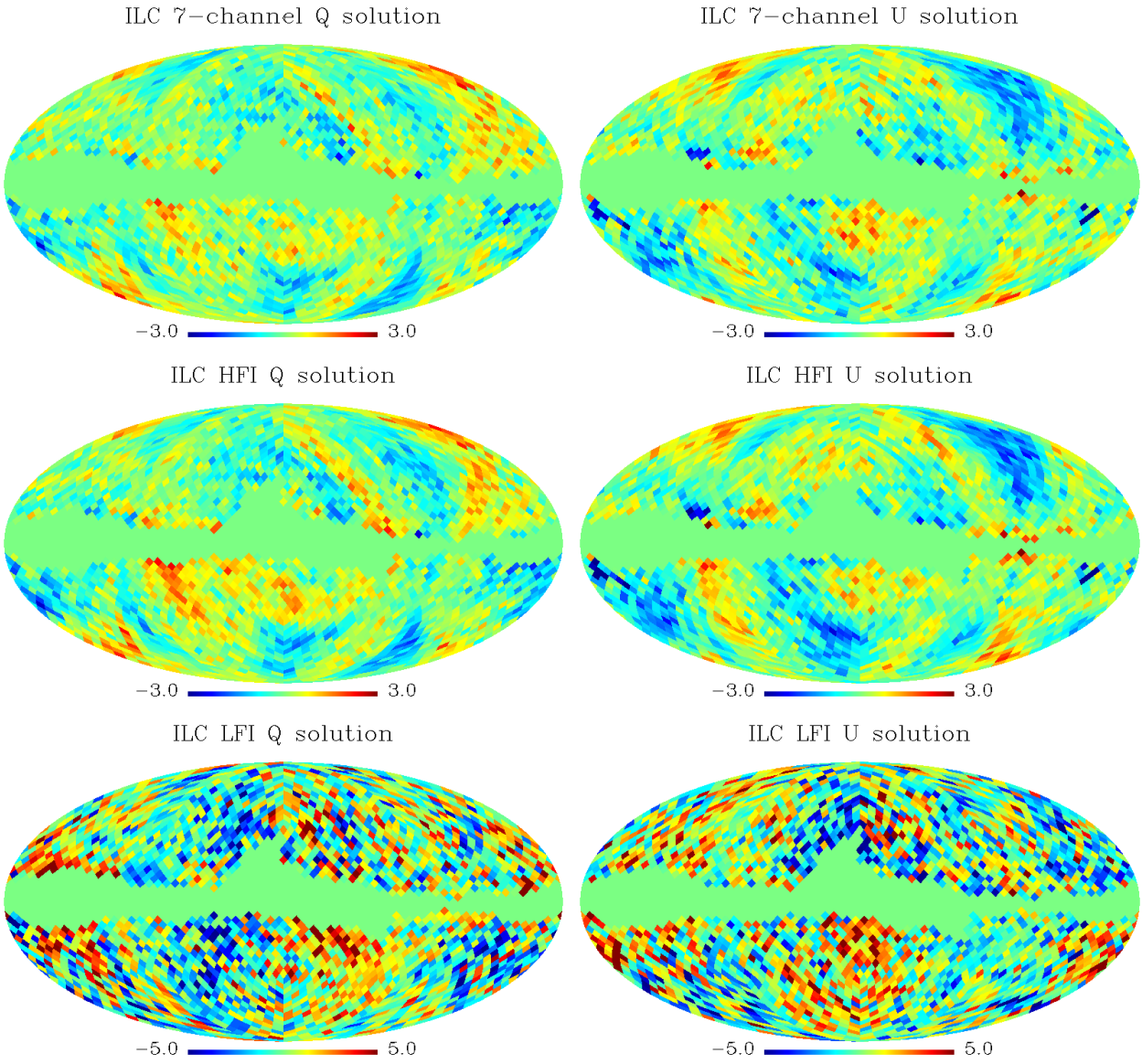

Figure 4.17: ILC solutions for Q and U. Top panels show the full 7-channel Planck solution, middle panels show the solution for just HFI channels, and the lower panels show the LFI solution. The HFI solution should exhibit residual synchrotron emission, and the LFI solution should exhibit residual dust emission.

Channel set	30	44	70	100	143	217	353	P_V	P_W
Full Q	-0.018	0.044	0.100	0.400	0.581	-0.088	-0.020	0.275	0.308
Full U	-0.007	0.021	0.124	0.266	0.694	-0.073	-0.024	0.075	0.098
LFI Q	1.4e-4	3.5e-4	0.9995	-	-	-	-	-0.051	-0.063
LFI U	-1.1e-4	-1.6e-4	1.0002	-	-	-	-	-0.087	-0.107
HFI Q	-	-	-	0.458	0.655	-0.090	-0.022	0.315	0.354
HFI U	-	-		0.311	0.794	-0.078	-0.027	0.101	0.130
70-143 Q	-	-	0.322	0.554	0.123	-	-	0.028	0.027
70-143 U	-	-	0.313	0.438	0.248	-	-	0.052	0.054

Table 4.3: ILC component separation coefficients for different sets of Planck dx8 data. P is the Pearson correlation coefficient calculated with the WMAP maps..

sub-percent level, consistent with the template fitting approach (template fitting is akin to ILC with three channels). For the pure HFI case, again less weight is given to the 100 GHz channel over the 143 GHz channel, with 46% and 66% for Q, and 31% and 79% for U respectively. Again all weights are less than unity thus minimising the amplification of instrumental noise. Finally, performing ILC with just the central three channels produces a fit that similarly weights all three channels with 31% for 70, 44% for 100, and 25% for 143 GHz (U). The highest correlation with the WMAP data is produced for the pure HFI case with a 32% and 35% for Q with V-band and W-band, and 10% and 13% for U.

4.5 Parametric Fitting

We now apply the parametric fitting procedure described in Chapter 2 to the dx8 data to separate components and recover an estimate of the CMB, synchrotron, and dust emission, along with associated spectral indices for both foregrounds. We use all seven polarisation channels and set the input variance of the spectral indices to the values obtained for the $N_{side} = 16$ dx8 maps off-plane in polarisation. Recall that the basic individual pixel likelihood is modified by the inclusion of prior assumptions about the distribution of the foreground spectral indices as:

$$-2\ln(\mathcal{L}) = \chi^2 + c \tag{4.10}$$

with

$$\chi^2 = \frac{1}{2}(d_i - s_i)^T N^{-1}(d_i - s_i) + \frac{(\beta_{s,i} - \bar{\beta}_s)^2}{2\Delta\beta_s^2} + \frac{(\beta_{d,i} - \bar{\beta}_{d,i})^2}{2\Delta\beta_d^2}, \tag{4.11}$$

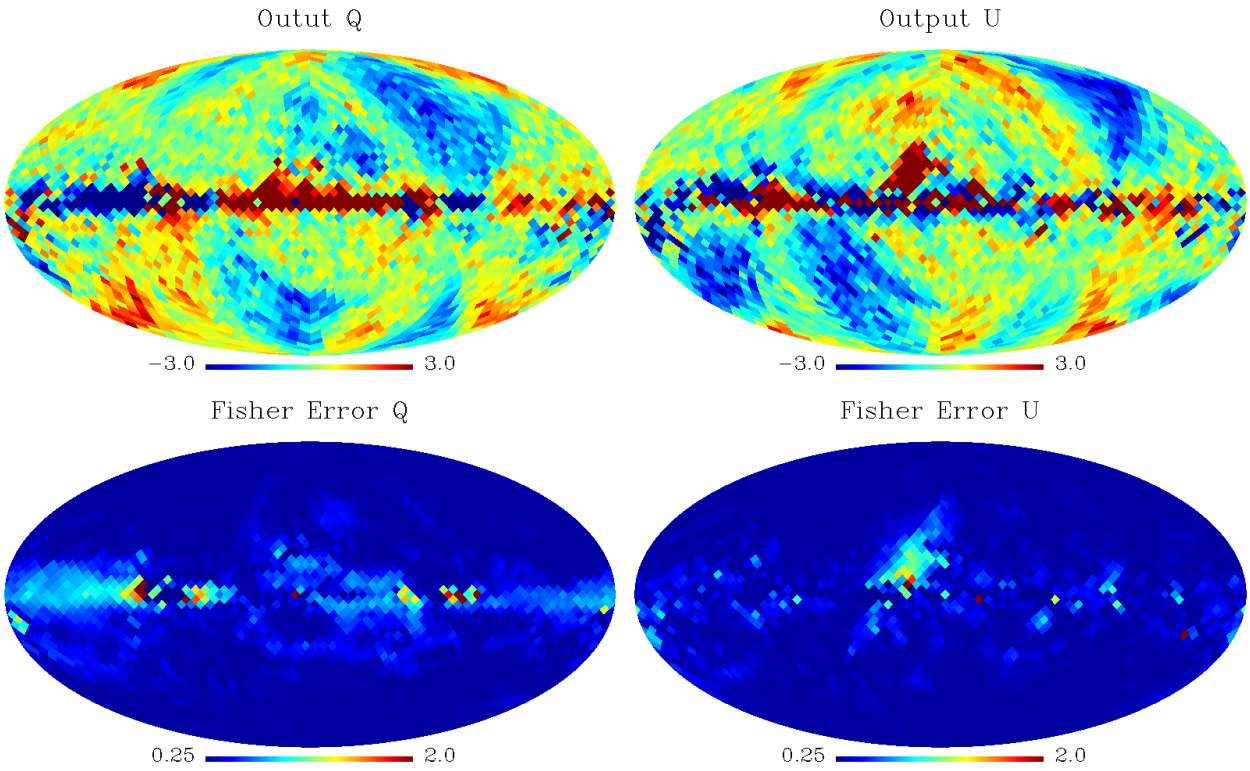

Figure 4.18: Parametric fitting solutions for CMB Q/U using Planck dx8 polarisation maps as input. Also shown are the Fisher errors (lower). No masking is used as each pixel is fit individually, but for any subsequent likelihood analysis, a Galactic mask is utilised.

which is extended to incorporate a spatial correlation of the spectral indices β_s and β_d by the modification of the spectral indices terms to

$$\frac{1}{2}(\beta_c - \bar{\beta}_c)^T C_{\beta_c}^{-1}(\beta_c - \bar{\beta}_c), \tag{4.12}$$

for each foreground component. Here C_{β_s} and C_{β_d} are the covariance matrices for the synchrotron and dust spectral indices, and are calculated similarly to the noise covariance matrix for the degraded-resolution maps as detailed in Chapter 2. For fitting synchrotron emission we impose a spatial correlation of 5° with a mean of -2.9 and variance 0.3^2, and for dust we again impose a 5° correlation angle, but with a mean of 1.5 and a variance 0.5^2. The maximum likelihood solution is found identically to Chapter 2 for the simulations, and Fisher errors per pixel are calculated for all components. The degraded resolution noise covariance matrix described in Chapter 2 is used. Figure 4.18 shows the maximum likelihood CMB solution for Q and U with errors. Since the parametric fitting solves per pixel we do not need to use a Galactic mask, but any subsequent likelihood analysis should employ a masking scheme, as the Galactic plane is significantly contaminated.

The structure in the recovered CMB maps is very similar to the ILC and template-fitting solutions. The systematic banding consistent with the scanning strategy remains a prominent feature in both

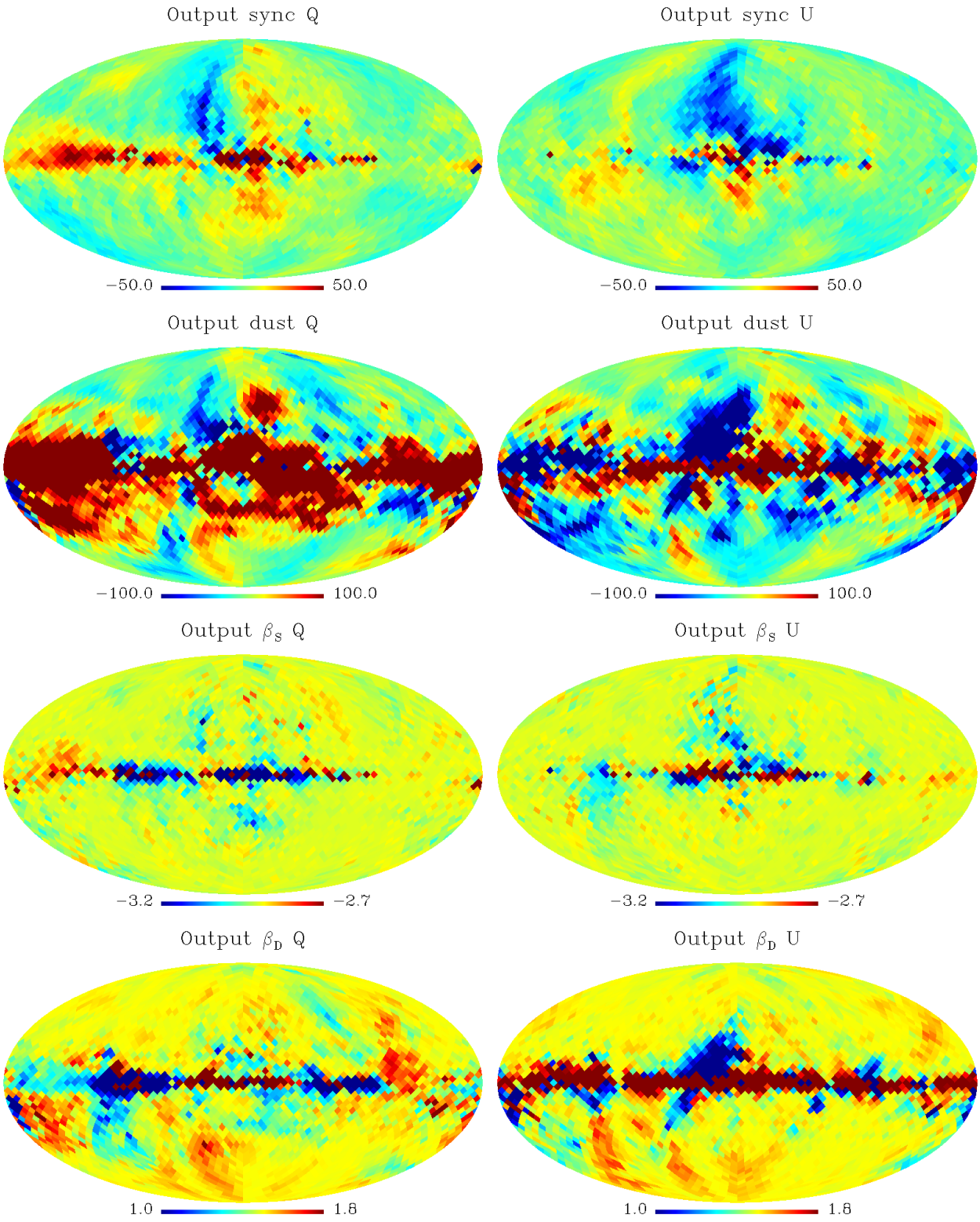

Figure 4.19: Parametric fitting solutions for synchrotron at 30 GHz and dust at 353 GHz foregrounds using Planck dx8 polarisation maps as input. Recovered spectral indices shown in lower panels. Away from the plane the indices are driven by the priors.

Q and U maps, at a higher level than for the ILC solution. The Galactic foregrounds show a high degree of correlation with the 30 GHz and 353 GHz templates, and the spectral indices are driven to the prior values away from the plane. Regions of stronger synchrotron emission exhibit a steeper index up to $\beta_s = -3.1$ near the plane, and in regions of strong dust emission, the dust spectral index drops to $\beta_d = 1.2$. The intensity of the foreground polarisation correlates well with the changing spectral index for both diffuse foregrounds.

4.6 Systematics

Foreground-cleaned maps shown in this chapter exhibit a level of systematics on large angular scales comparable to the CMB polarisation. Understanding the origin of these signals will tell us how far the polarisation data can be probed. We now briefly discuss the main sources of systematics in the Planck pipeline and how these can affect the full-sky maps.

At large angular scales, the signal-to-noise in the dx8 maps is high, but there is a strong level of systematics. One of the largest contributors to this is bandpass mismatch leakage, described in Section 4.1.1, which contributes to large-scale morphology (estimated at up to a few μK at 100 GHz (Planck internal communication). More recent estimates of the bandpass mismatch have produced more accurate full-sky correction maps, and following the initial data release in March 2013 successive pipeline iterations should improve these estimates further as the understanding of the frequency response of the detectors is improved.

Another important source of systematics is the calibration mismatch between detectors, which again operates on large angular scales. Due to its scanning strategy, Planck is unable to reconstruct the polarisation signal over the whole sky without combining detectors with different orientations. A mis-calibration between the detectors used to construct the maps will produce a leakage from intensity to polarisation. Estimations of the mismatch signal with focal plane simulations have shown that the leakage can contribute at least as much power as the CMB to the EE and BB power spectra (Planck internal communication). Figure 4.20 shows the simulated gain calibration residual estimating the potential signal in the polarisation maps after two sky surveys.

Far side lobes are the local maxima of the radiation pattern that are not in the main beam of the detector horns, and these produce an additive signal in the polarisation maps. They therefore affect gain calibration, especially at foreground frequencies. Maps estimating the far side lobe contribution by differencing individual surveys have shown this to be strong feature, strongly emulating the scanning strategy. This is shown in Figure 4.20. Also contributing to dipole leakage errors are averaging times between the raw and applied gains, and actual errors in determining gains from e.g. the analog-to-digital converter (ADC) nonlinearity correction. The ADC nonlinearity arises due to the way the time-averaged data is coded into digital data. Averaging over data points leads to a non-linearity between the input values and the coded values. Accurate determination of the

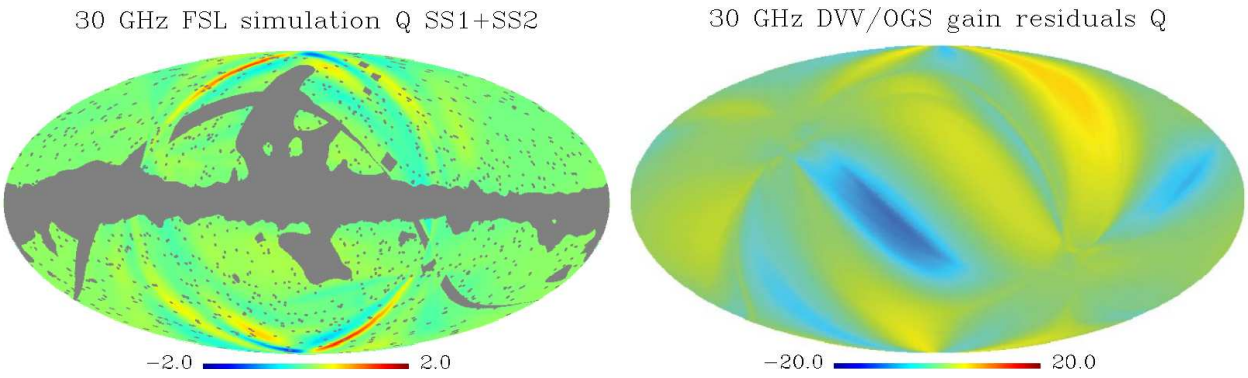

Figure 4.20: Left: Estimated far side lobe contamination at 30 GHz for the first two sky surveys. Right: Estimated gain calibration error assuming the ratio of DVVfix to OGS gain solutions represents the gain error. Of note is the similarity to the ILC, template-cleaned, and parametrically fit polarisation maps calculated in this chapter. Figures produced with simulations retrieved from the Planck wiki (Planck internal communication).

response of the ADC to the time-ordered data is crucial in decoding the correction function. The data used in this thesis has not been corrected for this effect, but future dx9+ data releases will contain gain correction profiles.

The physical orientation of the horns also leads to a further systematic error in computing spectra from maps, as errors in horn position angle lead to a mixing of E and B-modes. The crab nebula (a bright polarisation source) is used for calibration of horn orientation, and many LFI detectors have given discrepant angles between surveys, suggesting orientation errors of up to 1° (Planck internal communication). Linked to the orientation issue is the beam characterisation, which will vary between surveys, affecting both sidelobes and orientation estimation. There is a clear need for reliable and accurate polarisation maps for future foreground analyses. Bandpass correction is currently the largest systematic effect. Post-DX9 corrections should be at the sub-percent level, and the DX10 release will strongly improve the calibration factors with detailed analysis of multiple scans of the LMC/Tarantula nebula from survey 6. Further analysis of error propagation in combined calibration/dipole subtraction is still needed, and this should come post DX10. Another route is modification of component separation routines to parameterise the calibration and gain error, but it seems prudent to wait for the detailed polarisation analysis before modifying existing methods to fit errors.

4.7 QML Power Spectrum Estimates

The pseudo-C_ℓ estimator is constructed from the spherical harmonic transform of a map with coefficients

$$\tilde{a}_{\ell m} = \sum_i w_i \Delta T_i \Omega_i Y_{\ell m}(\theta_i), \tag{4.13}$$

where Ω_i is the solid angle of pixel i and w_i is a pixel weight function that can be set to unity for pixels outside the sky cut and to zero within. From these spherical harmonic coefficients we can construct an unbiased estimator of the power spectrum,

$$\hat{C}_\ell^p = M^{-1}_{\ell\ell'} \frac{1}{(2\ell+1)} \sum_m |\tilde{a}_{\ell m}|^2, \tag{4.14}$$

where M is a coupling matrix which can be expressed in terms of the power spectrum of the weight function w_i and the 3-j coefficients [157]. The pseudo-C_ℓ estimator is sub-optimal, and the estimator induced variance increases as the mask size is increased, though for modest sky cuts (removing ∼20 % of the sky), the estimator induced variance is small in comparison to the cosmic variance of the concordance ΛCDM cosmology [158].

4.7.1 The QML Estimator

The QML estimator [159] in the limit of negligible instrumental noise is

$$y_\ell = x_i x_j E^\ell_{ij}, \tag{4.15}$$

where x_i is the data vector. The matrix E^ℓ in equation 4.15 is

$$\mathbf{E}^\ell = \frac{1}{2} C^{-1} \frac{\partial C}{\partial C_\ell} C^{-1}, \tag{4.16}$$

where C is the covariance matrix $\langle x_i x_j \rangle$. The covariance matrix of the estimates y_ℓ is given by

$$F_{\ell\ell'} = \langle y_\ell y_{\ell'} \rangle - \langle y_\ell \rangle \langle y_{\ell'} \rangle = 2 \text{ Tr} \left[C\mathbf{E}^\ell C \mathbf{E}^{\ell'} \right]. \tag{4.17}$$

From the estimates in Equation 4.15, we can form an unbiased estimate of the CMB power spectrum

$$\hat{C}_\ell^q = F^{-1}_{\ell\ell'} y_{\ell'}, \tag{4.18}$$

with covariance matrix

$$\langle \Delta \hat{C}_\ell^q \Delta \hat{C}_{\ell'}^q \rangle = F^{-1}_{\ell\ell'}. \tag{4.19}$$

Let the data vector x_i consist of the harmonic coefficients $\tilde{a}_{\ell m}$. These coefficients are related to the true $a_{\ell m}$ coefficients on the uncut sky by a coupling matrix M,

$$\tilde{a}_{\ell m} = \sum_{\ell' m'} a_{\ell' m'} M_{\ell m \ell' m'}. \tag{4.20}$$

If some of the sky is removed by a sky cut, the matrix M in Equation 4.20 will be singular. This expresses the lack of information on anisotropies that lie within the Galactic mask, hence it is impossible to reconstruct all the $a_{\ell m}$ values from the harmonic coefficients $\tilde{a}_{\ell m}$ measured on the cut sky. For small masks and low multipoles however, it may be a good approximation simply to truncate the summation in (4.20) at certain values of ℓ' and m'. The true low multipole coefficients $a_{\ell m}$ can then be reconstructed by inverting the non-singular truncated matrix M. In this case, the QML estimator becomes

$$\hat{C}_\ell^q \approx \frac{1}{(2\ell+1)} \sum_m |a_{\ell m}|^2, \qquad a = \tilde{K}^{-1}\tilde{a}, \tag{4.21}$$

and is independent of the assumed form for the true power spectrum (the variance on the estimates however is given by cosmic variance and does depend on the assumed form for the input power spectrum). It is therefore possible to reconstruct the exact power spectrum coefficients for our particular realisation of the sky using a QML estimator, with estimator-induced variance reduced to negligible levels at low multipoles, provided the mask is conservative enough.

4.7.2 QML Results

We use the dx8 nominal mission block covariance matrices instead of degraded-resolution noise covariance matrices as described in Chapter 2. Figure 4.21 shows the normalised and scaled noise covariance matrices for the 100 GHz channel at $N_{side} = 8$ resolution, converted to HEALPix ring format. The structure is similar to the degraded-resolution covariance matrix with the addition of nominal-mission pixel covariances. Higher HEALPix resolution matrices exhibit similar morphology.

Figure 4.22 shows the QML estimation for the E and B-mode power spectra at low-ℓ. The E-mode estimation is good and within 1-2σ for most points, however the B-mode estimation bears little correlation to an $r = 0.1$ fiducial spectra (also plotted in black). The similarity in the two plots at higher ℓ suggests a possible E to B contamination, increasing the B-mode power.

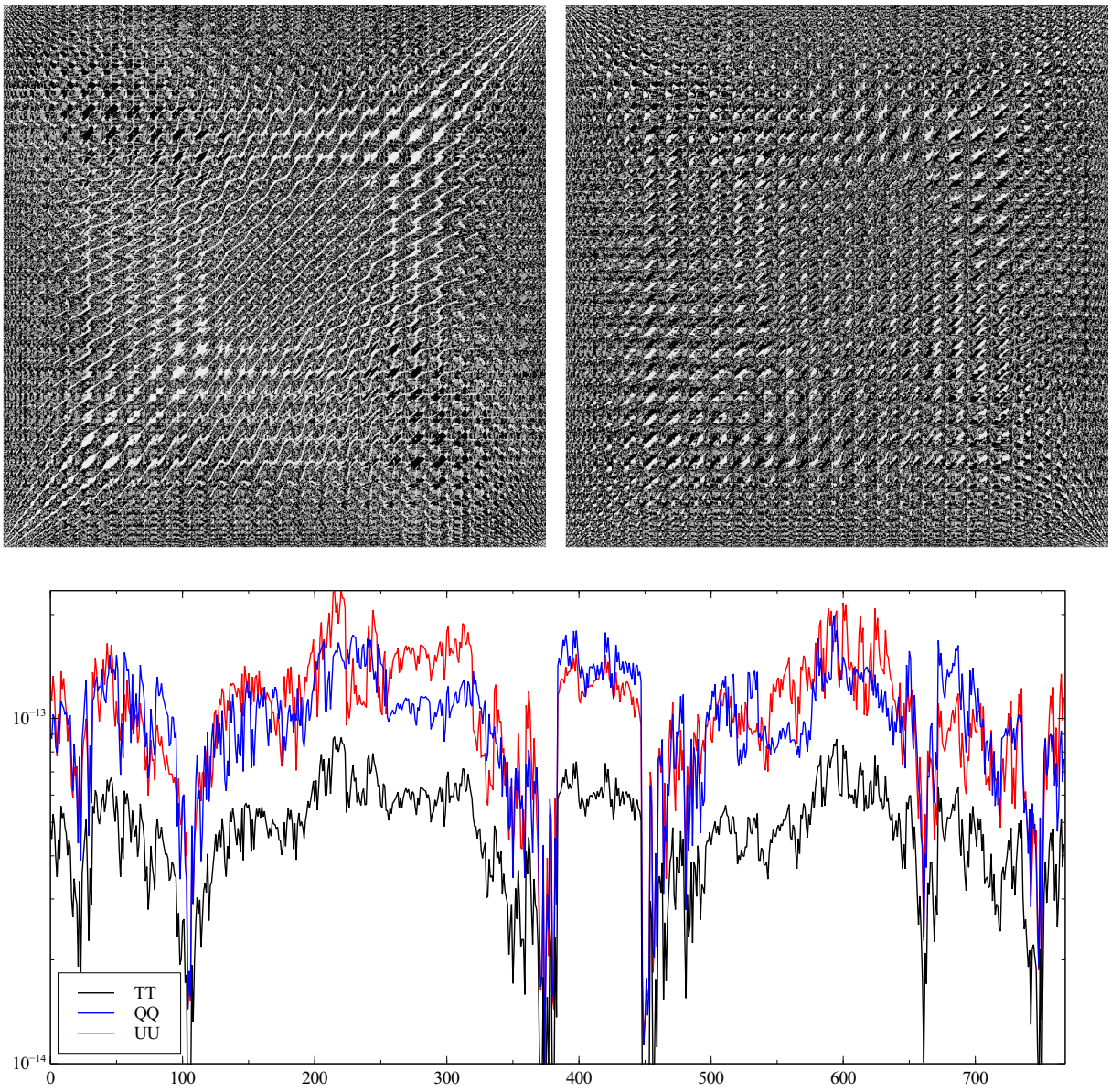

Figure 4.21: 100 GHz nominal mission noise QQ and QU covariance matrices at $N_{side} = 8$ resolution in HEALPix ring format. The structure is very similar to the degraded-resolution covariance matrices calculated in Chapter 2. The banding is due to the arrangement of pixels within the HEALPix map format. Bottom: Matrix diagonals for TT, QQ, UU.

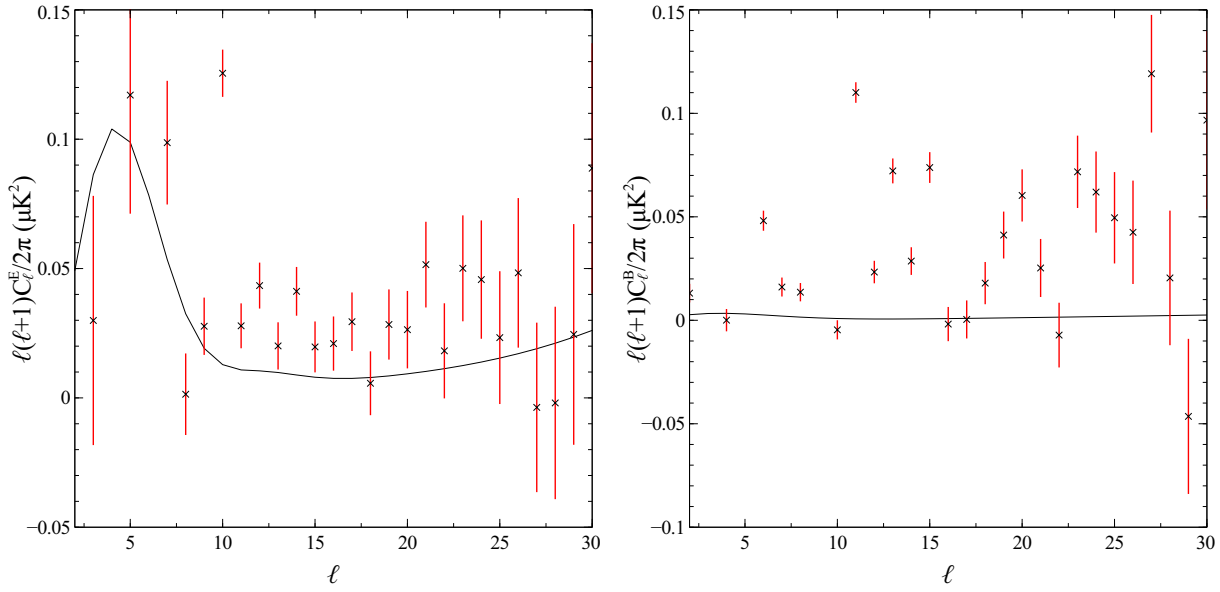

Figure 4.22: QML estimation for the E and B-mode power spectra computed at $N_{side} = 16$ resolution with covariance matrix as described in the text, and 1σ errors. The solid black lines show the fiducial spectra with r=0.1. The left panel shows the E-mode and the right panel shows the B-mode. The E-mode estimation is reasonable however the B-mode appears to be dominated by noise. The similar amplitudes suggest a possible E to B contamination.

4.8 Conclusion

In summary, we have shown that for the dx8 exchange data:

- The level of systematics is well below the level of the foregrounds, but above the CMB polarisation (Section 4.3).
- Systematics appear too dominant in polarisation for template fitting to recover the CMB polarisation (Section 4.3).
- ILC, template fitting, and parametric fitting all return a consistent signal dominated by systematics (Section 4.5).
- Whilst the foregrounds are consistent, the CMB polarisation seen by Planck shows a very poor correlation with the 5-year WMAP data (Section 4.2).
- The foreground contribution from synchrotron and dust is almost equal at 70 GHz, shows significantly more dust at 100 GHz, and is almost entirely dust at 143 GHz (Section 4.3).
- Parametric fitting works well and recovers a signal consistent with ILC and template fitting solutions, but dominated by systematics (Section 4.5).
- The data is not yet suitable for low resolution analyses as systematics associated with e.g. bandpass/gain calibration, leakage dominate the CMB signal in polarisation (Section 4.6).

In this chapter we have examined the Planck full-mission dx8 polarisation maps, released to the Planck community in November 2012. We have examined the effect of bandpass correction and updated the dx8 data to reflect this additive effect, which is up to $200 - 300\%$ in places. Whilst the polarised foregrounds dominate over the systematics at 100 and 143 GHz, after foreground cleaning with either ILC, template-fitting, or parametric fitting, the level of gain mismatch-type systematic consistent with Planck's scanning strategy is high and clearly evident in the component-separated maps. Template fitting is the simplest approach, and we have used several combinations of Planck and WMAP data to investigate the effect on the cleaned CMB. Worringly there appears to be little correspondence between cleaned Planck-only maps, and the WMAP 7-year data. A WMAP-Planck difference plot shows that the lowest residuals are $\sim 1\ \mu$K at the ecliptic poles, and increase to 8-10 μK at the antipoles. The highest correlation between Planck and WMAP is given when cleaning WMAP with the HFI 353 GHz channel, but for Planck-only cleaning the correlation with WMAP is very poor. ILC component separation with LFI and HFI separately shows that the HFI channels contribute strongly to the systematic effect, as LFI-only ILC, whilst noisier, gives a distinctly different CMB morphology more consistent with the WMAP data. This is perhaps to be expected as WMAP's frequency coverage coincides more closely with LFI's.

We have created a series of masks by balancing sky coverage with eliminating strong foreground emission, and have used these for template fitting and ILC component separation. We have examined the varying contribution of synchrotron and dust at Planck's central CMB channels, finding dust to dominate at 100 GHz and above. At 143 GHz, there is no contribution from the synchrotron template at 23 GHz. ILC weights 143 GHz as the strongest channel in both Q and U (58 and 69% respectively), with 100 GHz the next strongest contribution (40 and 26% respectively). For Planck-level noise, ILC solutions tend to amplify the noise of the cleaned polarisation maps to unacceptable levels. Blind techniques such as ILC are thus not ideally suited for detecting potential B-modes.

We apply the parametric fitting approach with correlated spectral indices outlined in Chapter 2, and solve for the maximum likelihood CMB solution and corresponding errors. The estimated CMB is heavily contaminated along the Galactic plane as expected, but produces an otherwise signal-dominated view of the CMB polarisation, with a high degree of correlation with the ILC and template-fitting solutions, although systematics are still evident in the cleaned maps. Future dx10+ simulations of the bandpass-mismatch, gain calibration, and polarisation leakage with a more complete understanding of the time-ordered data will mitigate the effect of the systematics and allow component separation methods to more accurately characterise the polarised Planck sky. In summary, the Planck data in their current state are not clean enough to perform precise low-resolution cosmological analyses.

Remember to look up at the stars and not down at your feet. Try to make sense of what you see and wonder about what makes the Universe exist. Be curious.
- Stephen Hawking

Chapter 5

Fisher Analysis and Parameter Degeneracies for Planck

Planck provides an accurate determination of many fundamental cosmological parameters. Indeed, an important part of the scientific case for Planck was the ability to constrain high-precision cosmological models, and discriminate between competing early universe theories. In this chapter we analyse parameter degeneracies present in the Planck data as at January 2012 (version 50 of the internal data exchange), by analysing the Fisher matrix as an approximation to the full parameter likelihood (generated using Cosmo MC), and performing a principal component analysis to generate coupled eigenvectors. We also investigate the v50 temperature power spectrum at intermediate multipoles by exploring the parameter space around the numerical maximum likelihood point and explore the behaviour of a strange oscillation present at $\ell \approx 900$. We check whether a better fit to lower multipoles can remove the oscillation while maintaining an acceptable χ^2 for the overall fit.

5.1 Parameter Degeneracies for Planck

Analysis of CMB data using CAMB [119] and CosmoMC [160] is now extremely fast and robust. Calculation of the temperature and polarisation power spectrum accurate to sub-percent level takes a matter of seconds on a fast desktop machine. Gaining another order of magnitude in accuracy by tweaking approximations and the recombination history takes only a little longer [161]. The data from Planck greatly increases the precision of available data on small scales, which will help to constrain physical models up to the limit imposed by geometrical degeneracies.

We first look at why geometrical parameter degeneracies exist. A parameter degeneracy effectively describes the indistinguishability of certain cosmological parameter combinations. The anisotropies that Planck observes are generated during recombination, and the conditions that existed then are projected onto the last-scattering surface. The mapping of physical scales at the last-scattering sur-

face onto observed angular scales depends only on the angular diameter distance to last-scattering. There are therefore degenerate combinations of late-time parameters such as the expansion rate H_0 and the curvature parameter Ω_K that will generate almost identical power spectra of primary anisotropies (the geometrical degeneracy discussed by Bond, Efstathiou & Tegmark [55]).

We can analyse degeneracies by performing a Fisher matrix analysis. Figure 5.1 shows an example of such a fit, with the fiducial C_ℓ^{fid} plotted with two additional models that give a good fit to the fiducial model. The fiducial model is described in more detail in Section 5.4, and is the maximum-likelihood model fit to the v50 internal Planck data release (given in Table 5.2).

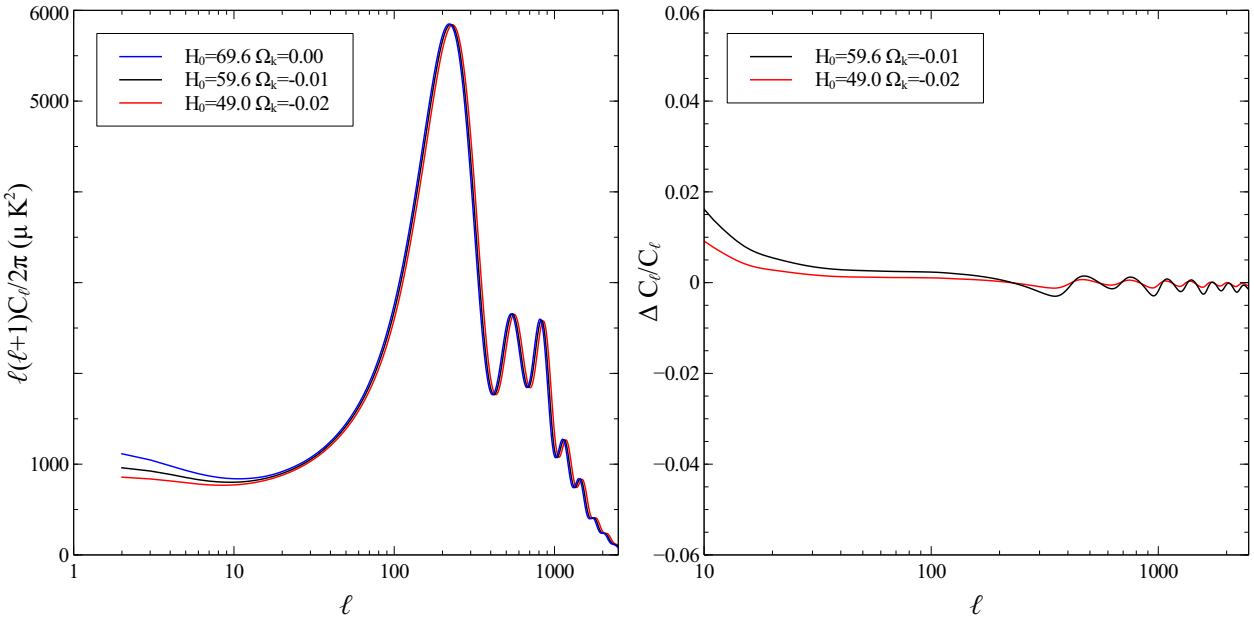

Figure 5.1: *L*eft: Temperature power spectrum calculated with CAMB for nearly degenerate geometries in non-flat ΛCDM models with lensing. *R*ight: Fractional differences with the maximum likelihood v50 fiducial model. All other parameters remain fixed at their fiducial values given in Table 5.2.

For this particular case, the geometric degeneracy is within the two-dimensional space of Ω_k and H_0 (or h). As expected, the power spectra are almost indistinguishable except at low multipoles. The geometrical degeneracy is not perfect - it is broken by gravitational lensing of the CMB, and a small part of the discrepancies between the models at high multipoles arise from numerical errors in the CAMB code, but these are likely to be very small indeed (with the CAMB accuracy switch set to high). When considering very precise models, one should take care not to accumulate numerical errors (in for example calculation of the Fisher matrix), as they can erroneously break the geometrical degeneracy, and make errors in the density parameters $\Omega_\Lambda h^2$ and $\Omega_k h^2$ appear weakly correlated. This problem would be acute for Planck in which the C_ℓ estimates are nearly cosmic-variance limited to high multipole. Differences between the models at low multipole are due to the late-time Sachs-Wolfe effect, and are smaller than cosmic variance limits.

5.1.1 Breaking Degeneracies

As shown in Figure 5.1 the power spectra are not entirely degenerate. On the largest scales this is due to the late-time ISW effect, but at smallest scales the spectra are very similar. Two effects lead to differences in the small scale power: numerical errors, and physical effects. Clearly for the purposes of cosmology and parameter constraints one should demand that the numerical effects are minimised, such that any degeneracy breaking is purely a result of physical effects. Previous studies have shown that by boosting CAMB's accuracy switches, the calculations will yield results that are accurate to at least 0.1% at high ℓ [162]. However, such boosting increases the computation time rather significantly, so for a large number of simulations a balance between speed and accuracy should be found. The numerical errors arise largely from interpolation of the spectrum from the sparse ℓ sampling, and increasing the accuracy just increases the sampling rate and uses an improved interpolation scheme (hence the longer computation time). Even at large scales, the numerical errors are below the differences from the late-time ISW effect, so we can concentrate on the physical effects that lead to degeneracy breaking.

Even in the absence of lensing, physical effects can break the geometric degeneracy in non-flat cosmologies at the 10^{-3} level [162]. Curvature has a very small effect on the evolution until recombination, so the physical sources of anisotropy are very similar in degenerate models. However, the last-scattering surface is not infinitesimally small, and has some finite thickness. In curved models, the change in the angular-diameter distance over the last-scattering thickness is different than for the flat case. It is smaller in closed models and larger in open models. If we consider an angular scale corresponding to an acoustic peak, then we will also see slightly larger scales at earlier times near the start of recombination which have not yet reached an extremum. In closed universes, the change in transverse comoving scale going through the last-scattering surface is smaller, and the perturbation probed earlier would be closer to an extremum. In open universes there is therefore a suppression of power in the acoustic peaks, and in closed universes a boost. Assuming that the thickness of recombination is a significant fraction of η_* (the conformal time at the peak of the visibility function giving the probability distribution of the position of last scattering), this effect is of the order $\sim 10^{-3} - 10^{-2}$ [163] for a typical parameter set. We are viewing last-scattering from a large distance ($d_A \gg \eta_*$), and curvature's effect on the fractional change in d_A through a fixed thickness increases with distance, so this effect is large compared to curvature's other effects.

In practice all observational data at small scales features the imprint of gravitational lensing, and thus we only measure the lensed power spectrum. Lensing effectively smooths the temperature anisotropies, damping the sharpness of the power spectrum peaks and troughs. This breaks the geometric degeneracy because the amount of lensing is proportional to the geometry and structure between us and the last-scattering surface. Lensing serves to amplify the differences between the nearly-degenerate models, allowing us to place much better constraints on Ω_Λ (or Ω_k). Of course, Planck returns noisy observations, and noise has the opposite effect to lensing in that it strengthens the degeneracy by decreasing our sensitivity to small differences in degenerate power spectra at

small scales. Given that no cosmological parameter can mimic the effect of lensing on small-scales, accurate measurement of the lensed spectra (coupled with the differences arising from the late-time ISW effect) give enough information to break the degeneracy and constrain Ω_Λ well.

5.1.2 Calculating C_ℓ Derivatives

The derivatives of C_ℓ with respect to the cosmic parameters can be calculated using CAMB. By varying one parameter within the cosmological model and recalculating spectra, the derivative can be approximated at each ℓ value. This can be achieved for all parameters except the dark energy equation of state parameter w by calculating $(C_\ell^+ - C_\ell^-)/2\Delta$ where C_ℓ^+s are generated with the cosmological parameter of interest increased by a few percent, and C_ℓ^-s are generated with the parameter decreased by a few percent. For w, since CAMB does not have in-built functionality for values of w less than -1, a forward finite difference method can be used which calculates the derivative as $-\frac{f(x+2h)-4f(x+h)+3f(x)}{2h}$. For exploring values of w less than -1, an add-on Parameterised Post Friedmann (PPF) module can be used to cross the equation of state divide (see Section 5.5). Derivatives of C_ℓ with respect to the baryon density Ω_b, the cold dark matter density Ω_{CDM}, the spatial curvature density Ω_k, the scalar spectral index n_s, the Hubble parameter H_0, the number of neutrino species n_ν, and the amplitude of density fluctuations A_s are shown in Figure 5.2. Clear degeneracies exist between H_0 and Ω_k, as well as between w and H_0 (for a constant equation of state). Calculating these derivatives is the basis for constructing the Fisher matrix from the Planck covariance matrix in the following section. Derivatives with respect to any cosmological parameters (not just the standard six) can be included and principal components for the particular model calculated.

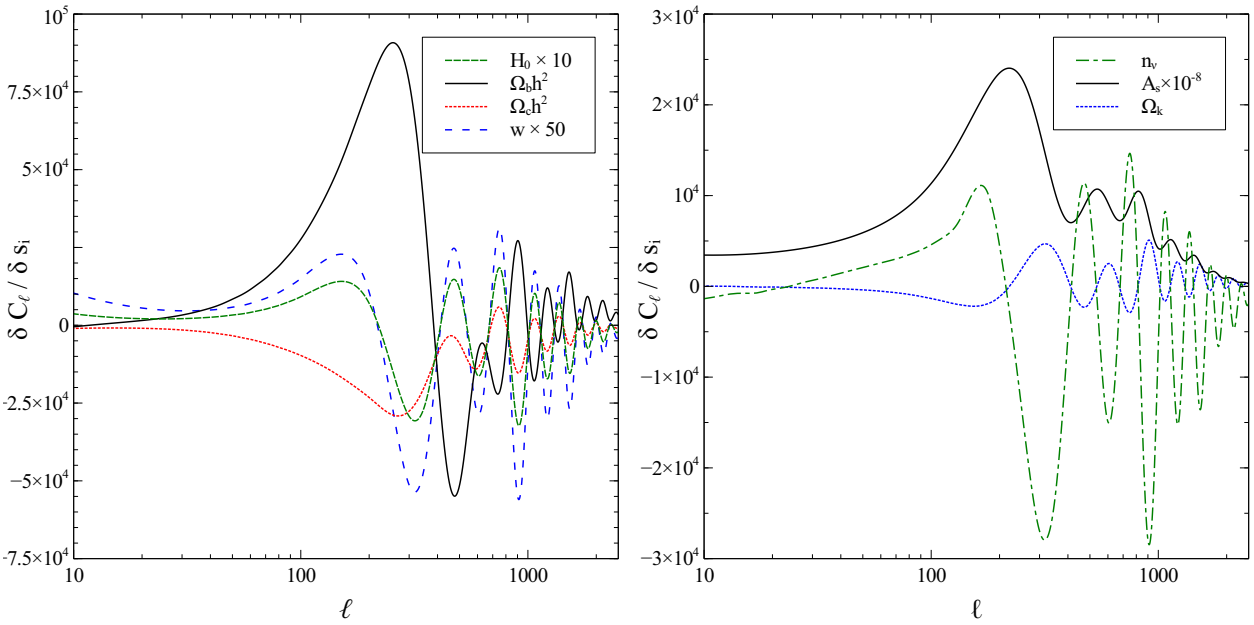

Figure 5.2: Derivatives of of C_ℓ with respect to the seven parameters of the model defined in the text. The derivatives with respect to H_0, w, and A_s have been multiplied by the factor indicated in the figure (e.g. the derivative of w has been multiplied by a factor of fifty).

5.2 Parameter Estimation for Planck

5.3 Fisher Approximation

Calculation of the full cosmological parameter set for Planck for even modest cosmologies is very computationally expensive, taking several days (though large grids of models can be run in parallel). Slight adjustments to the priors or sample space require a full rerun of the software and chains (using e.g. CosmoMC). An alternative method of exploring the parameter space is to consider the Fisher matrix approach, involving calculation of all power spectrum derivatives with all parameters of interest, followed by a simple χ^2 minimisation to explore the maximum-likelihood point. Although a Fisher matrix analysis is approximate, it is fast and can be used to gain physical insight into parameter degeneracies of complex models. It can also be used to assess whether an additional parameter or parameters might explain anomalous residuals in the data.

5.3.1 Fisher Framework

Following the formalism of Efstathiou and Bond (1998) [53], assume that the cosmological model is completely specified by a set of parameters $\mathbf{s}$. Let $P(\mathbf{s}|prior)$ be the prior probability distribution of the parameters $\mathbf{s}$, and $\mathcal{L}(\mathbf{s})$ be the likelihood of the parameters (given by Planck in this case). The distribution of the parameters, taking into account information from Planck, is given by Bayes'

theorem $P(\mathbf{s}) \propto \mathcal{L}(\mathbf{s})P(\mathbf{s}|prior)$. If the errors around the target model parameters are small, then an expansion of $\ln \mathcal{L}$ to quadratic order about the maximum-likelihood point gives

$$\mathcal{L} \approx \mathcal{L}_m \exp\left[-\frac{1}{2}\sum_{ij} F_{ij}\delta s_i \delta s_j\right], \tag{5.1}$$

where F_{ij} is the Fisher matrix, given by derivatives of the power spectrum with respect to the set of parameters $\mathbf{s}$

$$F_{ij} = \sum_{\ell} \frac{1}{(\Delta \mathrm{C}_\ell)^2} \frac{\partial \mathrm{C}_\ell}{\partial s_i}\frac{\partial \mathrm{C}_\ell}{\partial s_j}. \tag{5.2}$$

The parameter ΔC is the standard error on the estimated value for C_ℓ. For an experiment with N frequency channels, angular resolution $\theta_{c,fwhm}$ (for each channel c), and sensitivity $\sigma_{c,pix}$ per resolution element, and sampling a fraction of the sky f_{sky}, the standard error is given by [55] [164]

$$(\Delta \mathrm{C}_\ell)^2 \approx \frac{2}{(2\ell+1)f_{sky}}\left(\mathrm{C}_\ell + \overline{w}^{-1}\overline{\mathcal{B}}_\ell^{-2}\right)^2, \tag{5.3}$$

where

$$\overline{w} = \sum_c (\sigma_{c,npix}\theta_{c,fwhm})^{-2}, \qquad \overline{\mathcal{B}_\ell^2} = \sum_c \exp^{-\ell(\ell+1)/\ell_s^2} w_c/\overline{w}. \tag{5.4}$$

This assumes that the beam profile is Gaussian with a width given by $\ell_s = \sqrt{8\ln 2}(\theta_c)^{-1}_{fwhm}$. Assuming a uniform prior, the covariance matrix $\mathbf{M} \equiv \langle \delta s \delta s^* \rangle$ is given by the inverse of the Fisher matrix F. The variance of a particular parameter s_i, marginalised over the uncertainties in all the other parameters is given by $\sigma_i = M_{ii}$.

We can determine the cosmological parameters by utilising a χ^2 minimisation, assuming that the theoretical spectra of neighbouring points can be approximated by a Taylor Series expansion

$$C_\ell(s_i) = C_\ell(s_0) + \left(\frac{\partial C_\ell}{\partial s_i}\right)\Delta s_i \tag{5.5}$$

We first proceed by calculating the vector:

$$\mathbf{V} = \sum_{\ell_1 \ell_2} \frac{\partial C_{\ell_1}}{\partial s_i}\mathbf{C}^{-1}(C^{pl}_{\ell_2} - C^{fid}_{\ell_2}), \tag{5.6}$$

where C^{pl}_ℓ and C^{fid}_ℓ are the Planck and fiducial spectra respectively and $\mathbf{C}$ is the Planck covariance

matrix. For a parameter set of size n, we then construct the n×n Fisher matrix

$$F_{ij} = \sum_{\ell_1 \ell_2} \frac{\partial C_{\ell_1}}{\partial s_i} \mathbf{C}^{-1} \frac{\partial C_{\ell_2}}{\partial s_i}. \tag{5.7}$$

The new parameters are then calculated using this approximation as $s_i^{new} = s_i^{old} + F_{ij}\mathbf{V}$, which leads to a new estimation of the power spectrum using Equation 5.5. There is a new aspect to this analysis that has not been performed before. In previous works, the Fisher matrix analysis has been used to make forecasts of parameter accuracies for idealised experiments. Here we are using the real data C_ℓ^{Pl} (foreground corrected and averaged over frequencies), and the covariance for the real data, not idealised approximations such as Equations (5.3). and (5.4).

5.3.2 Results

The diagonal components of the covariance matrix are plotted in Figure 5.3. The covariance matrix is calculated for the foreground corrected frequency averaged CAM-SPEC spectra (internal Planck communication). The derivatives are calculated with respect to six cosmological parameters: the baryon density ω_b, the cold dark matter density ω_{CDM}, the spatial curvature density ω_k, the scalar spectral index n_s, the Hubble parameter H_0, and the number of neutrino species n_ν. The step sizes, initial values (from CosmoMC), and final values are given in Table 5.1. The reduced χ^2 drops from 1.3572 to 1.3559, indicating a small improvement in fit. The initial and final spectra are shown in Figure 5.4 along with the raw Planck data points, with the subplot showing the residual $C_\ell^{s_0} - C_\ell^{s_i}$ between the two spectra. The algorithm is very fast, taking less than a second on a fast desktop machine, and expansion to a larger parameter set could be easily achieved by simply computing additional derivatives and expanding the Fisher matrix calculation.

Parameter	ω_b	ω_{CDM}	ω_k	n_s	H_0	n_ν	$red.\chi^2$
s_o	0.02252	0.117055	0.0	0.975147	69.566	3.046	1.3572
s_i	0.02211	0.116767	0.00091	0.957975	68.046	2.556	1.3559
Step	0.0001	0.002	0.0003	0.02	0.01	0.1	

Table 5.1: The initial (s_0) and final (s_i) cosmological model computed using the Fisher approximation to the maximum-likelihood. Also given are the initial and final reduced χ^2 values, showing a small reduction with the new parameter set. The trial step sizes are also given for each parameter.

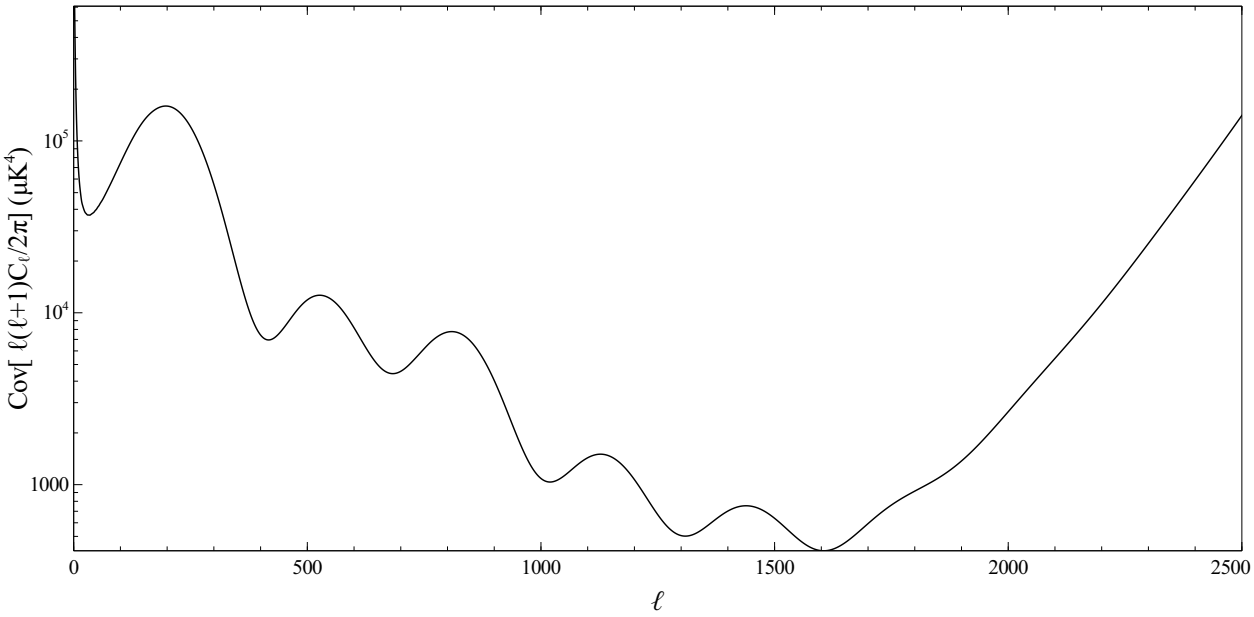

Figure 5.3: Diagonal components of the Planck covariance matrix (in units of μK^4).

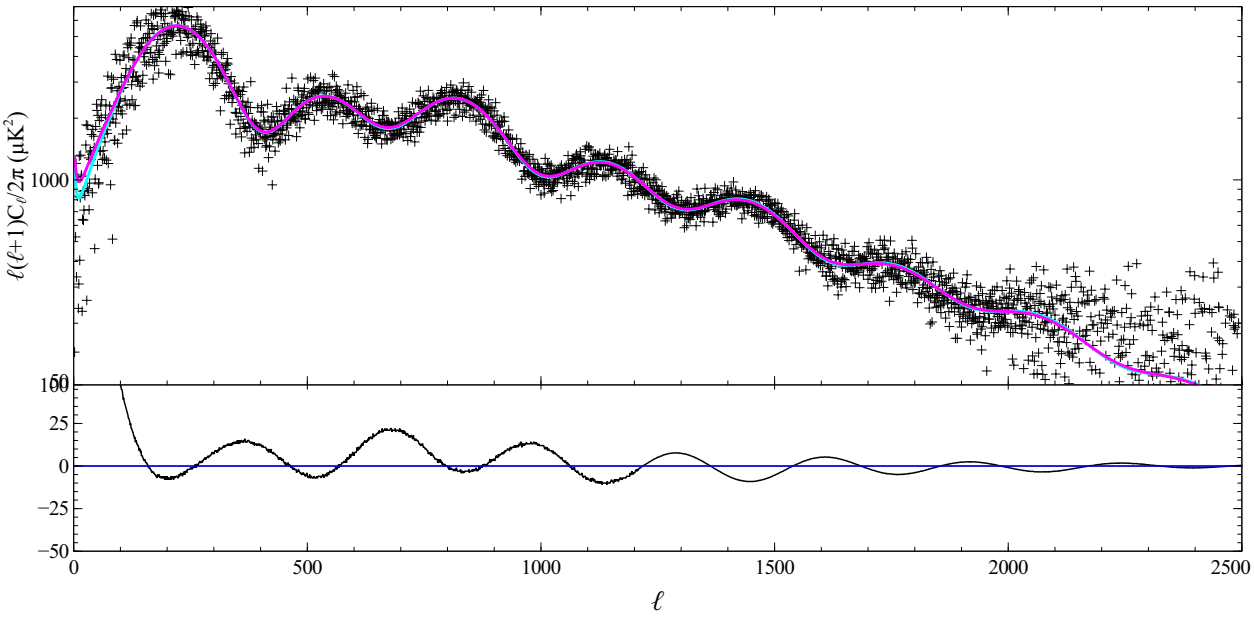

Figure 5.4: Initial v50 (magenta) and final (cyan) power spectra with improved fit to the data. Black points are the raw Planck power spectrum at each multipole, and subplot shows the residual $C_\ell^{s0} - C_\ell^{s_i}$.

5.4 Parameter Degeneracies

Degeneracies between cosmological parameters are not in all cases near-exact (e.g. $\omega_\Lambda - \omega_k$ as described earlier). In this section we will look at partial degeneracies among other parameters within the standard cosmology using the v50 Planck data. The derivatives of C_ℓ with respect to the six parameters used are shown earlier in Figure 5.2.

5.4.1 Eigenvectors of the Fisher Matrix

For a n-parameter cosmological model the Fisher matrix is a $n \times n$ symmetric matrix and therefore can be reduced to diagonal form

$$F = U\Lambda U^\dagger, \qquad \Lambda = \mathrm{diag}(\lambda_1, \lambda_2, ..., \lambda_n), \tag{5.8}$$

where U is a matrix composed of m rows of eigenvectors $\mathbf{u}_m$ which correspond to the eigenvalues λ_m. We assume that the eigenvectors are ordered such that $\lambda_1 \geq \lambda_2 ... \geq \lambda_m$. From our original variables (the cosmological parameters), we can construct a set of new orthogonal variables $\mathbf{X}$

$$\mathbf{X} = U^\dagger \mathbf{s}, \qquad \mathbf{s}^\dagger F \mathbf{s} = \mathbf{X}^\dagger \Lambda \mathbf{X}. \tag{5.9}$$

The new variables are orthogonal linear combinations of the cosmological parameters, and can be constructed for each model parameterisation. The most accurately determined orthogonal variable will have the highest eigenvalue, and the least well determined will have the smallest. These variables are called the principal components of the experiment, and will be different for e.g. Planck and WMAP. Well-determined, or 'high-order' components represent high-confidence variables, and poorly-determined or 'low-order' components represent low-confidence variables. We have computed the eigenvalues and eigenvectors (i.e. the principal components) for the six-parameter model described earlier in this Chapter.

The best-fitting v50 cosmological model parameters calculated with CosmoMC used for the central values are shown in Table 5.2, with the maximum-likelihood TT, TE, and EE spectra shown in Figure 5.5 with the WMAP 7-year data for comparison. The full cosmological model used in the CosmoMC fit is detailed in Appendix A. The temperature-only agreement with WMAP is good, diverging slightly at multipoles above 1000. The TE spectrum also shows good agreement across the entire WMAP multipole range (with a slight deficiency at very low ℓ). The EE spectrum also shows reasonable agreement given the error bars, less accurate in part due to WMAP's limited polarisation sensitivity, with errors rapidly increasing above $\ell = 500$.

The Fisher matrix is computed with the v50 covariance matrix and is shown in Table 5.3.

Parameter	x_i	x_i^-	x_i^+	x_i^{--}	x_i^{++}
$\Omega_b h^2$	0.225195E-01	0.215097E-01	0.230846E-01	0.214961E-01	0.231432E-01
$\Omega_{DM} h^2$	0.117055E+00	0.111524E+00	0.125483E+00	0.110441E+00	0.126053E+00
θ	0.104226E+01	0.104083E+01	0.104323E+01	0.104056E+01	0.104353E+01
τ	0.962171E-01	0.565664E-01	0.136208E+00	0.519821E-01	0.150749E+00
n_s	0.975147E+00	0.952815E+00	0.992148E+00	0.949895E+00	0.998513E+00
$log[10^{10} A_s]$	0.310959E+01	0.303483E+01	0.318542E+01	0.302498E+01	0.321304E+01
A_{PCA1}	0.486145E+01	0.233479E+01	0.923209E+01	0.204268E+01	0.956799E+01
A_{PCA2}	0.142690E+02	0.108467E+02	0.165178E+02	0.104651E+02	0.166693E+02
psr	0.986696E+00	0.770520E+00	0.999991E+00	0.741329E+00	0.999991E+00
A_{CIB217}	0.418630E+02	0.304760E+02	0.598932E+02	0.302365E+02	0.610974E+02
A_{CIB143}	0.178181E+01	0.163805E-02	0.499726E+01	0.163805E-02	0.499726E+01
A_{SZ143}	0.267254E+01	0.133640E+01	0.299995E+01	0.106399E+01	0.299995E+01
$cibr$	0.234671E+00	0.438541E-03	0.999615E+00	0.438541E-03	0.999615E+00
Ω_Λ	0.711588E+00	0.660056E+00	0.740488E+00	0.656084E+00	0.746436E+00
Age/Gyr	0.136947E+02	0.136214E+02	0.138412E+02	0.136049E+02	0.138676E+02
Ω_m	0.288412E+00	0.259512E+00	0.339944E+00	0.253564E+00	0.343916E+00
z_{re}	0.114343E+02	0.798950E+01	0.145081E+02	0.747192E+01	0.154748E+02
H_0	0.695660E+02	0.657391E+02	0.719244E+02	0.655231E+02	0.725067E+02

Table 5.2: The best-fitting cosmological model with foreground parameters fit with CosmoMC for the internal v50 data release. Also shown are the upper/lower 1σ (+/-) and upper/lower 2σ(++/--) estimates. The foreground 'nuisance' parameters are calculated in the likelihood and are used to estimate the point-source, CIB and SZ foregrounds (detailed in Appendix A).

The matrix is diagonal and shows the 6 parameters in the toy model for CAMB in this simplified run. As discussed, diagonalizing a matrix is equivalent to finding the matrix's eigenvalues, which are the entries of the diagonalized matrix. Similarly, the eigenvectors make up the new set of axes corresponding to the diagonal matrix, or for the Planck case, a linear set of combinations of the fundamental parameters contained in the Fisher matrix above. The eigenvalues and corresponding eigenfunctions of the Fisher matrix are shown in the columns of the matrix in Table 5.4.

Each component that is greater than 0.5 has been shown in bold, to highlight which physical variable contributes significantly to each principal component. Adding T_{CMB} to the analysis, including the derivative in the Fisher matrix calculation, we again diagonalise the Fisher matrix, shown in Table 5.5.

The principal components given here are not unique and depend on the scaling of the parameters, as well as the fiducial form of the variables e.g. whether one uses physical parameters as input to CAMB or raw densities. One should therefore be careful when assigning physical interpretation to the principal components. The value of such analyses lies in assessing whether a set of observational points s_i lie within a sub-space of n-dimensional hyperspace, that is whether there are

s_i	Ω_b	Ω_{CDM}	n_s	H_0	n_ν	Ω_k
ω_b	0.345E+09	-0.108E+09	0.560E+07	-0.137E+06	2.150e+06	4.480e+07
ω_{CDM}	-0.108E+09	0.527E+08	-0.258E+07	0.587E+05	-920000.	-1.99000e+07
n_s	0.560E+07	-0.258E+07	0.755E+06	-0.289E+04	45100.0	247000.
H_0	-0.137E+06	0.587E+05	-0.289E+04	0.715E+02	-1120.00	-24200.0
n_ν	2.15000e+06	-920000.	45100.0	-1120.00	17500.0	379000.
ω_k	4.48000e+07	-1.99000e+07	247000.	-24200.0	379000.	9.12000e+06

Table 5.3: Fisher matrix calculated for a six-parameter model with the v50 Planck covariance matrix and derivatives calculated as described in the text.

Eigenvalues	3.86985e+08	1.86272e+07	1.78615e+06	194192.	92.0470	0.0699025
$1/\sqrt{\lambda}$	5.08338e-05	0.000231700	0.000748240	0.00226926	0.104231	3.78228
ω_b	**0.941303**	-0.311875	0.0158140	-0.000388668	0.00609879	0.128043
ω_{CDM}	0.336628	**0.895549**	-0.0278311	0.000727449	-0.0113438	-0.289432
n_s	-0.0177505	0.251524	**-0.531753**	-0.000470379	0.00726711	**0.808459**
H_0	0.0177360	-0.193551	**-0.845250**	0.00354167	-0.0536262	-0.494861
n_ν	0.000844759	0.000148456	0.0420309	0.0739132	**-0.995705**	0.0366109
ω_k	1.26266e-05	-2.02865e-05	0.000337697	**-0.997258**	-0.0740027	0.000313655

Table 5.4: Diagonalised Fisher matrix corresponding to the eigenvalues and eigenvectors of the principal components for the six-parameter model. Each component greater than 0.5 has been shown in bold to highlight which physical variable contributes significantly to each principal component.

degeneracies among the physical parameters that are unresolved by the experiment. The standard deviation of the principal component is given by $\lambda_i^{-1/2}$, thus to some extent such analyses can be used to analyse the constraining power of an experiment. An important point to note is how many physical parameters can be determined to a high precision rather than how many principal components can be determined to high accuracy. The principal components for Planck are nearly equivalent to physical variables, with X_1, X_2, X_3, X_4, and X_5 coupling strongly to $\omega_b, \omega_{CDM}, H_0, \omega_k$ and n_ν respectively. The strongest degeneracy within this six-parameter model is with n_s and H_0, weighted with 0.53 and 0.84 respectively, and will dominate the errors on these parameters. Small degeneracies between the densities will also lead to errors, and these are in a sense fundamental, because they cannot be removed by making more accurate observations of the CMB temperature anisotropies, as Planck is very close to being cosmic-variance limited. Accurate polarisation measurements on large scales however can constrain the tensor component and thus help to break these degeneracies further (we have not included a tensor component in this work, but see Chapter 1 for a discussion).

Eigenvalues	3.96735e+08	1.98022e+07	747695.	617158.	50.3020	0.188573	-743.806
$1/\sqrt{\lambda}$	5.02053e-05	0.000224721	0.00115648	0.00127292	0.140996	2.30282	-
ω_b	**-0.928950**	0.309769	-0.0159209	0.000385683	-0.00381968	-0.202032	0.00307185
ω_{CDM}	0.364775	**0.855978**	-0.0372621	0.000700002	-0.00784647	-0.362311	-0.0390054
n_s	0.0588726	-0.377300	0.297110	0.00180256	-0.0317310	**-0.870767**	0.0816058
H_0	-0.0195896	0.156423	**0.953367**	-0.000574170	-0.0262545	0.254915	-0.0238187
n_ν	-0.00324319	-0.0147235	-0.0326522	-0.00426064	**-0.974975**	0.0100040	-0.219116
ω_k	6.35796e-05	0.000214251	6.29318e-05	**-0.999984**	0.00343041	-0.00188077	0.00406993
T_{CMB}	0.0114292	0.0656150	-0.0103968	0.00309067	-0.218264	0.0677719	**0.971192**

Table 5.5: Diagonalised Fisher matrix corresponding to the eigenvalues and eigenvectors of the principal components for the seven-parameter model including T_{CMB}. Each component greater than 0.5 has been shown in bold to highlight which physical variable contributes significantly to each principal component.

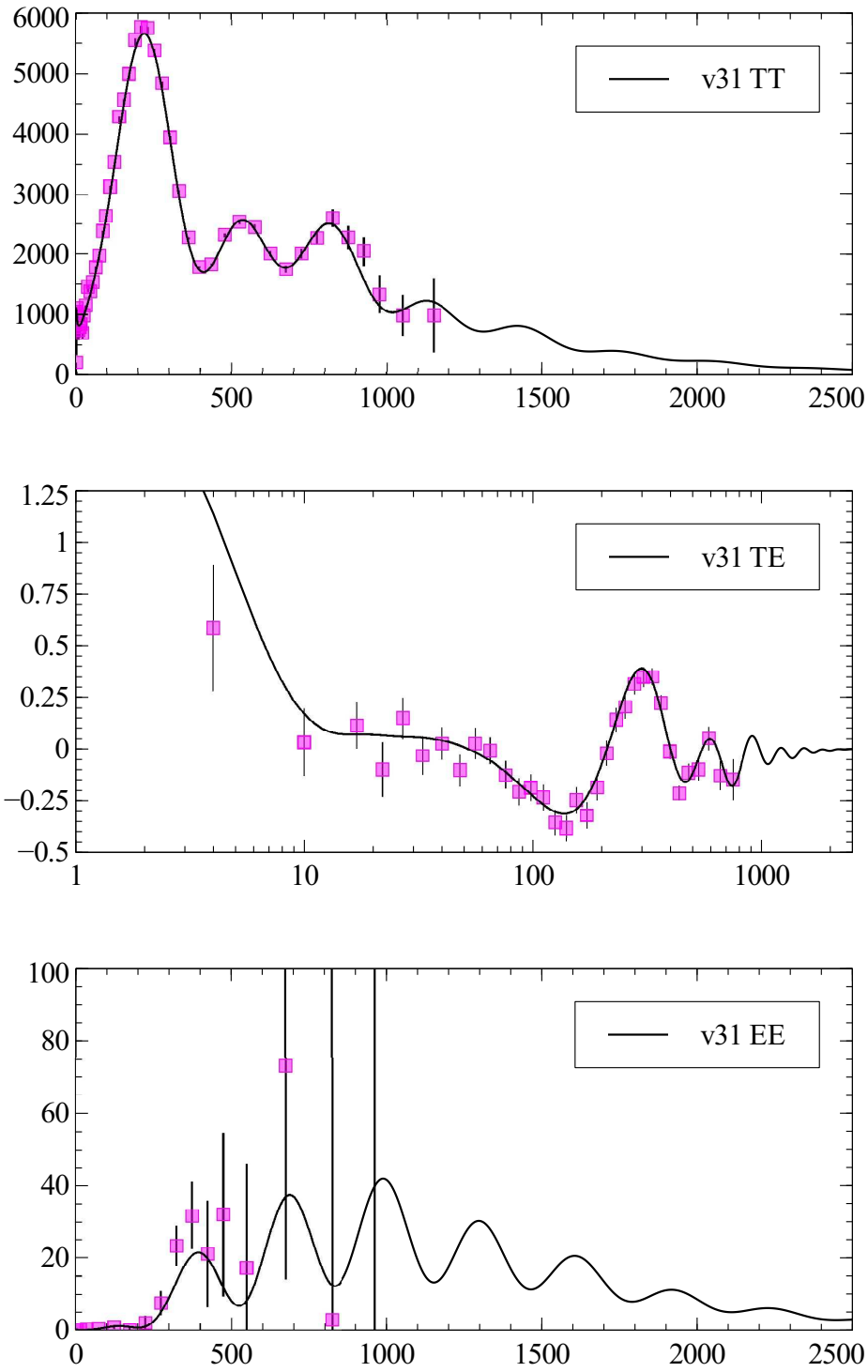

Figure 5.5: *Top:* $\ell(\ell+1)C_\ell/2\pi$ Temperature auto power spectrum generated with CAMB from the best-fitting v50 parameter set. Also plotted in magenta for comparison is the WMAP 7-year TT power spectrum with symmetric error bars. *Centre:* TE cross power spectrum from the best-fitting v50 parameter set with WMAP 7-year TE power spectrum and error bars. Note plotted for TE is $(\ell+1)C_\ell/2\pi$. *Bottom:* $\ell(\ell+1)C_\ell/2\pi$ EE power spectrum with the WMAP 7-year EE power spectrum with symmetric error bars.

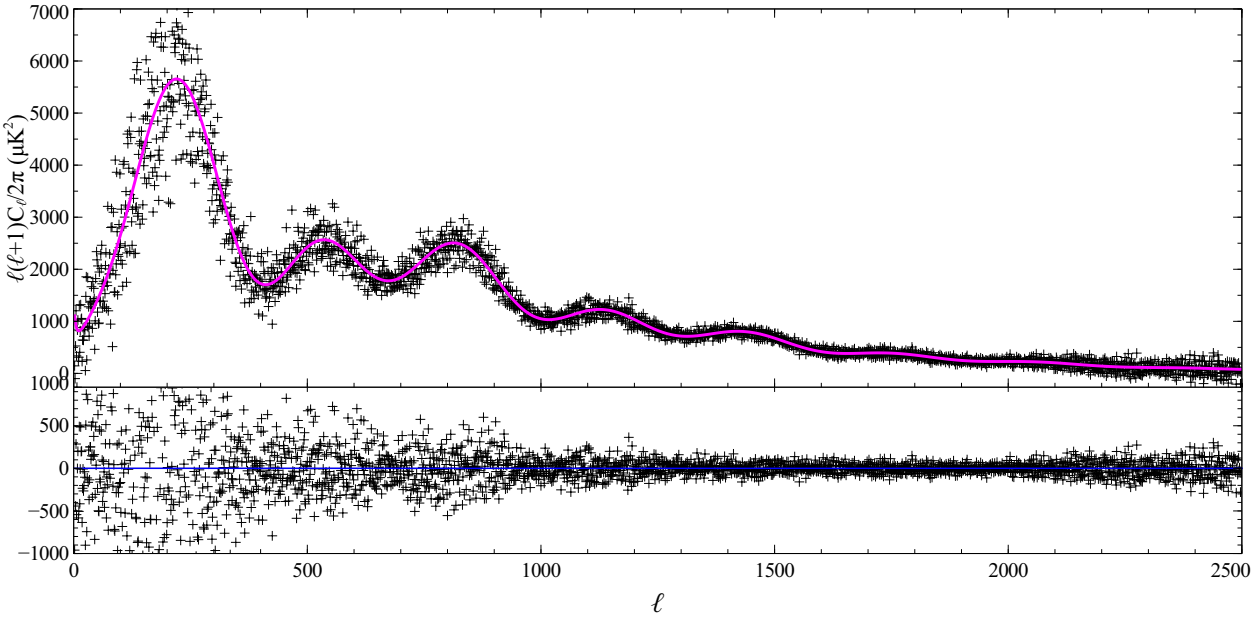

Figure 5.6: Raw unbinned power spectrum points (black) plotted with the v50 best-fitting power spectrum (magenta). The subplot shows the difference in μK.

5.5 Oscillations in the Power Spectrum

An interesting feature appears in the residuals of the Planck v50 temperature power spectrum at $\ell \approx 700 - 1000$ which is not removed by either modifying CosmoMC chains or the Fisher matrix approach detailed above. The feature appears as a sinusoidal oscillation which dies out above $\ell = 1000$. Planck is the one of the few instruments with enough sensitivity to potentially extract new physics from the CMB power spectrum, and some early-universe models (e.g. monodromy) do give rise to characteristic oscillations about the standard cosmology which may be detectable following the full survey data release. In this section we investigate how the Fisher matrix analysis we presented earlier performs in minimising the oscillation for an extended parameter set, and how far we have to push the model away from the CosmoMC-derived maximum-likelihood point to do so, and the effect on the residuals across the entire ℓ range. Given the parameter degeneracies, it is likely that minimising the $\ell \approx 800 - 1000$ oscillation will generate additional features elsewhere in the multipole range.

5.5.1 Quantising the Planck Data

Instead of a simple group-binning, we weight the C_ℓs by their variance estimate from the covariance matrix, then group the C_ℓs into equal-noise bins in units of μK^2. The resultant binned spectrum is shown in Figure 5.7 with the improved estimate of the v50 power spectrum. Typically ~ 25 raw points contribute to each data bin, with the oscillation clearly visible.

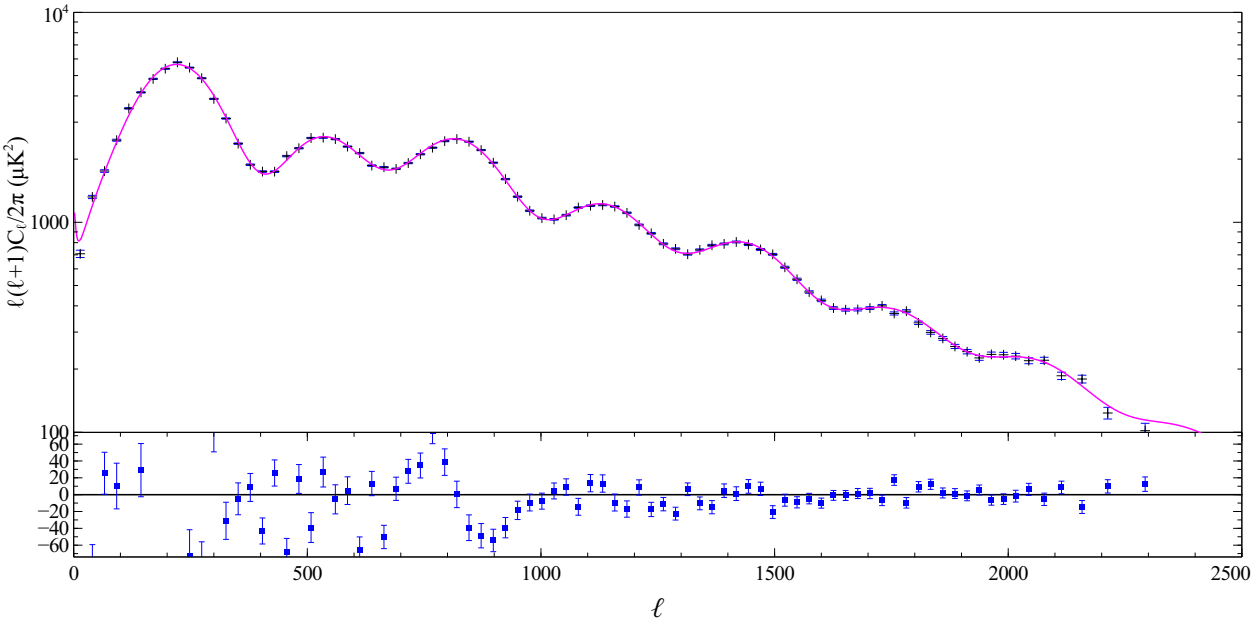

Figure 5.7: Planck v50 temperature power spectra (blue on main plot) with improved spectrum fit (magenta). Subplot shows residual $C_\ell^{Planck} - C_\ell^{fid}$ and errors calculated from the covariance matrix. Note the marked oscillation between $\ell \sim 800 - 1000$.

5.5.2 Testing Models

Within a simple six-parameter cosmological model, $\partial H_0/\partial C_\ell$ exhibits the largest oscillation around the multipole range $\ell \sim 800 - 1000$. To illustrate this point, the effect of adjusting the value of H_0 is shown in Figure 5.8. The reduced χ^2 increases from 1.3572 to 1.4108 as we decrease H_0 from 69.566 to 68.566, an increase of 5%. The χ^2 statistic accurately captures the variability in the power spectrum and weights all bins by the corresponding levels in the covariance matrix. The oscillation is lessened in a model with $H_0 = 68.266$, but residuals at high and low-ℓ then quickly increase and increase the χ^2. Any further decrease in H_0 beyond 68.266 causes noticeable oscillations above $\ell = 1000$, while the original oscillation at $\ell \sim 800 - 1000$ remains in the residuals. Of course, H_0 itself is degenerate with ω_k and we could have also modified this parameter instead of H_0 with similar effect (reducing the oscillation would lead to a slightly-closed Universe). No other change in the standard six-parameter cosmology reduces the amplitude of the oscillation beyond what is shown in Figure 5.8 without hugely affecting other parts of the spectrum.

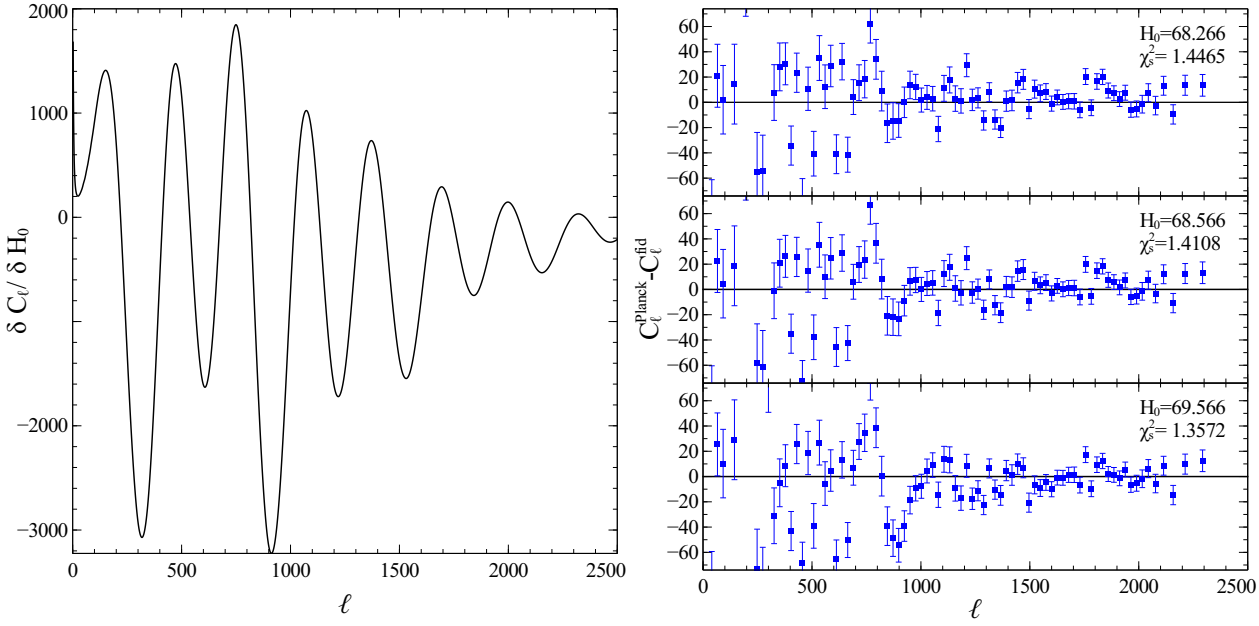

Figure 5.8: *L*eft:Derivative of the temperature power spectrum with respect to H_0. *R*ight: Absolute residuals between the Planck temperature power spectrum and the fiducial model, with varying values of H_0 (indicated on plots), and reduced χ^2_s statistic. A lower value of H_0 reduces the oscillation but inflates errors elsewhere. All other parameters remain unchanged.

Another possible source of oscillations such as the one found in the v50 spectrum is a modified equation of state for dark energy. Dark energy models with a single scalar field cannot cross the equation of state divide set by a cosmological constant. General models that do allow crossing require additional degrees of freedom to ensure gravitational stability [165] [166]. The main CAMB code supports smooth dark energy models with a constant equation of state with $w = -1$. An add-on Parameterised Post-Friedmann (PPF) module [167] allows for crossing the divide (i.e. $w < -1$).

To demonstrate the effect that w alone has on the spectra, Figure 5.9 shows three models with varying w_0 from -1 to -1.04. As H_0 is degenerate with w_0, the effect on the residuals is very similar and the oscillation is again reduced, at the expense of inflating errors elsewhere in the spectrum. At $w = -1.04$, χ^2_s rises to 1.3616, an increase of 4% over the $w_0 = -1$ case. All other parameters are left unchanged.

The power of the Fisher matrix analysis is to recover the set of parameters that minimise the oscillations and includes the parameter degeneracies. Following the formalism detailed earlier, we minimse Δs with respect to an extended parameter set shown in Table 5.6, and examine the residuals.

Parameter	ω_b	ω_{CDM}	ω_k	n_s	H_0	n_ν	A_s	w	$red.\chi^2$
s_o	0.02252	0.117055	0.0	0.9751	69.566	3.046	2.241×10^{-9}	-1.00	1.3572
s_i	0.02211	0.11656	-0.026	0.9511	69.216	2.896	2.127×10^{-9}	-1.03	1.3564
Step	0.0001	0.002	0.0003	0.002	0.01	0.1	1×10^{-11}	0.001	

Table 5.6: The initial (s_0) and final (s_i) cosmological model computed using the Fisher approximation to the maximum-likelihood with an extended parameter set. Also given are the initial and final reduced χ^2 values, showing a small reduction with the new parameter set. The trial step sizes are also given for each parameter.

For the extended set of parameters, Δs is close to the best fit model for the standard case, and although the χ^2 drops very slightly, the residuals are unreduced, so adding curvature, $w \neq -1$, or changing n_ν or A_s does not reduce the oscillation. Successive internal data releases will provide more information on whether this strange oscillation is really a feature of the data, or is simply a noise or instrumental artifact. Exotic cosmologies can produce oscillations of this sort, for example monodromy [168] and at this stage it is probably too premature to make any firm speculations regarding the outcome. Multiple methods for calculation of the power spectrum also exist within the collaboration, however differences in spectra between codes are too small to account for these oscillations. No simple addition of parameters help to fit the oscillation. Although it is visually striking, it is not particularly significant - perhaps a 2.5-3σ fluctuation of which one is expected in this number of band-averaged data points. The most plausible explanation is that it is a statistical fluke. The statistical significance of a particular fitted monodromy model is not high - consistent with the feature being a fluke. This work was part of a larger effort to get a feel for the data, and features like this are not unexpected. A year or so after this work was completed following the public data release, this conclusion was confirmed by the extensive grid of models presented in the main parameters paper [10].

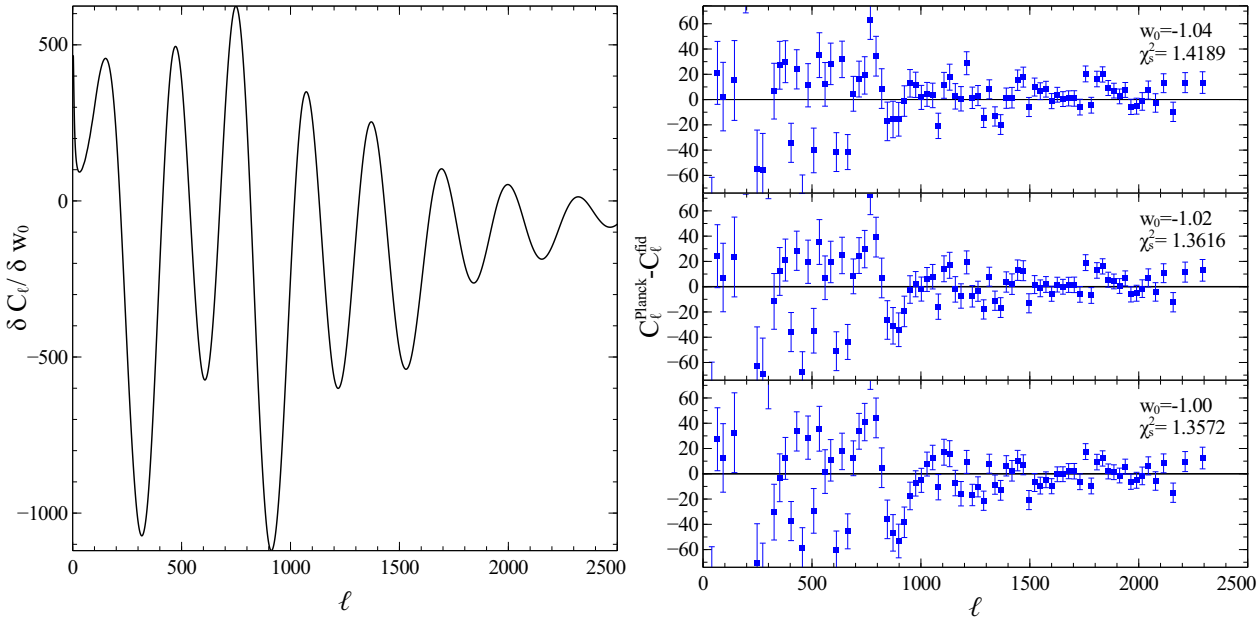

Figure 5.9: *L*eft:Derivative of the temperature power spectrum with respect to w_0. *R*ight: Absolute residuals between the Planck temperature power spectrum and the fiducial model, with varying values of w_0 using the CAMB Parameterised Post Friedmann module (indicated on plots), and χ^2_s statistic. A lower value of w_0 reduces the oscillation but inflates errors elsewhere. All other parameters remain unchanged.

5.6 Conclusion

High precision CMB anisotropy observations from Planck will hugely improve our knowledge of the fundamental cosmological parameters. In this Chapter we have analysed the degeneracies present in the v50 internal data release of the nominal mission and corresponding covariance matrix. The geometrical degeneracy between Ω_Λ and Ω_k for models with identical matter densities is nearly exact and can be broken from observations of CMB lensing. It is broken to a higher precision by additional data, such as distances to Type 1a supernovae. We have analysed a Fisher-matrix approach to exploring the maximum-likelihood chain generated with CosmoMC, and found a small improved model located very near the v50 maximum-likelihood point. The Fisher matrix defines a set of principal components, or linear combinations of parameters s_i defining the CMB power spectrum. We have used the Fisher matrix to extract principal components for the Planck data in its current stage (January 2012), and find that the principal components are largely representative of the original cosmological parameters s_i. The five highest principal components couple strongly to $\omega_b, \omega_{CDM}, H_0, \omega_k$ and n_ν, with a strong degeneracy between n_s and H_0. The small couplings between parameters are however important at the precision of Planck. The CosmoMC chains we have worked with are based on a foreground model themselves, and so small adjustments to e.g. the point source amplitudes, or diffuse components could have large effects on the power spectrum and therefore parameter estimation. High accuracy subtraction of foregrounds prior to power spectrum

likelihoods is necessary to achieve the highest reliability parameter estimation from Planck. Further work on successive data releases will be essential to characterise such foregrounds and their effects on the resultant cosmological models.

We also look at an oscillation in the power spectrum between $\ell \sim 800 - 1000$ and examine whether this can be mitigated by sampling around the best-fitting point. We find that while the oscillation can be significantly damped by either lowering the expansion rate or favouring a slightly open Universe, the overall χ^2 of the fit rises by $\sim 5\%$, and additional oscillations arise in other parts of the spectrum. Nevertheless the behaviour of this oscillation persists, and it will be interesting to note whether it remains significant in future data releases. Its source could well be instrumental and in which case it should not feature when more in-flight instrumental systematic measurements are calculated. No simple extension of the ΛCDM model can fit the oscillation and so it appears to be a statistical fluke.

In summary for the v50 MCMC chains:

- The principal components couple strongly to the basic model parameters (Section 5.4).
- A Fisher matrix approximation finds a small improvement near the cosmoMC maximum, validating such methods (Section 5.3).
- A strange oscillation persists in the data even with a slightly better fitting model (Section 5.5).

Astronomy compels the soul to look upwards and leads us from this world to another
- Plato

Chapter 6

Conclusion

The Planck satellite was launched in 2009, and the consortium delivered the primary data products to the community in March 2013, composed from 15 months of observation, the nominal mission length. The data provide strong evidence in favour of a Universe that is spatially flat, accelerating at the present day, and composed of: 4.9% matter, 26.8% dark matter, and 68.3% dark energy. While Planck has exquisitely mapped the temperature fluctuations, more attention has now been turned to the polarisation signal. Characterising the polarisation of the CMB is currently one of the central focusses of experimental cosmology and has the power to considerably improve estimates of several cosmological parameters and enhance our understanding of the components and evolution of our Universe. Polarisation measurements may provide significant further evidence in favour of an inflationary phase, and allow us to estimate, or greatly improve constraints on, both the energy scale at which inflation occurred and its dynamics.

In summary we have:

- Modelled the microwave sky using high and low temperature templates to simulate the Planck sky (Section 2.3).
- Performed a low-resolution parametric fitting foreground separation to recover an input B-mode at $r = 0.1$ (Section 2.4).
- Shown that this method reliably recovers an input B-mode but can be improved at higher resolutions by incorporating correlated foreground spectral indices into the likelihood (Section 2.5).
- Analysed the accuracy of our foreground simluations by comparing them to the dx8 Planck data and found that synchrotron is well modelled in polarisation, but dust is poorly modelled (Section 3.3).
- Calcualted polarisation power spectra for varying mask sizes and found that at 143 GHz a conservative mask can be used, but at 217 GHz a larger mask is necessary to avoid aliased

foreground power (Section 3.6.1).

- Found a poor correlation between Planck and WMAP for CMB polarisation (Section 4.2).
- Shown that ILC, template fitting and parametric fitting all give consistent results dominated by systematics (Section 4.5).
- Calculated low-resolution qml power spectra and found good E-mode but poor B-mode estimation (Section 4.7).
- Performed a Fisher analysis on the Planck v50 data to improve a basic model fit (Section 5.3).
- Found that the principal components of the Fisher matrix approximation couple strongly to the model parameters (Section 5.4).
- Investigated a strange oscillation in the temperature power spectrum and found that no simple extension removed the oscillation without increasing discrepencies elsewhere (Section 5.5).

In this thesis we have addressed the major obstacle that must be overcome if we wish to achieve this with Planck and other experiments mapping the polarisation signal; the presence of foreground radiation which contaminates all Planck sky maps in both temperature and polarisation. The issue of foreground contamination is particularly important given the difference in amplitude between the total CMB intensity field, and the typical B-mode polarisation amplitude imprinted at recombination by primordial gravitational waves generated during inflation. Even if an inflationary B-mode is large enough to be theoretically detectable with Planck, foreground contamination and systematics will be the limiting step in extracting it. We have concentrated our work on the two strongest diffuse foregrounds: electron synchrotron and thermal dust emission. In Chapter 2 we investigated the simulation of these foregrounds in temperature and polarisation by using existing low and high frequency templates as tracers of the intensity emission, and power laws in frequency to generate noisy component maps at the Planck observing frequencies. An artificial B-mode polarisation signal at the $r = 0.1$ level was injected into polarised CMB maps and coadded to produce simulations of the Planck observations. We examined the change in synchrotron polarisation when switching from using a 408 MHz temperature template to the WMAP 23 GHz polarisation template and the effect that applying a depolarisation factor has on the simulated polarisation morphology (and in Chapter 4 observe that the WMAP template indeed models the synchrotron polarisation more accurately). We then developed a parametric fitting component separation algorithm to extract the polarised CMB, thermal dust, and synchrotron components from these noisy simulations and perform a likelihood analysis with posteriors that suggest a well-recovered input B-mode. Our results are consistent with previous works and our method extends those by incorporating a spatial correlation of the foreground spectral indices which leads to a stability of the posteriors in r at higher resolution simulations. The $r = 0.1$ B-mode was recovered reliably at all resolutions tested, and the output Q and U maps show good correlation with the input maps. Our method also recovers the foregrounds to a high precision, with residuals consistent with the noise level. This

work could be extended further by investigating the posterior stability at even higher resolutions (matrix calculations at higher resolutions were not possible with the computing facilities available), or with a varying correlation length to check for consistency with single spectral index fitting.

In Chapter 3 we examined the Planck dx8 polarisation data and correlation with the WMAP 7-year data. We performed template fitting, ILC, and parametric fitting component separation and compared the output maps. The different methods produced similar polarisation maps. We compared the ILC polarisation maps produced using just LFI channels and HFI channels, and found that the difference between these is similar in morphology to the systematic effect seen in other foreground-cleaned CMB maps, hinting at an underlying systematic in either the LFI or HFI channels. The foreground-cleaned CMB polarisation maps correlate weakly with the WMAP data, which is an issue of concern, and coupled with the systematic effects suggests that the Planck large-scale polarisation data is not currently accurate enough to perform precision cosmology with. This may change with future data exchanges incorporating ADC nonlinearity corrections and further bandpass and gain mismatch estimations.

In Chapter 4 we looked at the correlation of the Planck data with the sky model, and found that the synchrotron foreground is morphologically similar to the sky observed with Planck in polarisation, however the dust model is far from accurate. This was as expected given the synchrotron emission is based on WMAP data, and the dust model is based on a fiducial model of the galactic magnetic field. The typical level of synchrotron polarisation is typically overestimated by the PSM, but including a depolarisation factor greatly reduces the discrepancy. The dust was found to be polarised highly at up to $\sim 15\%$ in small clouds with a low background, rather than a global $\sim 5\%$ as assumed in the PSM. The Planck data allow us to form much more accurate dust and synchrotron simulations in both temperature and polarisation for future work characterising foregrounds, and the large lever arm in frequency that Planck provides increases the reliability of foreground templates.

In Chapter 5 we examined degeneracies present in the v50 internal data release, and analysed a Fisher-matrix approach to exploring the MCMC chain generated with CosmoMC, and found a small improved model located near the v50 maximum-likelihood point. We extracted principal components, and found that most of the variance in estimates comes from the lowest order components, and that the principal components are largely representative of the original cosmological parameters. We also found that an oscillation in the power spectrum between $\ell \sim 800 - 1000$ can be significantly damped by lowering the expansion rate, but the overall χ^2 of the fit rises by $\sim 5\%$, and additional oscillations arising from the shape of $\partial C_\ell / \partial \Omega_k$ appear in other parts of the spectrum. Nevertheless the behaviour of this oscillation persists, and the conclusion that it is a statistical fluke was indeed confirmed in the 2013 Planck papers.

There are several experiments currently observing the polarised microwave sky. Ground-based observatories include BICEP2 [47], Polarbear [169], ACTpol [170], SPTpol [171], C-BASS [172], Quijote [48] and QUIET [173]. The SPTpol team has recently reported a detection of a lensing B-mode using first-season data from the South Pole Telescope polarisation-sensitive receiver [174],

calculated by comparing a B-mode template for the lensing signal with estimates of the lensing potential and the SPTpol data. They find a non-zero correlation at 7.7σ significance, which constitutes the first measurement of a cosmological B-mode signal. This observation will certainly be improved upon with more data from SPTpol and other ground-based observatories, which mostly survey small sections of the sky. More accurate foreground removal will also be facilitated by more precise data mapping synchrotron and dust polarisation, and indeed C-BASS and Quijote are primarily sensitive to synchrotron emission at 5 GHz, and between 11-40 GHz respectively. All of these experiments have similar or higher sensitivity than Planck, allowing for more precise foreground characterisation, however do not probe the largest scales therefore their data will remain complementary to Planck's. Balloon-borne experiments such as SPIDER [49] and EBEX [175] typically experience a much lower atmospheric contamination but are usually restricted to flights above Antarctica.

CMB polarisation is currently a very active field of research. On the largest scales foregrounds represent the ultimate limit on how well experiments hunting a primordial B-mode can perform. At smaller scales and in the more distant future, CMB lensing should provide the dominant source of confusion for measurements targeting the signal from recombination around $\ell \sim 100$. Lens reconstruction with polarisation and delensing will become important tools to mitigate this confusion, essential for all the experiments listed above. Looking further still into the future, two proposed space-based satellites; CMBPol [176] and COrE [142] have been designed primarily with B-modes in mind, and if successful (neither proposal has yet been accepted), will observe the entire sky from the L2 point over a large frequency range just as Planck has. Our work on the impact of foregrounds on the potential of CMB polarisation surveys sounds a note of caution as to their viability. We have seen that foreground emission may prevent this potential from being realised, however measurements of the foreground emission provided by the upcoming generation of CMB polarisation experiments should allow a more rigorous assessment of the viability of such experiments. The prospect of finding evidence strongly supporting inflation through a ground or space-based B-mode observation would constitute a discovery of profound and lasting significance to cosmology.

Appendix A

CAM-SPEC Cosmological Model Parameters

Here we define the parameters used in the cosmological model described in Chapter 5

Parameter	Definition
$\Omega_b h^2$	Baryon physical density today
$\Omega_{CDM} h^2$	Cold Dark Matter physical density today
θ	The ratio of the sound horizon to the angular diameter distance
τ	Reionisation optical depth
n_s	Scalar spectrum power-law index ($k_0 = 0.05\text{Mpc}^{-1}$)
$\log(A_s)$	Log power of the primordial curvature perturbations ($k_0 = 0.05\text{Mpc}^{-1}$)
A_{PCA1}	Point-source correlation coefficient for Planck at 143 GHz
A_{PCA2}	Point-source correlation coefficient for Planck at 217 GHz
psr	Contribution of Poisson point-source power to $\mathcal{D}_{3000}^{143\times143}$ for Planck
A_{CIB143}	Contribution of CIB power to $\mathcal{D}_{3000}^{143\times143}$ at the Planck CMB frequency for 143 GHz (in μK^2)
A_{CIB217}	As for 143 but for 217 GHz
A_{SZ143}	Contribution of tSZ to $\mathcal{D}_{3000}^{143\times143}$ at 143 GHz (in μK^2)
$cibr$	CIB correlation coefficient between 143 and 217 GHz
Ω_Λ	Dark energy density divided by the critical density today
Age/Gyr	Age of the Universe in Gyr
Ω_m	Matter density (inc. massive neutrinos) today divided by the critical density
z_{re}	Redshift at which Universe is half reionised
H_0	Current expansion rate in km/s/Mpc

References

[1] Penzias, A. A., Wilson, R. W., 1965. *ApJ*, 142:419

[2] Smoot, G. F., Bennett, C. L., Kogut, A., et al., 1992. *ApJ Letters*, 396:L1

[3] Lange, A. E., Ade, P. A., Bock, J. J., et al., 2001. *Phys. Rev. D*, 63(4):042001

[4] Hinshaw, G., Larson, D., Komatsu, E., et al., 2013. *ApJ*, 208:19

[5] Riess, A. G., Filippenko, A. V., Challis, P., et al., 1998. *AJ*, 116:1009

[6] Schmidt, B. P., Suntzeff, N. B., Phillips, M. M., et al., 1998. *ApJ*, 507:46

[7] Perlmutter, S., Aldering, G., Goldhaber, G., et al., 1999. *ApJ*, 517:565

[8] Hawkins, E., Maddox, S., Cole, S., et al., 2003. *MNRAS*, 346:78

[9] Abazajian, K. N., Adelman-McCarthy, J. K., Agüeros, M. A., et al., 2009. *ApJ*, 182:543

[10] Planck Collaboration, Ade, P. A. R., Aghanim, N., et al., 2013. *AA*, 182

[11] Zwicky, F., 1933. *Helvetica Physica Acta*, 6:110

[12] Rubin, V. C., Ford, W. K., Jr., 1970. *ApJ*, 159:379

[13] Koopmans, L. V. E., Treu, T., 2003. *ApJ*, 583:606

[14] Vikhlinin, A., Kravtsov, A., Forman, W., et al., 2006. *ApJ*, 640:691

[15] Viel, M., Bolton, J. S., Haehnelt, M. G., 2009. *MNRAS*, 399:L39

[16] Tanaka, T., Abe, K., Hayato, Y., et al., 2011. *ApJ*, 742:78

[17] Bernabei, R., Belli, P., Cappella, F., et al., 2008. *European Physical Journal C*, 56:333

[18] The Planck Collaboration, 2006. *ESA Reports*

[19] Kovac, J. M., Leitch, E. M., Pryke, C., et al., 2002. *Nature*, 420:772

[20] Hubble, E., 1929. *Proceedings of the National Academy of Science*, 15:168

[21] Baade, W., 1975. *Evolution of stars and galaxies*. MIT Press

[22] Planck Collaboration, Ade, P. A. R., Aghanim, N., et al. *AA*, 536

[23] Starobinskii, A. A., 1979. *ZhETF Pisma Redaktsiiu*, 30:719

[24] Mukhanov, V. F., Chibisov, G. V., 1981. *ZhETF Pisma Redaktsiiu*, 33:549

[25] Linde, A. D., 1979. *Reports on Progress in Physics*, 42:389

[26] Guth, A. H., 1981. *Phys. Rev. D*, 23:347

[27] Barbón, J. L. F., Espinosa, J. R., 2009. *Phys. Rev. D*, 79(8):081302

[28] Bertschinger, E., 2001. *Proceedings of Cosmology 2000*

[29] Riotto, A. *High Energy Physics*, 101

[30] Gibbons, G. W., Hawking, S. W., 1977. *Phys. Rev. D*, 15:2738

[31] Zarrouki, R., Sakhi, Z., Bennai, M., 2011. *General Relativity and Gravitation*, 43:1515

[32] Ross, G. G., Sarkar, S., 1996. *Nuclear Physics B*, 461:597

[33] Rendall, A. D., 2005. *Classical and Quantum Gravity*, 22:1655

[34] Tye, S.-H. H., 2008. Gasperini, M., Maharana, J., editors, *String Theory and Fundamental Interactions*, vol. 737 of *Lecture Notes in Physics, Berlin Springer Verlag*. 949

[35] Hirai, S., Takami, T. *Classical and Quantum Gravity*, 27-3

[36] Cheng, C., Huang, Q.-G., Ma, Y.-Z., 2013. *JCAP*, 7:018

[37] Dimopoulos, K., Lazarides, G., 2006. *Phys. Rev. D*, 73(2):023525

[38] Lee, A. T., Ade, P., Balbi, A., et al., 1999. Maiani, L., Melchiorri, F., Vittorio, N., editors, *3K cosmology*, vol. 476 of *American Institute of Physics Conference Series*. 224–236

[39] Netterfield, C. B., Ade, P. A. R., Bock, J. J., et al., 2002. *ApJ*, 571:604

[40] Miller, A., Beach, J., Bradley, S., et al., 2002. *ApJ*, 140:115

[41] Padin, S., Cartwright, J. K., Mason, B. S., et al., 2001. *ApJ Letters*, 549:L1

[42] Dicke, R. H., Peebles, P. J. E., Roll, P. G., et al., 1965. *ApJ*, 142:414

[43] Sachs, R. K., Wolfe, A. M., 1967. *ApJ*, 147:73

[44] Bennett, C. L., Halpern, M., Hinshaw, G., et al., 2003. *ApJ*, 148:1

[45] Silk, J., 1968. *ApJ*, 151:459

[46] QUIET Collaboration, Araujo, D., Bischoff, C., et al., 2012. *ApJ*, 760:145

[47] Ogburn, R. W., IV, Ade, P. A. R., Aikin, R. W., et al., 2010. *Society of Photo-Optical Instrumentation Engineers (SPIE) Conference Series*, vol. 7741

[48] Rubiño-Martín, J. A., Rebolo, R., Tucci, M., et al., 2010. Diego, J. M., Goicoechea, L. J., González-Serrano, J. I., et al., editors, *Highlights of Spanish Astrophysics V*. 127

[49] Filippini, J. P., Ade, P. A. R., Amiri, M., et al., 2010. *Society of Photo-Optical Instrumentation Engineers (SPIE) Conference Series*, vol. 7741

[50] Kamionkowski, M., Kosowsky, A., Stebbins, A., 1997. *Phys. Rev. D*, 55:7368

[51] Zaldarriaga, M., Seljak, U., 1997. *Phys. Rev. D*, 55:1830

[52] Hu, W., Okamoto, T., 2002. *ApJ*, 574:566

[53] Efstathiou, G., Bond, J. R., 1999. *MNRAS*, 304:75

[54] Eisenstein, D. J., Hu, W., Tegmark, M., 1999. *ApJ*, 518:2

[55] Bond, J. R., Efstathiou, G., Tegmark, M., 1997. *MNRAS*, 291:L33

[56] Komatsu, E., Dunkley, J., Nolta, M. R., et al., 2009. *ApJ*, 180:330

[57] Mandolesi, N., Bersanelli, M., Butler, R. C., et al., 2010. *A&A*, 520:A3

[58] Lamarre, J.-M., Puget, J.-L., Ade, P. A. R., et al., 2010. *A&A*, 520:A9

[59] Battaglia, P., Franceschet, C., Zonca, A., et al., 2009. *Journal of Instrumentation*, 4:2014

[60] Planck Collaboration, Ade, P. A. R., Aghanim, N., et al. *AA*, 536

[61] Planck Collaboration, Ade, P. A. R., Aghanim, N., et al., 2011. *A&A*, 536:A2

[62] Planck Collaboration, Ade, P. A. R., Aghanim, N., et al., 2011. *A&A*, 536:A7

[63] Draine, B. T., Lazarian, A., 1998. *ApJ Letters*, 494:L19

[64] Kogut, A., 1996. *American Astronomical Society Meeting Abstracts*, vol. 28 of *Bulletin of the American Astronomical Society*. 1295

[65] Draine, B. T., Lazarian, A., 1998. *ApJ*, 508:157

[66] Planck Collaboration, Ade, P. A. R., Aghanim, N., et al., 2011. *A&A*, 536:A20

[67] Górski, K. M., Hivon, E., Banday, A. J., et al., 2005. *ApJ*, 622:759

[68] Platania, P., Bensadoun, M., Bersanelli, M., et al., 1998. *ApJ*, 505:473

[69] La Porta, L., Burigana, C., Reich, W., et al., 2008. *A&A*, 479:641

[70] Kogut, A., et al., 2007. *ApJ*, 665:355

[71] Kovac, J., et al., 2002. *Nature*, 420:772

[72] Baumann, D., Jackson, M. G., Adshead, P., et al., 2008. *AIP Conf. Proc.*, 1041(arXiv:0811.3919. CERN-PH-TH-2008-230):10

[73] Bevis, N., Hindmarsh, M., Kunz, M., et al., 2007. *Phys. Rev. D*, 76(4):043005

[74] Zaldarriaga, M., Seljak, U., 1997. *Phys. Rev. D*, 55(4):1830

[75] Stepanov, R., Arshakian, T. G., Beck, R., et al., 2008. *A&A*, 480:45

[76] Ginzburg, V. L., Syrovatskii, S. I., 1965. *AA*, 3:297

[77] Rybicki, G. B., Lightman, A. P., 1979. *Radiative processes in astrophysics / George B. Rybicki, Alan P. Lightman*. Wiley, New York :

[78] Zainal Abidin, Z., Leahy, J. P., Wilkinson, A., et al., 2003. *New Astronomy Reviews*, 47:1151

[79] Page, L., Hinshaw, G., Komatsu, E., et al., 2007. *ApJ*, 170:335

[80] Miville-Deschênes, M., Ysard, N., Lavabre, A., et al., 2008. *A&A*, 490:1093

[81] De Zotti, G., et al., 1999. *AIP Conf. Proc.*, 476:204

[82] Grimes, P. K., King, O. G., Yassin, G., et al., 2007. *Electronic Letters*, 43:21:1146

[83] Page, L., et al., 2007. *Astrophys. J. Suppl.*, 170:335

[84] Wolleben, M., Landecker, T. L., Reich, W., et al., 2006. *A&A*, 448:411

[85] Sokoloff, D. D., Bykov, A. A., Shukurov, A., et al., 1998. *MNRAS*, 299:189

[86] Dunne, L., Maddox, S. J., Ivison, R. J., et al., 2009. *MNRAS*, 394:1307

[87] Hiltner, W. A., 1949. *ApJ*, 109:471

[88] Lazarian, A., Cho, J.-Y., 2003. *Recent Research Development in Astronomy Astrophysics, Vol 1 Part II*:255

[89] Berkhuijsen, E. M., Horellou, C., Krause, M., et al., 1997. *A&A*, 318:700

[90] Davis, L., Jr., Greenstein, J. L., 1951. *ApJ*, 114:206

[91] Lazarian, A., Finkbeiner, D., 2003. *New Astronomy Reviews*, 47(11-12):1107 . Proceedings of the Workshop on The Cosmic Microwave Background Radiation and its Polarization

[92] Benoit, A., et al., 2003. *AA*, 399:L19

[93] Sethi, S., Prunet, S., Bouchet, F., 1998. *Fundamental parameters in Cosmology*, 1

[94] Gold, B., et al., 2009. *Astrophys. J. Suppl.*, 180:265

[95] Bennett, C., et al., 2003. *Astrophys. J. Suppl.*, 148:97

[96] Keating, B., Timbie, P., Polnarev, A., et al., 1998. *ApJ*, 495:580

[97] Kogut, A., 1999. de Oliveira-Costa, A., Tegmark, M., editors, *Microwave Foregrounds*, vol. 181 of *Astronomical Society of the Pacific Conference Series*. 91

[98] Draine, B. T., Lazarian, A., 1999. de Oliveira-Costa, A., Tegmark, M., editors, *Microwave Foregrounds*, vol. 181 of *Astronomical Society of the Pacific Conference Series*. 133

[99] Draine, B. T., Li, A., 2001. *The Astrophysical Journal*, 551(2):807

[100] Ali-Haïmoud, Y., Hirata, C. M., Dickinson, C., 2009. *MNRAS*, 395:1055

[101] De Oliveira-Costa, A., Tegmark, M., Finkbeiner, D., et al., 2000. *The Astrophysical Journal*, 567(2)

[102] Dobler, G., Draine, B., Finkbeiner, D. P., 2009. *ApJ*, 699:1374

[103] Mason, B., Robishaw, T., Finkbeiner, D., 2008. *Frontiers of Astrophysics*, 395:373

[104] Battistelli, E. S., et al., 2006. *ApJ*, 645:L141

[105] Dickinson, C., et al., 2007. *MNRAS*, 379:297

[106] López-Caraballo, C. H., Rubiño-Martín, J. A., Rebolo, R., et al., 2011. *ApJ*, 729:25

[107] Tegmark, M., Efstathiou, G., 1996. *MNRAS*, 281:1297

[108] Cardoso, J.-F., Martin, M., Delabrouille, J., et al., 2008. *IEEE-JSTSP*, 54

[109] Delabrouille, J., Cardoso, J. F., Patanchon, G., 2003. *MNRAS*, 346:1089

[110] Hobson, M. P., Jones, A. W., Lasenby, A. N., et al., 1998. *MNRAS*, 300:1

[111] Stolyarov, V., Hobson, M. P., Ashdown, M. A. J., et al., 2002. *MNRAS*, 336:97

[112] Dunkley, J., Amblard, A., Baccigalupi, C., et al., 2009. Dodelson, S., Baumann, D., Cooray, A., et al., editors, *American Institute of Physics Conference Series*, vol. 1141 of *American Institute of Physics Conference Series*. 222–264

[113] Armitage-Caplan, C., Dunkley, J., Eriksen, H. K., et al., 2011. *MNRAS*, 418:1498

[114] Eriksen, H. K., Jewell, J. B., Dickinson, C., et al., 2008. *ApJ*, 676:10

[115] Larson, D. L., Eriksen, H. K., Wandelt, B. D., et al., 2007. *ApJ*, 656:653

[116] Eriksen, H. K., et al., 2006. *New Astron. Rev.*, 50:861

[117] Metropolis, N., Rosenbluth, A. W., Rosenbluth, M. N., et al., 1953. *JCP*, 21:1087

[118] Dunkley, J., Spergel, D. N., Komatsu, E., et al., 2009. *ApJ*, 701:1804

[119] Lewis, A., Challinor, A., Lasenby, A. *ApJ*

[120] Seljak, U., Zaldarriaga, M., 1996. *ApJ*, 469:437

[121] Haslam, C. G. T., Salter, C. J., Stoffel, H., et al., 1982. *AApS*, 47:1

[122] Davies, R. D., Watson, R. A., Gutierrez, C. M., 1996. *MNRAS*, 278:925

[123] Platania, P., Burigana, C., Maino, D., et al., 2003. *A&A*, 410:847

[124] Miville-Deschênes, M.-A., Ysard, N., Lavabre, A., et al., 2008. *A&A*, 490:1093

[125] Reich, W., 1982. *AApS*, 48:219

[126] Jonas, J. L., Baart, E. E., Nicolson, G. D., 1998. *MNRAS*, 297:977

[127] Delabrouille, J., Betoule, M., Melin, J.-B., et al., 2013. *A&A*, 553:A96

[128] Giardino, G., Banday, A. J., Górski, K. M., et al., 2002. *A&A*, 387:82

[129] Taylor, J. H., Cordes, J. M., 1993. *ApJ*, 411:674

[130] Finkbeiner, D. P., Davis, M., Schlegel, D. J., 1999. *ApJ*, 524:867

[131] Tucci, M., Martínez-González, E., Vielva, P., et al., 2005. *MNRAS*, 360:935

[132] Amblard, A., Cooray, A., Kaplinghat, M., 2007. *Phys. Rev. D*, 75(8):083508

[133] Betoule, M., Pierpaoli, E., Delabrouille, J., et al., 2009. *A&A*, 503:691

[134] Dunkley, J., Amblard, A., Baccigalupi, C., et al., 2009. S. Dodelson, D. Baumann, A. Cooray, J. Dunkley, A. Fraisse, M. G. Jackson, A. Kogut, L. Krauss, M. Zaldarriaga, & K. Smith , editor, *American Institute of Physics Conference Series*, vol. 1141 of *American Institute of Physics Conference Series*. 222–264

[135] Efstathiou, G., Gratton, S., 2009. *JCAP*, 6:011

[136] Strong, A. W., Moskalenko, I. V., Reimer, O., 2000. *ApJ*, 537:763

[137] Finkbeiner, D. P., Davis, M., Schlegel, D. J., 1999. *ApJ*, 524:867

[138] Planck Collaboration, Abergel, A., Ade, P. A. R., et al., 2011. *A&A*, 536:A24

[139] Tegmark, M., de Oliveira-Costa, A., 2001. *Phys. Rev. D*, 64(6):063001

[140] Efstathiou, G., Gratton, S., Paci, F., 2009. *MNRAS*, 397:1355

[141] Zaldarriaga, M., 1998. *PhD Thesis*

[142] The COrE Collaboration, Armitage-Caplan, C., Avillez, M., et al., 2011. *White Paper*

[143] Stivoli, F., Baccigalupi, C., Maino, D., et al., 2006. *MNRAS*, 372:615

[144] Rubiño-Martín, J. A., López-Caraballo, C. H., Génova-Santos, R., et al., 2012. *Advances in Astronomy*, 2012:351836

[145] de Oliveira-Costa, A., Tegmark, M., O'dell, C., et al., 2003. *Phys. Rev. D*, 68(8):083003

[146] Delabrouille, J., Betoule, M., Melin, J.-B., et al., 2013. *A&A*, 553:A96

[147] Planck collaboration, Ade, P. A. R., Aghanim, N., et al., 2013. *ArXiv e-prints 1303.5075*

[148] Planck Collaboration, Ade, P. A. R., Aghanim, N., et al., 2013. *ArXiv e-prints 1303.5069*

[149] Zacchei, A., Maino, D., Baccigalupi, C., et al., 2011. *A&A*, 536:A5

[150] Planck HFI Core Team, Ade, P. A. R., Aghanim, N., et al., 2011. *A&A*, 536:A6

[151] Planck Collaboration, Aghanim, N., Armitage-Caplan, C., et al., 2013. *ArXiv e-prints 1303.5063*

[152] Planck Collaboration, Aghanim, N., Armitage-Caplan, C., et al., 2013. *ArXiv e-prints 1303.5064*

[153] Planck Collaboration, Ade, P. A. R., Aghanim, N., et al., 2013. *ArXiv e-prints 1303.5067*

[154] Zonca, A., Franceschet, C., Battaglia, P., et al., 2009. *Journal of Instrumentation*, 4:2010

[155] Hinshaw, G., Nolta, M. R., Bennett, C. L., et al., 2007. *ApJ*, 170:288

[156] Page, L., Hinshaw, G., Komatsu, E., et al., 2007. *ApJ*, 170:335

[157] Wandelt, B. D., Hivon, E., Górski, K. M., 2001. *Phys. Rev. D*, 64(8):083003

[158] Efstathiou, G., 2003. *MNRAS*, 346:L26

[159] Tegmark, M., 1997. *Phys. Rev. D*, 55:5895

[160] Lewis, A., Bridle, S., 2002. *Phys. Rev.*, D66:103511

[161] Cyr-Racine, F.-Y., Sigurdson, K., 2011. *Phys. Rev. D*, 83(10):103521

[162] Howlett, C., Lewis, A., Hall, A., et al., 2012. *JCAP*, 4:027

[163] Zaldarriaga, M., Seljak, U., Bertschinger, E., 1998. *ApJ*, 494:491

[164] Knox, L., 1995. *Phys. Rev. D*, 52:4307

[165] Hu, W., 2005. *Phys. Rev. D*, 71(4):047301

[166] Feng, B., Wang, X., Zhang, X., 2005. *Physics Letters B*, 607:35

[167] Hu, W., Sawicki, I., 2007. *Phys. Rev. D*, 76(10):104043

[168] Peiris, H. V., Easther, R., Flauger, R., 2013. *JCAP*, 9:018

[169] Kermish, Z. D., Ade, P., Anthony, A., et al., 2012. *Society of Photo-Optical Instrumentation Engineers (SPIE) Conference Series*, vol. 8452 of *Society of Photo-Optical Instrumentation Engineers (SPIE) Conference Series*

[170] Niemack, M. D., Ade, P. A. R., Aguirre, J., et al., 2010. *Society of Photo-Optical Instrumentation Engineers (SPIE) Conference Series*, vol. 7741 of *Society of Photo-Optical Instrumentation Engineers (SPIE) Conference Series*

[171] Austermann, J. E., Aird, K. A., Beall, J. A., et al., 2012. *Society of Photo-Optical Instrumentation Engineers (SPIE) Conference Series*, vol. 8452 of *Society of Photo-Optical Instrumentation Engineers (SPIE) Conference Series*

[172] King, O. G., Copley, C., Davies, R., et al., 2010. *Society of Photo-Optical Instrumentation Engineers (SPIE) Conference Series*, vol. 7741 of *Society of Photo-Optical Instrumentation Engineers (SPIE) Conference Series*

[173] QUIET Collaboration, Araujo, D., Bischoff, C., et al., 2012. *ApJ*, 760:145

[174] Hanson, D., Hoover, S., Crites, A., et al., 2013. *Physical Review Letters*, 111(14):141301

[175] Reichborn-Kjennerud, B., Aboobaker, A. M., Ade, P., et al., 2010. *Society of Photo-Optical Instrumentation Engineers (SPIE) Conference Series*, vol. 7741 of *Society of Photo-Optical Instrumentation Engineers (SPIE) Conference Series*

[176] Baumann, D., Jackson, M. G., Adshead, P., et al., 2009. Dodelson, S., Baumann, D., Cooray, A., et al., editors, *American Institute of Physics Conference Series*, vol. 1141 of *American Institute of Physics Conference Series*. 10–120